Fundamental Properties of a Spatially Oscillating Jet Emitted by a Fluidic Oscillator

vorgelegt von
MSc.
Florian Ostermann
geb. in Berlin

von der Fakultät V – Verkehrs- und Maschinensysteme
der Technischen Universität Berlin
zur Erlangung des akademischen Grades

Doktor der Ingenieurwissenschaften
- Dr.-Ing. -

genehmigte Dissertation

Promotionsausschuss:

Vorsitzender:	Prof. Dr.-Ing. Dirk Oberschmidt
Gutachter:	Prof. Dr.-Ing. Christian Oliver Paschereit
Gutachter:	Prof. Dr.-Ing. Julien Weiss
Gutachter:	Prof. Dr.-Ing. Sven Olaf Grundmann
Gutachter:	Dr. Rene Woszidlo

Tag der wissenschaftlichen Aussprache : 19. April 2018

Berlin 2018

Danksagung

Diese Dissertation entstand während meiner Tätigkeit als wissenschaftlicher Mitarbeiter am Fachgebiet für experimentelle Strömungsmechanik der Technischen Universität Berlin. Ich möchte mich an dieser Stelle bei allen bedanken, die mich bei meinen Experimenten, Auswertungen und Publikationen, die zu dieser Arbeit beitrugen, unterstützt haben. Ein besonderer Dank geht natürlich an meinen Doktorvater Prof. Dr. Christian Oliver Paschereit für die Möglichkeit zur Promotion an diesem tollen Fachgebiet. Sie haben ein wunderbares Arbeitsumfeld geschaffen, in dem das Forschen und Arbeiten Spaß macht und man sich gegenseitig hilft. Ich bedanke mich für Ihr Vertrauen, Ihren Zuspruch und Ihrer Unterstützung.

Ein ganz großes Dankeschön geht an Dr. Rene Woszidlo für die außerordentlich gute Unterstützung und Betreuung meiner Arbeit. Ich hatte an unseren langen und sehr fruchtbaren Telefonaten und Diskussionen auch nach 5 Jahren noch immer viel Spaß. Deine offene und humorvolle Art hat mir auch neben der Arbeit viel weitergeholfen und Freude bereitet. Vielen Dank, für deine nötige Geduld und Hartnäckigkeit. Vor allem bedanke ich mich für die Zeit die du dir für meine Arbeit und mich unabhängig von Tageszeit und Wochentag genommen hast.

Ein weiterer großer Dank geht an die Gutachter Prof. Dr. Julien Weiss und Prof. Dr. Sven Olaf Grundmann für die Bereitschaft das Gutachten für diese Dissertation zu übernehmen. Außerdem bedanke ich mich auch bei Prof. Dr. Dirk Oberschmidt für die spontane Übernahme des Vorsitzes.

Ich bedanke mich bei Dr. Navid Nayeri für seine offenen Ohren und Hilfsbereitschaft. Du hast immer eine offene Tür für mich gehabt. Außerdem hast du bei so manchen finanziellen Engpässen geholfen und dafür gesorgt, dass das Projekt auch ohne Förderung am Laufen bleibt. Ich möchte außerdem einen großen Dank an das Elsa-Neumann-Stipendium und an die DFG richten, ohne deren finanzielle Unterstützung diese Arbeit nie entstanden wäre. Für die große Hilfsbereitschaft möchte ich gerne meinen Kollegen danken. Besonders hervorheben möchte ich David Holst, Marvin Schönlau und Heiko Stolpe für Unterstützung bei der Inbetriebnahme des Windkanals und streikender Messtechnik, Moritz Sieber für die vielen konstruktiven Anregungen und Marvin Jentzsch für das blitzschnelle Kontrolllesen der Arbeit. Ein ganz großer Dank geht natürlich auch an Hajo Schmidt und Lemmy, die in unserem gemeinsamen Büro immer für gute Stimmung gesorgt haben und bei so manchem Frust mit motivierenden Worten aushalfen. Die Arbeit wäre natürlich auch nicht ohne die tatkräftige Hilfe unserer Werkstatt, unserem Sekretariat und unserer IT möglich gewesen. Vielen Dank für eure Unterstützung und der schnellen Hilfe bei den zumeist zeitkritischen Fragen und Aufgaben.

Ein großer Teil der Arbeit wurde von Studenten während ihrer Abschlussarbeiten unterstützt, ohne die ich die Versuchsaufbauten und Experimente niemals geschafft hätte: vielen Dank dafür. Ein besonderer Dank geht dabei an meine beiden studentischen Hilfskräfte Johan Feldwisch „Marc“ und Sascha Martinke.

Natürlich wäre auch ohne meine Familie und Freunde die Arbeit nicht möglich gewesen. Ich bedanke mich für die lustigen Abende und vielen tollen Aktionen bei meinen Freunden. Bei meiner Familie bedanke ich mich für die stets motivierenden Worte und Unterstützung: ich bin froh, dass ich euch habe. Ein besonderer Dank geht dabei an meine Eltern, die stets an mich

geglaubt und durch ihren Zuspruch und Unterstützung diese Arbeit überhaupt erst ermöglicht haben. Außerdem möchte ich mich ganz besonders bei meiner Freundin Kim bedanken. In den letzten Jahren wäre ich ohne dich häufig sehr verzweifelt gewesen. Du hast immer zu mir gehalten und mich versucht aufzubauen, wenn ich mal wieder gestresst und frustriert nach Hause gekommen bin. Danke, dass du mir den Rücken freigehalten und mich immer wieder aufgebaut und motiviert hast. Du bist einfach toll! Ein ganz spezieller Dank gilt auch unserer Tochter Pia, die gerade in den letzten anstrengenden Monaten mir mit ihrem Lächeln häufig den Tag rettete und mir damit in Erinnerung rief, worauf es im Leben ankommt.

Abstract

A jet is a fundamental flow scenario underlying several technical applications. Recently, spatially oscillating jets emitted by fluidic oscillators are employed to enhance mixing or control separation. Fluidic oscillators are able to emit a jet that spatially oscillates within a plane. Although their efficacy has been proven for many applications, the reasons for their performance remain unknown due to the lack of knowledge on the underlying, fundamental flow fields. The present work aims to analyze these flow fields in order to explain the underlying flow physics and to identify possible reasons for the high effectivity of spatially oscillating jets in various applications. The fundamental flow field of spatially oscillating jets emitted into a quiescent environment and into a crossflow are assessed experimentally. The complexity of the flow fields, which is caused by the three-dimensionality and the temporal unsteadiness, necessitates intermediate steps that break down the complexity. The individual steps undertaken to assess the complex flow field of spatially oscillating jets and the corresponding results are summarized in four publications that are the basis for this cumulative dissertation.

Various phase-averaging methods are evaluated for their suitability to phase-average the flow field of a spatially oscillating jet. Phase-averaging based on a pressure signal extracted from inside the fluidic oscillator is found to be appropriate. This method is used to phase-average the internal flow field of a fluidic oscillator. The time-resolved flow field allows to identify the driving mechanism behind the spatial oscillation. It is revealed that the volume flow through the feedback channels is the driving parameter of the oscillation frequency. Besides the spatial oscillation of the jet, the internal dynamics inside the oscillator also cause the jet properties (i.e., massflow and momentum) to oscillate temporally. Extending the results from the internal flow field, the three-dimensional fundamental flow field of a spatially oscillating jet emitted into a quiescent environment is investigated. Head vortices are identified inside the flow field, which are created at either side when the jet is fully deflected. The quantitative analysis of jet properties reveals that the entrainment of spatially oscillating jets is significantly enhanced compared to that of conventional steady jets, which indicates an improved mixing performance. The jet force of the spatially oscillating jet exceeds the theoretical force determined from assuming a top-hat velocity profile at the outlet. This difference reveals that the jet momentum is underestimated in most studies that use spatially oscillating jets for flow control. The experiences from these first studies regarding the acquisition of three-dimensional data and phase-averaging methods enable to investigate the complex, three-dimensional, time-resolved flow field of a spatially oscillating jet interacting with a crossflow. It is shown that the jet achieves a considerable penetration into the spanwise direction. Dominant, prevailing, streamwise vortices are identified in the flow field. They are suspected to be one reason for the high effectiveness of spatially oscillating jets in flow control. The driving mechanism behind these vortices is described by an analogy to a vortex-generating jet with a changing deflection angle. For high Strouhal numbers, a considerable wake is formed downstream of the jet because the crossflow is not able to adapt to the changing deflection angle. It is proposed that with further increasing Strouhal number, the flow field approaches a quasi-steady state.

The results of the individual publications are reviewed regarding their applicability and transferability to other studies. Possible shortcomings of the present work are discussed and the importance of the specific flow field properties is emphasized. Throughout this work, suggestions are made how to optimize the flow field properties to meet specific requirements for applications.

Zusammenfassung

Ein Strahl beschreibt ein fundamentales Strömungsszenario, welches vielen technischen Anwendungen zugrunde liegt. In den letzten Jahren werden räumlich oszillierende Strahlen, welche durch Fluidische Oszillatoren erzeugt werden, für Mischungsverbesserung und Strömungskontrolle eingesetzt. Fluidische Oszillatoren erzeugen einen Strahl, der innerhalb einer Ebene räumlich oszilliert. Obwohl ihre Effektivität in vielen Anwendungen bewiesen wurde, sind die Gründe für ihre Wirksamkeit weitestgehend unbekannt, da nur wenige Informationen über die zugrundeliegenden Strömungsfelder vorhanden sind. Die vorliegende Arbeit zielt darauf ab diese Strömungsfelder zu analysieren, deren Strömungsphysik zu erklären und mögliche Ursachen für die Effektivität räumlich oszillierender Strahlen in verschiedenen Anwendungen zu identifizieren. Das fundamentale Strömungsfeld räumlich oszillierender Strahlen mit und ohne Querströmung wird experimentell untersucht. Auf Grund der Dreidimensionalität und der zeitlichen Abhängigkeit, weisen die Strömungsfelder eine hohe Komplexität auf. Die Untersuchung wird daher in einzelne Zwischenschritte aufgeteilt. Die Zwischenschritte und ihre Resultate sind in vier Veröffentlichungen zusammengefasst und bilden die Basis der vorliegenden kumulativen Dissertation.

Um eine passende Phasenmittelungsmethode für einen räumlich oszillierenden Strahl zu entwickeln, wird die Eignung verschiedener Phasenmittelungsansätze verglichen. Die Phasenmittelung anhand eines Drucksignals aus dem Oszillatorinneren wird als eine passende Methode identifiziert. Sie ermöglicht die zeitliche Auflösung des internen Strömungsfeldes eines fluidischen Oszillators. Das gewonnene Strömungsfeld ermöglicht die oszillationsverursachende, interne Dynamik zu analysieren. Dadurch wird gezeigt, dass der Volumenstrom durch die Rückführkanäle der treibende Parameter hinter der Oszillationsfrequenz ist. Die interne Dynamik verursacht neben der räumlichen Oszillation auch eine zeitliche Oszillation der Strahleigenschaften, wie zum Beispiel Massenstrom und Impuls. Die Untersuchung des internen Strömungsfelds wird erweitert durch eine Analyse des dreidimensionalen externen Strömungsfeldes eines räumlich oszillierenden Strahls in ruhender Umgebung. Im Strömungsfeld sind Kopfwirbel zu erkennen, welche zum Zeitpunkt der maximalen Auslenkung des Strahls gebildet werden. Die quantitative Analyse der Strahleigenschaften weist darauf hin, dass die Mischungseigenschaften im Vergleich zu einem konventionellen Freistrahl deutlich verbessert sind. Anhand der Strahlkraft wird deutlich, dass der Strahlimpuls in den meisten Studien, welche räumliche oszillierende Strahlen für die Strömungskontrolle verwenden, unterschätzt wird. Die Erfahrungen der ersten Studien hinsichtlich der Erfassung dreidimensionaler Daten und Phasenmittelungsmethoden ermöglichen das komplexe, dreidimensionale, zeitaufgelöste Strömungsfeld eines räumlich oszillierenden Strahls in Interaktion mit einer Querströmung zu untersuchen. Es zeigt, dass der räumlich oszillierende Strahl eine deutlich größere Fläche stromab der Düse beeinflusst als ein stetiger Strahl. Zudem sind dominante, in Strömungsrichtung gerichtete Wirbel im Strömungsfeld vorhanden. Es wird angenommen, dass diese Wirbel ein Grund für die hohe Effektivität räumlich oszillierender Strahlen in der Strömungskontrolle sind. Die Wirbel lassen sich durch eine Analogie zu wirbelerzeugenden Strahlen mit veränderten Ausblaswinkeln erklären. Bei hohen Strouhal-Zahlen bildet sich hinter der Düse ein beständiger Nachlauf, da sich die Querströmung nicht mehr an den sich ändernden Ausblaswinkel anpassen

kann. Es wird vermutet, dass sich das Strömungsfeld mit weiter zunehmender Strouhalzahl einem zeitlich unabhängigen Zustand annähert.

Die Ergebnisse der einzelnen Publikationen werden hinsichtlich ihre Anwendbarkeit und Übertragbarkeit diskutiert. Mögliche Defizite der vorliegenden Arbeit werden erörtert und die Bedeutung der Strömungsfeldeigenschaften hervorgehoben. Zusätzlich werden Verbesserungsvorschläge gemacht welche diese Eigenschaften für bestimmte Anwendungen optimieren.

Contents

List of Figures

List of Tables

Chapter 1 | Introduction

What is the similarity between blow dryers, car exhausts, gush springs, and breathing out? All are examples of jets. A jet describes a fundamental flow scenario where a fluid is ejected through an orifice into an ambient fluid that may rest or may be in motion. Jets are experienced in nature and in everyday life as well as in technical applications. Some examples include, but are not limited to air conditioning, central venous catheters, volcanoes, or flow control actuators. The multitude of applications has motivated extensive research on jets. The review by v. Krzywoblocki (1956) that collects publications investigating jets analytically or experimentally before the mid-1950s lists more than 1000 elements in its bibliography. Since the research on jets is ongoing, it is expected that the number of studies on jets has multiplied till today. The present work contributes to this by investigating the fundamental properties of a spatially oscillating jet emitted by a fluidic oscillator.

In the following, an overview of the fundamentals of jets is provided. It is followed by an introduction of fluidic oscillators and the reasons for why spatially oscillating jets are of interest and why only little information has been available so far. Finally, the objectives of the pursued work are defined, and it is specified how the publications address these objectives.

1.1 Steady Jets

Generally, the flow field of a subsonic, steady jet emitted into a quiescent environment may be seen as a special case of shear flow. The flow field can be split into three zones. The first zone starts immediately after the jet leaves the orifice: the potential core zone. In this zone the maximum velocity in the jet's center at each streamwise position is constant and equal to the outlet velocity. A shear layer is formed between the jet and the quiescent environment. The size of the shear layer increases with distance to the orifice. In zone two (i.e., the transitional zone), the potential core is terminated by the shear layers from the sides of the jet coalescing. Hence, viscous mixing occurs in the complete jet from this position on. Correspondingly, all velocities downstream of the start of the transitional zone are smaller than the outlet velocity. In the far field, the jet evolves into a self-similar profile. This third zone is referred to as the zone of self-similarity and indicates the starting point of the jet being fully developed. Beyond this streamwise position, the jet behavior is independent of the orifice geometry. In this zone, all jets can be replaced by a jet originating from a point source of momentum at a virtual origin. Schlichting and Gersten (2006) describe this zone analytically for planar and axisymmetric jets. Comprehensive information on the turbulence quantities in the self-similar zone are provided by Wygnanski and Fiedler (1969).

In contrast to the self-similar zone, the jet properties in the first two zones are dependent on the orifice and nozzle geometry. Jet properties of three-dimensional jets that are emitted through various orifice geometries are experimentally investigated by Sforza et al. (1966). Most of the studies on steady jets emitted into a quiescent environment are limited to the subsonic regime.

An example for a study on supersonic jets is Zaman (1996) who investigates the evolution of supersonic jets ejected through various orifices.

In most applications, jets are not emitted into a quiescent environment. Instead, they interact with a crossflow. The fundamental flow field of a jet in crossflow (JICF) is considerably more complex because, generally, it is three-dimensional and several additional flow features are created. A considerable amount of research has been conducted, which aims to describe these flow features (e.g., Fric and Roshko, 1994; Kelso et al., 1996). Besides the jet bending into the direction of the crossflow, following prominent flow features may be found in the flow field of a JICF:

- Shear layer vortices are formed inside the jet's shear layer at the windward side of the jet close to the orifice (Fric and Roshko, 1994; Kelso et al., 1996; Muppidi and Mahesh, 2005). The crossflow imposes an adverse pressure gradient to the jet, which causes the windward side of the jet to separate upstream of the orifice. This results in an acceleration at the leeward side of the jet, which, in interaction with the crossflow, results in the shear layer vortices. Fric and Roshko (1994) and Becker and Massaro (1968) note that the shear layer vortices exhibit a similarity to the Kelvin-Helmholtz instability of steady jets emitted into a quiescent environment.

- Downstream of the orifice, wake vortices are formed in the near field. Fric and Roshko (1994) suggest that these tornado-like vortices are similar to the shedding of vortices experienced from a two-dimensional, solid cylinder that replaces the jet.

- Upstream of the orifice, the horseshoe vortex, also known as the necklace vortex, is formed by the crossflow (Fric and Roshko, 1988; Kelso and Smits, 1995). This vortex is caused by the adverse pressure gradient imposed by the jet, which causes the crossflow to separate and form the vortex. The vortex is bent around the jet.

- The most prominent flow feature is the counter-rotating vortex pair because it prevails far downstream and dominates the far field (Fearn and Weston, 1974). Various explanations for the driving mechanism behind these vortices may be found throughout the literature. For example, Muppidi and Mahesh (2006) use a two-dimensional model to show that the deformation of the jet may be one reason for the counter-rotating vortex pair.

Note that the described flow features are existent in the incompressible case of a JICF. Compressibility effects may change the flow field significantly (e.g., Gruber et al., 1995; Papamoschou and Hubbard, 1993). A review summarizing research on the fundamental flow field behind JICF is provided by Margason (1993) and Mahesh (2013).

1.2 Unsteady Jets

The previous discussion of the fundamental flow fields is limited to steady jets. Several studies investigate the flow field of unsteady jets. For example, Crow and Champagne (1971) excite a natural instability of a steady jet, which results in an increased entrainment of ambient fluid. Other examples are provided by Platzer et al. (1978) and Bremhorst and Hollis (1990) who show that the entrainment of a pulsed jet emitted into a quiescent environment is significantly enhanced, which indicates a superior mixing performance compared to steady jets. Bremhorst

(1979) summarizes that the jet properties of unsteady jets differ significantly from that of a steady jet. The results suggest that unsteady jets may be beneficial for specific applications that require a high mixing performance. Building on this, studies of the fundamental properties of pulsed jets in crossflow were conducted for example by Johari et al. (1999) and Eroglu and Breidenthal (2001). They reveal that depending on the duty cycle and the pulsing frequency the penetration of the jet into the crossflow can be increased significantly. Additional vortex rings are created, which dominate the flow field. For an optimized duty cycle and pulsing frequency, the mixing rate of pulsed jets is enhanced by up to 50% compared to steady jets in crossflow.

Pulsing a jet introduces a temporal unsteadiness. It is also possible to impose a spatial unsteadiness. The properties of spatially oscillating jets in a quiescent environment are assessed by several studies. However, controversies regarding the entrainment of spatially oscillating jets in these studies are evident. Whereas Platzer et al. (1978) reveal that the entrainment of a spatially oscillating jet is higher than that of a steady jet, Srinivas et al. (1988) and Raman et al. (1993) argue that the entrainment is smaller. Mi et al. (2001) addresses these controversies and attributes the differences to the employed setups. Based on their data, they conclude that the entrainment of a spatially oscillating jet is smaller. It is noteworthy that these studies investigate spatially oscillating jets that oscillate within one plane in a windshield wiper manner. Other means of spatial oscillation are also possible but less common. One example is Wong et al. (2008) who investigate the flow field of a precessing jet.

1.3 Fluidic Oscillators

A convenient way to generate spatially oscillating jets are fluidic oscillators. The word "fluidic" is a made-up word combined from fluid and logic. Fluidic oscillators are part of a large group of components called fluidics. A summary and the theory behind several fluidic devices is provided by Kirshner and Katz (1975). Fluidics were developed in the late 1950s at the Harry Diamond Laboratories as an alternative to electric components (Angrist, 1964). Fluidic oscillators are based on fluidic switches or amplifiers. Connecting the control ports with each other yields a self-oscillating device: a fluidic oscillator (Spyropoulos, 1964).

Several designs of fluidic oscillators exist with varying internal mechanisms that cause the spatial oscillation. They can be categorized in three general categories based on the number of feedback channels. Figure 1.1 portrays the conceptual design of the three categories. Figure 1.1 (a) illustrates the working principle of the feedback-free oscillator. A detailed assessment of the internal flow field is provided by Gregory et al. (2005) and Tomac and Gregory (2014). Two inserted jets with a steady supply collide inside the mixing chamber. Shear layer instabilities of the resulting jet cause the spatial oscillation of the exiting jet. The oscillation frequency mainly depends on the supply rate and the size of the oscillator.

Fluidic oscillators with one feedback channel are called sonic oscillators (figure 1.1, b). A steady supply of fluid forms a jet downstream of the inlet nozzle. The jet attaches to either side of the wall due to the Coanda effect. It induces a low pressure which is transferred through the feedback channel to the opposite wall. The low pressure draws the jet to the opposite wall where the same process is repeated. Hence, the oscillation frequency primarily depends on the length of the feedback channel.

The last category of fluidic oscillators entails two feedback channels (figure 1.1, c). In this concept, the main jet attaches to either side of the mixing chamber. Some fluid is separated into

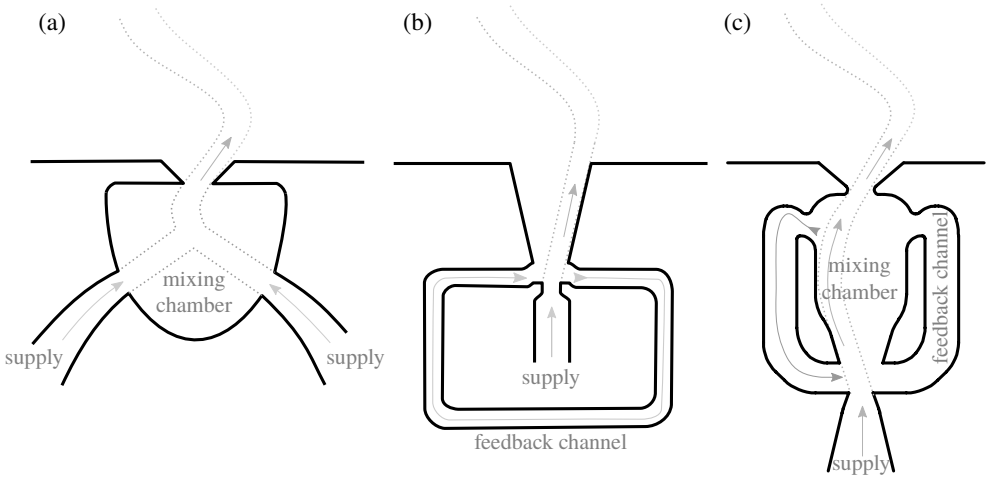

Figure 1.1: Different categories of fluidic oscillators. (a) The feedback-free oscillator (Stouffer and Bower, 1998), (b) the sonic oscillator (Spyropoulos, 1964), and (c) the two feedback channel oscillator (Raghu, 2001).

the feedback channel and led back to the inlet where it interacts with the main jet and causes the main jet to flip to the other side. In this concept the volume flow through the feedback channel is the driving mechanism. Therefore, the oscillation frequency is primarily dependent on the scale of the oscillator and the supply rate.

All oscillators depicted in figure 1.1 emit a spatially oscillating jet. Several modifications of these concepts exist. For example, placing a splitter at the outlet causes the oscillator to emit two alternating pulsed jets. Furthermore, it may be beneficial to combine several fluidic concepts. One example for a combination of two fluidic concepts is the suction and oscillatory blowing oscillator (SaOB oscillator) introduced by Arwatz et al. (2008). They use an ejector to suck in fluid through two ports. An adjacent sonic oscillator equipped with a splitter at the outlet generates two pulsed jets. They use this combination of suctioning and pulsed blowing for flow control purposes. Another example is employed by Bauer et al. (2014). They use a large-scale master oscillator that triggers the oscillation of an array of smaller oscillators. This setup allows for changing the supply rate and oscillation frequency independently. One historic review on fluidic oscillator concepts is presented by Campagnuolo and Lee (1969). A more recent, comprehensive review on the discussed fluidic oscillator concepts and their development is provided by Gregory and Tomac (2013).

The oscillation frequency of fluidic oscillators ranges from the order of one Hertz (Viets, 1975) to several kilo Hertz (Gregory et al., 2007) depending on the oscillator geometry, size, and supply rate. The working principle of fluidic oscillators involves no moving parts, which makes them reliable and thus attractive for technical applications. Examples include windshield washers, Jacuzzi nozzles, or sprinklers. In recent years, they have proven beneficial in flow control applications. They have successfully been used in separation (Cerretelli and Kirtley, 2009; Seele et al., 2009), noise (Raman and Raghu, 2000, 2004), and combustion control (Guyot et al., 2009) as well as for the enhancement of mixing (Lacarelle and Paschereit, 2012). A specific example for the performance of fluidic oscillators is provided by Schmidt et al. (2015). They employ fluidic oscillators for separation control on a flap adjacent to the back of a bluff

body to reduce the drag. They achieve net drag improvements of 18 % compared to the blunt rear end configuration. Another example is provided by Jentzsch et al. (2017). They use fluidic oscillators for reducing spanwise flow on a swept-back wing. This reduces the pitching moment coefficient, which stabilizes the airplane. Koklu and Owens (2017) compare various separation control techniques on a generic model. They reveal that fluidic oscillators outperform several other means of separation control.

1.4 Motivation and Objectives

Spatially oscillating jets emitted by fluidic oscillators are effective and efficient in flow control applications as summarized in the previous section. However, the reasons for this performance remain unknown due to the lack of knowledge on the underlying mechanisms and the fundamental flow fields. This lack is due to various challenges experienced when investigating the flow field of spatially oscillating jets. The three-dimensionality and unsteadiness propose a challenge to experimental investigations. The naturally oscillating flow field does not provide a trigger signal for phase-locked measurements, which makes it challenging to acquire time-resolved data. However, time-resolved data is required for studying the flow features of a spatially oscillating jet and identifying underlying flow physics. The three-dimensionality adds to this because most measurement techniques are not suitable for acquiring time-resolved data of a three-dimensional flow field at a high resolution. Numerical studies are also burdened with the required temporal and spatial scales. Furthermore, the absence of experimental data for a quantitative validation of the numerical results leaves assumptions on the flow field derived from numerical studies uncertain. Due to these challenges, mainly investigations on the global effect of spatially oscillating jets or the qualitative, time-averaged flow fields exist. Most of these studies are also limited to specific use-cases involving to many parameters, which makes the transferability to other studies questionable. It is noteworthy that there are a few exceptions that are mainly focused on the time-resolved internal flow field of fluidic oscillators (e.g., Bobusch et al., 2013a; Gregory et al., 2009; Wassermann et al., 2013). These studies are discussed in the introduction of each publication provided in this work.

The present work addresses the lack of knowledge on the underlying flow field of spatially oscillating jets. The objective is to identify possible reasons for the suitability of fluidic oscillators in applications by assessing the fundamental flow fields of a spatially oscillating jet emitted into a quiescent environment and a crossflow. The number of parameters is reduced to a necessary minimum to simplify the investigations and to allow a comparison of the results to other fundamental flow fields such as steady jets. Therefore, compressibility effects are not included in this study, although they were investigated in an associated publication (von Gosen et al., 2015). Throughout the publications, suggestions are made how different parameter may affect the results. The work provides a comprehensive insight into the general, fundamental flow fields underlying most of the applications of spatially oscillating jets. Possible reasons for the high effectivity of fluidic oscillators are identified, analyzed, and discussed. This allows for more detailed investigations in the future to validate the suggestions made in this work. Furthermore, the results of this work may be used for validating numerical studies that may enable more parametric variations.

The present manuscript summarizes results of the work done to fulfill the mentioned objectives. In the beginning of the manuscript, details on the setup and the data analysis are provided

extending the information from the individual publications. The publications included in this manuscript contain the results of the presented work. The publications are ordered sequentially by their publication or submission date because each publication builds on the results from the previous one. Publication **I** investigates various phase-averaging techniques in order to identify a suitable method for the pursued work. It highlights one method that is suitable for naturally oscillating flow fields such as that of the spatially oscillating jet. This method is employed in publication **II** to investigate the internal flow field of a fluidic oscillator. The governing mechanism of the oscillation is revealed as well as some suggestions for potential improvements in the design are provided. Publication **III** investigates the three-dimensional flow field of a spatially oscillating jet emitted by a fluidic oscillator into a quiescent environment. It provides an insight into the flow field thereby highlighting dominant flow features. Publication **III** also focuses on the jet properties of the oscillating jet which are expected to be beneficial for flow control such as the entrainment. In publication **IV**, the time-resolved fundamental flow field of a spatially oscillating jet emitted into a crossflow is analyzed. It provides a comprehensive overview of the flow features for different velocity ratios and Strouhal numbers. It discusses the influence of the oscillation frequency and includes an analysis of the vortex dynamics that are believed to be beneficial for applications. Furthermore, quantitative application-relevant information such as the jet trajectory is extracted from the flow field.

The manuscript is concluded by a discussion of the individual papers extending the respective conclusions of the publications. For each publication, the contribution to the objective of this work as well as limitations of the results, the impact on other studies and suggested future work are discussed. Finally, some concluding remarks summarize the achievement of the entire work and discuss possible future studies that build up on the presented results.

Chapter 2 | Experimental Details

The main information on the experimental setup is described in each publication individually. In this chapter, additional details on the experimental setups are provided and the reasons for some specific decisions on the setup are discussed. First, the employed fluidic oscillators are examined. Subsequently, general details on the measurement equipment valid for all publications are provided. Finally, specific challenges and details of each individual setup are discussed.

2.1 Employed Fluidic Oscillators

Two fluidic oscillator designs are employed in the present work. Both oscillators exhibit a similar working principle as they both have two feedback channels (figure 2.1). One design appears more streamlined; thus, it is referred to as the curved oscillator. Correspondingly, the other oscillator is referred to as the angled oscillator. These particular designs are chosen because they have been used in several flow control studies (e.g., Crittenden and Raghu, 2009; Raman and Cornelius, 1995; Schmidt et al., 2015; Seele et al., 2009). The design of the angled oscillator appears rather basic and simplified. The plain walls are beneficial for PIV measurements in the internal flow field because of less optical interference with the laser sheet. Therefore, it was investigated first to get an impression of the internal and external flow field of a spatially oscillating jet in publications **I** and **II**. Learning from the results of publication **II**, the curved design was employed in the subsequent investigations (i.e., publications **III** and **IV**). A detailed discussion of this decision is provided in section 5.2.

The fluidic oscillators are manufactured in varying sizes. In publications **I**-**III** the oscillator throat (i.e., the smallest cross-sectional area at the outlet) is $25 \times 25\,\mathrm{mm}^2$ yielding a hydraulic diameter of $d_h = 25\,\mathrm{mm}$, which is considerably large compared to the size of the oscillators in most applications. This scaled-up design allows for an easier investigation of the internal and external flow field because the flow features are also enlarged. Furthermore, the comparably large cavities of the internal geometry simplify the installation of pressure taps and provide

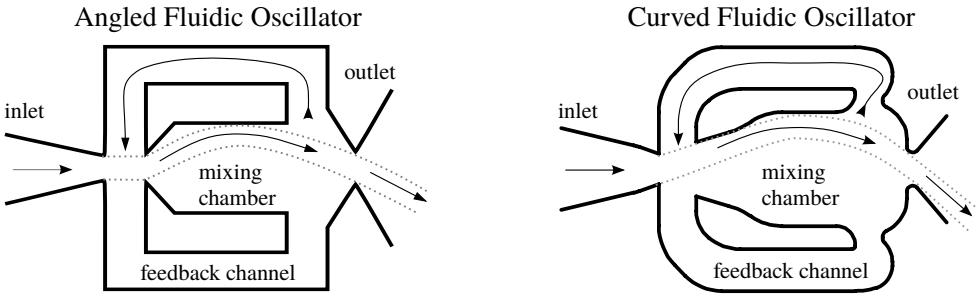

Figure 2.1: The employed fluidic oscillator designs.

simplified access to the internal geometry for polishing or cleaning. In publication **IV**, the size of the wind tunnel restricts the oscillator size. Therefore, the throat size is reduced to $10 \times 10\,\mathrm{mm}^2$ with a hydraulic diameter of $d_h = 10\,\mathrm{mm}$.

All employed oscillators are milled from acrylic glass. Extensive polishing of the surfaces provides unhindered optical access for laser and camera for the internal velocity measurements. Although no optical access was required in publication **IV**, the small oscillator is also milled from acrylic glass and polished afterward because the transparent surfaces allow the laser to pass through the oscillator, which reduces reflections on the visible oscillator surface. A cover plate encloses the oscillators' geometry and is fixed in place with screws. Vacuum grease is applied in between the geometry and the cover plate to assure airtightness, which was validated multiple times. A plenum is added upstream of the inlet and a honeycomb is installed inside the inlet to provide homogenous inflow conditions. In publication **IV**, an additional filter mat aims to further decrease the level of turbulence at the oscillator inlet. The level of turbulence is minimized in order to decouple the inflow conditions from the supply chain upstream of the oscillator thereby increasing the comparability to other studies.

The amount of pressurized air that is supplied to the fluidic oscillators is controlled by a massflow controller. A seeding generator is placed in the pressure supply chain downstream of the massflow controller. It provides seeding particles to the jet emitted by the fluidic oscillator. The amount of seeding is controlled by a bypass equipped with a high precision, manual valve.

Table 2.1 provides an overview of the employed fluidic oscillators in each publication and the range of investigated supply rates. The outlet velocity U_{bulk} is the theoretical outlet velocity that assumes that the supplied massflow $\dot{m}_{supply}$ ejects into ambient conditions (i.e., density ρ_0, speed of sound a_0, and kinematic viscosity ν_0) with a top-hat velocity profile (Eq. 2.1). In fact, the actual maximum jet velocity exceeds this theoretical velocity as shown and explained in publication **III**.

$$U_{bulk} = \frac{\dot{m}_{supply}}{\rho_0 A_{outlet}} \tag{2.1}$$

Determining the jet Mach number Ma_{jet} that is based on the bulk velocity and the ambient speed of sound $a_0 \approx 340\,\mathrm{m/s}$ (Eq. 2.2) yields $\mathrm{Ma}_{jet} < 0.3$ for all scenarios in table 2.1. Generally, it is reasonable to neglect any compressibility effects in this velocity regime. Therefore, the flow is considered incompressible in all publications.

$$\mathrm{Ma}_{jet} = \frac{U_{bulk}}{a_0} \tag{2.2}$$

Table 2.1: Overview of the employed fluidic oscillators.

Publication	Design	d_h (mm)	Supply Rate (kg/h)	U_{bulk} (m/s)	Re_{jet} ($\cdot 10^3$)	f_{osc} (Hz)
I	angled	25	10 - 100	3.8 - 38	6.0 - 60	2.8 - 22
II	angled	25	10 - 100	3.8 - 38	6.0 - 60	2.8 - 22
III	curved	25	20 - 80	7.4 - 30	12 - 49	4.9 - 19
IV	curved	10	6.4 - 44	15 - 100	9.7 - 65	23 - 140

The jet Reynolds number Re_{jet} is based on the theoretical bulk outlet velocity and the hydraulic diameter (Eq. 2.3). The Reynolds numbers indicate a turbulent flow inside the oscillator for all scenarios because it is well within the turbulent regime of a pipe flow $\mathrm{Re}_{jet} > 4000$. The oscillation frequency f_{osc} is determined from a fast Fourier transformation of the reference signal. It is evident that the smaller scale of the oscillator in publication **IV** results in a higher oscillation frequency. It is noteworthy that the jet Strouhal number St_{jet} (Eq. 2.4) is approximately constant in the limited range $0.01 < St_{jet} < 0.02$ for all scenarios independently of the supply rate, the design, and the size of the oscillator. The reason for this observation and its consequences are discussed in publication **III** and in section 5.3.

$$\mathrm{Re}_{jet} = \frac{U_{bulk} \cdot d_h}{\nu_0} \tag{2.3}$$

$$\mathrm{St}_{jet} = \frac{f_{osc} \cdot d_h}{U_{bulk}} \tag{2.4}$$

2.2 Pressure Measurements

Only very few details on the pressure measurements are provided in the publications. The primary focus of the pressure measurements is to acquire a reference signal for phase-averaging (Section 3.1). Hence, the actual pressure is of less importance. Instead, it is more important to acquire pressure information clearly exhibiting the oscillation frequency. For finding a suitable position, pressure taps are installed throughout the internal geometry of the fluidic oscillator (figure 2.2, left). Note that these positions are only valid for the angled oscillator design employed in publications **I** and **II**. The other oscillators are equipped with fewer pressure taps. Figure 2.2 (right) illustrates the geometry of one pressure tap. Small holes with a diameter of 0.8 mm are drilled from the inside of the geometry in order to achieve a sharp edge between geometry and pressure hole. Another hole is drilled from the opposite side and a small tube with an inner diameter of 2.1 mm is glued inside. The pressure sensor inlet is flush to this tube. The inner diameters of this assembly are optimized regarding the frequency response by using the approach of Bergh and Tijdeman (1965). Based on this approach, the resonance frequency of the pressure taps is approximately 1000 Hz. At this frequency, the amplitude is increased by a factor of 7. The phase-lag induced by the pressure tap is negligible compared to the oscillation period duration.

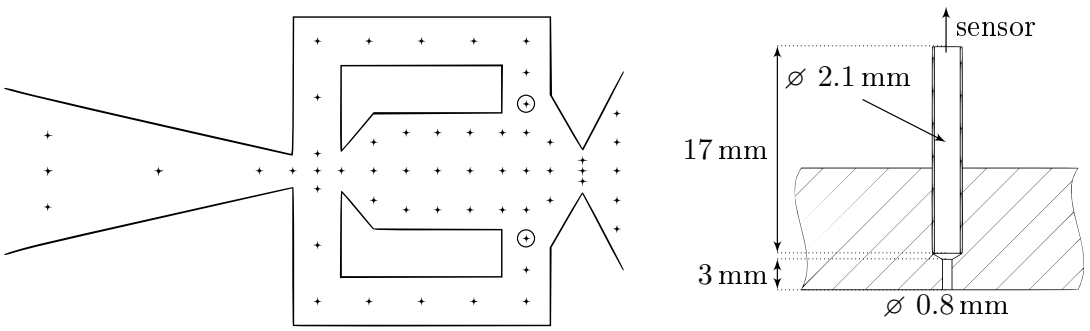

Figure 2.2: Pressure tap positions (left) and pressure tap geometry (right).

Pressure sensors by Sensortechnics are employed for the time-resolved pressure measurements. Their response time is faster than 10 µs, which enables to resolve frequencies two orders of magnitude higher than the oscillation frequencies of the investigated fluidic oscillators. An adequate pressure sensor range is chosen for each position individually varying from 10 to 50 mbar. The signals of the pressure sensors are amplified using an in-house amplifier and digitized by a cDAQ system (by National Instruments) composed of NI 9215 analog modules and a NI 9188 mainframe. The signal is sampled at 16 381 Hz. This sampling rate is multiple orders of magnitude higher than the oscillation frequencies. Furthermore, it is high enough that possible anti-aliasing effects are out of the range of interest. The sampling rate is a prime number in order to avoid any phase-locking to the oscillation frequency.

The setup enables time-resolved pressure measurements. The positions are evaluated for the oscillation amplitude in the fast Fourier transformation (FFT). The position with the highest ratio between oscillation frequency and other frequencies is found to be located at the feedback channel inlet. This position is circled in figure 2.2 (left). Due to the 180° phase-lag, the amplitude is doubled when the signals from the symmetrical positions are subtracted from each other. The resulting signal serves as the reference signal for phase-averaging, which is described in detail in publication **I** and section 3.1. The complete, time-resolved pressure field for the angled fluidic oscillator is measured by Gärtlein (2014) and for the curved oscillator by Feldwisch (2015).

2.3 Particle Image Velocimetry

Particle image velocimetry (PIV) is a suitable measurement technique for the pursued objectives in the present work. PIV acquires planar two- or three-dimensional velocity data without disturbing the flow field.

In publications **I** and **II** a high-speed mono PIV system is employed for the acquisition of velocity data from the internal and external flow field of a fluidic oscillator. It was decided to employ a high-speed PIV system because the data provides a reliable benchmark for developing phase-averaging techniques. The high-speed PIV system consists of a high-speed Nd:YLF laser (Quantronix Darwin Duo 100) and a high-speed camera (Photron Fastcam SA 1.1). The laser is able to emit a double laser pulse at a repetition rate of up to 10 kHz. The energy per pulse is 60 mJ at a repetition rate of 1 kHz. An adjustable laser arm by ILA GmbH is mounted to the laser, which includes the optical lenses that span up the laser sheet. The camera is able to record up to 5400 monochrome images per second at a resolution of 1024×1024 pixels and a bit depth of 12 bits. The timing between the components is ensured by a synchronizer by ILA GmbH. In publications **I** and **II**, the PIV is sampled at 1500 Hz, which is two orders of magnitude higher than the oscillation frequency. This frequency was chosen as a compromise between measurement duration (i.e., captured oscillation periods) and temporal resolution (i.e., samples per period). For each measurement, approximately 11 000 snapshots are acquired over 7.3 seconds. The PIV snapshots are post-processed using PIVView2C v3.5 by PIVTec. The exact timestamp of each PIV snapshot is acquired by the cDAQ system that is also used for the acquisition of the pressure signals as described in section 2.2. Since the trigger signals for the camera and the laser are too short to be acquired reliably at the set sampling rate, an auxiliary signal provided by the synchronizer is used instead. The timestamps provided by the auxiliary signal are configured to be located in between the two laser pulses.

A stereoscopic particle image velocimetry (stereo PIV) system is used in publications **III** and **IV**. Compared to the high-speed mono PIV system, it is able to measure all three velocity components within a plane. Furthermore, the cameras have a higher image resolution, which is expected to achieve a higher quality and spatial resolution of the images. The stereo PIV system consists of an EverGreen 200 laser by Quantel laser and two pco.2000 cameras by PCO AG. The laser is able to provide 15 double laser pulses per second, each with an energy of up to $200\,\mathrm{mJ}$. A laser arm that provides the optical lenses for spanning up the laser sheet is mounted to the laser. The cameras are able to record 14 monochrome images per second with an image resolution of 2048×2048 pixels and a bit depth of 14 bits. A synchronizer by ILA ensures the timing between the individual components. In publications **III** and **IV**, the PIV sampling rate is set to 5 Hz and 6 Hz respectively because at small acquisition rates the cameras work more reliably. For each measurement, 8000 PIV snapshots are acquired over approximately 25 minutes. The images are post-processed by PIVView3C v3.6 by PIVTec. The timestamp is provided by the camera trigger signal. The increasing flank of the camera trigger signal is defined as the timestamp of the corresponding snapshot.

2.4 Internal Flow Field of a Fluidic Oscillator

Several challenges are faced when performing PIV measurements in the internal flow field of a fluidic oscillator. The internal geometry prevents placing a target at the region of interest for calibration. Therefore, the internal geometry itself is employed for the calibration by identifying points with known coordinates. Points inside the measurement plane are selected to avoid perspective errors.

The laser that passes through the internal geometry causes reflections at the wall of the oscillator, which provokes an overexposure to the camera. A mask made of paper is placed between camera and measurement plane to shade these reflections. However, the mask causes a loss of velocity data close to the wall. During the post-processing of the flow fields, the wall of the oscillator is padded with zeros and the missing velocities close to the wall are interpolated. Unfortunately, this may cause streamlines to end or begin at the wall, which results in local massflow sinks and sources. Therefore, it is proposed for future studies when investigating the flow field inside a nozzle to interpolate the velocities while obeying the continuity equation. This was not realized for the data of publication **II**. Later, a corresponding approach was used for the visualization of the internal flow field of the curved oscillator by Sieber et al. (2016a).

The geometry acts as a set of lenses by refracting the laser sheet, which results in an inhomogeneous illumination inside the oscillator. Shadows cast by the screws fixing the cover plate to the geometry add to this. The inhomogeneous illumination prevents the measurement of the complete internal flow field at once. Therefore, the laser position is changed three times with the goal to illuminate all regions of the flow field at least once. However, a few regions remain in the shadow for all three laser positions. Velocities in these regions are determined from mirroring at the line of symmetry. Eventually, this approach was sufficient to acquire the complete internal flow field of the angled (publication **II**) and curved (Ostermann et al., 2015; Sieber et al., 2016a) fluidic oscillator.

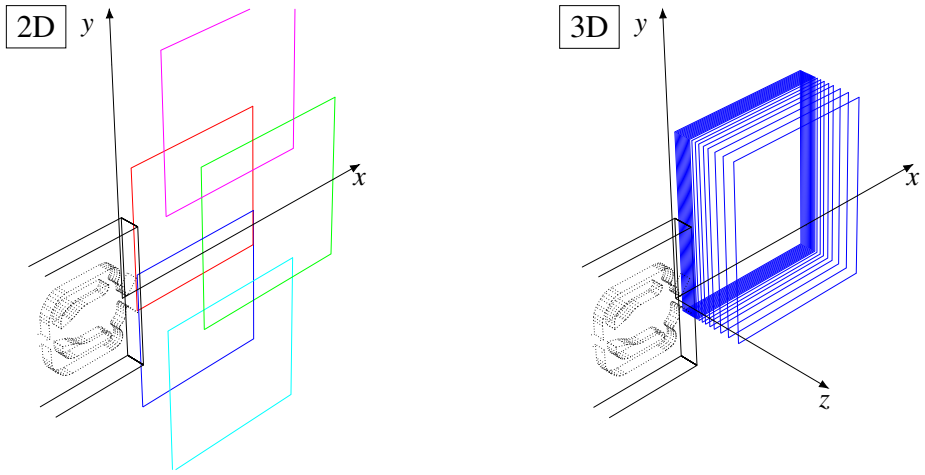

Figure 2.3: Outer limits of the PIV fields that are acquired of the external flow field by using the mono high-speed PIV system (2D) and the traversable stereo PIV system (3D).

2.5 Jet Emitted into a Quiescent Environment

The flow field of the oscillating jet extends in streamwise and lateral direction due to the changing deflection angle of the jet. For an effective acquisition of the flow field, a compromise between spatial resolution and spatial extent of the measurements is required. One suitable approach requires to split the region of interest into several windows which are measured individually. In publications **I** and **II**, five windows of the flow field are measured sequentially using the high-speed PIV system (figure 2.3, 2D). The individual windows overlap by approximately 25 %. The windows located farther downstream capture a larger region of the flow field at a smaller spatial resolution. This is accepted because the velocity gradients decrease in streamwise direction, hence a sparser spatial resolution is sufficient for capturing the main flow features. The windowing of the flow field allows for a comparably high spatial resolution of 0.25 vectors per millimeter on average (i.e., 6.25 vectors per d_h). During post-processing the velocities from all windows are interpolated onto a global grid. The overlapping regions between the windows are averaged with a linear weighting that provides a smooth transition between the windows. The total captured flow field extends from 40 to $600\,\mathrm{mm}$ in x-direction (i.e., 1.6 to $24\,d_h$ in streamwise direction) and from -500 to $480\,\mathrm{mm}$ in y-direction (i.e., -20 to $19\,d_h$ in lateral direction) with the origin being located in the center of the oscillator nozzle throat.

In publication **III**, the stereo PIV system is employed to measure the complete three-dimensional external flow field. The fluidic oscillator is traversable for acquiring the three-dimensional flow field plane-by-plane. It was decided to move the oscillator instead of the PIV system in order to avoid the higher risk of alignment errors, which is induced by moving the laser arm. In total, 22 x-y-planes that are scattered in z-direction parallel to the oscillation plane are acquired individually per flow field (figure 2.3, 3D). The locations of the planes are chosen in accordance to anticipated gradients. Therefore, more planes are located near the oscillator exit and fewer planes are located away from the jet exit with the last plane already being located in a quasi-quiescent environment. The smallest distance between the planes is $3\,\mathrm{mm}$ (i.e., $0.12\,d_h$) and the largest distance is $28\,\mathrm{mm}$ (i.e., $1.12\,d_h$). The measured volume extends from

30 to 350 mm in x-direction (i.e., 1.2 to 14 d_h), from −50 to 350 mm in y-direction (i.e., −2 to 14 d_h), and from −15 to 138 mm in z-direction (i.e., −0.6 to 5.5 d_h). The final resolution in the x-y-plane is 0.36 vectors per millimeter (i.e., 9 vectors per d_h), which is higher than in the first investigation using the high-speed PIV system. It is evident that this measurement volume captures only approximately one quarter of the complete flow field to $x = 14\,d_h$. One other quarter is resolved by mirroring the 180°-phase-shifted volume at the x-z-plane at $y = 0$. Subsequently, the other half of the flow field is determined by mirroring the volume at the x-y-plane at $z = 0$. It is noteworthy that the mirroring does not consider possible meandering of the jet. Therefore, a meandering correction is applied to the jet properties in publication **III**.

Another challenge for PIV measurements in the external flow field of a jet is the selection of an appropriate pulse distance between the laser pulses because of large differences between the velocities inside the jet and the velocities in the quiescent environment. This is of particular interest in publication **III** because this study investigates the entrainment of the spatially oscillating jet, which induces small velocities over a large area. A large pulse distance would resolve these small velocities at a high accuracy. However, it is not able to capture the high velocities inside the jet because particles leave the measurement plane or leave the post-processing interrogation window, which complicates the correct determination of these high velocities. In all publications, the pulse distance was adjusted for each plane and supply rate individually. This is achieved by performing short test measurements and identifying the maximum displacement of the particles. The pulse distance is adjusted to yield a maximum displacement of 7 pixels inside the plane. With an interrogation window size of 24×24 pixels, this is approximately one third of the interrogation window length, which is suggested as the maximum reliably resolvable displacement by Keane and Adrian (1990). However, modern PIV-processing options such as the multigrid refinement increases the maximum resolvable displacement (Scarano and Riethmuller, 2000), which leaves the conducted approach safe for selecting a suitable pulse distance for the maximum displacement. Boillot and Prasad (1996) suggest that the minimum resolvable displacement is one particle diameter in the image. Since the particles have only a diameter of approximately 1 µm, they are captured by one pixel only. Therefore, this suggestion would lead to a minimum resolvable distance of one pixel. Fortunately, modern PIV post-processing algorithm are able to reliably resolve displacements down to 0.1 pixel by fitting a Gaussian function to the peak of the correlation coefficient. Thus, the minimum resolvable displacement is 1/70th of the maximum resolvable displacement. Since this range is not very large, it supports the necessity to optimize the pulse distance for each plane individually to capture a maximum of the velocities.

2.6 Jet Emitted into a Crossflow

In publication **IV** the fluidic oscillator is placed inside a wind tunnel in order to investigate the interaction between a spatially oscillating jet and a crossflow. The wind tunnel was built in the 1970s and is located at the Hermann-Föttinger-Institut of the Technische Universität Berlin. Prior to the presented work, the wind tunnel was mainly used for fundamental investigations on shear layers. For the present work, the wind tunnel was refurbished and prepared specifically for the pursued measurements. Publication **IV** provides only very limited information on the wind tunnel. Furthermore, no detailed documentation of the wind tunnel exists. Therefore, this section provides some additional constructive details that are of interest for publication **IV**.

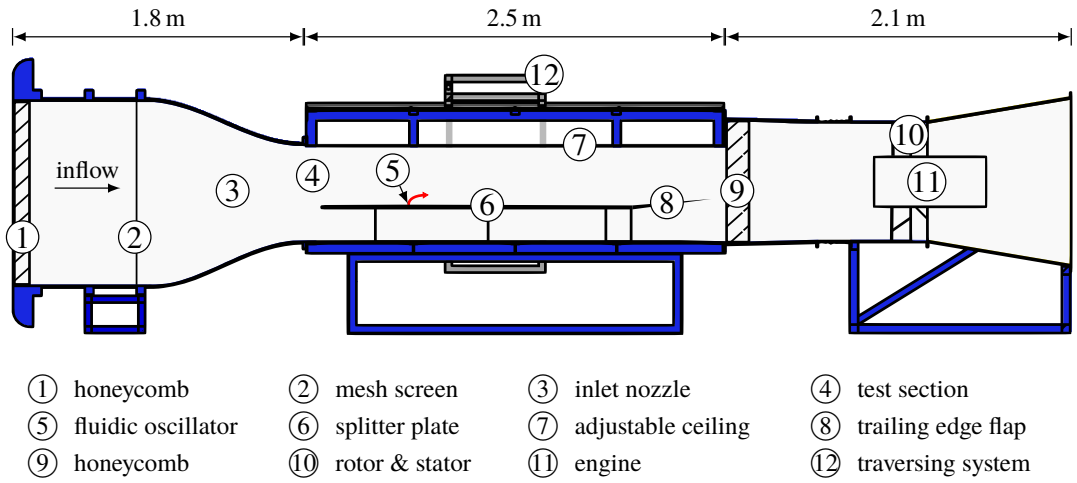

Figure 2.4: The wind tunnel employed in publication **IV** with annotated parts.

A more comprehensive, general discussion on the wind tunnel is provided in the bachelor's thesis by Winter (2015) who also describes the constructive modifications undertaken during the refurbishment.

The employed wind tunnel is a suctioning Eifel wind tunnel. This type of wind tunnel promises a small degree of turbulence, which makes it a suitable choice for the pursued studies. However, working with a suctioning wind tunnel is challenging due to the negative pressure difference between the wind tunnel and the environment. Any leakage induces unwanted local lateral flow. Therefore, considerable amount of work is invested to ensure airtightness between the individual wind tunnel components as well as sealing hoses, power-, and data lines which are required inside the wind tunnel.

A slice through the wind tunnel is illustrated in figure 2.4. A honeycomb is installed at the inlet to straighten the inflow (figure 2.4, 1). Small scale turbulence is eliminated by a mesh screen that is located downstream of the honeycomb (figure 2.4, 2). The inlet nozzle has a contraction ratio of 4:1 (figure 2.4, 3). The adjacent test section has a cross-section of $0.55 \times 0.55\,\mathrm{m}^2$ and a length of 2.5 m (figure 2.4, 4). The test section is a welded structure of steel. A considerable amount of constructive inaccuracies is due to the welding, which were tried to be alleviated during the refurbishment by inserting new, adjustable walls and a new modular floor in the test section. In order to allow PIV measurements inside the test section, the walls are made of acrylic and conventional glass, thus providing optical access from all sides. However, struts in between the windows obstruct the optical access partially. The struts are necessary for the stiffness of the test section. The test section ceiling is made of acrylic glass to provide an access for the laser light (figure 2.4, 7). It is flexible, which allows the streamwise pressure gradient to be adjusted. The floor of the test section is assembled of interchangeable modules of wood, which enables an easy modification according to the requirements of other setups. The test section struts as well as the floor are painted black to minimize possible reflections of the laser. The velocity inside the test section is determined by using a Pitot-static tube that is installed at sufficient distance from the wall.

The fluidic oscillator is installed inside a splitter plate (figure 2.4, 5 & 6) in order to achieve a reproducible boundary layer. The oscillator is held by a turntable that allows to rotate the oscillator with respect to the direction of the crossflow. The splitter plate reduces the cross-section of the test section to $0.37 \times 0.55\,\mathrm{m}^2$, which provides space for the installation of the oscillator below the splitter plate. The oscillator and supply hoses are enclosed by a NACA 0020 housing that aims to reduce the pressure loss below the splitter plate. The splitter plate is made of acrylic glass to let the laser light pass through, which reduces reflections. It is assembled from interchangeable modular parts that allow to change the boundary layer thickness. The splitter plate is equipped with a rounded nose and a trailing edge flap to adjust the stagnation point (figure 2.4, 8). The splitter plate is equipped with pressure taps, which are used to measure the streamwise pressure gradient over the splitter plate. For the experiments in publication **IV**, tripping is installed at the splitter plate nose to assure a fully turbulent boundary layer.

A second honeycomb is installed downstream of the test section to reduce possible upstream propagating swirl caused by the axially oriented rotor (figure 2.4, 9 & 10). Downstream of this honeycomb, the tunnel geometry transitions from a square shape to a round shape which encloses the rotor. The blades of the rotor are manually adjustable for increasing the efficiency of the wind tunnel. A 12.5 kW engine powers the rotor (figure 2.4, 11). The engine-rotor combination, manufactured by Turbon, is able to provide a volume flow rate of up to 31 000 m^3/h. Without the splitter plate being installed, the maximum achievable velocity inside the test section is 23 m/s. With the splitter plate being installed, the additional blockage results in a maximum velocity of up to 25 m/s above the splitter plate. Note that the engine-rotor combination is structurally decoupled from the test section, which prevents vibrations from being transferred to the test section.

Some crossflow properties of the wind tunnel are measured in a bachelor's thesis by Martinke (2016) with a hot wire anemometry system at the position of the oscillator. He states that the level of turbulence is 0.15 %. Furthermore, he measured the boundary layer properties. His results on the boundary layer thickness δ_{99} as well as the displacement thickness δ_1 and momentum thickness δ_2 are summarized in table 2.2 for three velocities. It is evident that the shape factor is approximately 1.4 for all velocities, which validates the desired fully turbulent boundary layer.

Table 2.2: Boundary layer properties at the position of the oscillator (Martinke, 2016).

Crossflow Velocity (m/s)	δ_{99} (mm)	δ_1 (mm)	δ_2 (mm)	Shape Factor
5	20	2.9	2	1.45
10	18.2	2.5	1.8	1.39
15	15.8	2.2	1.6	1.38

The three-dimensional flow field of the spatially oscillating jet in publication **IV** is investigated by measuring the velocities plane-by-plane using a stereo PIV system. The planes are oriented in streamwise direction. A two-axis traversing system is mounted to the wind tunnel, which allows for moving the complete PIV system in streamwise and spanwise direction. Fixing the PIV system to the wind tunnel is advantageous because the relation between the coordinate systems is fixed. Therefore, bumping the PIV system or the wind tunnel does not make a complete new calibration necessary. Furthermore, the orientation of the streamwise and spanwise axis coincides reliably after arranging the traversing system along the test section once. However, fixing the PIV system to the wind tunnel is also disadvantageous because possible vibrations of the wind

tunnel are transferred to the PIV system. This shaking may result in slight relative movements between the individual components. Possible vibrations are minimized by reinforcing the frame holding the PIV system. Furthermore, an examination of the results did not exhibit any unusual errors, which indicates that this effect has no impact on the quality of the results.

Although the traversing system allows to move the PIV system two-dimensionally without restrictions, an optical access is not given at every position due to the struts required for the structural integrity of the test section. These struts may hinder the view of the cameras or block the laser. Therefore, the position of the oscillator is chosen carefully prior to the measurements. However, the problem persists especially for measurements of the cross-sections, which may not be conducted at every streamwise position. This adds another reason to choose streamwise oriented planes to measure the three-dimensional flow field.

Chapter 3 | Data Processing

Several data processing methods are employed to extract meaningful data at a sufficient quality from the acquired flow fields. Most of the methods are only mentioned as a side note in the publications. In this chapter, more information on the motivation and implementation of the employed data processing methods is provided. First, it is motivated why phase-averaging is necessary for investigating the flow fields of spatially oscillating jets. Subsequently, various smoothing approaches are compared for their suitability and applicability to the investigated flow fields. Last, Eulerian and Lagrangian data analysis methods that are employed in the publications are introduced and discussed.

3.1 Phase-Averaging

The internal and external flow field of a fluidic oscillator contains stochastic and periodic flow features. A triple decomposition of the flow field allows to distinguish between these effects. The instantaneous velocity field of each snapshot $\mathbf{u}_i(\mathbf{x}, t)$ can be decomposed into the constant time-averaged flow field $\overline{\mathbf{u}}(\mathbf{x})$, a periodic component depending on the instantaneous phase-angle $\tilde{\mathbf{u}}(\mathbf{x}, \phi(t))$ (i.e., the jet oscillation), and a time-dependent stochastic component $\mathbf{u}'(\mathbf{x}, t)$ that is not correlated to the dominant frequency (i.e., stochastic flow features) (Eq. 3.1).

$$\mathbf{u}_i(\mathbf{x}, t) = \overline{\mathbf{u}}(\mathbf{x}) + \tilde{\mathbf{u}}(\mathbf{x}, \phi(t)) + \mathbf{u}'(\mathbf{x}, t) \tag{3.1}$$

Isolating the periodic flow field $\overline{\mathbf{u}} + \tilde{\mathbf{u}}$ enables to investigate a representative oscillation period. The stochastic noise or other flow features not correlated to the oscillation are eliminated. Additionally, it enables to take advantage of the flow field symmetry that exhibits a 180° phase-lag, which is the case in all publications.

The periodic flow field $\overline{\mathbf{u}} + \tilde{\mathbf{u}}$ can be found by conditionally averaging according to the instantaneous phase-angle (i.e., phase-averaging). Usually, this is achieved by phase-locked measurements. However, the flow field of the fluidic oscillator is naturally oscillating without an external trigger available. Therefore, the oscillation frequency varies. In the beginning of this work, considerable effort was invested in finding phase-averaging techniques suitable for the flow field of a fluidic oscillator. The investigated methods and their advantages and disadvantages are extensively discussed in publication **I** and are thus not repeated here. However, it shall be emphasized that the phase-averaging method based on a reference signal which is extracted from inside the fluidic oscillator is employed for the complete work. The reasons for this are discussed in section 5.1. Phase-averaging also enables to acquire flow field data at sampling rates below the oscillation frequency while still achieving a quasi-time-resolved flow field. This is essential for the PIV measurements in publications **III** and **IV**.

Equation 3.1 denotes the triple decomposition for the velocity field. Generally, any quantity extracted from the flow field may be triple decomposed based on the reference signal. In most cases this is beneficial because the employed phase-averaging method that averages snapshots

within a phase-angle window blurs the velocities, which may result in a decreased velocity amplitude and an increased jet width. Hence, velocity amplitude sensitive quantities such as the maximum jet velocity or the jet momentum are extracted from instantaneous snapshots and phase-averaged thereafter in publication **III**. This sequence still eliminates stochastic noise in these quantities, but it prevents an underestimation.

3.2 Interpolation and Smoothing

For a detailed analysis of experimental data, a sufficient data quality is necessary. While most data sets are sufficient for showing average velocity fields, derivatives such as the vorticity or the Q-criterion require high-quality data because the spatial derivatives are very susceptible to noise. Furthermore, a sufficient spatial resolution is necessary to approximate the local derivatives. Usually, experimentally acquired data does not meet these requirements and post-processing of the raw data only yields noisy information on the derivatives, which complicates advanced analysis of the data (e.g., automated vortex tracing). In publications **III** and **IV**, the acquired data from stereo PIV measurements suffers from noise induced by stochastic local turbulence as well as measurement uncertainties. Generally, the reconstructed out-of-plane velocity component exhibits a higher uncertainty. Therefore, the uncertainty of the data is anticipated to be dependent on the direction of the vector. Additionally, the combined three-dimensional flow field exhibits a sparse spatial resolution in the third dimension, while the other two dimensions are sampled at a comparably high resolution. Hence, a detailed assessment of the flow field requires interpolation to compensate for the differences in spatial resolution and smoothing to increase the quality of the data set for advanced post-processing.

Generally, an interpolation includes every measured data point. Hence, it retains the noise, which induces local minima and maxima. These local extreme values cause an artificially increased vorticity. Some interpolation methods such as the spline interpolation add to this effect because they tend to oscillate around constant values. Hence, smoothing is necessary, which alters data points to minimize the local derivatives. Alternatively, a regression may be employed, which interpolates and smooths data simultaneously.

Finding a suitable approach for smoothing the data is challenging because the correct solution is unknown. Most smoothing approaches require a smoothing parameter that controls the smoothing intensity. Setting this smoothing parameter is subjective and poses the risk of over-smoothing the data, which may eliminate important flow features. Hence, it is preferred to employ a smoothing algorithm that objectively optimizes its intensity. Several smoothing approaches are available and tested for the investigated data sets. These smoothing approaches may be categorized in mathematical and physical approaches. Generally, better results are to be expected when more information on the data is provided to smoothing approaches. Therefore, the physical approaches are more reliable because these approaches do not only consider the data but also expect the data to follow physical laws. However, it is not always possible to provide the additional data required for physical validation. Furthermore, the physical methods are more expensive in terms of calculation time and hardware requirements. In the following, some selected smoothing methods that were considered for the present data are presented.

DCT-PLS

Garcia (2010) suggests a mathematical, spatial smoothing approach based on penalized least

squares (PLS) and discrete cosine transforms (DCT) for spatially smoothing of raw PIV data. In the DCT-PLS, the risk of over-smoothing is reduced by optimizing the smoothing intensity using the generalized cross validation (GCV) that is proposed by Craven and Wahba (1978) for optimizing the smoothing intensity of splines. The DCT-PLS is capable of replacing missing or erroneous data and may therefore also serve as a regression. In its generalized implementation, it is able to handle n-dimensional data with uniform spacing in all directions.

Fourier and POD Smoothing

Fourier smoothing is a temporal smoothing approach. It decomposes the flow field into its Fourier modes and recombines only the dominant Fourier modes, neglecting the others. Therefore, it is basically a multi-band-pass filter in the frequency domain. The approach also allows to simultaneously phase-average and smooth measurement data as proposed by Sonnenberger et al. (2000). A similar alternative is the POD smoothing that also includes a mode decomposition. It is based on the proper orthogonal decomposition (POD) of the flow field. However, defining a cut-off criterion for the frequency amplitude or energy content of the modes is subjective. One method for finding an optimum cut-off criterion is provided by Brindise and Vlachos (2017). They use the DCT to identify large scale structures inside the POD modes and the Shannon entropy for quantifying the amount of noise in the POD modes. The Shannon entropy of the discrete cosine transformed modes converges with increasing POD mode numbers. A conventional convergence criterion is used to find the threshold for the mode numbers that are eventually kept for the recombination of the smoothed flow field. Both, the Fourier and the POD smoothing perform best when being applied on the raw data instead on the phase-averaged data because the higher number of samples improves the results.

DCS

The divergence correction scheme (DCS) is a physical, spatial smoothing approach. It forces velocity data to fulfill the continuity equation. Hence, it requires three-dimensional velocity vectors of an incompressible flow field. The DCS is implemented by solving an overdetermined system of linear equations that eliminates the divergence in the flow field. Over-smoothing is avoided by finding the solution most similar to the raw data. Therefore, the smoothing effect of the DCS is usually very small. Wang et al. (2017) provide a fast implementation of the DCS. They also include a direction-dependent weighting because in most data sets one direction suffers from more uncertainty and noise than the other directions, which is the case in tomographic PIV as well as in three-dimensional data reconstructed from stereo PIV planes.

DFS

The divergence-free smoothing (DFS) is suggested by Wang et al. (2016) for volumetric PIV data. They aim to improve spatial smoothing by conducting mathematical smoothing and a DCS simultaneously. This is implemented by recomposing the flow field from a set of predefined divergence free bases. Calculating these bases is very expensive in terms of memory requirements. The bases are sorted by their roughness. Smooth bases are preferred in the recombination. The smoothing parameter that is the cut-off number of the bases is optimized using a GCV similar to the DCT-PLS. The DFS is able to replace missing values and eliminate outliers. Thus, the DFS can be employed as a regression. It is noteworthy, that the memory requirement for determining

the divergence-free bases necessitates to split the data in multiple windows which significantly reduces the performance of this method compared to the other methods.

In the previous paragraphs, several smoothing approaches are described. However, the list of appropriate smoothing approaches is not exhausted and may be extended for example by a simple convolution (i.e., n-dimensional moving average) or a Kriging regression (de Baar et al., 2014). Furthermore, the results differ depending on the sequence: Is the raw data smoothed before phase-averaging or after phase-averaging. In fact, phase-averaging itself can also be regarded as a temporal smoothing approach. It is evident that an immense number of possibilities exist to smooth the experimental PIV data. However, all methods suffer from not knowing the correct solution, which makes it challenging to choose one. Therefore, some smoothing possibilities were evaluated using a generic, divergence-free flow field derived from a periodic, generic velocity potential (Eq. 3.2). Note that this velocity potential is completely artificial and does not capture any real flow field effects. Isolated samples are extracted from the generic flow field to mimic the spatial and temporal resolution of the data from publication **III**. These samples are superimposed with random and velocity-correlated Gaussian noise. An extract of the original generic flow field is shown in figure 3.1. The smoothed results are added for a qualitative comparison. All results are phase-averaged and spline-interpolated.

$$F = 5 \cdot \left(\sum_n a_n \sin\left(2\pi n t\right) \right) \sin\left(\frac{x}{30}\right) \sinh\left(\frac{y}{30}\right) + z \cdot \left(\sum_n a_n \cos\left(2\pi n t\right) \right) \tag{3.2}$$

$$\text{with } a_n = \{1.8; 0.6; 0.6; 0.2; 0.08; 0.002\}$$

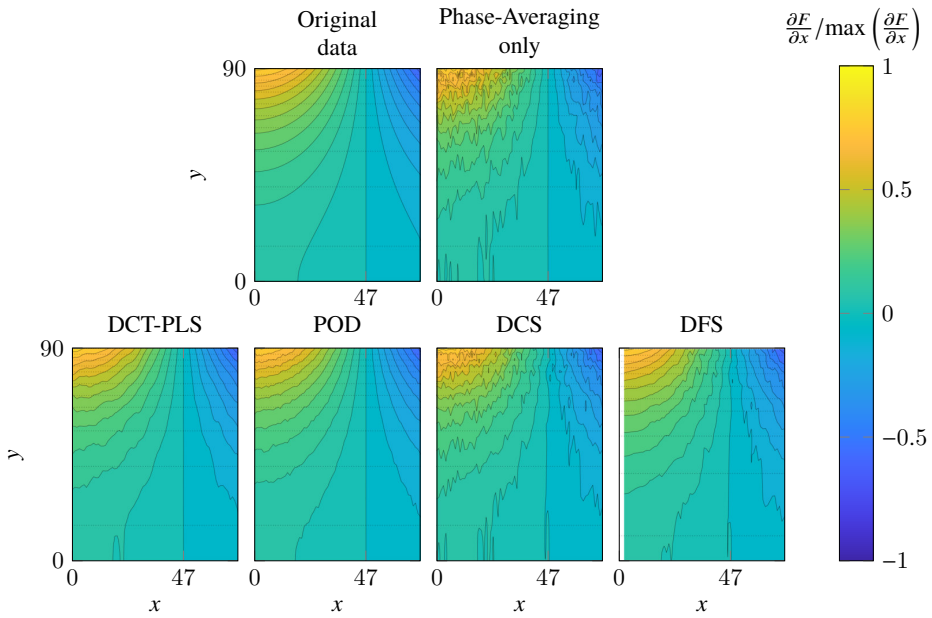

Figure 3.1: Qualitative comparison of smoothing approaches applied on the generic velocity field component $\partial F/\partial x$ (Eq. 3.2). The shown data is extracted at $z = 9$ and $t = 0.125$.

Most of the presented smoothing approaches perform well on this generic scenario and were

considered for the data of publications **III** and **IV**. The results even improve, when combining the smoothing approaches. However, although some combinations perform remarkably well on generic data, their effect on real data remains unknown. Eventually, it was decided to reduce the amount of smoothing to a necessary minimum, in order to prevent any chance of over-smoothing. The amount of smoothing was adjusted for each individual analysis. The three-dimensional flow fields visualized in publication **III** and publication **IV** were phase-averaged, spline-interpolated, and three-dimensionally smoothed with the DCT-PLS. For quantitative data, such as the entrainment in publication **III** or the vortex tracing in publication **IV**, no smoothing beside phase-averaging was applied. If necessary, spline interpolations were employed to interpolate values in between the individual PIV planes. In publication **I** and publication **II**, no smoothing besides phase-averaging and occasionally a running average were applied on the data.

3.3 Eulerian Post-Processing Methods

The PIV measurements capture the velocities inside the flow field. This velocity information enables to determine the local velocity magnitude as well as the velocity vector angle. More advanced Eulerian data analysis methods are able to extract more information from the velocities field. Integrating velocities along artificial curves, surfaces, or volumes yields global values that describe the flow field and may simplify the comparison to other flow fields. Examples are the massflow and the momentum, which are of special interest in publications **II** and **III**. In publication **III**, the momentum and the massflow are integrated over the surface of a volume that increases with the streamwise coordinate. The information is used to calculate the jet force and assess the entrainment as a function of the streamwise coordinate in comparison to the entrainment of steady jets. Furthermore, the momentum and massflow should be zero when integrating over the surface of a closed volume if the pressure and density gradients are assumed to be negligible. In publication **III**, it is shown that the acquired data obeys the conservation of massflow and momentum, which provides additional confidence in the quality of the data.

The local derivatives of the velocity field are also of interest. One example is the rotation of the velocity vector field, which yields the vorticity. The vorticity indicates the position and strength of vortices and shear layers. However, it is very susceptible to noise because noise hinders the correct approximation of the local derivatives. Therefore, a sufficient data quality is required, which may be achieved by smoothing the flow field as described in section 3.2.

The vorticity does not indicate vortices and shear layers separately. Therefore, other methods are required to distinguish between shear layers and vortices. Several methods for identifying a vortex exist and some are summarized by Jeong and Hussain (1995). The Λ-definition, the λ_2-criterion, and the Q-criterion are tested for the data set in publications **III** and **IV**. Eventually, the Q-criterion is employed for the identification of vortices in publications **III** and **IV** because it appeared as most robust. However, the vortex cores identified by the other methods are very similar.

3.4 Lagrangian Post-Processing Methods

In Eulerian post-processing methods, the instantaneous flow field is investigated from a fixed position. In contrast, the Lagrangian post-processing methods focus on virtual particles in the flow thereby considering the past and the future of every particle. Generally, Lagrangian

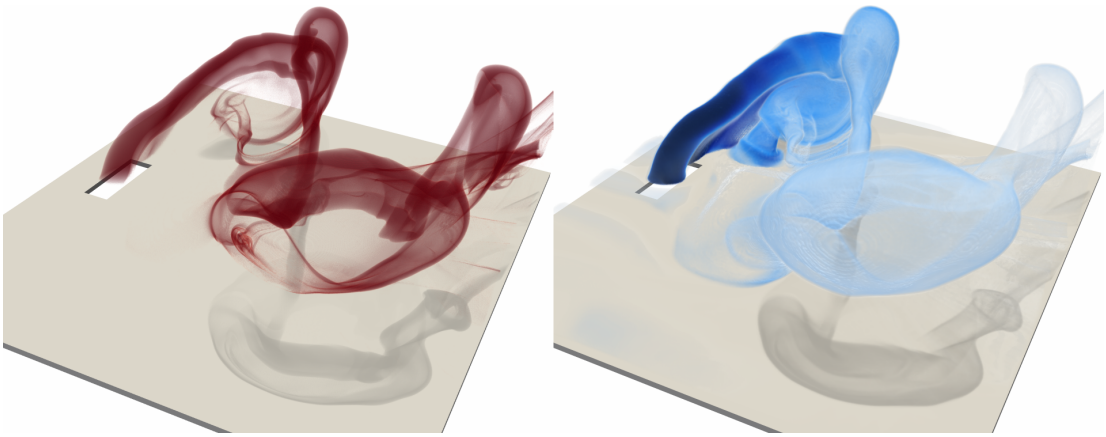

Figure 3.2: Streakvolume of a spatially oscillating jet in crossflow (left) and FTLE of the flow field (right).

post-processing methods require time-resolved data except in stationary flow fields. The phase-averaged data in the publications may be considered as quasi-time-resolved flow field. Hence, Lagrangian post-processing methods are suitable. The flow fields are interpolated onto an equidistant, high-resolution grid. Virtual particles are placed inside the flow field and traced through time by using the fourth order Runge-Kutta method. Since the flow fields are periodic, the virtual particles may be traced over more than one period. Therefore, the time is not limited. Boundary conditions applied in publication **IV** partially eliminate the spatial borders of the measured volume for the particles. These boundary conditions mimic the undisturbed crossflow in all directions but the wall and the streamwise direction.

One Lagrangian post-processing method suitable for visualizing time-resolved, three-dimensional flow fields are streakvolumes (figure 3.2, a). Streakvolumes consist of particles that originate from a defined region. Hence, a streakvolume is also a collection of streaklines. The streakvolume may be determined by two ways. First, a connected polygon described by a sufficient number of nodes is ejected at the origin of interest and traced in time along the streaklines. In a complex flow field, the volume is going to be deformed and convoluted which significantly increases the number of nodes required for describing the polygon. Therefore, this approach is very demanding in terms of memory and calculation power. Since the flow field of a spatially oscillating jet is very complex, this approach is not pursued. Instead, the streakvolume is determined by tracing an initially structured, high-resolution grid of virtual particles back in time. Particles that are found to originate from the origin of interest are highlighted, which yields an implicit representation of the instantaneous streakvolume. A similar approach is suggested by Xue et al. (2004). The quality of this streakvolume depends on the initial resolution of particles. Therefore, it is only a downsampled representation and it is not able to capture small scale structures which are located between the particles. A high initial resolution of the particle starting points alleviates this but degrades the performance due to the higher number of particles to be traced. In order to compensate this, a grid-refinement is used in this study. In each iteration the particle starting point grid resolution is doubled. Particles which have at least one neighboring particle whose origin differs from the other neighbors' origins are traced in time to determine the corresponding particle origin. The other particles are estimated to be from the same origin as their neighbors.

This grid-refinement approach allows to determine the streakvolume of the three-dimensional flow field of the spatially oscillating jet with moderate calculation time. In publication **IV**, one instantaneous streakvolume is determined from tracing approximately 20 million virtual particles over a maximum of two oscillation periods with a time step size of 1/360th of one period length (figure 3.2, left). The calculation of this instantaneous streakvolume took around one hour on a machine equipped with an Intel Core i7-3820 CPU and 64 GB memory. The resulting streakvolumes appear similar to ink visualizations and exhibit similar advantages and disadvantages. It is advantageous that the streakvolume provides an intuitive understanding of the flow field and highlights dominant flow structures. Since not only one timestep is considered, one instantaneous snapshot of the streakvolume already provides some information about the past of the flow field. However, this is also a disadvantage because flow features that are formed once are convected and do not dissipate because the phase-averaged flow field does not contain stochastic turbulence. Therefore, the streakvolume may indicate a flow structure at one point where it is not existent from the Eulerian perspective. Besides that, the streakvolume only highlights flow features consisting of particles from the origin of interest. Other flow features are not visible. These disadvantages are eliminated by using the finite time Lyapunov exponent (FTLE) as visible in figure 3.2 (right).

Haller and Yuan (2000) employ the FTLE to define and identify Lagrangian coherent structures inside a flow field. The FTLE quantifies the separation or attraction rate of infinitesimally close trajectories. For the calculation, neighboring virtual particles are placed very close to each other (order of 1 µm) and traced forward or backward in time. Although this distance between the particles seems very small, it is sufficient that the particle trajectories separate. The forward FTLE highlights regions of diverging trajectories. In contrast, the backward FTLE indicates regions of converging trajectories. In the present work, only the backward FTLE is employed because it yields a more intuitive representation of the flow field (figure 3.2, right). It highlights shear layers and vortices. Hence, it is a suitable tool to visualize and identify Lagrangian coherent structures in the flow field.

The implementation of the FTLE is very similar to the streakvolume as it is calculated for particles placed on an equidistant, high-resolution grid. However, for every particle on the grid, neighboring particles are added in each Cartesian direction. In each iteration the grid is refined based on a threshold value regarding the gradient of the FTLE. High gradients are refined, while small gradients are interpolated from the previous grid. For one instantaneous FTLE field, over 55 million particles are traced over a maximum of two oscillation periods with a time step size of 1/360th of one period length. The calculation of the FTLE field that is shown in figure 3.2 (right) took around five hours. In publication **III**, the FTLE is used to provide a qualitative overview of the flow field. In publication **IV**, a combination of the streakvolume and the FTLE is used for visualizing the flow field. This combination allows to distinguish between flow features in the crossflow and in the jet. Furthermore, the streakvolumes are used to quantify the penetration of the jet into the crossflow.

Further details on the Lagrangian post-processing methods and various possibilities to further improve the performance are provided by Godbersen (2017). Two award-winning videos of Lagrangian coherent structures of a spatially oscillating jet in a quiescent environment and in a crossflow are showcased by Sieber et al. (2016a) and Ostermann et al. (2017) respectively.

Chapter 4 | Publications

Publication I
Ostermann, F., Woszidlo, R., Nayeri, C. N., & Paschereit, C. O. Phase-Averaging Methods for the Natural Flowfield of a Fluidic Oscillator. *AIAA Journal*, 53(8), pp. 2359–2368, 2015. ISSN 1533-385X. doi:10.2514/1.J053717.

This is a postprint of the article published in AIAA Journal. The final authenticated version is available online at https://doi.org/10.2514/1.J053717.

Publication II
Woszidlo, R., Ostermann, F., Nayeri, C. N., & Paschereit, C. O. The time-resolved natural flow field of a fluidic oscillator. *Experiments in Fluids*, 56(6), pp. 125f, 2015. ISSN 1432-1114. doi:10.1007/s00348-015-1993-8.

This is a postprint of the article published in Experiments in Fluids. The final authenticated version is available online at Springer via http://dx.doi.org/10.1007/s00348-015-1993-8.

Publication III
Ostermann, F., Woszidlo, R., Nayeri, C. N., & Paschereit, C. O. Properties of a spatially oscillating jet emitted by a fluidic oscillator. *submitted to Journal of Fluid Mechanics*, 2018. ISSN 1469-7645.

This article is a preprint of the article submitted to the Journal of Fluid Mechanics.

Publication IV
Ostermann, F., Woszidlo, R., Nayeri, C. N., & Paschereit, C. O. The interaction between a spatially oscillating jet emitted by a fluidic oscillator and a crossflow. *submitted to Journal of Fluid Mechanics*, 2018. ISSN 1469-7645.

This article is a preprint of the article submitted to the Journal of Fluid Mechanics.

Phase-Averaging Methods for the Natural Flow Field of a Fluidic Oscillator

Florian Ostermann*
Technische Universität Berlin, Berlin, 10623, Germany

Rene Woszidlo†
The University of Kansas, Lawrence, KS 66045, USA

Christian N. Nayeri‡ and Christian O. Paschereit§
Technische Universität Berlin, Berlin, 10623, Germany

The presented study examines various methods for phase-averaging the naturally oscillating flow field of a scaled-up fluidic oscillator. No external trigger is employed to control the oscillation of the flow. Mathematical and signal conditioning approaches for phase-averaging the data are categorized and described. The results of these methods are evaluated for their accuracy in capturing the natural flow field. The respective criteria are based on the minimum fluctuation in oscillation period length, the conservation of velocity amplitudes, and the number of snapshots per phase-averaging window. Although all methods produce reasonable qualitative results, only two methods are identified to provide the desired quantitative accuracy and suitability for the investigated flow field. The first method is based on conditioning a time-resolved pressure signal from the feedback channels in the oscillator. An autocorrelation applied to the reference signal improves the period identification. The second method employs a mathematical approach by means of proper orthogonal decomposition. Because the conventional use of POD reveals shortcomings in quantitative accuracy, it is modified by imposing an even distribution of snapshots per phase angle window. The results demonstrate the feasibility and improved accuracy of the modified POD. Therefore, accurate phase-averaging can be conducted without the need for a time-resolved reference signal.

Nomenclature

a	modal coefficient
d_h	hydraulic diameter, m
F	Fourier transform
g	reference signal
H	Hilbert transform
p	pressure, Pa
t	time, s
U	velocity magnitude, m/s
u	velocity in x-direction, m/s
v	velocity in y-direction, m/s
x	Cartesian x coordinate, m
y	Cartesian y coordinate, m
R	correlation matrix
sgn	signum function
a	analytical
$outlet$	property at the oscillator outlet
λ	eigenvalue
ω	angular frequency
Φ	decomposed mode
ϕ	phase angle, °

*PhD Student, Hermann-Föttinger-Institut, AIAA Student Member.
†Visiting Assistant Professor, Aerospace Engineering, AIAA Member.
‡Research Associate, Hermann-Föttinger-Institut, AIAA Member.
§Professor, Hermann-Föttinger-Institut, AIAA Senior Member.

I. Introduction

FLUIDIC Oscillators, also known as flip-flop nozzles or sweeping jet actuators, generate an oscillating jet when continuously supplied with a pressurized fluid. The internal flow is bistable and oscillates between two states. Figure 1(left) conceptually illustrates the internal dynamics of an oscillator which incorporates two feedback channels. This oscillator design is similar to the design investigated in the current study. Other types of oscillators exist (e.g., with only one feedback channel or without feedback channels) which involve different oscillation mechanisms. A more detailed review was presented by Gregory et al[1]. For the oscillator shown in figure 1, the jet enters the mixing chamber and attaches to either side. Part of the main jet is deviated into the feedback channel and guided back to the chamber inlet. Here, the flow interacts with the main stream and causes it to separate from the wall and to flip over to the other side of the mixing chamber where the process is re-initiated. This results in the oscillation of the emitted jet in a sweeping pattern. The photograph on the right side of figure 1 depicts the oscillating jet with water as a working fluid. Fluidic oscillators do not contain any moving parts. Therefore, they are attractive devices in numerous applications (i.e., windshield spray nozzles or shower heads)[2]. In recent years, fluidic oscillators have become of particular interest as flow control actuators. They have a proven high efficacy in a wide field of applications including combustion[3], noise[4] and separation control[5–7]. Despite the advantages and proven performance, the literature offers only limited information on the underlying mechanisms. Additional fluidic oscillator investigations are necessary to improve the understanding of flow phenomena inside and outside the oscillator and to validate numerical calculations enabling the optimization of these devices. For high-frequency naturally oscillating flow fields such as those emitted by fluidic oscillators, it is challenging to acquire time-resolved data, because the oscillation frequency exceeds the sampling rate of most available optical measurement systems such as particle image velocimetry (PIV). Therefore, phase-averaging of the recorded data is necessary. By using phase-averaging methods, all snapshots or signals within a certain interval are averaged. This yields a phase-averaged oscillation period and minimizes stochastic noise. Phase-averaging of a naturally oscillating flow field is not trivial due to the naturally fluctuating period lengths and the absence of external triggers. Various approaches to obtain phase-averaged data from an oscillating flow field have been pursued. One possibility is to force the oscillation with an external trigger[8]. However, this eliminates the self-sustaining natural oscillations and may affect natural flow phenomena. Other approaches attempt to lower the oscillation frequency by changing the working fluid or enlarging the oscillator[9, 10]. In these studies, signal conditioning[10] and mathematical methods[9] were used to phase-average the flow field.

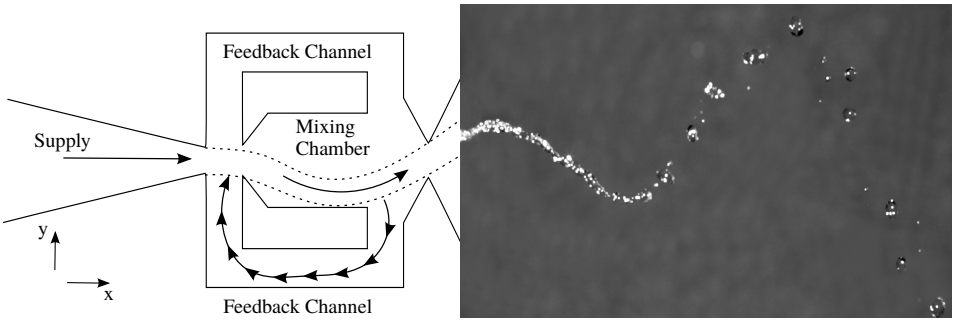

Fig. 1 Working principle of a fluidic oscillator.

The current study is aimed at examining various methods to obtain the time-resolved features of the internal and external flow field of a fluidic oscillator with a high quantitative accuracy. Experiments are conducted on a scaled-up fluidic oscillator similar to the design shown in figure 1 with the goal to establish a method applicable to higher jet velocities and oscillation frequencies. The advantages and disadvantages of these methods are evaluated and their

accuracy is judged based on several criteria. The most suitable method is described in detail and applied to yield the time-resolved internal and external flow field. The results of the examined flow field are discussed in the preliminary work by Gärtlein et al.[11].

II. Setup and Instrumentation

The time-resolved study of fluidic oscillators is usually prevented by high oscillation frequencies and maximum sampling rates of the measurement equipment. In order to lower the oscillation frequency, previous experiments chose water as the working fluid [9]. In the present study, the oscillator is scaled-up and pressurized air is used as the supply fluid. The increased size lowers the frequency enabling time-resolved measurements of the internal and external flow field with a high-speed PIV system (figure 2). The scaled-up oscillator with an outlet area of 25 mm × 25 mm is CNC machined from a solid piece of acrylic glass (PMMA). It is covered by a plate, which is verified to provide an airtight seal. The oscillator is mounted on a metal stand emitting its jet into an unobstructed, quiescent environment. The fluidic oscillator is supplied by a constant mass flow maintained by a digital controller by Bronkhorst® Mättig with a range of 0 to 100 kg/h (accuracy: ±0.6 kg/h full scale). The area ratio from the plenum to the inlet of the oscillator is approximately 10:1. A honeycomb installed upstream of the inlet provides homogenous inflow conditions. The origin of the coordinate system is located at the center of the outlet nozzle.

Inside the oscillator, 55 pressure taps are symmetrically installed at selected positions based on the study by Bobusch et al.[9] Unused taps are sealed to prevent additional entrainment or leakage. The diameter and length of the pressure taps are optimized by using the calculation for the dynamic response of tubes[12]. This ensures time-resolved pressure measurements with insignificant phase delay, conservation of amplitude, and reduction of possible resonance effects. The diameter of the pressure taps is set to 0.8 mm. Differential pressure sensors (HDO Series by Sensortechnics) with a range of 0 to 50 mbar (accuracy: ±0.1 mbar full scale) and a response rate of 10 kHz are connected to the internal taps. A microphone and a hotwire probe may be positioned at the outlet of the oscillator. The PIV system includes one high-speed camera (Photron Fastcam SA1), one laser with an optical arm (Quantronix Darwin Duo 100 /Nd:YLF), a synchronizer (ILA Synchronizer), and an aerosol generator for oil droplets with an average diameter of 0.5 µm (Palas AGF 10.0). This system is capable of recording up to 10,920 double frames with a maximum resolution of one mega pixel at a maximum sampling rate of 5 kHz. In this study a sampling rate of 1.5 kHz is chosen, which is sufficient to acquire time-resolved flow field data. When supplied with the highest available mass flow rate (i.e., 100 kg/h), the emitted jet oscillates at a maximum frequency of 23 Hz with an exit velocity of $U_{outlet} = 37\,\mathrm{m/s}$ (assuming incompressibility and ambient air properties). The pulse distance is adjusted according to the maximum velocity. The spatial resolution is approximately 2 mm with a maximum interrogation window size of 16 × 16 pixels and an overlap of 50 %. Measurements of pressure and PIV are executed simultaneously by two independent systems. If not noted otherwise, all investigated phase-averaging methods are applied to the same data set, which is obtained at an outlet velocity of $U_{outlet} = 19\,\mathrm{m/s}$. At this supply rate, the average oscillation frequency is 12.5 Hz. In general, the trends are independent of the supply rate, if not a describing statement or figure is added. The investigated field of view is symmetric and covers the complete oscillation pattern.

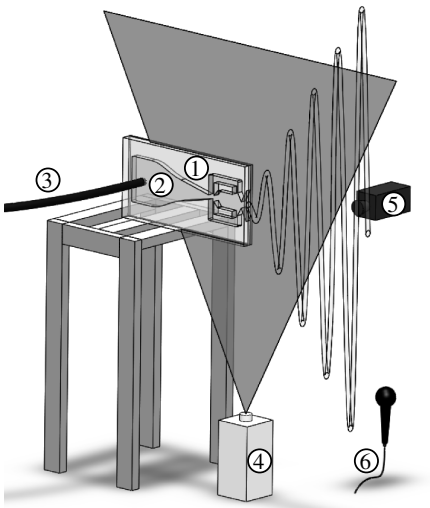

Fig. 2 Sketch of the experimental setup.

III. Phase-Averaging Methods

Various methods may be applied to phase-average a naturally oscillating flow field. These methods can be grouped into signal conditioning and mathematical methods. The signal conditioning methods require a time-resolved measurement signal which clearly identifies the oscillation periods. In contrast, mathematical methods correlate the phase between randomly acquired PIV snapshots. The general steps of both approaches are outlined in figure 3. In subsequent sections, selected methods of both groups are described in detail. Additionally, the effect of the phase-averaging window size is discussed.

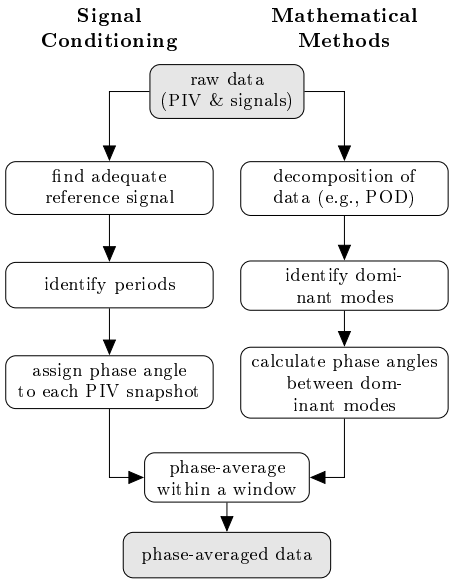

Fig. 3 General phase-averaging steps.

A. Signal Conditioning Approaches

It is possible to determine a phase angle for every time step by applying signal conditioning methods on a time-resolved reference signal which clearly reveals the individual oscillation periods.

1. Possible Sources for a Reference Signal

Various sources for a reference signal were investigated during this study. Hotwire anemometry, microphones, and pressure transducers have high possible sampling rates. However, the hotwire probe and microphone may present a disturbance to the outer flow field due to the required proximity to the outlet. Furthermore, external probes would be disadvantageous for experiments involving a free-stream. Optical measurement techniques (e.g., PIV) may be used as a potential reference signal because they do not disturb the flow field. However, they are often limited by low sampling rates making them insufficient for high-frequency oscillating flow fields. One exception is offered by Laser-Doppler-Velocimetry (LDV), which is capable of acquiring a reference signal at high sampling rates. However, simultaneous PIV measurements are conducted in this study yielding an undesirable complexity of the setup to avoid any potential interference between the PIV and LDV laser systems. As a solution, data from pressure taps inside the oscillator are chosen as reference signals. Resonance effects and phase delay in the pressure taps and ducts have to be considered for the design of the pressure tap geometry. Additionally, the source of the reference signal needs to be close to the flow field of interest to avoid phase-lags larger than one oscillation period. Otherwise, this may cause errors due to fluctuating period lengths.

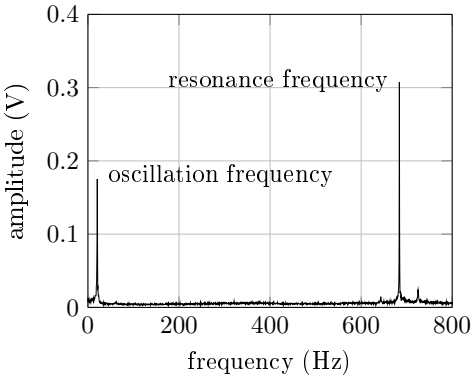

Fig. 4 Spectrum of the reference signal (U_{outlet} = 35 m/s).

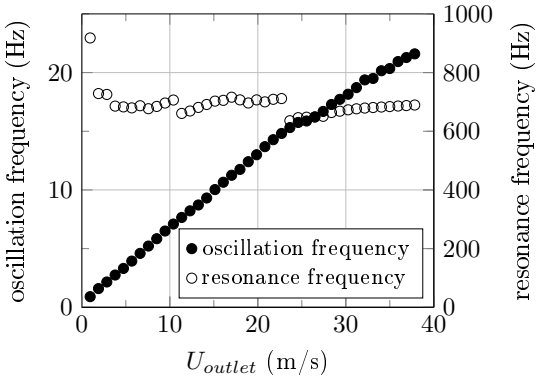

Fig. 5 Oscillation and resonance frequency as a function of the supply rate.

2. Improvement of Signal Quality

The quality of the reference signal is crucial for the correct identification of the oscillation periods. In this study, the reference signals from the pressure taps inside the feedback channels are dominated by a resonance phenomenon. The spectrum for a selected supply rate reveals two distinct peaks (figure 4). The first peak indicates the oscillation frequency whereas the second peak marks the resonance frequency. Figure 5 shows the resonance and oscillation frequency as a function of supply rate. It is evident that the oscillation frequency increases linearly with supply rate. In contrast, the resonance frequency remains approximately constant. This implies that the resonance frequency is only affected by the geometry. It is noteworthy that both the resonance frequency and oscillation frequency fluctuate around a mean value. The pressure measurements exhibit the mean resonance frequency at about 700 Hz. If the feedback channel is acoustically modeled as a straight duct with open ends (duct length equals the length from feedback channel inlet to outlet), a standing wave is generated with a wavelength that is twice the duct length. The resulting frequency corresponds well to the observed resonance frequency. A cross-correlation between the pressure signals of both feedback channels reveals a phase relation between the resonance phenomena of both channels. The resonance can be either in phase or 180° out of phase depending on the supply rate. The reasons for this dependence are not yet understood. A similar phenomenon was observed by Koso et al.[13]. The phase-averaged results do not extract the resonance effects because the oscillation frequency is one order of magnitude lower than the resonance frequency. Nevertheless, it is suspected that the resonance effects may increase the turbulence level inside the jet.

The quality of the reference signal is improved by subtracting the signals from two symmetrically positioned pressure taps (figure 6). This increases the amplitude of the oscillation because of the 180° phase-lag between the feedback channels. A fifth order low-pass digital Butterworth filter is applied to the reference signal. The cutoff frequency is chosen in consideration of the oscillation frequency. The amplitude of the oscillation is preserved and a phase-lag is avoided by applying the filter forwards and backwards. It is noted that a constant phase-lag would not necessarily disturb the phase-averaging process because the beginning of the physical cycle is based on other criteria.

3. Oscillation Period Identification

After a proper reference signal is determined, the individual oscillation periods have to be identified. Although the pressure signal is chosen as a reference signal, the described period identification methods are applicable to all sources of a reference signal. The simplest period identification method requires subtracting the mean value from the reference signal and defining one period at every other change of sign (figure 7, top). However, this method (referred to

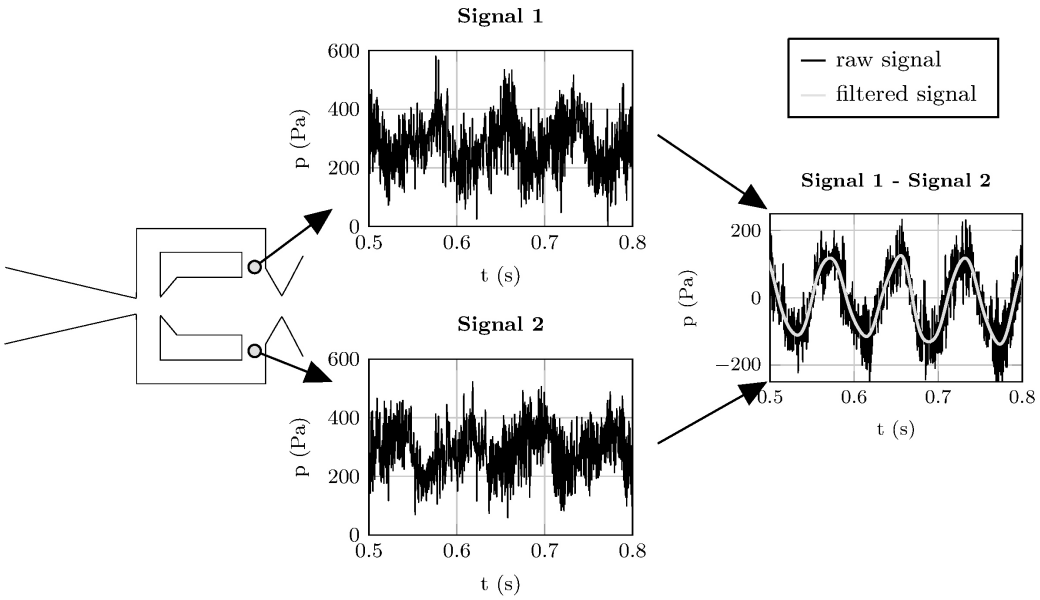

Fig. 6 Signal improvement by subtracting signals from two symmetrically aligned pressure taps.

as 'zero-crossing' method) is very susceptible to noise and amplitude fluctuations, which causes varying local mean values. For comparison with other phase-averaging methods, the 'zero-crossing' method is applied to a reference signal extracted from high-speed PIV data. Since this approach neither includes any mathematical methods modifying the data nor introduces any phase-lags due to the reference signal source, it yields a reliable result. The results are referred to as the 'benchmark method' in the following.

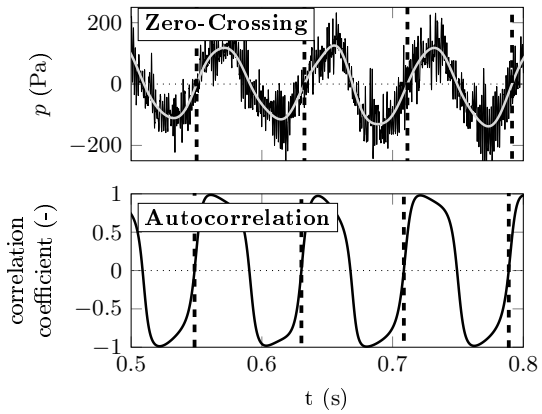

Fig. 7 Period identification in a reference signal (dashed: oscillation period starting points, dark: raw data (top) or correlation coefficient (bottom), light: filtered signal).

The drawback of the previously described 'zero-crossing' method is alleviated by applying an autocorrelation to the reference signal. A fragment of the reference signal is correlated with a shifting fragment of the same signal. This yields an oscillating correlation coefficient where every other change of sign marks a full period (figure 7, bottom). The autocorrelation method is less susceptible to local fluctuations, because the calculation of the correlation coefficient

takes the local mean and root mean square (RMS) value into account. When applying the autocorrelation, two additional parameters become important and need to be examined: the size and the position of the fragment to be correlated. The position of the fragment is found to have no significant influence on the quality of the results. The size of the fragment defines the frequency of interest, but may also impose a dominant frequency upon the reference signal. Although the naturally oscillating flow field has a dominant frequency, deviations of the frequency are expected and have to be properly extracted by the phase-averaging algorithm. Figure 8 depicts the mean value and standard deviation of the individual oscillation periods with respect to the autocorrelated fragment size. Although the average period length is constant for a wide range of fraction lengths, the standard deviation changes. For small fragment lengths the correlation coefficient does not reveal the expected frequency, which is also evident in the plot of the average period length (figure 8). For large sample lengths, a decrease in the standard deviation is noticeable. This indicates an imposition of the dominant frequency and thus eliminates the natural fluctuations in the instantaneous period lengths. For a fragment length between 0.5 and 1.0 of the mean period length, a constant standard deviation is observed, which indicates unaffected periods while successfully isolating the frequency of interest. Although the standard deviation increases with the supply rate due to flow effects, this range of fragment lengths is found appropriate for all supply rates. It may change for other studies though and should always be investigated. In the following sections, a fragment length of one half average oscillation period is chosen. Alternatively, an iterative method using fragments of the phase-averaged reference signal for the autocorrelation of the next iterative step was investigated, but did not yield any improved quality. Another approach correlating a generic fragment with the reference signal also did not yield improved results.

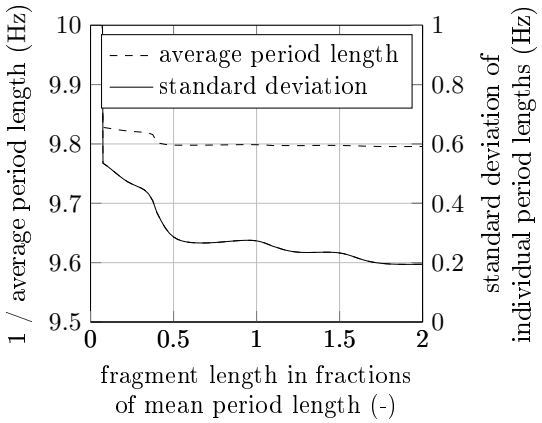

Fig. 8 Average individual period length and its standard deviation (U_{outlet} = 15 m/s).

A challenge of using the autocorrelation method arises when comparing phase-averaged results. Due to applying the autocorrelation, the start of one oscillation period is not based on a physical criterion but rather on the choice of the signal fragment. In order to compare results, phase-aligning is necessary. This may be accomplished, for example, by comparing the phase-averaged reference signal. A phase-lag is determined by cross-correlating or finding the least difference between both phase-averaged signals. All phase-averaged pressure data and flow field results are then shifted to a common starting point.

4. Determining the Instantaneous Phase Angles

Both the 'zero-crossing' and the 'autocorrelation' method define the oscillation periods in the reference signal by identifying period starting points. The oscillation periods are then evenly divided into a number of phase angle windows where the number of windows depends on the window size. The influence of this parameter is discussed in

section III-C. Snapshots are assigned to the appropriate phase angle window based on their time stamp (Eq. 1). All snapshots within one phase angle window are averaged yielding a phase-averaged oscillation period. The accuracy of the described methods is increased by using the half-period starting points because this yields a finer resolution of the natural fluctuations.

$$\phi = 180° \cdot \frac{\text{time stamp} - \text{appropriate half-period starting time}}{\text{instantaneous half-period duration}} + \begin{cases} 0°, & \text{if first half-period} \\ 180°, & \text{if second half-period} \end{cases} \tag{1}$$

B. Mathematical Methods

Two suitable mathematical methods for phase reconstruction of a naturally oscillating flow are selected and described in this section. The first method applies the Hilbert transformation[14, 15] to a reference signal and the second method employs proper orthogonal decomposition[16, 17] (POD) directly to the PIV snapshots.

1. Hilbert Transformation

The Hilbert transform is used to calculate the instantaneous phase angle and frequency. It is defined over an integral using the Cauchy principal value and can be calculated using a fast Fourier transform (FFT) and an inverse Fourier transform (Eq. 2).

$$F(H(g))(\omega) = F(g)(\omega)(-i \cdot \operatorname{sgn}(\omega)) \tag{2}$$

$H(g)$ is the Hilbert transform of g, $F(g)$ the Fourier transform of g, and $\operatorname{sgn}(\omega)$ is the signum function. The Hilbert transform can be interpreted as a phase shifter, which shifts a sinusoidal function with a positive frequency by $-90°$. By applying the Hilbert transform to a time-resolved measurement signal $g(t)$, the analytical signal g_a can be written as Eq. 3.

$$g_a = g + i \cdot H(g) \tag{3}$$

With this analytical signal the phase can be reconstructed by calculating the angle between the real and imaginary part (Eq. 4).

$$\phi = \arctan(H(g)/g) \tag{4}$$

Hence, the instantaneous phase angle ϕ and frequency can be calculated with the Hilbert transformation for an arbitrary time signal g. This phase angle is assigned to the simultaneously acquired PIV snapshots which are then phase-averaged accordingly. The quality of the results is improved by applying a fifth order digital Butterworth low-pass filter (cutoff frequency = 2· oscillation frequency) to the reference signal, as the Hilbert transformation is very sensitive to noise. In this study, this phase-averaging method is called 'Full Hilbert'. The Hilbert transformation may be extended by an empirical mode decomposition which decomposes the reference signal into intrinsic mode functions prior to applying the regular Hilbert transform. This method is called the Hilbert-Huang transformation[18], but is not investigated in this study.

2. Proper Orthogonal Decomposition

The second mathematical approach employs the method of proper orthogonal decomposition (POD), which is mainly used to detect coherent structures. POD decomposes a field into its unique modes sorted by their energy contents. The velocity $u(x,t)$ can be decomposed into the mean velocity u_0 and the sum of the products of the modes $\Phi_i(x)$ with their time dependent modal coefficients $a_i(t)$ for every instance in time (Eq. 5).

$$u(x,t) = u_0 + \sum_{i=1}^{N} a_i(t)\Phi_i(x) \tag{5}$$

The residual of this approximation is minimized if the sum of the square deviation is minimized. This corresponds to minimizing the residual kinetic energy and leads to an eigenvalue problem (Eq. 6).

$$\mathrm{R}\Phi_i = \lambda_i \Phi_i \tag{6}$$

R is the correlation matrix of the velocity fluctuations and the eigenvalues λ_i are twice the kinetic energy u^2 captured by each mode. In practice, the modes and the coefficients can be calculated with a singular value decomposition. The modes are sorted by descending content of energy. Bobusch et al.[9] suggested that the flow field of the fluidic oscillator oscillates harmonically between the first two modes (i.e., modes with the most energy content) with a phase shift of approximately 90°. Accordingly, a phase angle for each PIV snapshot can be calculated with the corresponding time dependent modal coefficients $a_1(t)$ and $a_2(t)$ (Eq. 7), which are normalized by their respective eigenvalues.

$$\phi = \arctan\left(\frac{a_2\sqrt{2\lambda_1}}{a_1\sqrt{2\lambda_2}}\right) \tag{7}$$

Thus, the phase angle is calculated by employing the POD directly to the flow field without the need for a reference signal. In fact, the PIV snapshots are not required to have equally spaced timestamps. Additional details on the mathematical background of this method are described by Berkooz et al.[16] and Legrand et al.[17, 19]

3. Possible Improvements

Both the Hilbert transformation and the POD may be used to determine the phase angle for each PIV snapshot. In section IV-A it is shown that these mathematical methods have drawbacks in correctly reconstructing the time information within a period. Improvements may be achieved by using only the period starting point information and evenly distributing the phase angles within one period similar to the approach described in section III-A. However, time-resolved data is required for this approach. The Hilbert transformation is applied to a time-resolved reference signal. Thus, it may be used to identify the period starting points. This approach is referred to as 'Partial Hilbert' in the following sections. The POD is not capable of identifying period starting points because it is generally applied to data with insufficient sampling rates. In section IV-B additional means of improving the accuracy of the POD method without the need for time-resolved data are explored.

C. Influence of the Averaging Window Size

In order to obtain phase-averaged results, a phase angle range must be defined wherein all apposite snapshots are averaged. The angle range is referred to as the averaging window size. The window size is defined by its total angle size and the according result is assigned to the median phase angle (e.g., a total window size of 10° for a phase angle of 0° refers to $\phi = 0° \pm 5°$). The choice of window size must balance the reduction of signal noise with the preservation of inherent flow characteristics. In order to determine the optimum window size, an RMS value is considered. Here, the

phase-averaged velocity field obtained for a particular window size is subtracted from the phase-averaged result of the next larger window size. For each phase angle, the standard deviation of the entire flow field difference is calculated. Spatially and temporally averaging the standard deviation yields a value which is not representative of the flow field, but it is used for judging the quality of the results. The increment in window size is constant for this analysis. The respective RMS value is expected to obtain its minimum if the most flow effects are retained with minimal noise. According to this approach, the optimum total window size for $U_{outlet} = 19\,\mathrm{m/s}$ is approximately 3°, yielding an average of 91 snapshots per phase-averaging window (figure 9). It was found that the relative approximate error is less than 3 % for more than 50 snapshots per window, which confirms the convergence of the averaging process. For the sake of simplification, this window size is chosen for all supply rates. The optimum window size does vary with changing supply rates within a small range, which is most likely caused by differing signal quality. Any additional increase in the temporal resolution of the phase-averaged data is limited by the data quality, because the flow features which are to be resolved eventually obtain the same order of magnitude as the noise.

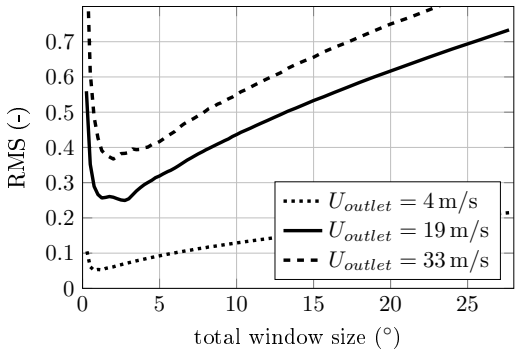

Fig. 9 Optimizing the averaging window size (autocorrelation method of differential pressure signal).

The averaging of all snapshots collected in one window may yield reduced amplitudes due to potentially substantial changes within the respective time frame. In order to increase the retained velocity amplitude, Zilberman et al.[20] applied an iterative approach. The snapshots within a window are cross-correlated with the respective phase-averaged result. The snapshot data is then shifted accordingly and phase-averaged again until the changes in the results reach a convergence criterion. This approach was also pursued in the current study. However, due to already small window sizes, the signal noise is of the same order as any possible shift. Therefore, this iterative method did not yield any improved results.

IV. Results

In this section, the previously described phase-averaging methods are evaluated for their accuracy in revealing the natural flow field. The comparison is based on several criteria (i.e., velocity field data, unsteady oscillation frequency, and snapshot distribution). Significant discrepancies are observed with POD, thus this method is examined separately and modified to yield improved results. The advantages and disadvantages of all methods are summarized and one selected procedure is employed to accurately reveal the phase-averaged internal and external flow field of a fluidic oscillator.

A. Comparison between Methods

A comparison between the described phase-averaging methods is challenging because no exact results of the naturally oscillating flow field are available for proper validation. A visual examination of the velocity distribution may be the first step. In figure 10 the phase-averaged results as produced by the discussed methods are shown. The

velocity plot is extracted from one point on the center line of the flow field where, due to symmetry, the fluctuation frequency is doubled. Consequently, the gradients are higher and discrepancies between the individual results are more pronounced. The same results are found at other positions as well. All results are phase-aligned by using the v-component of the phase-averaged velocity obtained using the benchmark method (i.e., zero-crossing method with a PIV signal as a reference signal). Although the qualitative behavior of the oscillation is properly covered by all methods, substantial quantitative differences are evident. The amplitude of the velocity is a dominant indicator for the accuracy of a phase-averaging method because averaging the wrong snapshots causes a significant loss in amplitude. The small amplitudes obtained by the benchmark method indicate the poor quality of the phase-averaging algorithm. In contrast, the amplitudes of the velocity magnitude for the other methods are equal and at the same phase angle. Especially the autocorrelation and both Hilbert methods show a remarkable agreement. The results of the POD differ from the others regarding the temporal duration of the velocity peaks. The reasons for these quantitative deviations are discussed separately in the following section because POD is frequently applied in other research to unsteady flow fields. Another possibility is the investigation of the RMS value of all snapshots averaged within a phase window. Higher RMS values indicate a larger deviation from the mean value and are indicators for incorrect phase angle allocation. However, some methods such as POD minimize the RMS value within a window by maximizing the variance between individual modes. Evidently, this does not necessarily yield the 'true' solution.

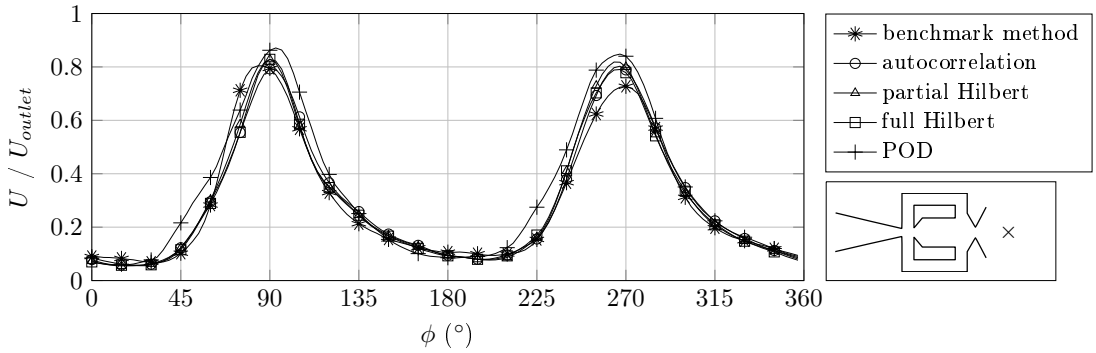

Fig. 10 Phase-averaged velocity profiles at ($x/d_h = 4$, $y/d_h = 0$). Every fifth data point marked.

In addition to the visual examination, two additional approaches to compare methods are pursued in this study. The first approach compares the duration of the individual oscillation periods. The individual periods are identified based on zero-crossing from 359° to 0° for all methods except for the full Hilbert method. The individual periods are used to evaluate a resulting period length. For the full Hilbert method, the instantaneous frequency determined by the Hilbert transformation is used. In a naturally oscillating flow field, the period length is expected to fluctuate. The method yielding the least period length fluctuations may be considered most accurate. The probability density of the local period lengths for each method is presented in figure 11. The average period length is approximately equal for all methods which supports their general applicability. However, the full Hilbert method generates broad fluctuations in the instantaneous period length. This is likely caused by a non-sinusoidal reference signal which results in fast changing instantaneous frequencies. The least variation in period length is evident for the autocorrelation, benchmark, and POD method.

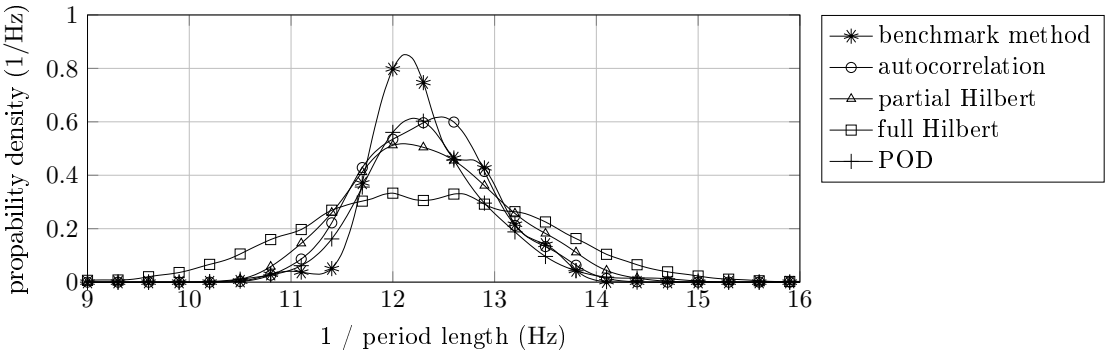

Fig. 11 Probability density of individual period length for various methods.

The comparison discussed in figure 11 addresses the correct identification of the oscillation periods. Furthermore, in a naturally oscillating flow field the snapshots should be evenly distributed over all phase angle windows of one period. Recall that 10,920 snapshots are recorded at a constant sampling rate of 1.5 kHz. This is another possibility to ensure the accuracy of the phase-averaging methods. In figure 12 it is evident that the full Hilbert method and especially the POD have some drawbacks in the accurate allocation of phase angles. This observation is consistent for all supply rates except for the full Hilbert method. The phase angle allocation for this method is improved for higher supply rates because more oscillation periods are covered within the reference signal. It is noteworthy that the range of phase angles with high velocity magnitude (figure 10) corresponds to the phase angle windows with the least number of snapshots for the POD method. Consequently, the high velocities are stretched over a wider range of phase angles. At other locations within the flow field, the properties are stretched/compressed accordingly. Possible sources of this problem for the POD are investigated in section IV-B. Figure 12 also reveals that the snapshots per phase angle are evenly distributed for all methods which identify a period oscillation start. This is expected due to the definition of the phase angle assignment.

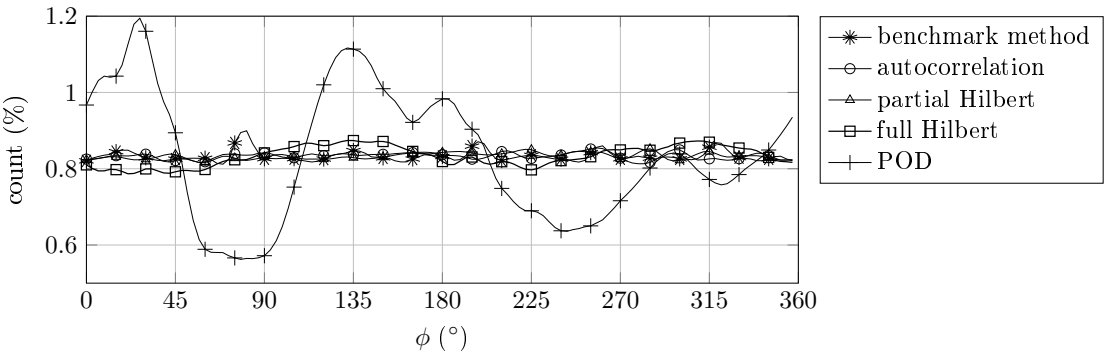

Fig. 12 Distribution of snapshots per phase angle window. Every fifth data point marked.

It can be concluded that according to figure 10, the benchmark method does not sufficiently phase-average the data because it decreases the velocity amplitudes. In fact, the period identification method ‘zero-crossing’ is highly sensitive to noise, making it a poor choice for most applications. Furthermore, the reference signal extracted from PIV is not suitable for high oscillation frequencies due to the usually low sampling rates of optical measurement methods. POD and full Hilbert have some drawbacks in allocating the correct phase angle, which reduces the accuracy of the phase-averaged results (figures 11 and 12). The phase-averaging, based on conditioning a reference signal extracted from pressure signals, is found to yield reliable results in this study. Nevertheless, due to the susceptibility to signal noise, applying an autocorrelation is required. This must be handled carefully in order to avoid the imposition of a

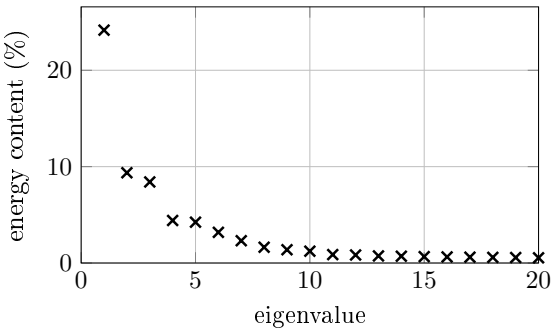

Fig. 13 Energy content of the eigenvalues.

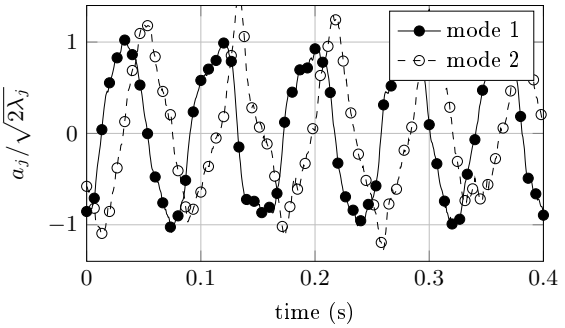

Fig. 14 Time-dependent mode coefficients. Every tenth data point marked.

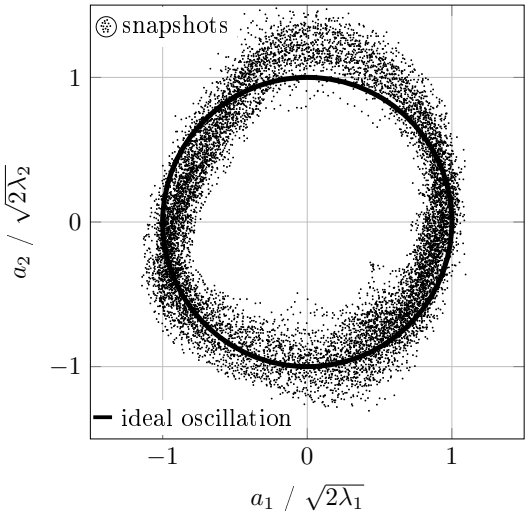

Fig. 15 Phase portrait of modal coefficients $a_1(t)$ and $a_2(t)$ of the external flow field.

dominant frequency. The partial Hilbert method may also be a good alternative. This method defines a period starting point at the extreme values of a period where low gradients cause the method to be susceptible to noise. The POD is of particular interest for studies where no reference signal is available. This motivates the discussion of potential improvements in the subsequent section.

B. Challenges with POD and According Modifications

The POD method is frequently used for examining and phase-averaging unsteady flow fields.[9, 21–23] It is a very attractive tool for phase-averaging flow fields because it requires neither a reference signal nor time-resolved snapshots of the flow field. Despite these advantages, POD has limitations in reconstructing the correct oscillation period of the investigated flow field causing quantitative deficiencies. Due to the general interest in POD, the shortcomings of this method are investigated in more detail. A modification is also suggested which significantly improves the accuracy of the POD approach.

Phase-averaging using POD requires the calculation of phase angles between dominant modes, which are normalized by their respective eigenvalues (Eq. 7). For an ideal harmonic oscillation between two modes, the modes exhibit approximately equal energy content, the time-resolved normalized mode coefficients are sinusoidal, and they have a 90°

phase shift. In the case of a fluidic oscillator, mode one has more than twice the energy of mode two (figure 13). The time-resolved normalized mode coefficients are shown in figure 14. Although a 90° phase-shift is evident, the mode coefficients show discrepancies. The amplitude of the normalized mode 2 coefficient is higher than the amplitude of the mode 1 coefficient. Additionally, the shape of the mode coefficients differs. It is noteworthy that the differences between the individual oscillation periods are higher for mode two than for mode one. These observations lead to a distorted phase portrait (figure 15). Consequently, the phase angle calculation (Eq. 7) leads to a periodic distortion of the flow field properties, thereby reducing the accuracy of the POD method. The described observations for the POD modes are likely caused by oscillating velocity amplitudes at the exit and decreasing velocity magnitude downstream of the exit due to entrainment. Moreover, information may be lost because the higher modes are neglected for the phase angle allocation. In order to improve the results, a modification is suggested by imposing a constant distribution of snapshots per phase angle window. This assumption was previously justified based on a constant sampling rate in conjunction with a naturally fluctuating flow field. It may be assumed that although the allocated phase angle value is erroneous, the correct phase angle sequence is revealed by the POD. Instead of phase-averaging the snapshots according to their determined phase angle, the snapshots are sorted sequentially by these phase angles and evenly allocated to a predetermined number of phase angle windows. In this study all 10,920 snapshots are sorted in ascending order based on their assigned phase angle. A window size of 3° yields 120 phase angle windows within one oscillation period. Therefore, 91 snapshots per phase angle window are desired to obtain an equal distribution of snapshots per phase angle window. Based on this, the first 91 snapshots are assigned to the first phase angle window, the next 91 snapshots to the second phase angle window, and so forth until all phase angle windows have the same amount of snapshots available for phase-averaging. In order to incorporate all available snapshots and to avoid a minor phase delay, the number of snapshots should be a multiple of the number of phase angle windows. The modified approach imposes an even distribution of snapshots while maintaining the POD determined temporal sequence of the snapshots. Note that this modified POD is only applicable for snapshots which are randomly distributed throughout the oscillation periods.

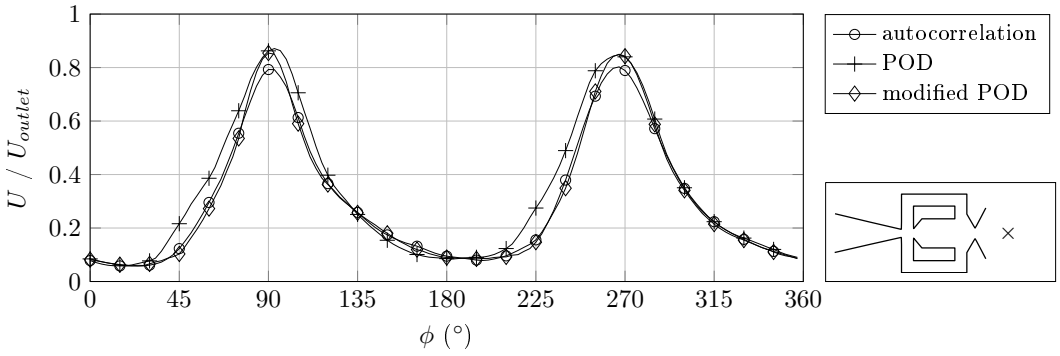

Fig. 16 Phase-averaged velocity profiles at (x/d_h = 4, y/d_h = 0). Every fifth data point marked.

In figure 16 the phase-averaged results of the conventional and modified POD method are compared to the autocorrelation method at the same position as in figure 10. As expected, the conventional POD approach yields deviations. In contrast, the modified POD shows good agreement with the autocorrelation method. This is noteworthy because the two methods are based on completely different approaches (i.e., mathematical vs. signal conditioning method). This result assures confidence that both methods are accurate in revealing the naturally oscillating flow field. In fact, the modified POD yields even higher amplitudes of the phase-averaged velocity, indicating a better phase-averaged result. Nevertheless, some problems with the modified POD method are identified. Various regions of the flow field may be recorded separately in order to improve the spatial resolution. The POD methods encounter problems especially in flow regions where the oscillation is not fully captured. It is suspected that the flow field patterns

caused by the oscillation of the jet are either incomplete or not dominant enough for proper identification by the POD methods. Consequently, the POD methods are only applicable if the complete oscillation cycle is covered within one acquired field of view. If this condition is met, the modified POD method provides a simple and accurate tool in future studies and to other researchers.

C. Summarized Comparison and Applied Method

The previous sections describe and compare various phase-averaging methods. Each method is accompanied by certain advantages and disadvantages which are summarized in table 1. Based on various criteria, the methods which yield the most accurate results in this study are identified.

Table 1 Summary of the investigated phase-averaging methods.

Method	Description	Advantages	Disadvantages
Benchmark method	• applied to time-resolved PIV signal • period starting points identified by zero-crossing of velocity v-component	• reliable results due to simplicity	• susceptible to variations in local mean values • high sampling rate of PIV measurements required
Autocorrelation	• signal fragment correlated with time-resolved reference signal • period starting point identified by zero-crossing of correlation coefficient	• insensitive to noise • yields most promising results in this study	• may impose a dominant oscillation frequency depending on fragment length
Partial Hilbert	• applied to filtered time-resolved reference signal • period starting points identified by zero-crossing of instantaneous phase angle	• no imposing of a dominant oscillation frequency	• sensitive to noise • based on locating extreme values within the signal
Full Hilbert	• applied to filtered time-resolved reference signal • yields instantaneous phase angle for every data point	• assignment of instantaneous phase angle to every snapshot without additional processing	• deficits in reconstructing the correct time information • sensitive to noise
POD	• mode decomposition of every PIV snapshot • phase angles obtained directly from modal coefficients	• no time-resolved data necessary • only PIV snapshots required	• incorrect phase angle allocation due to uneven energy contents between modes one and two
Modified POD	• mode decomposition of every PIV snapshot • based on phase angle sequence, snapshots are evenly distributed over desired number of windows	• no time-resolved data necessary, only PIV snapshots required • phase-averaging directly applied to local data field	• only applicable when oscillatory behavior is dominant within data field • if more PIV regions are acquired, phase-alignment and transition between the regions may be challenging

It is found that all approaches are suitable for phase-averaging the flow field of the fluidic oscillator. However, some methods have drawbacks in quantitative accuracy (e.g., the full Hilbert and conventional POD method). The autocorrelation and modified POD method yield the most accurate results in this study. Although the modified POD approach has the great advantage of not requiring time-resolved data, it may have problems with flow fields not covering the entire oscillation and sufficiently capturing the dominant structures. Furthermore, phase-aligning and combination

of various flow fields without an overlap may be challenging. Therefore, a reference signal in combination with the autocorrelation approach is chosen for phase-averaging the flow field data of the fluidic oscillator in this study. The applied processing steps are summarized in the following overview:

1) At the beginning of the phase-averaging process, a proper reference signal must be found. In this study, pressure signals from the feedback channel, the outlet, and the outer region of the fluidic oscillator are suitable to meet the requirements. Further improvements in signal quality are achieved by subtracting two signals from symmetrically positioned pressure taps and applying a digital low-pass filter.
2) The reference signal is autocorrelated with an extracted sample size from one half to one full expected period length. The sign change of the correlation coefficient defines the start of each half oscillation period. Afterward, the half oscillation cycle is divided into equally sized phase angle windows. The simultaneously acquired PIV snapshots are assigned to the appropriate window by evaluating their time stamps.
3) All phase angles within a 3° range are averaged.

This procedure is successfully employed in order to phase-average the internal and external flow field of a fluidic oscillator as illustrated in figure 17. The time-resolved flow field allows a detailed investigation of various instantaneous flow field properties (e.g., jet velocity, jet width, deflection angle, and entrainment). The preliminary results of this investigation are presented by Gärtlein et al.[11].

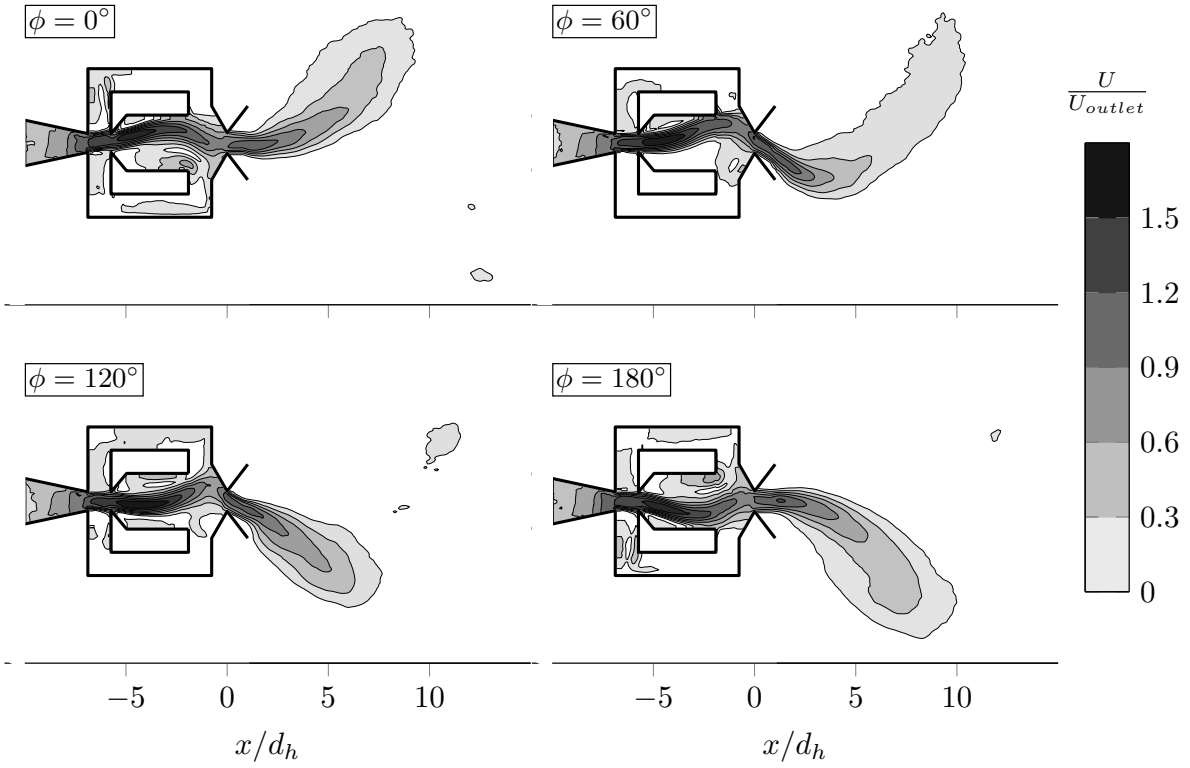

Fig. 17 Phase-averaged flow field.

V. Conclusion

Various methods for phase-averaging the natural flow field from a fluidic oscillator are analyzed. They are grouped into mathematical and signal conditioning methods. Selected methods are discussed in detail and evaluated for their accuracy based on several criteria. These criteria include the minimum fluctuation in instantaneous period length, the conservation of velocity amplitudes, and the number of snapshots per phase-averaging window. All methods are found to be suitable for phase-averaging the data, however with differing accuracy. The POD shows drawbacks in the correct temporal reconstruction of the external flow field of the oscillator. It is found that the POD artificially alters the time information by stretching and shrinking phases of the oscillation. A modified POD approach is introduced which imposes an even distribution of snapshots per phase angle window by using the phase angle sequence determined by the conventional POD. Although based on completely different approaches, the modified POD method yields excellent agreement with other methods involving a time-resolved reference signal. This agreement provides additional confidence that the modified POD is capable of revealing the naturally oscillating flow field of the fluidic oscillator. This modified POD method is a simple and accurate phase-averaging tool without requiring time-resolved data and may also be a suitable tool for other studies investigating oscillating flow fields. However, the POD method does have limitations in identifying the dominant modes if the oscillatory pattern is not fully covered within the field of view. In this study, a method also suitable for phase-averaging a flow field comprised from various PIV sections is desired. Additionally, phase-aligning is challenging because of the absence of a common signal if no overlap between the sections is present which is the case for the acquisition of three-dimensional flow fields. These reasons led to the pursuit of a phase-averaging method based on conditioning a time-resolved reference signal. After evaluating the advantages and disadvantages of the investigated approaches, the autocorrelation method is chosen. The subtracted signal between two symmetrically aligned pressure taps inside the feedback channels is used as the reference signal. This signal is digitally filtered and an autocorrelation is employed for the accurate identification of the oscillation periods. The PIV snapshots are averaged within a prescribed window size which is optimized with regards to minimizing noise while maintaining flow features. This procedure is successfully applied to yield the time-resolved internal and external flow field of a fluidic oscillator. It is also suitable for oscillating flow fields with higher velocities and oscillation frequencies. Furthermore, a conventional PIV system with lower sampling rates may be employed as long as a simultaneously recorded reference signal is obtainable and resolved in time. By acquiring the pressure signal inside the oscillator, other experiments such as the interaction of the jet with an external stream may be analyzed with this method as well.

Acknowledgments

The authors thankfully acknowledge the helpful discussions and assistance of the team at the Hermann-Föttinger-Institut. Especially the input of Moritz Sieber was highly appreciated. The authors also thank Dr. Jesse Little and Joshua Gray for the editorial review of the paper.

References

[1] Gregory, J., and Tomac, M. N., "A Review of Fluidic Oscillator Development," *AIAA 43rd Fluid Dynamics Conference*, 2013. doi:10.2514/6.2013-2474.

[2] Stouffer, R., "Oscillating spray device," Patent US 4151955, 1979. URL `http://www.patentlens.net/patentlens/patent/US_4151955/en/`.

[3] Guyot, D., Paschereit, C. O., and Raghu, S., "Active Combustion Control Using a Fluidic Oscillator for Asymmetric Fuel Flow Modulation," *International Journal of Flow Control*, Vol. 1, No. 2, 2009, pp. 155–166. doi:10.1260/175682509788913335.

[4] Raman, G., and Raghu, S., "Cavity Resonance Suppression Using Miniature Fluidic Oscillators," *AIAA Journal*, Vol. 42, No. 12, 2004, pp. 2608–2612. doi:10.2514/1.521.

[5] Seele, R., Tewes, P., Woszidlo, R., McVeigh, M. A., Lucas, N. J., and Wygnanski, I. J., "Discrete Sweeping Jets as Tools for Improving the Performance of the V-22," *AIAA Journal of Aircraft*, Vol. 46, No. 6, 2009, pp. 2098–2106. doi:10.2514/1.43663.

[6] Woszidlo, R., and Wygnanski, I. J., "Parameters Governing Separation Control with Sweeping Jet Actuators," *AIAA 29th Applied Aerodynamics Conference*, 2011. doi:10.2514/6.2011-3172.

[7] Woszidlo, R., Stumper, T., Nayeri, C., and Paschereit, C. O., "Experimental Study on Bluff Body Drag Reduction with Fluidic Oscillators," *52nd Aerospace Sciences Meeting*, 2014. doi:10.2514/6.2014-0403.

[8] Gregory, J. W., Gnanamanickam, E. P., Sullivan, J. P., and Raghu, S., "Variable-Frequency Fluidic Oscillator Driven by a Piezoelectric Bender," *AIAA Journal*, Vol. 47, No. 11, 2009, pp. 2717–2725. doi:10.2514/1.44078.

[9] Bobusch, B. C., Woszidlo, R., Bergada, J. M., Nayeri, C. N. N., and Paschereit, C. O., "Experimental study of the internal flow structures inside a fluidic oscillator," *Experiments in Fluids*, Vol. 54, No. 6, 2013. doi:10.1007/s00348-013-1559-6.

[10] Wassermann, F., Hecker, D., Jung, B., Markl, M., Seifert, A., and Grundmann, S., "Phase-locked 3D3C-MRV measurements in a bi-stable fluidic oscillator," *Experiments in Fluids*, Vol. 54, No. 3, 2013. doi:10.1007/s00348-013-1487-5.

[11] Gaertlein, S., Woszidlo, R., Ostermann, F., Nayeri, C., and Paschereit, C. O., "The Time-Resolved Internal and External Flow Field Properties of a Fluidic Oscillator," *52nd Aerospace Sciences Meeting*, 2014. doi:10.2514/6.2014-1143.

[12] Bergh, H., and Tijdeman, H., *Theoretical and experimental results for the dynamic response of pressure measuring systems*, Nationaal lucht-en ruimtevaartlaboratorium, 1965.

[13] Koso, T., Kawaguchi, S., Hojo, M., and Hayami, H., "Flow Mechanism of a Self-Induced Oscillating Jet Issued from a Flip-Flop Jet Nozzle," *JSME-KSME Fluids Engineering Conference*, Vol. 5, 2002.

[14] Wlezien, R. W., and Way, J. L., "Techniques for the Experimental Investigation of the Near Wake of a Circular Cylinder," *AIAA Journal*, Vol. 17, No. 6, 1979, pp. 563–570. doi:10.2514/3.61178.

[15] Luo, H., Fang, X., and Ertas, B., "Hilbert Transform and Its Engineering Applications," *AIAA Journal*, Vol. 47, No. 4, 2009, pp. 923–932. doi:10.2514/1.37649.

[16] Berkooz, G., Holmes, P., and Lumley, J. L., "The Proper Orthogonal Decomposition in the Analysis of Turbulent Flows," *Annual Review of Fluid Mechanics*, Vol. 25, No. 1, 1993, pp. 539–575. doi:10.1146/annurev.fl.25.010193.002543.

[17] Legrand, M., Nogueira, J., and Lecuona, A., "Flow temporal reconstruction from non-time-resolved data part I: mathematic fundamentals," *Experiments in Fluids*, Vol. 51, No. 4, 2011, pp. 1047–1055. doi:10.1007/s00348-011-1111-5.

[18] Huang, N. E., and Wu, Z., "A review on Hilbert-Huang transform: Method and its applications to geophysical studies," *Reviews of Geophysics*, Vol. 46, No. 2, 2008. doi:10.1029/2007rg000228.

[19] Legrand, M., Nogueira, J., Tachibana, S., Lecuona, A., and Nauri, S., "Flow temporal reconstruction from non time-resolved data part II: practical implementation, methodology validation, and applications," *Experiments in Fluids*, Vol. 51, No. 4, 2011, pp. 861–870. doi:10.1007/s00348-011-1113-3.

[20] Zilberman, M., Wygnanski, I., and Kaplan, R. E., "Transitional boundary layer spot in a fully turbulent environment," *Physics of Fluids*, Vol. 20, No. 10, 1977, p. S258. doi:10.1063/1.861739.

[21] Oudheusden, B. W. v., Scarano, F., Hinsberg, N. P. v., and Watt, D. W., "Phase-resolved characterization of vortex shedding in the near wake of a square-section cylinder at incidence," *Experiments in Fluids*, Vol. 39, No. 1, 2005, pp. 86–98. doi:10.1007/s00348-005-0985-5.

[22] Perrin, R., Braza, M., Cid, E., Cazin, S., Barthet, A., Sevrain, A., Mockett, C., and Thiele, F., "Obtaining phase averaged turbulence properties in the near wake of a circular cylinder at high Reynolds number using POD," *Experiments in Fluids*, Vol. 43, No. 2-3, 2007, pp. 341–355. doi:10.1007/s00348-007-0347-6.

[23] Oberleithner, K., Sieber, M., Nayeri, C. N., O.Paschereit, C., Petz, C., Hege, H.-C., Noack, B. R., and Wygnanski, I. J., "Three-dimensional coherent structures in a swirling jet undergoing vortex breakdown: stability analysis and empirical mode construction," *Journal of Fluid Mechanics*, Vol. 679, 2011, pp. 383–414. doi:10.1017/jfm.2011.141.

This is a post-peer-review, pre-copyedit version of an article published in **Experiments in Fluids No. 56:125**.
The final authenticated version is available online at Springer via http://dx.doi.org/10.1007/s00348-015-1993-8.

The Time-Resolved Natural Flow Field of a Fluidic Oscillator

R. Woszidlo · F. Ostermann · C.N. Nayeri · C.O. Paschereit

Received: 3 February 2015 / Revised: 30 April 2015 / Accepted: 2 May 2015

Abstract The internal and external flow field of a fluidic oscillator with two feedback channels are examined experimentally within the incompressible flow regime. A scaled-up device with a square outlet nozzle is supplied with pressurized air and emits a spatially oscillating jet into quiescent environment. Time-resolved information are obtained by phase-averaging pressure and PIV data based on an internal reference signal. The temporal resolution is better than a phase angle of 3°. A detailed analysis of the internal dynamics reveals that the oscillation mechanism is based on fluid feeding into a separation bubble between the jet and mixing chamber wall which pushes the jet to the opposite side. The total volume of fluid transported through one feedback channel during one oscillation cycle matches the total growth of the separation bubble from its initial size to its maximum extent. Although the oscillation frequency increases linearly with supply rate, sudden changes in the internal dynamics are observed. These changes are caused by a growth in reversed flow through the feedback channels. The time-resolved properties of the emitted jet such as instantaneous jet width and exit velocity are found to oscillate substantially during one oscillation cycle. Furthermore, the results infer that the jet's oscillation pattern is approximately sinusoidal with comparable residence and switching times.

Rene Woszidlo
The University of Kansas, Aerospace Department
1530 W 15th St
Lawrence, KS 66045, USA
E-mail: rene@ku.edu

Florian Ostermann
Technische Universität Berlin
Müller-Breslau-Straße 8
10623 Berlin, Germany
E-mail: florian.ostermann@tu-berlin.de

Keywords Fluidic Oscillator · Sweeping Jet · Particle Image Velocimetry · Phase-Averaged Flow

1 Introduction

Fluidic oscillators are devices which emit a continuous but spatially oscillating jet when supplied with a pressurized fluid. These oscillations are self-induced and self-sustained, solely based on the internal fluid dynamics without requiring any moving parts. A snapshot of an oscillating water jet is illustrated in figure 1 (right) which is emitted by an oscillator similar in design to the geometry discussed in this study. Figure 1 (left) conceptually illustrates the internal dynamics. The main jet enters into a mixing chamber where it attaches to either side wall due to the Coanda effect. A portion of the main jet stream returns through the respective feedback channel to the oscillator's inlet where it causes the jet to detach and flip to the opposite side. There, the same process occurs to complete one oscillation cycle. The exact details of the oscillation mechanism are addressed in the current study. The oscillation frequency may range from the order of 1 Hz up to several kHz (Gregory et al 2007) depending on the oscillator's size, geometry, supply rate, and the fluid's properties.

Fluidic oscillators were developed more than half a century ago at the Harry Diamond Research Laboratories with the initial intention of providing the basis for control circuits as fluid logic elements. With the rapid development of electronic alternatives, fluidic devices became obsolete and have mainly been used for water applications such as windshield washer nozzles, sprinklers, and shower heads. Since their initial development, various types and designs of fluidic oscillators have been patented (e.g. Stouffer 1979, Luxton and Nathan 1991,

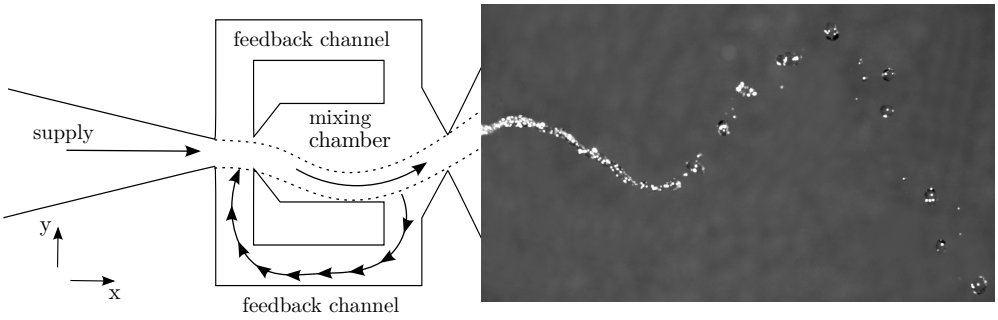

Fig. 1 Working principle of a fluidic oscillator

and Raghu 2001). The main difference between various designs is the number of feedback channels which also determines the underlying mechanism that causes the jet to oscillate. For the design without feedback channels (Gregory et al 2007; Raghu 2001), the jet's oscillations are solely based on the shear layer instability between two interacting jets. The second category of fluidic oscillators incorporates just one feedback loop (e.g. Spyropoulos 1964). The oscillation mechanism for this category is based on a pressure signal being sent through one feedback channel which draws the jet over to the opposite side. Therefore, the oscillatory behavior is mainly governed by the geometry of the feedback channel. The current study focuses on an oscillator with two feedback loops where a flow of fluid through the feedback channels causes the oscillations of the main jet (figure 1).

An extensive review of the historical development and contemporary research of fluidic oscillators was presented by Gregory and Tomac (2013). In recent years, these devices have gained renewed interest as flow control actuators. Numerous studies have demonstrated their potential for separation control (e.g. Seele et al 2009, Cerretelli and Kirtley 2009, Phillips and Wygnanski 2013, and Woszidlo et al 2014), combustion control (e.g. Guyot et al 2009), and noise control (e.g. Raman and Raghu 2004). Although fluidic oscillators have been successfully employed for flow control, the information available on their fundamental internal and external dynamics remain limited. Experimental studies are challenging due to their commonly small size which is associated with high frequencies and high exit velocities. Furthermore, no external trigger is available to phase-average the data. The oscillations are accompanied by natural fluctuations which add to the difficulties of obtaining time-resolved information on the flow field. Some initial insight was provided by a few recent studies. Gregory et al (2009) employed a secondary system (i.e. a piezoelectric bender) to control the jet oscillations which provided them with an external trigger signal. However, with this system the oscillations were not controlled by the natural internal dynamics. A design similar to the one utilized in the current study was investigated by Bobusch et al (2013a) with water as a working fluid. Using water lowers the oscillation frequency and exit velocity for a given Reynolds number and circumvents compressibility effects. The method of proper orthogonal decomposition was employed to obtain time-resolved information on the internal flow field only. Despite limited temporal and spatial resolution, Bobusch et al (2013a) provided insight into the internal dynamics for the first time. A novel approach to obtaining time-resolved data on a fluidic oscillator with one feedback channel was documented by Wassermann et al (2013) who employed phase-locked three-dimensional three-components magnetic resonance velocimetry. They also noted the challenges of triggering into the natural oscillations of the device. The precursor of the current study was presented by Gaertlein et al (2014) with a preliminary analysis of the time-resolved internal and external flow field of a fluidic oscillator. Numerical studies have been sparse because they are burdened by the absence of a suitable data set for proper validation. A numerical parametric study by Bobusch et al (2013b) addressed the effects of some geometric features. Beside understanding the internal dynamics of fluidic oscillators, the external properties of oscillating jets are of crucial interest for the wide range of possible applications. The main question on how an oscillating jet interacts with a freestream has yet to be answered.

The presented work aims to improve the detailed understanding of fluidic oscillators by experimentally examining the incompressible time-resolved internal and external flow field. The natural flow field is phase-averaged based on the reference signal method developed by Ostermann et al (2015a). The following sections describe the experimental setup and data analysis methods. The time-resolved flow field is discussed in section 4 by evaluating the detailed dynamics and underlying mechanisms. In view of potential applications, emphasis is placed on the oscillation pattern of the external jet.

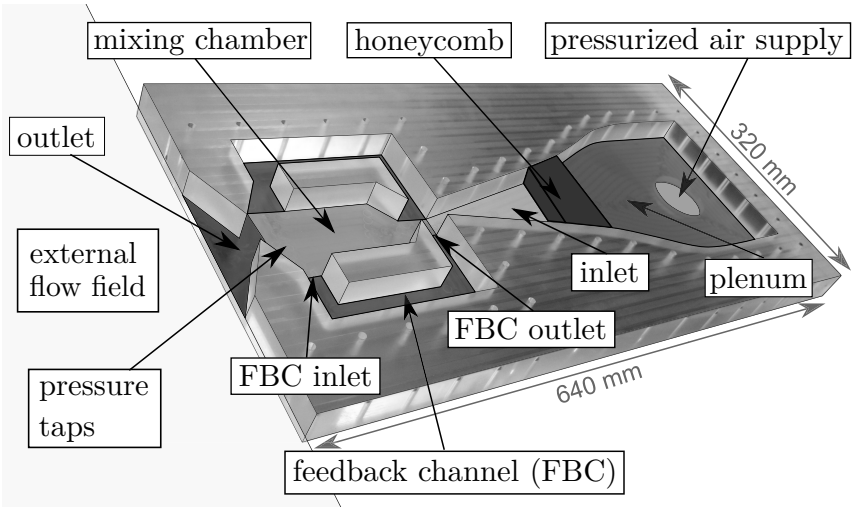

Fig. 2 Examined fluidic oscillator with denotations of main regions.

2 Setup and Instrumentation

The particular fluidic oscillator examined in this study is illustrated in figure 2 (left). The oscillator is scaled up in comparison to previous flow control applications (e.g., Woszidlo and Wygnanski 2011) in order to reduce the oscillation frequency and exit velocity, and to improve the visual accessibility. Optical access is enabled by machining the oscillator out of acrylic glass with a constant cavity depth of 25 mm. A cover plate (also made from acrylic glass) ensures an airtight seal. Compressed air is supplied into the plenum and monitored by a digital mass flow meter (F-203AV by Bronkhorst®-Mättig) with an accuracy better than 0.6 % full scale. The average temperature of the supplied air is 293 K. A temperature sensor is installed inside the pressure supply system to allow a continuous monitoring and to ensure the correct calibration conditions of the mass flow meter. The plenum's width contracts to the smallest inlet diameter with a ratio of 10 to 1. A piece of honeycomb upstream of the inlet ensures homogenous inflow conditions. The internal sections of the oscillator are marked in figure 2 (left) to be referenced throughout this paper. The square outlet of the oscillator is 25 mm × 25 mm which equates to a hydraulic diameter of $d_h = 25\,\text{mm}$.

Inside the fluidic oscillator, 55 small orifices are distributed symmetrically to measure the time-resolved pressure. The pressure transducers (HDO Series by Sensortechnics) have a range of ±2000 Pa with a response time of 0.1 ms and an accuracy better than 0.2 % full scale. The sampling rate is fixed at 16 kHz which is three orders of magnitude higher than the oscillation frequency. The orifice diameter (0.8 mm) and length of the connection to the transducer (20 mm) are optimized to avoid resonance effects and amplitude reduction by employing the calculation of the dynamic response of tubes. Even for the highest oscillation frequency (≈ 23 Hz), the expected phase delay is negligible. All pressure measurements are recorded simultaneously with a multichannel DAQ system from National Instruments™.

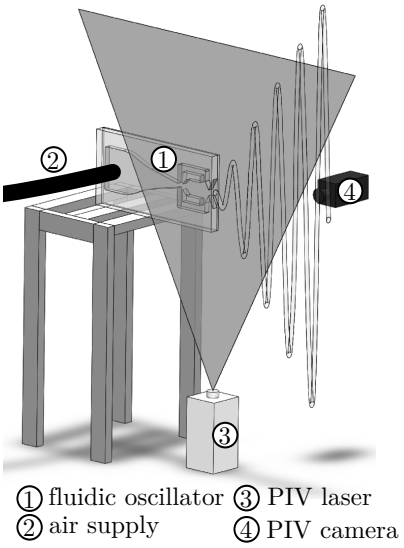

Fig. 3 Schematic of the general setup

The fluidic oscillator is positioned on a pedestal so that the jet emits into unobstructed, quiescent environment (figure 3). The internal and external flow field are measured with Particle Image Velocimetry (PIV) by means of one high-speed camera (Photron Fastcam SA1.1) with a resolution of one megapixel and a 60 mJ Nd:YLF Laser (Quantronix Darwin Duo 100). The laser sheet penetrates the oscillator and the external flow field through the plane of symmetry. An aerosol generator

is integrated into the air supply system to seed the jet with particles less than 1 µm in size. Prior to measurements of the external flow field, the system is run for a sufficiently long time to distribute enough seeding throughout the laboratory so that the entrained air also contains seeding particles. The PIV sampling rate is constant at 1.5 kHz to record a total of 10,920 double pictures per test case. This amount of pictures enables a high temporal resolution during the phase-averaging process. Despite the constant PIV sampling rate, no phase-locking occurs due to the natural fluctuations in oscillation frequency. The post-processing of the PIV data is performed by using the commercial software PIVview2C 3.5. The interrogation window size is set to 16×16 pixels with an overlap of 50 % for the external flow field and 12×12 pixels with an overlap of 50 % for the internal flow field. This yields a spatial resolution of approximately 2 mm.

As expected from the different refractive indices of air and acrylic glass, the illumination of the internal cavities is non-homogeneous. In order to maximize data quality, measurements with different laser positions yield results for different areas of the internal geometry. These sections are individually phase-averaged through the process described in the following section and then phase-aligned based on the simultaneously recorded pressure data. The overlap regions are evaluated to assess the quality of the individual measurements which deviate less than 5 % and then averaged to provide a smooth transition. Through this process the entire internal flow field is spatially resolved. A similar process is applied to the external flow field to improve the spatial resolution. Four measurement windows (two in x-direction and two in y-direction) are recorded with a 10 % overlap in y-direction and a 20 % overlap in x-direction. The combination of these four windows yields the external flow field over 20 nozzle diameters.

3 Data Analysis

In order to obtain time-resolved flow field information with a high quality, the measurement data are phase-averaged. Ostermann et al (2015a) evaluated various phase-averaging methods for the specific application on a fluidic oscillator. They employed the same experimental setup and measurement techniques as in the present study. Two methods were identified to yield the most accurate results. The first method is based on proper orthogonal decomposition which does not require any time-resolved data. However, the entire jet oscillation has to be covered within one PIV window which limits the spatial resolution. Therefore, the second method is applied which is based on using pressure data as a reference signal to identify the phase angle of each individual PIV snapshot in each measurement window. The most suitable reference signal is found to be the differential signal between two pressure sensors positioned symmetrically in the feedback channel inlets (figure 4, left). Because the feedback tube acts similar to a resonator with open ends, a high resonance frequency (one order of magnitude higher than the oscillation frequency) is imposed on the pressure signal. A numerical low pass filter is applied forward and backward to reduce the noise while maintaining phase and amplitude information. The entire reference signal is correlated with a segment of the same signal. This segment is approximately half of an oscillation period in length. The resulting distribution of the correlation coefficient marks each individual half oscillation cycle (figure 4, right). With this information, a phase angle is assigned to each simultaneously recorded PIV snapshot. All data within a prescribed phase angle window are averaged. The size of the phase angle window is 3° for the present study which was identified by Ostermann et al (2015a) as the most suitable for the given data set because it sufficiently reduces noise while maintaining the detailed flow features. It is verified that the averaging process for each window converges. All PIV measurement windows and pressure data are phase-averaged in the described manner. Figure 5 compares an instantaneous PIV snapshot with the respective phase-averaged velocity field for an arbitrary phase angle. The phase-averaged flow field visualizes the same features at a reduced noise. Additional information on the method and its validation can be found in Ostermann et al (2015a).

The autocorrelation method does not provide a consistent starting point for all windows. Therefore, they are phase-aligned based on the phase-averaged pressure signal. The windows' position is chosen so that a sufficient overlap is maintained in order to assess the agreement between different measurements and to provide a smooth transition between the windows. The smooth transition is achieved by a weighted average of the overlapping data points. With this process, the entire internal and external flow field is available for one oscillation cycle with high spatial and temporal resolution. However, the definition of the cycle starting point remains arbitrary. The literature does not offer any quantitative definition. Usually any reference to phase angles is based on qualitative criteria such as the jet's internal or external deflection state. In the current study, the cycle start is chosen to be the zero difference (with a sign change from negative to positive) in the reference signal which refers to the zero differential pressure between the two feedback channel inlets. Qualitatively, this definition marks the instance where the jet exits the oscillator at

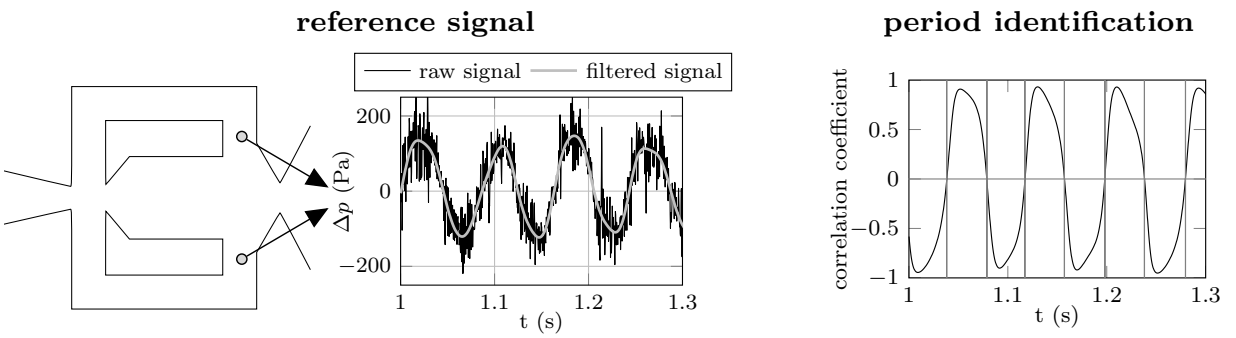

Fig. 4 Period identification from an improved reference signal. Differential pressure signal from two taps (left). Period identification based on correlation method (right).

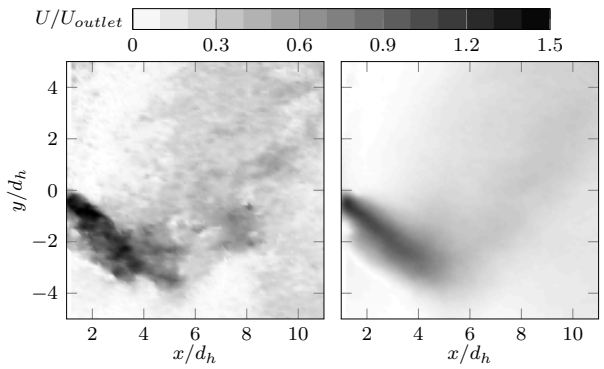

Fig. 5 Comparison between a PIV snapshot (left) and the appropriate phase-averaged flow field (right)

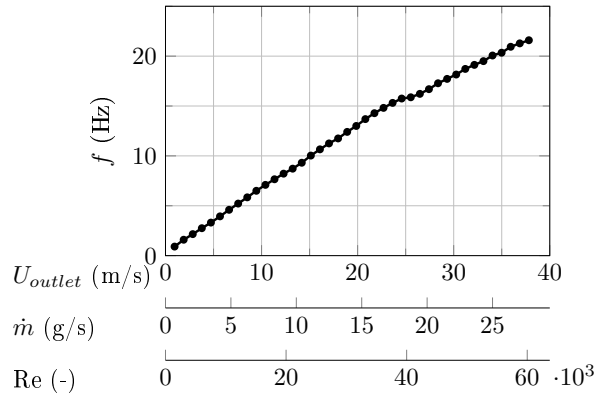

Fig. 6 The jet's oscillation frequency vs. supply rate

almost zero deflection. However, this definition and the accompanying qualitative observations are specific to the particular oscillator used in this study and would be different for other oscillator designs and sizes.

4 Results

The aforementioned phase-averaging method yields the continuous internal and external flow field for various supply rates which range from 0.7 to 27.8 g/s. Figure 6 illustrates the mean oscillation frequency f as a function of outlet velocity U_{outlet}, supply rate $\dot{m}$, and Reynolds number Re. The frequency is obtained from spectral analysis of the pressure data. The outlet velocity is based on the smallest cross-section in the oscillator's outlet nozzle and on the assumption of ambient conditions at the outlet. With a calculated Mach number of 0.11 for the highest mass flowrate, this assumption is well within the common limits of incompressibility. The Reynolds number is based on the outlet velocity and the hydraulic diameter (i.e., $d_h = 25\,\text{mm}$) of the square outlet. It is noted that all Reynolds number values are within the turbulent regime of a common pipe flow. As expected, the oscillation frequency increases linearly with supply rate which has been observed in almost all literature on fluidic oscillators. The linear trend is also evident for very low supply rates ($U_{outlet} \leq 1\,\text{m/s}$). Therefore, even lower oscillation frequencies than 1 Hz may be achievable. A minimum supply rate required to obtain oscillations is not noticed in this study. A small deviation from the linear dependency of f is observed around $U_{outlet} = 25\,\text{m/s}$. This deviation is caused by subtle changes in the internal dynamics which have a significant impact on the jet's maximum deflection angle. More detail on these changes is discussed in the subsequent section.

The time-resolved information of the flow field is examined to address the internal dynamics such as the switching mechanism, and the oscillation pattern of the external jet. For structural clarity, the internal and external flow field are addressed individually in the following two sections. All flow field discussions are based on $U_{outlet} = 15\,\text{m/s}$ (Re = 25,000, Ma = 0.04) because this value yields representative results. In addition, selected properties are examined as a function of supply

rate. Note that all supply rates are well within the incompressible regime.

4.1 Internal Dynamics

The internal flow field is characterized by various dynamics especially within the mixing chamber and feedback channels. Figure 7 (left) visualizes the internal distribution of the velocity magnitude U for various phase angles ϕ during half an oscillation cycle. The right column of figure 7 illustrates the respective streamlines to enhance the visibility of the dynamics. The number, integration length, and origin of the streamlines is kept constant for all phase-angles. The streamlines should solely be regarded as a tool for visualization because they not provide a quantitative measure of vortex strength or velocity magnitude. An animation of the internal flow field including the streamlines and velocity magnitude is available in a supplemental video (Online Resource 1). Additionally, an animation of the time-resolved Finite-Time-Lyapunov-Exponent (FTLE) based on Haller (2001) is available in Online Resource 2. This exponent reveals detailed flow dynamics inside the oscillator. Both videos are intended to complement the following discussion.

At the start of the cycle ($\phi = 0°$), the main jet is in the process of attaching to the upper wall of the mixing chamber. The jet separates at the sharp inlet wedge and encloses a separation bubble with the wall. It should be noted that without any feedback channels the jet would remain attached in a stable state and the jet would steadily exit the device at a fixed deflection. Instead, the jet impinges on the converging wall of the outlet nozzle which directs a portion of the fluid into the upper feedback channel ($\phi = 60°$). This fluid returns to the inlet where it feeds into the separation bubble at a low momentum. The bubble grows in size and moves downstream, thereby pushing the main jet off the wall ($\phi = 120°$). The resulting curvature of the main jet increases the impingement angle on the outlet nozzle wall which in turn diverts even more fluid into the feedback channel. This self-amplifying process causes a rapid growth of the separation bubble which eventually pushes the main jet entirely to the opposite side ($\phi = 180°$). There, it encloses a new separation bubble with the lower wall which initiates the switching mechanism with the opposite side. The separation bubble from the upper wall opens into the feedback channel inlet and dissipates with the decreasing flow through the feedback channel. This dissipation can be tracked with the remnants of the separation bubble from the lower wall.

The process of fluid feeding into the separation bubble is identified as the underlying mechanism for the switching of the jet. If the shape of the mixing chamber walls is more streamlined so that no initial separation bubble is present, the fluid from the feedback channels just pushes in between the main jet and the wall to deflect it to the opposite side (Ostermann et al 2015b). Besides the described switching mechanism, a few additional dynamics are noteworthy. At the start of the cycle ($\phi = 0°$), it is evident that parts of the main jet are shaved off by the inlet wedge to penetrate into the feedback channel outlet. In combination with the opposing flow from the channel inlet, a pair of vortices forms in the left corner. These vortices persist until they are overcome by the flow entering the feedback channel inlet. The described dynamic is likely to delay the jet attachment process and the initiation of a sustained stream into the feedback channel inlet. A larger distance between the wedges may reduce this effect and thereby accelerate the switching process which in turn would yield an increased oscillation frequency for the same supply rate. This suggestion was verified numerically by Bobusch et al (2013b). Additional detail on the mass flow through the feedback channels is discussed shortly.

Another observation relates to flow separation within the feedback channels. At various instances throughout an oscillation cycle, the flow separates around the sharp inside corners of the channel path and forms recirculation areas in the outer corners. This separation causes unnecessary losses and a reduction of the effective channel width. A more streamlined channel geometry can potentially increase the oscillator's performance. An essential part of the oscillator's geometry is the shape of the outlet nozzle. The angle and shape of the converging nozzle walls are expected to determine the amount of fluid being diverted into the feedback channel which affects the switching process and therefore the oscillation frequency. Furthermore, the angle also governs the jet's deflection at the outlet which may be altered by adjusting the divergence angle or shape. It should be noted that the emitted jet does not, at any instance, attach to the diverging nozzle walls. Therefore, this part of the nozzle may be omitted which may be beneficial for some applications. However, a smaller divergence angle may force the jet to attach to this wall and thereby increase the jet's maximum deflection (Ostermann et al 2015b). Some initial alterations of the nozzle geometry were also investigated by Bobusch et al (2013b).

As previously mentioned, the flowrate through the feedback channels is a governing parameter for the internal oscillation mechanism. It was suggested experimentally and numerically by Bobusch et al (2013a,b) that the total volume of fluid transported through the feedback channel during one oscillation cycle is independent of the supply rate at least within the incompressible regime. This observation is explained with the separation

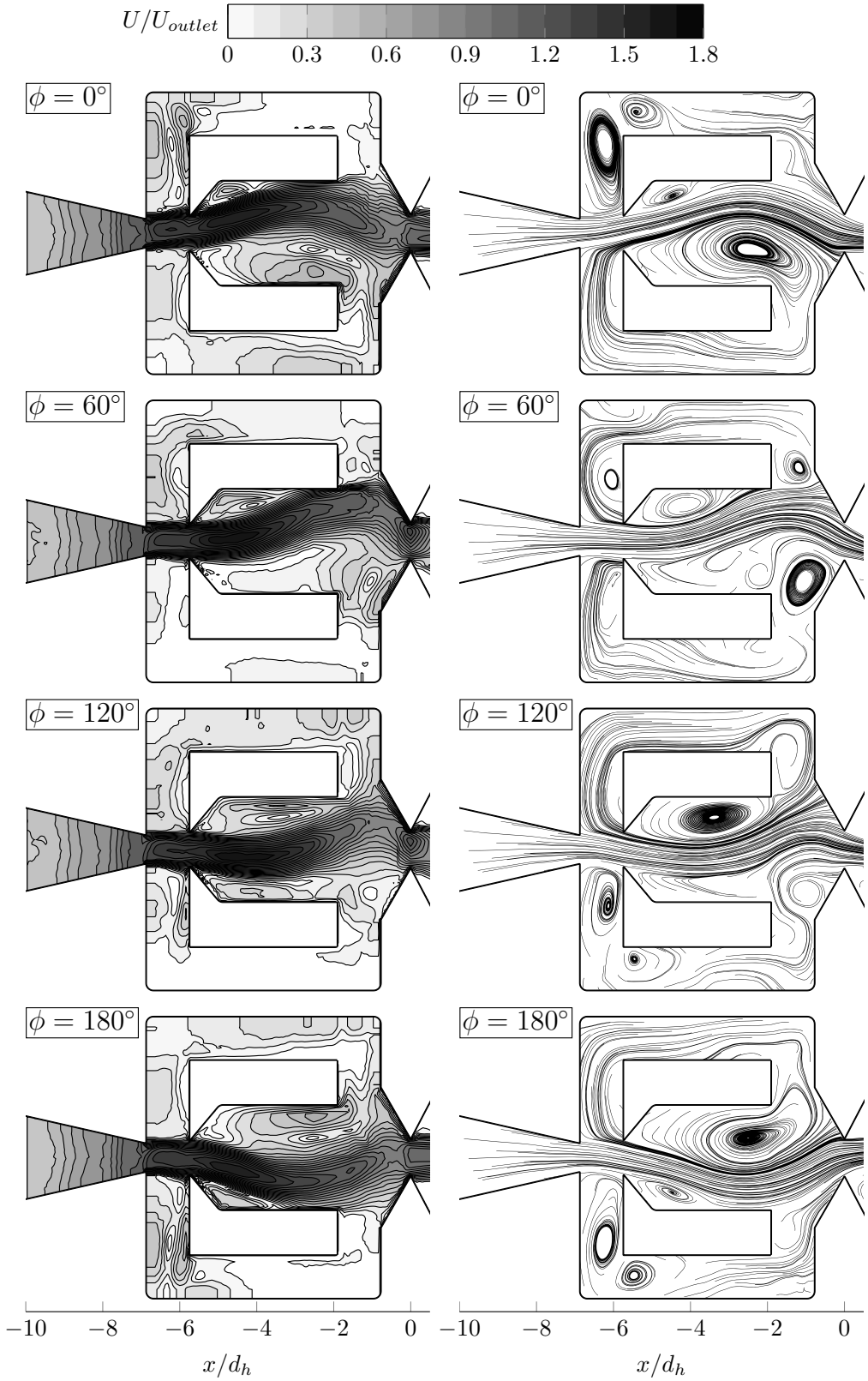

Fig. 7 The oscillator's internal flow field (left) and corresponding streamlines (right)

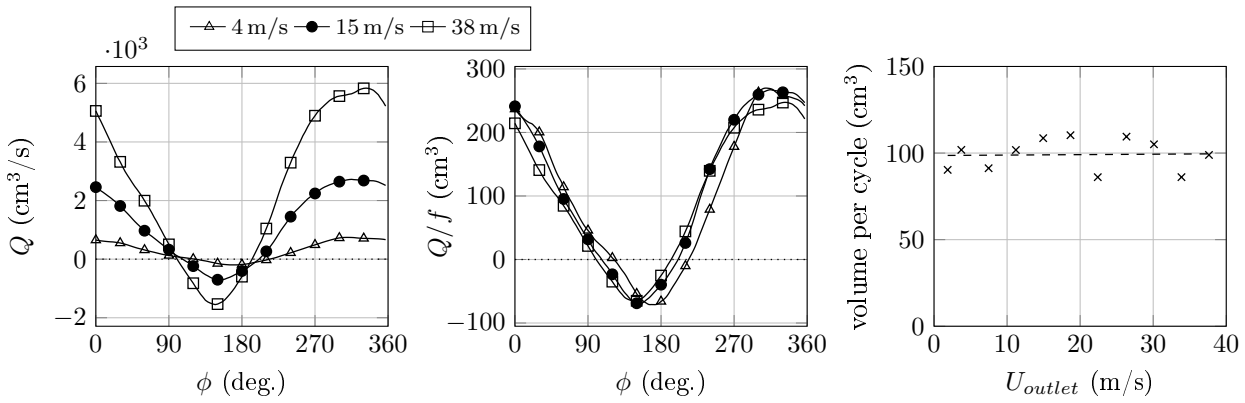

Fig. 8 Volume flow through lower feedback channel (every 10th data point marked)(left). The same volume flow normalized by the corresponding oscillation frequency (every 10th data point marked)(center). Total volume transported through feedback channel per oscillation cycle (right).

bubble between the main jet and wall having to grow by a fixed but design-specific volume to push the jet to the opposite side. This hypothesis is confirmed in the current study for air as the working fluid. Figure 8 (left) shows the volume flow Q through a cross-section at the center of the feedback channel for various supply rates. As expected, the extreme values increase with supply rate due to the increasing internal velocities. However, the volume flowrates occur over shorter periods of time because of the shorter cycle durations. When normalized by the oscillation frequency (figure 8, middle), the data collapse onto a single curve within the measurement accuracy. This infers that the total volume transported through the feedback channel per oscillation cycle is independent of supply rate. The argument is confirmed in figure 8 (right) by integrating the flowrate over one cycle for the entire range of considered supply rates. The data scatter is likely due to the limited spatial resolution over the small width of the feedback channel. However, a linear regression indicates the constant total volume. This result supports the argument that the volumetric growth of the recirculation bubble is the underlying mechanism governing the switching process. Further evidence for this statement is visualized in figure 9. The growth of the recirculation bubble from its initial size to its maximum extent is outlined. The difference in area multiplied by the oscillator depth matches the total volume per oscillation cycle (figure 8, right). These findings infer that the oscillation frequency mainly depends on the time it takes to transport the required volume through the feedback channel. This implies that the oscillation frequency may be increased by improving the flowrate through the feedback channel or by reducing the required total volume.

Although the internal dynamics appear to be very consistent and widely independent of supply rate, some

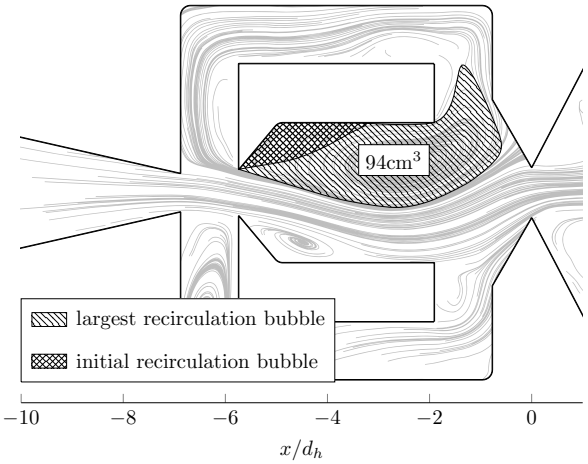

Fig. 9 Estimation of volume fed to the recirculation bubble.

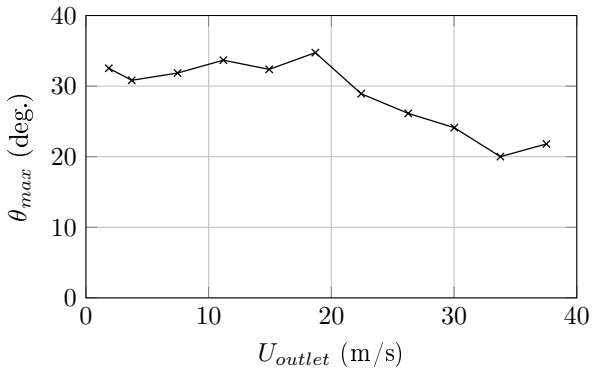

Fig. 10 Maximum jet deflection angle at the outlet

changes take place at higher velocities. These changes are not just noticed in the frequency shift at around $U_{outlet} = 25\,\mathrm{m/s}$ (figure 6) but are most obvious in the jet's maximum deflection at the outlet. The deflection

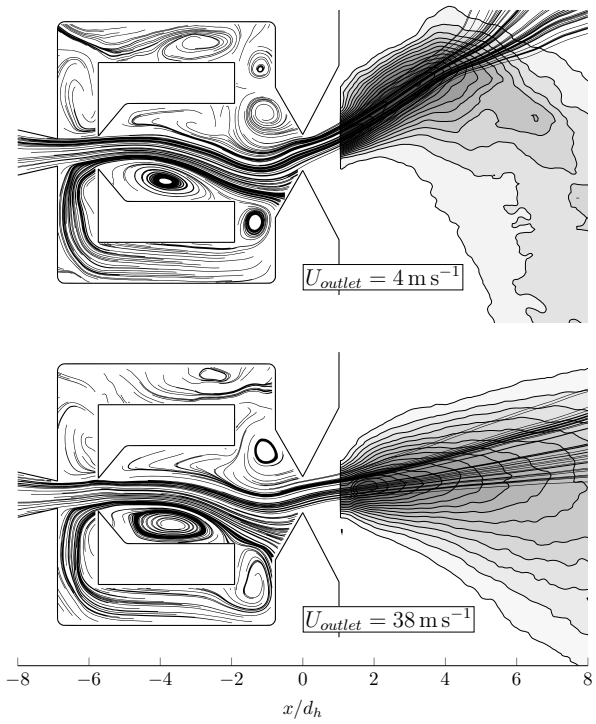

Fig. 11 Instantaneous internal and external flow field for two supply rates ($\phi = 267°$)

angle θ is obtained from the u and v component of the highest velocity magnitudes. Figure 10 depicts this angle at the outlet as a function of the supply rate. A significant drop in θ_{max} is observed at a similar value for U_{outlet} where the discrepancy in frequency occurs. These differences are visualized by the internal and external flow field for a small and a large supply rate at the same phase angle (figure 11). It is apparent that the jets' external deflection angles differ significantly. However, the internal changes are not as obvious. The main difference between the two supply rates is observed in the area of the feedback channel inlet. For the higher supply rate, the cavity vortex formed at the inlet is larger and extends deeper into the feedback channel. This affects the jet's approach path to the inner wall of the outlet nozzle which has a significant impact on the jet's exit angle. It is not exactly clear what causes the changing vortex dynamics at the feedback channel inlet. The main reason is suspected to be the internal jet width which increases with supply rate due to increasing turbulence levels. As noted in figure 8 (left), the increased jet width amplifies the reversed flow into the feedback channel outlet which also impacts the dynamics at the feedback channel inlet. Furthermore, the larger jet width within the mixing chamber affects the dynamics due to the confined space of the internal geometry. As previously

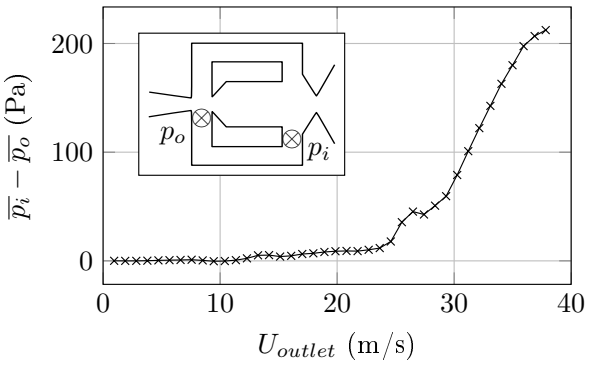

Fig. 12 Time-averaged pressure difference in the feedback channel

suggested, the shape and geometry of the nozzle's inner walls are a determining factor for the jet's external deflection. Although the changes in jet width are gradual, a threshold value may be reached beyond which the jet's impingement onto the wall is altered with significant consequences. Because it is suggested that the changing dynamics are most evident within the feedback channel, the pressure difference between its inlet and outlet ought to be most revealing. Figure 12 presents the time-averaged pressure difference between the inlet and outlet as a function of supply rate. An almost unchanged behavior is noticeable up to $U_{outlet} \approx 25\,\mathrm{m/s}$ before a rapid increase in pressure difference occurs, which is consistent with the discrepancy in oscillation frequency and the decline in deflection angle.

4.2 External Dynamics

The previous discussion of the internal dynamics relates directly to the external flow field properties which are of particular interest in view of potential applications. In this section, a general overview of the external flow field is provided, followed by an evaluation of the oscillation pattern based on the instantaneous deflection angle. Furthermore, the properties of the jet at the outlet are discussed. Two corresponding animations are available in Online Resource 3 and 4. The video in Online Resource 3 depicts the external FTLE field similar to the corresponding video for the internal flow field (Online Resource 2). The video in Online Resource 4 combines the internal and external flow field with the velocity magnitude. Again, these animations are intended to complement the following discussions.

Figure 13 illustrates the instantaneous velocity magnitude throughout the external flow field for half an oscillation cycle. For comparison, the flow field of a steady jet is added. This jet originates from the same device with sealed feedback channels and streamlined

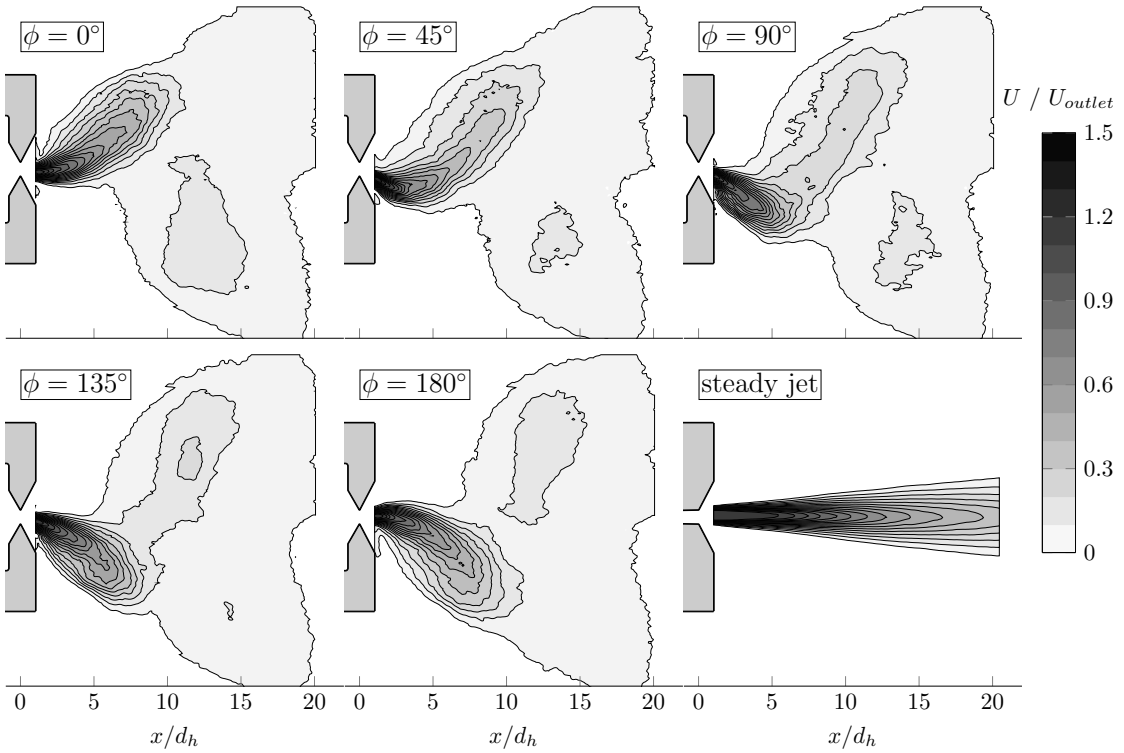

Fig. 13 Half oscillation period of the external flow field

mixing chamber. Note that the coordinate origin is located in the center of the smallest nozzle cross-section. Due to the sweeping motion of the jet, the impacted area is substantially larger than that of the non-oscillating jet. The lateral extent of the affected region is almost twice as large as the corresponding distance from the nozzle, which is consistent with the maximum deflection angle being close to ±45°. This large impact zone is the key feature of fluidic oscillators, especially for applications where a widespread distribution of fluid is desired. One distinct observation is made at the outer edge of the jet when fully deflected (figure 14, left). A vortex forms due to the shear layer. However, only one vortex develops, moves downstream, and dissipates when the jet switches back to the opposite side. This observation may explain the seemingly stationary pair of vortices detected in other studies (e.g. Woszidlo et al 2014) with a surface pattern visualization on an adjacent wall (figure 14, right). The time-averaging effect of the visualization technique depicts an enlarged footprint of the vortex on both sides of the jet's sweeping range although the presence of the vortices alternates. Even though the jet's sweeping motion only enables the formation of distinct vortices at the outer edges, the steep velocity gradients cause a significant distribution of vorticity over the entire affected area.

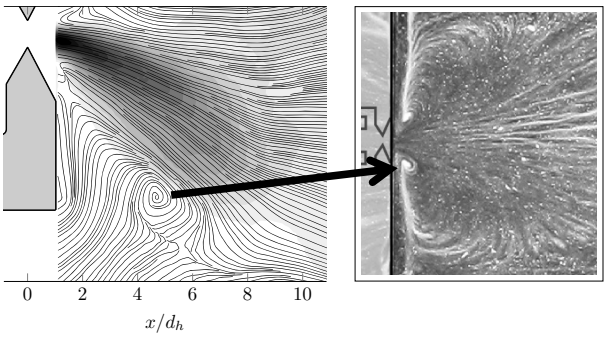

Fig. 14 Vortex in the external flow field in comparison to a flow visualization (Woszidlo et al 2014)

In view of applications which require a particular oscillation pattern, the time-resolved deflection angle is of interest. The oscillation pattern is assessed by obtaining the jet deflection from each instantaneous jet profile throughout one oscillation cycle (figure 15). Because of the jet's considerable lateral extent, an appropriate comparison of the jet's properties at different instances in time has to be performed at a fixed radial distance from the nozzle. Therefore, the coordinate system is transformed to polar coordinates with the polar angle ψ and radial distance r. In figure 15, the jet's instantaneous deflection angle is obtained along an arch with $r/d_h = 1.4$.

The first impression indicates a smooth and approximately sinusoidal oscillation pattern (figure 15, top). However, a more detailed analysis of the jet's transient behavior reveals a distinct overshoot in the deflection angle and changing oscillation speeds. Therefore, the angular velocity of the changes in deflection is calculated (figure 15, bottom), which reveals more distinct features. Three phases are defined within the pattern. The first phase corresponds to the mentioned overshoot in jet deflection, which is characterized by a rapid decrease in angular velocity up to the maximum deflection angle. The jet does not reside at this angle and quickly moves back to a smaller deflection where it remains with a decreasing angular velocity. This behavior is referred to as the "deceleration" phase. It is followed by a fast acceleration which marks the movement of the jet to the opposite side (i.e. acceleration phase). Based on these phases, two characteristic time scales are defined. During the overshoot and deceleration phase the jet is considered to be in its deflected state. The associated duration is referred to as the "dwelling time". The duration of the acceleration phase is named the "switching time". These two time scales are assessed for the entire range of considered supply rates (figure 16). Based on these definitions, the jet dwells on the sides for approximately as long as it takes to switch to the opposite side. Although the maximum deflection decreases significantly (figure 10), the same external oscillation pattern is observed. Therefore, the respective time scales remain almost unchanged. In relation to the internal flow field, one more interesting observation can be made from the transient jet deflection. The maximum jet deflection angle is obtained at approximately $\phi = 60°$, which does not coincide with the internal jet being fully attached to one of the walls as may be expected. Instead, the maximum deflection occurs while the internal jet is switching from one side to the other.

Although the sweeping pattern appears smooth and sinusoidal, the instantaneous jet properties at different deflections vary significantly. Figure 17 identifies these variations at the outlet. The jet properties oscillate by up to 10% around their corresponding mean value. Note that the mass flow and momentum are based on the depth of the outlet. The phase angles for the extreme values in jet velocity, mass flow, and momentum coincide. Furthermore, the minima in jet width (i.e. the normal width of the local velocity profile with $U \geq 50\% U_{max}$) correspond to the maxima in jet deflection angle. Because the jet exits the nozzle at an off-center angle, the effective outlet size is reduced. The opposite is true for the zero deflection angle, which is accompanied by the largest jet width and the smallest jet velocity. The oscillation in mass flow can be explained by two observations. The first observation is the blockage effect of the growing recirculation bubble. Due to its size, the bubble presents considerable blockage to the mass flow supply. The second observation is the impingement of the jet on the converging walls of the outlet nozzle which causes a significant adverse pressure gradient. The oscillations in pressure are even detected in the settling chamber upstream of the oscillator. At the largest extent of the separation bubble at approximately $\phi = 180°$ (figure 7), the blockage effect is at its maximum and the jet impinges on the inner nozzle wall. This instance coincides with the minimum in mass flow at the outlet (figure 17). Therefore, these effects work in tandem for this particular oscillator geometry. However, the relative impact of either effect can not be quantified with the existing data set and oscillator geometry. Similar oscillations in the jet's properties were observed by Bobusch et al (2013a) with water as a working fluid. These findings may affect the oscillator's applications, especially if an even distribution of fluid is desired. No information is available yet to whether the oscillatory output impacts the performance for flow control purposes.

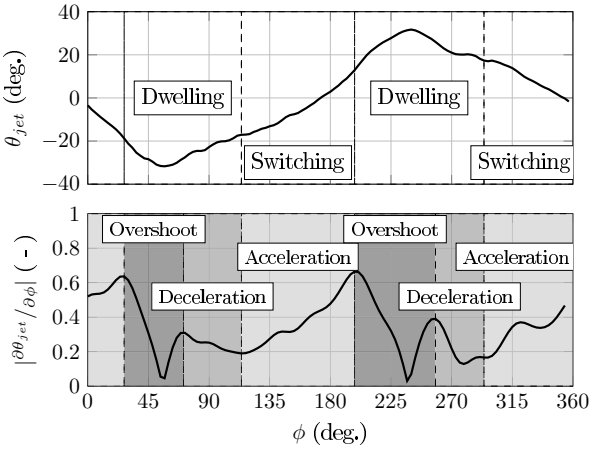

Fig. 15 Time-resolved deflection angle (top) and corresponding angular velocity (bottom) at $r/d_h = 1.4$

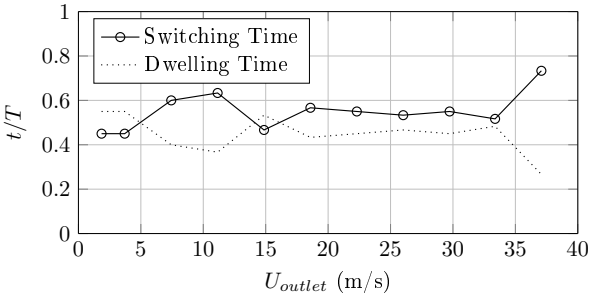

Fig. 16 Oscillation time scales as a function of the supply rate ($r/d_h = 1.4$)

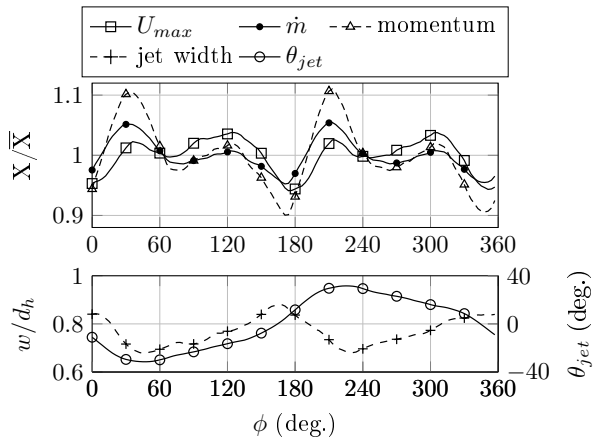

Fig. 17 Jet properties at the outlet. Every 10th data point marked

The instantaneous properties of the jet (e.g., jet velocity and jet width) may also be evaluated in the external flow field. Gaertlein et al (2014) suggested that the jet width is increasing with radial distance at a higher rate than a corresponding steady jet. At the same time, the jet's velocity is decaying faster with radial distance. However, these observations are solely based on two-dimensional flow field data which neglects a potential meandering of the jet in and out of the laser plane. Gaertlein et al (2014) also estimate the entrainment of the jet by introducing an effective jet depth based on the conservation of momentum. Although this estimation suggests that the oscillating jet entrains substantially more fluid than a steady jet, its accurate quantitative determination requires three-dimensional flow field information. Therefore, the quantitative evaluation of the external flow field is left for future studies.

5 Conclusion

The presented work examines the time-resolved internal and external flow field of a fluidic oscillator within the incompressible regime. Time-resolved pressure and PIV data are phase-averaged based on a simultaneously recorded reference signal in the feedback channel inlets. The underlying mechanism governing the jet's oscillatory movement is identified from the internal flow field. A recirculation bubble between the jet and the chamber wall grows by fluid from the feedback channels feeding into it. The growing bubble pushes the jet off the wall and over to the opposite side. Although the flowrate through the feedback channel increases with jet velocity, the total transported volume per oscillation cycle remains independent of supply rate. This volume is confirmed to match the volumetric growth of the recirculation bubble. Therefore, the oscillation frequency is mainly dependent on the required volumetric growth and on how fast this required volume is provided through the feedback channels. The study of the internal dynamics leads to various potential design modifications. The initial separation bubble may be averted entirely by streamlining the inner walls of the mixing chamber. Furthermore, the feedback channels may be streamlined to prevent unnecessary losses due to separation. The amount of fluid diverted into the feedback channels and the jet's deflection angle are most influenced by the design of the outlet nozzle.

Although the internal dynamics are consistent over the range of considered supply rates, some subtle changes occur. These changes are attributed to an increased jet width due to increasing turbulence levels. A wider jet causes increased reversed flow through the feedback channels, which affects the jet's impingement angle on the inner nozzle walls. Once a certain threshold value is reached, the jet's maximum deflection angle drops significantly. Despite the changes in deflection angle, the oscillation pattern is consistently sinusoidal. The jet spends a comparable amount of time for dwelling in its deflected state and for switching over to the opposite side. During the oscillatory movement, the jet's properties also oscillate by up to 10% around their mean value at the exit. The sweeping pattern in conjunction with the oscillatory output are significant features when considering the oscillators' applications. Especially when a homogenous distribution of fluid is desired, these characteristics have to be designed accordingly. Their relevance to flow control applications is currently unknown but should be addressed in future research.

In summary, it should be noted that the described observations of the internal and external dynamics may be specific to the investigated oscillator geometry and therefore may be different for other designs. However, the results provide some fundamental insight and potential guidelines for the development and optimization of fluidic oscillators with specific properties.

References

Bobusch BC, Woszidlo R, Bergada JM, Nayeri CNN, Paschereit CO (2013a) Experimental study of the internal flow structures inside a fluidic oscillator. Experiments in Fluids 54(6), doi:10.1007/s00348-013-1559-6

Bobusch BC, Woszidlo R, Krüger O, Paschereit CO (2013b) Numerical investigations on geometric parameters affecting the oscillation properties of a fluidic oscillator. AIAA 21st Computational Fluid Dynamics Conference doi:10.2514/6.2013-2709

Cerretelli C, Kirtley K (2009) Boundary layer separation control with fluidic oscillators. Journal of Turbomachinery 131(4), doi:10.1115/1.3066242

Gaertlein S, Woszidlo R, Ostermann F, Nayeri CN, Paschereit CO (2014) The time-resolved internal and external flow field properties of a fluidic oscillator. 52nd Aerospace Sciences Meeting doi:10.2514/6.2014-1143

Gregory J, Tomac MN (2013) A review of fluidic oscillator development. AIAA 43rd Fluid Dynamics Conference doi:10.2514/6.2013-2474

Gregory JW, Sullivan JP, Raman G, Raghu S (2007) Characterization of the microfluidic oscillator. AIAA Journal 45(3):568–576, doi:10.2514/1.26127

Gregory JW, Gnanamanickam EP, Sullivan JP, Raghu S (2009) Variable-frequency fluidic oscillator driven by a piezoelectric bender. AIAA Journal 47(11):2717–2725, doi:10.2514/1.44078

Guyot D, Paschereit CO, Raghu S (2009) Active combustion control using a fluidic oscillator for asymmetric fuel flow modulation. International Journal of Flow Control 1(2):155–166, doi:10.1260/175682509788913335

Haller G (2001) Lagrangian structures and the rate of strain in a partition of two-dimensional turbulence. Physics of Fluids 13(11):3365, doi:10.1063/1.1403336

Luxton RE, Nathan G (1991) Controlling the motion of a fluid jet. Patent, US 5060867 A

Ostermann F, Woszidlo R, Gaertlein S, Nayeri CN, Paschereit CO (2015a) Phase-averaging methods for the natural flow field of a fluidic oscillator. AIAA Journal (accepted for publication)

Ostermann F, Woszidlo R, Nayeri CN, Paschereit CO (2015b) Experimental comparison between the flow field of two common fluidic oscillator designs. 53rd AIAA Aerospace Sciences Meeting

Phillips E, Wygnanski I (2013) Use of sweeping jets during transient deployment of a control surface. AIAA Journal 51(4):819–828, doi:10.2514/1.j051683

Raghu S (2001) Feedback-free fluidic oscillator and method. Patent, US 6,253,782 B1

Raman G, Raghu S (2004) Cavity resonance suppression using miniature fluidic oscillators. AIAA Journal 42(12):2608–2612, doi:10.2514/1.521

Seele R, Tewes P, Woszidlo R, McVeigh MA, Lucas NJ, Wygnanski IJ (2009) Discrete sweeping jets as tools for improving the performance of the V-22. AIAA Journal of Aircraft 46(6):2098–2106, doi:10.2514/1.43663

Spyropoulos CE (1964) A sonic oscillator. Harry Diamond Laboratories pp 27–52

Stouffer R (1979) Oscillating spray device. Patent US 4151955

Wassermann F, Hecker D, Jung B, Markl M, Seifert A, Grundmann S (2013) Phase-locked 3D3C-MRV measurements in a bi-stable fluidic oscillator. Experiments in Fluids 54(3), doi:10.1007/s00348-013-1487-5

Woszidlo R, Wygnanski IJ (2011) Parameters governing separation control with sweeping jet actuators. AIAA 29th Applied Aerodynamics Conference doi:10.2514/6.2011-3172

Woszidlo R, Stumper T, Nayeri CN, Paschereit CO (2014) Experimental study on bluff body drag reduction with fluidic oscillators. 52nd Aerospace Sciences Meeting doi:10.2514/6.2014-0403

Properties of a spatially oscillating jet emitted by a fluidic oscillator

Florian Ostermann[1]†, Rene Woszidlo[1], C. Navid Nayeri[1] and C. Oliver Paschereit[1]

[1]Technische Universität Berlin, Berlin, 10623, Germany

(Received xx; revised xx; accepted xx)

The experimental study investigates the flow field and properties of a spatially oscillating jet emitted by a fluidic oscillator into a quiescent environment. The aspect ratio of the outlet throat is one. Stereoscopic particle image velocimetry is employed to measure the velocity field plane-by-plane. Simultaneously acquired pressure measurements provide a reference for phase correlating the individual planes yielding three-dimensional, time-resolved velocity information. Lagrangian and Eulerian visualization techniques illustrate the phase-averaged flow field. Circular head vortices, similar to the starting vortex of a steady jet, are formed repetitively when the jet is at its maximum deflection. They are convected downstream at a constant convection velocity. The quantitative jet properties are determined from instantaneous velocity data using a cylindrical coordinate system that takes into account the changing deflection angle of the jet. The jet properties vary throughout one oscillation cycle. The maximum jet velocity decays much faster than that of a comparable steady jet indicating a higher momentum transfer to the environment. The entrainment rate of the spatially oscillating jet is larger than for a steady jet by a factor of four. Most of the massflow is entrained from the direction normal to the oscillation plane, which is accompanied by a significant increase in jet depth compared to a steady jet. The high entrainment rate results from the enlarged contact area between jet and ambient fluid due to the spatial oscillation. The jet's total force exceeds that of an idealized steady jet by up to 30 %. The results are independent of the investigated oscillation frequencies.

1. Introduction

Properties of turbulent jets have been researched for several decades because they represent a fundamental flow field in fluid mechanics as well as being of importance for various technical applications such as fuel injection and flow control. Several studies investigated the fundamental flow field for axisymmetric and asymmetric steady jets in a quiescent environment (some examples include Sforza *et al.* 1966; Wygnanski & Fiedler 1969; Zaman 1996). Specifically the jet's entrainment of surrounding fluid as an indicator for mixing performance is of interest and focus of many studies (e.g., Ricou & Spalding 1961; Faris 1963; Krothapalli *et al.* 1981). The jet properties and the entrainment change significantly for unsteady jets (Bremhorst 1979). Temporally unsteady jets (i.e., pulsating jets) are jets with temporally changing jet properties (e.g., the supply rate). Platzer *et al.* (1978) reveal that the entrainment of a pulsed jet is significantly higher than that of a steady jet. Bremhorst & Hollis (1990) confirm this result and identify periodically created head vortices that increase Reynolds stresses thereby enhancing mixing performance.

Spatially oscillating jets (i.e., flapping jets) are another group of unsteady jets. These

† Email address for correspondence: florian.ostermann@tu-berlin.de

jets have a constant supply rate; however, their exit direction oscillates periodically. One means to generate a spatially oscillating jet is provided by fluidic oscillators. These devices are able to generate an oscillating jet without any moving parts involved, which makes them robust and attractive for technical applications. They were developed in the Harry Diamond Laboratories in the 1950s, initially with the intention for use as binary switches. In recent years, the interest in fluidic oscillators has been renewed due to their performance in flow control (e.g., Seele *et al.* 2009; Phillips & Wygnanski 2013; Schmidt *et al.* 2015) as well as mixing enhancement (Lacarelle & Paschereit 2012; Mi *et al.* 2001). A comprehensive review on spatially oscillating jets from fluidic oscillators and their applications is provided by Gregory & Tomac (2013). Initial studies on spatially oscillating jets were performed by Viets (1975) and Simmons *et al.* (1978). Viets (1975) investigated fluidic oscillators as thrust ejector devices. They showed that the spreading of the jet is significantly enlarged compared to steady jets. The same was found by Simmons *et al.* (1978) who analysed the flow field of a spatially oscillating planar jet in co-flow. They also state that the velocity decay rate is greater than that of a steady jet. The entrainment of spatially oscillating jets has been controversial. Srinivas *et al.* (1988) and Raman *et al.* (1993) argued that the entrainment of a spatially oscillating planar jet is less than that of a two-dimensional steady jet. In contrast, Platzer *et al.* (1978) indicated that the entrainment of a spatially oscillating planar jet is considerably higher than that of a comparable steady jet. All these studies performed one-dimensional measurements with hotwire anemometry along the centre line of the planar jet at various distances to the nozzle neglecting the direction of the flow and potential three-dimensional effects. The results were also discussed by Mi *et al.* (2001). They conducted two-dimensional measurements with a direction-sensitive hotwire system. Their results confirmed that the entrainment of a spatially oscillating planar jet is indeed higher but they contented that Platzer *et al.* (1978) overestimated the entrainment due to neglecting three-dimensional effects. All these studies investigated a quasi-two-dimensional oscillating planar jet. However, most applications involve oscillating jets with an aspect ratio of the order of one.

Woszidlo *et al.* (2015) and Sieber *et al.* (2016) investigated qualitatively the centre plane flow field of a spatially oscillating jet with a throat aspect ratio of one. They revealed the existence of two alternating vortices at the either side of the flow field. Ostermann *et al.* (2015*a*) added some quantitative jet properties. Their results indicate a greater velocity decay rate than a steady jet. Furthermore, they conservatively estimated the entrainment by determining an effective jet depth from assuming conservation of momentum. They suggested that the entrainment is significantly higher than that of a steady jet. However, their data was limited to two-dimensional velocity data without assessing the three-dimensional flow field, which left their results unproven. This shortcoming is addressed in the presented study that focuses on the three-dimensional, time-resolved flow field, jet properties, entrainment and forces of a spatially oscillating jet emitted from one fluidic oscillator with unit aspect ratio.

2. Setup and Instrumentation

Several methods for generating spatially oscillating jets exist. In this study, a fluidic oscillator equipped with two feedback channels emits the oscillating jet (figure 1a). The basic principle of this type of oscillator was investigated and characterized in various studies (Woszidlo *et al.* 2015; Sieber *et al.* 2016). The jet's spatial oscillation is caused solely by the internal dynamics and the geometry. The oscillating flow field is self-induced and self-sustained.

For the study, the smallest cross-section of the fluidic oscillator outlet (i.e., the nozzle

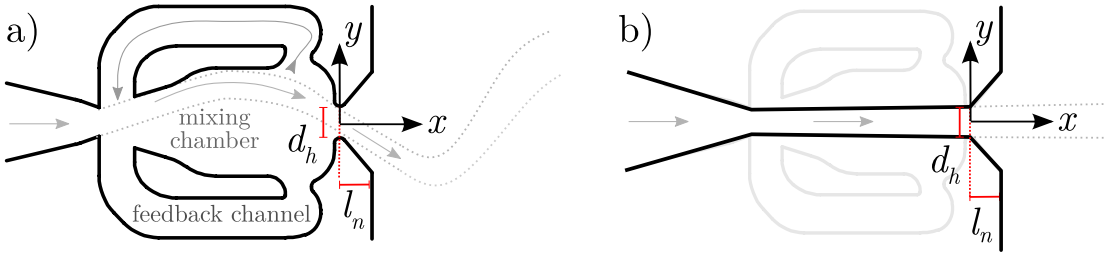

FIGURE 1. Two tested nozzle geometries. a) The fluidic oscillator, and b) the steady jet configuration. Denoted are the used coordinate origin, the hydraulic diameter d_h, and the length of the outlet nozzle's diverging part l_n.

throat) is $25 \times 25\,\mathrm{mm}^2$ that results in a hydraulic diameter d_h of 25 mm. The divergent part of the nozzle has a length $l_n = 1.1\,d_h$ and an opening angle of $\pm 50°$. The coordinate system origin is located in the centre of the nozzle throat at mid-depth of the oscillator. The oscillator is milled from acrylic glass. A cover plate seals the internal cavities. The oscillator is equipped with pressure sensors (HDO Series by Sensortechnics) for time-resolved pressure measurements inside the oscillator. Their response time is faster than 100 µs, which allows for the acquisition of a time-resolved reference signal. A massflow controller (HFC-D-307 by Teledyne Hastings Instruments) controls the amount of pressurized air supplied to the fluidic oscillator. It is able to measure up to 200 kg/h at a precision of better than 0.7 % full scale. Downstream the massflow controller, a portion of the air is diverted through a seeding generator and then merged again with the main air flow into the oscillator (figure 2). That assures that the air supply contains seeding particle without additional massflow being added by the seeding generator. An additional seeding generator adds particles to the environment. The fluidic oscillator is mounted on a metal stand (figure 2). A wooden plate with dimensions of $1.2 \times 1.2\,\mathrm{m}^2$ ($48 \times 48 d_h^2$) surrounds the oscillator outlet to provide a solid boundary to the external flow field. The supply massflow is used for determining the theoretical bulk velocity based on the assumption of a top-hat velocity profile and ambient conditions (i.e., ambient density ρ_0) at the throat of the oscillator (Eq. 2.1). This assumption is reasonable because for the highest supply rate, a Mach number of 0.11 is estimated at the outlet throat. Therefore, compressibility effects are neglected in this study.

$$U_{bulk} = \frac{\dot{m}_{supply}}{\rho_0 A_{outlet}} \tag{2.1}$$

A stereoscopic particle image velocimetry (PIV) system measures flow velocities in the external flow field. The system consists of a laser (Evergreen 200 by Quantel) with a maximum energy of 200 mJ and two cameras (pco.2000 by PCO AG) with a resolution of 4 megapixels. Each camera is equipped with a Scheimpflug adapter and a 100 mm objective by Canon. A synchronizer by ILA GmbH assures the timing between the components of the measurement equipment. The measurement plane is spanned in x-y direction from $x = 30\,\mathrm{mm}(1.2 d_h)$ to $350\,\mathrm{mm}(14 d_h)$ and from $y = -50\,\mathrm{mm}(-2 d_h)$ to $350\,\mathrm{mm}(14 d_h)$. It is noteworthy that the y-direction captures only half of the flow field. However, the results are mirrored to the other half by considering the flow field's symmetry that is validated by the available negative y data. The fluidic oscillator and the wall plate are mounted on a one-axis traversing system that allows moving the complete setup in z-direction. This enables measuring various planes sequentially without requiring a new PIV calibration. The z-locations of the planes are chosen in accordance to velocity gradients. The smallest distance between two planes is 3 mm close to the centre plane and the largest distance is 28 mm when farthest away from the centre plane. The z-direction

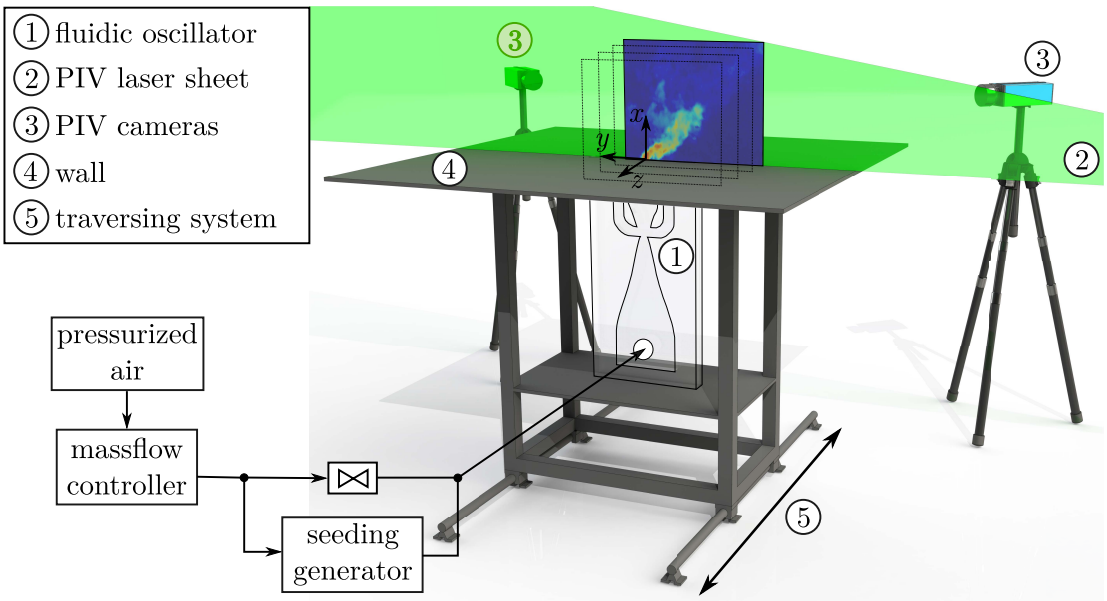

FIGURE 2. The experimental setup.

extends from $z = -15\,\mathrm{mm}(-0.6d_h)$ to $138\,\mathrm{mm}(5.5d_h)$ and consists of 22 planes. The z-direction extends to negative z values to confirm symmetry in this direction. The pulse distance between the laser pulses is adjusted for each plane and supply rate individually to obtain an optimum in resolvable velocities. It varies from 20 to 400 µs. A series of 6000 double images at a sampling rate of 5 Hz is acquired for each individual plane. This sampling rate is smaller than the oscillation frequency. Therefore, phase-averaging is employed during post-processing, which is discussed in more detail in section 3. The sampling frequency does not lock with the flow field because the oscillation frequency fluctuates naturally. The double images are post-processed by using PIVView3C version 3.6 by PIVTech. The final resolution of the results with an analysing window overlap of 50 % is 120x146 vectors yielding a spatial resolution of 0.36 vectors per mm in x and y direction. The PIV camera trigger signal (i.e., the timestamp for every PIV velocity field) as well as the pressure signals from inside the oscillator are acquired simultaneously through a cDAQ system by National Instruments at a sampling rate of 16,381 Hz that is several orders of magnitude higher than the jet's oscillation frequencies. This allows for the correlation of timestamps between the PIV snapshots and the pressure signal inside the oscillator, which enables phase-averaging the data and temporally aligning the individual measurement planes (ref. section 3).

In addition to the oscillating jet, measurements are conducted on a steady jet for comparison. This jet is emitted from a steady jet nozzle that is similar to the fluidic oscillator but the feedback channels and part of the mixing chamber are omitted to prevent the spatial oscillation (figure 1b). Otherwise, all geometric properties are the same including the nozzle diameter d_h and the length of the diverging nozzle l_n. The same stereoscopic PIV system is used for these measurements. However, only cross-sections at various distances from the nozzle (i.e., planes in y-z direction) are recorded.

3. Data Analysis

The jet properties of traditional steady jets are commonly described in global Cartesian coordinates (figure 3, left) or axisymmetric cylindrical coordinates oriented along the flow

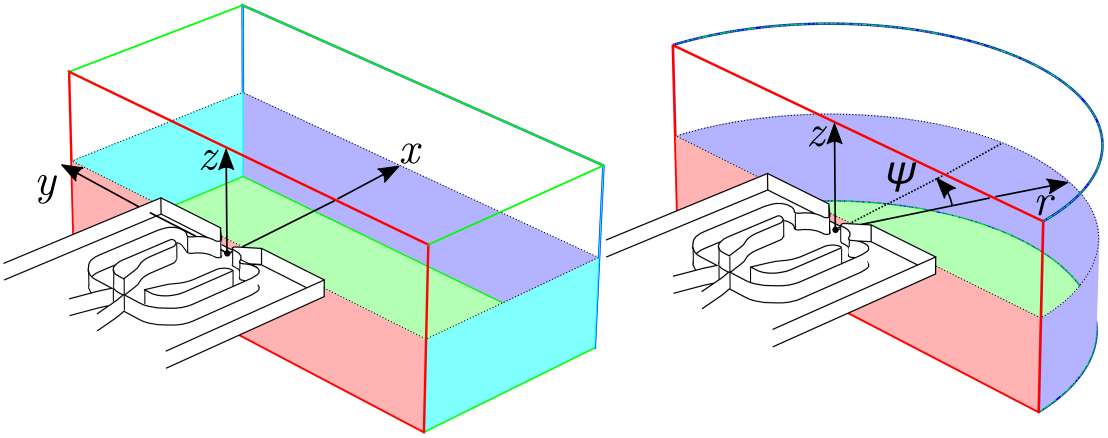

FIGURE 3. Coordinate systems used for analysing the flow field. Left: Cartesian coordinates, right: cylindrical coordinates.

direction of the jet (i.e., only streamwise and radial coordinates). For a spatially oscillating jet, neither of these coordinate systems is suitable because they do not take into account the spatial movement of the jet. For that reason, the jet properties are investigated using a cylindrical coordinate system (figure 3, right) with the jet being oriented in radial direction. The origin of the coordinates is in the centre of the outlet nozzle. Equations 3.1 - 3.2 transfer velocities and coordinates from the Cartesian coordinate system to the cylindrical coordinate system. The cylindrical coordinate system provides a more suitable comparison to conventional steady jets because r describes the jet's distance from the nozzle independently of the instantaneous jet deflection angle.

$$\begin{pmatrix} x \\ y \\ z \end{pmatrix} = \begin{pmatrix} r\cos\psi \\ r\sin\psi \\ z \end{pmatrix} \tag{3.1}$$

$$\begin{pmatrix} u_r \\ u_\psi \\ u_z \end{pmatrix} = \begin{pmatrix} \cos\psi & \sin\psi & 0 \\ -\sin\psi & \cos\psi & 0 \\ 0 & 0 & 1 \end{pmatrix} \cdot \begin{pmatrix} u_x \\ u_y \\ u_z \end{pmatrix} \tag{3.2}$$

Several data processing steps are required to extract jet properties from the sequentially measured two-dimensional velocity fields. The general procedure is illustrated in figure 4. Depending on the quantity of interest, different steps are taken. The top row describes the procedure to yield the time-resolved, three-dimensional flow field. The phase-averaging process is based on a reference signal extracted from inside the oscillator as described by Ostermann *et al.* (2015*b*). The differential pressure between the oscillator's feedback channels is used as the reference signal. A Butterworth lowpass filter is applied forward and backward for additional improvement in signal quality. An autocorrelation of the signal with a signal fragment of approximately half an oscillation period is used for identifying half period starting points. Since the reference signal and PIV snapshots are acquired simultaneously, the half period starting points are mapped to the PIV snapshot timestamps, which enables the ensemble-averaging of all snapshots within a phase angle window of 3°. Accounting for phase-jitter or weighting of snapshots according their position inside the window is not employed in favour of having a larger amount of snapshots available, which allows for a smaller phase angle window. Ostermann *et al.* (2015*b*) validated that the deviation of structures within one phase angle window is less than the signal noise of the PIV data. The phase-averaged results are phase-aligned to a

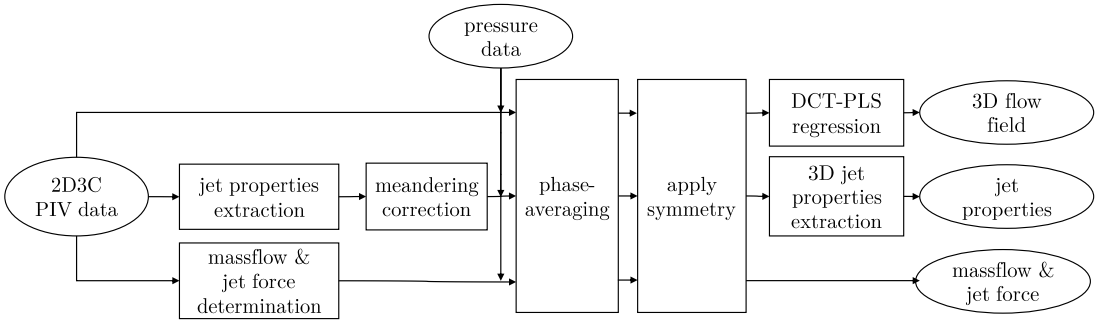

FIGURE 4. Flow chart illustrating the data processing.

common period starting point by using the reference signal. Thereby, all individual planes are combined to one three-dimensional flow field which is mirrored in the y-direction with a 180° phase shift (i.e., the x-z plane at $y = 0$) and in the z-direction without a phase shift (i.e., the x-y plane at $z = 0$). In order to increase the spatial resolution in z-direction, velocities in between the planes are interpolated and smoothed by using a regression procedure provided by Garcia (2010). This approach is based on discrete cosine transformations for regression and a generalized cross-validation for adjusting the smoothing parameters.

The described phase-averaging procedure cancels out stochastic noise isolating a representative oscillation period, which is suitable for a qualitative investigation of flow features. However, the phase angle window size of 3° and possible meandering of the jet makes investigating jet properties (e.g., maximum velocity, deflection angle, or jet dimensions) challenging because velocities are lowered and the jet structures may be blurred. Therefore, the jet properties are extracted from the instantaneous data for each plane individually (figure 4, second row). Meandering in the z-direction causes the jet to randomly deviate slightly from its main flow direction. Therefore, a meandering correction is applied by using the most probable value at each plane for every phase angle window instead of the mean value. The most probable value is determined from a probability density fit based on a normal kernel function. The determination of the phase angles for the instantaneous snapshots is similar to the previously described phase-averaging method of the three-dimensional flow field. The flow field symmetry in z-direction is accounted for by mirroring the jet properties at $z = 0$. The symmetry in y-direction requires a localization of the jet by identifying the maximum velocity between one phase angle and its 180° counterpart for every r. The corresponding values at the point of maximum velocity are then mirrored at $y = 0$ and if necessary phase-shifted by 180°. This procedure yields the jet properties as a function of the phase angle ϕ, the distance to the nozzle r, and the PIV plane z. In a last step, the 3D properties are extracted by determining the global values of all planes. Additional information is provided when discussing the jet properties in section 4.2.

The global quantities such as massflow and jet forces are determined in the same manner except for the meandering correction and the application of the symmetry (figure 4, third row). The meandering correction is not performed because the global quantity is independent of the position of the jet. The flow field symmetry is accounted for by adding the quantity of each phase angle with its 180° counterpart (i.e., the y-symmetry) and doubling it (i.e., the z-symmetry). Additional details on the determination of massflow and jet forces are discussed in section 4.3.

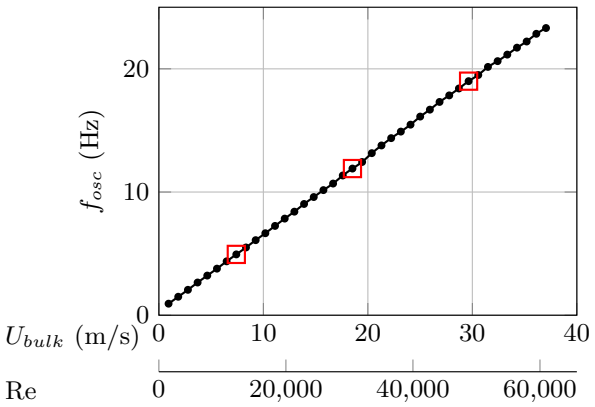

FIGURE 5. The oscillation frequency as a function of the supply rate. The considered cases for the PIV measurements are marked by squares.

4. Results

In the subsequent sections, the flow field and jet properties of a spatially oscillating jet issued into a quiescent environment are discussed. First, the three-dimensional, phase-averaged flow field is examined qualitatively in order to identify dominant flow structures. This global overview educates the subsequent quantitative evaluation of jet properties followed by the assessment of entrainment and jet forces. The objective of the presented material is to provide a foundational understanding of the flow field and properties of a spatially oscillating jet. It is noted that the parameter space involved with spatially oscillating jets is extensive and can certainly not be fully explored in the current study.

It is anticipated that the flow field of periodic jets is affected by the oscillation frequency and jet velocity independently. However, for the employed fluidic oscillator design, the jet velocity and oscillation frequency are coupled. Figure 5 shows the oscillation frequency as a function of the supply rate. It is evident that the oscillation frequency is linearly dependent on the supply rate, which was observed by several other studies on similar fluidic oscillator designs operating in the incompressible regime. The effect of the frequency is connected to the jet Strouhal number (e.g., Choutapalli *et al.* 2009). The jet Strouhal number St is dependent on the jet exit velocity U_{bulk}, the oscillation frequency f_{osc}, and a characteristic length scale d_h (Eq. 4.1). Considering the linear slope and the negligible offset of the oscillation frequency over the supply rate leaves a constant Strouhal number over all supply rates. Therefore, it is not possible to change the Strouhal number in this study. In fact, Schmidt *et al.* (2017) show that for this particular oscillator design the Strouhal number is independent of oscillator size and working fluid as long as no compressibility effects are present. That means, changing the Strouhal number would require to change the design (e.g., internal geometry) or including compressibility effects, which is beyond the scope of this study.

$$St = \frac{f_{osc} \cdot d_h}{U_{bulk}} = 0.015 \tag{4.1}$$

The jet Reynolds number is affected by the supply rate. The Reynolds numbers based on the hydraulic diameter of the exit and the bulk velocity are well within the turbulent regime of a pipe flow (figure 5). Therefore, no sudden changes in the internal boundary layer or internal dynamic are expected (Woszidlo *et al.* 2015). The limited range of investigated Reynolds number in combination with the constant Strouhal number make it reasonable that the normalized results of this study exhibit the same behaviour independent of the

supply rate. For that reason, all results shown in the following are extracted from only one supply rate of $U_{bulk} = 19\,\mathrm{m/s}$, if not denoted otherwise. The corresponding Reynolds number based on the hydraulic exit diameter d_h is 30,000.

4.1. *General flow field*

It is anticipated that the flow field of a spatially oscillating jet includes the periodic spatial oscillation as well as stochastic turbulence. The phase-averaging process eliminates the stochastic turbulence and potential small-scale flow features, which enables a fundamental visualization and discussion of dominant flow structures. Figure 6 illustrates the three-dimensional flow field for several phase angles ϕ over half an oscillation period providing initial qualitative insight into the flow field characteristics. Figure 6 (left) depicts the backward finite time Lyapunov exponent (FTLE). This Lagrangian analysis tool traces virtual particles through the flow field in time. It quantifies the attraction rate of streaklines meeting in almost one point. The result is an intuitive representation of the flow field due to its similarity to smoke or ink visualizations. It enhances coherent structures such as vortices and shear layers in the flow field. More information on the FTLE are provided by Haller (2001). The supplementary material includes an animation of the FTLE (Movie 1). Figure 6 (right) shows Eulerian quantities. An iso-surface of the velocity magnitude delineates the time-dependent position of the jet. An x-y slice through the Q-criterion is added at $z = 0$. The shading reflects the values of Q for $Q > 0$, which provides an indication for the presence of vortices (Jeong & Hussain 1995).

As anticipated, the most prominent flow feature is the jet moving from side to side spreading fluid over a large area (figure 6, A). The opening angle of the covered area is $\approx 100°$, which corresponds to the opening angle of the diverging part of the nozzle. Ostermann *et al.* (2015*a*) suggest that the jet attaches to the walls of the diverging part of the nozzle. Hence, the opening angle is independent of the supply rate but dependent on the oscillator design. The influence of the opening angle is beyond the scope of this study.

When the jet switches to the sides, it trails a wake of accelerated fluid. That means that the shear layer on the trailing side is stretched while the shear layer on the leading side is squeezed. Hence, the velocity gradients on the leading side are expected to exceed the gradients at the trailing side. This effect is visible in the FTLE of the deflected jet because it considers the temporal evolution of the flow field. That is why the FTLE on the trailing side is smaller than that on the leading side of the deflected jet (figure 6, B). It is noteworthy that the total time required for the jet to switch from one side to the other decreases with the supply rate due to the increasing oscillation frequency. However, the phase-averaged switching speed $\Delta\psi/\Delta\phi$ is independent of the supply rate, because the oscillation frequency is linearly dependent on the supply rate.

When the jet is fully deflected, a circular head vortex is created, which is clearly visible in the FTLE (figure 6, C). For additional confirmation and illustration, a vortex tube following the vortex vectors starting from maximum Q in the x-y plane is added in figure 6 (right). The two-dimensional footprint of this vortex was previously observed by Woszidlo *et al.* (2015) and Sieber *et al.* (2016). Its creation mechanism is suspected to be similar to that of the starting vortex known from steady jets. However, in this flow field the vortex is not only present when the jet is initiated but repeats on either side despite the steady supply. It is convected downstream where it causes local recirculation zones while the main jet moves back to the other side. Figure 7 shows the position of the two head vortices as a function of the oscillation phase angle. The vortices are traced by observing the position of the outer vortex leg footprint at $z = 0$ (figure 6, right arrow of C). It is evident that the angular position ψ of the vortex changes only close to the

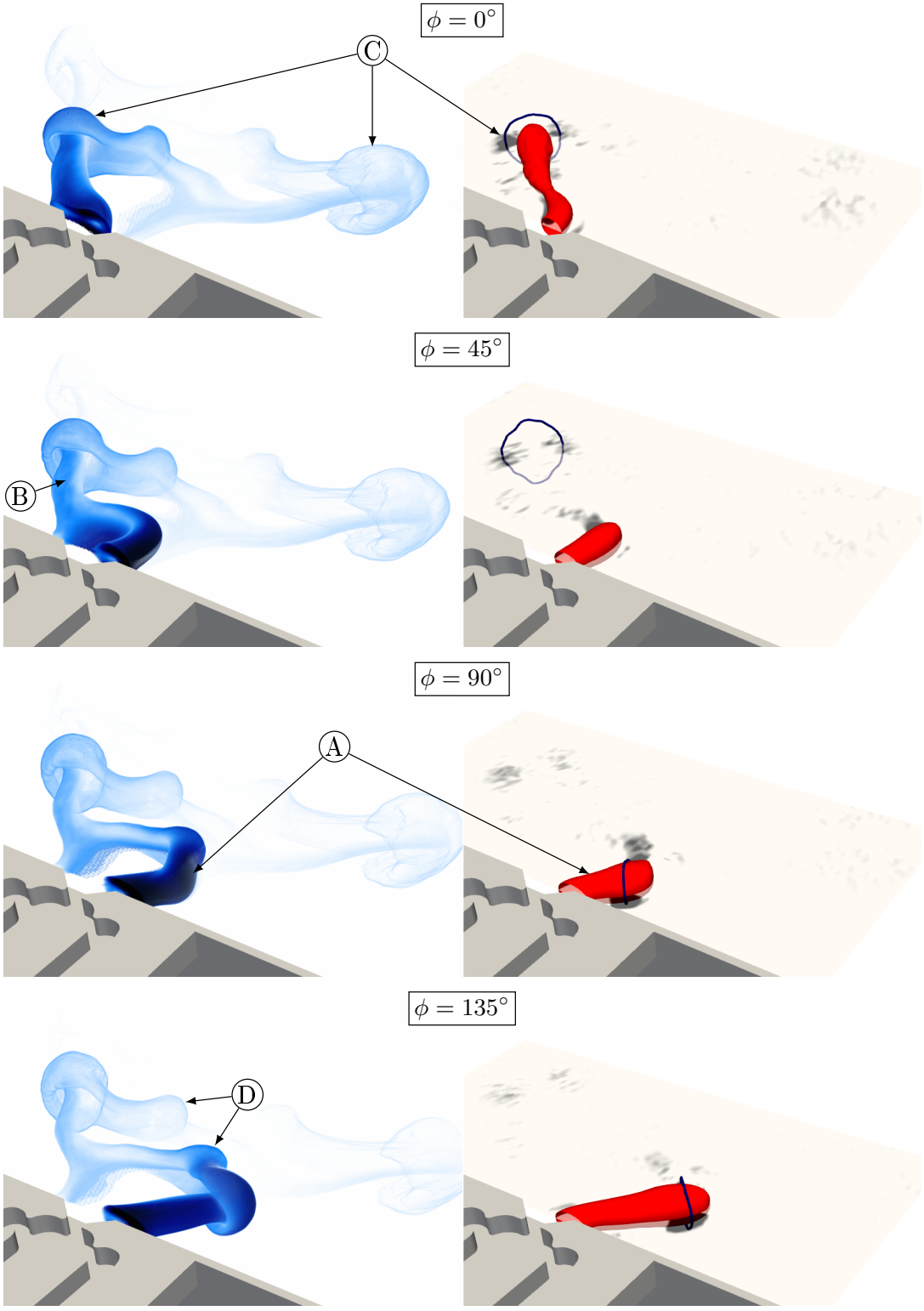

FIGURE 6. The three-dimensional flow field. Left: the backward finite time Lyapunov exponent. Right: the Q-criterion for $Q > 0$ in the plane of $z = 0$, an isosurface of $0.35\,U_{bulk}$, and a tube indicating the dominant vortex core. The annotations are referred to throughout the text. Note that the top half of the boundary wall is omitted to provide unobstructed view.

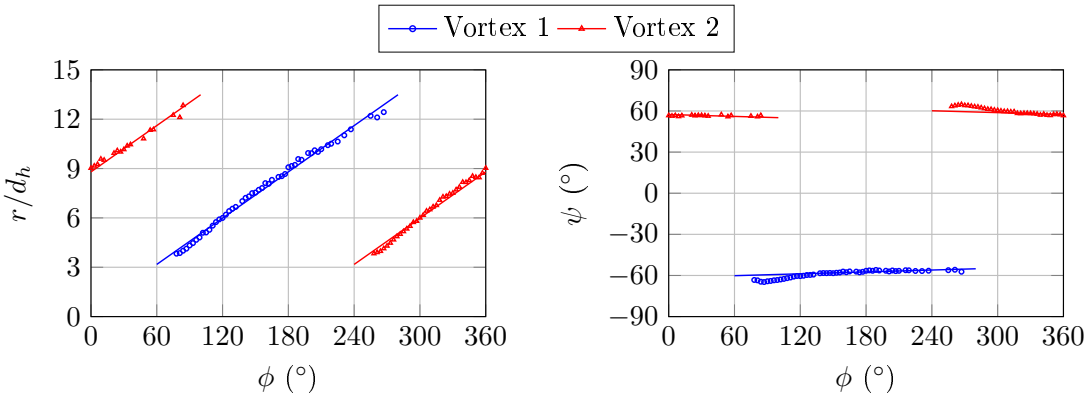

FIGURE 7. The position of the outside leg of the circular head vortex at $z = 0$. The solid lines are linear regression lines. Left: the distance to the nozzle. Right: the angular position. Vortex 1 and 2 are the vortices at either side of the flow field.

nozzle and remains constant downstream. Hence, the vortex is convected along the jet in a straight path away from the nozzle. The slope of r over ϕ is approximately constant indicating a constant convection velocity. Considering the time for one oscillation cycle, the convection velocity approximately $0.25\,U_{bulk}$. This is slow compared to the head vortices of pulsed jets. Choutapalli *et al.* (2009) identify a convection velocity of $0.6\,\overline{U_{max}}$. Note that they use the time-averaged maximum velocity that is smaller than the actual maximum velocity of the jet. If that is taken into account, a convection velocity of 40 % of the maximum velocity U_{max} is obtained, which is almost twice as high as the convection velocity of the observed head vortex of a spatially oscillating jet. It is noteworthy, that due to the limited time the jet resides in its deflected state, the head vortex observed in the phase-averaged flow field is not followed by subsequent vortices. This may explain the smaller convective speed.

4.2. *Jet properties*

This section focuses on the local properties of the spatially oscillating jet which include the jet's deflection angle, the maximum velocity magnitude and the jet depth. The jet properties are calculated from instantaneous snapshots, corrected for meandering, and phase-averaged thereafter (section. 3). The maximum velocity magnitude $U_{max}(r, \phi)$ is defined as the maximum velocity magnitude of all measured planes for each position r and for each phase angle ϕ. The local deflection angle $\theta_{jet}(r, \phi)$ is the direction of the maximum velocity vector for each recorded plane. The jet's depth is represented by the extent in z-direction for the distance where the local maximum velocity of each plane $U_{max,z}(r, z, \phi) \geqslant 0.5\,U_{max}(r, \phi)$. The same definitions apply to the according steady jet that is added for comparison. Note that the instantaneous jet width may also be extracted from each plane. However, due to its sweeping motion, the jet forms a thin shear layer in the direction of motion while trailing accelerated fluid behind it. This effect dilutes the meaning of the jet's width, especially at larger distances from the nozzle. Therefore, the jet width does not offer any physically conclusive quantity and is omitted here.

Spatially oscillating jets are characterized by their oscillation pattern and maximum deflection angle. Figure 8 depicts the deflection angle θ_{jet} and the maximum velocity U_{max} at one position r as a function of the phase angle ϕ. The temporal behaviour of jet deflection angle and maximum velocity characterizes the oscillation pattern that is dependent on this specific oscillator design. It is evident in figure 8 that the maximum deflection angle is approximately 45° which emphasizes the significantly larger volume

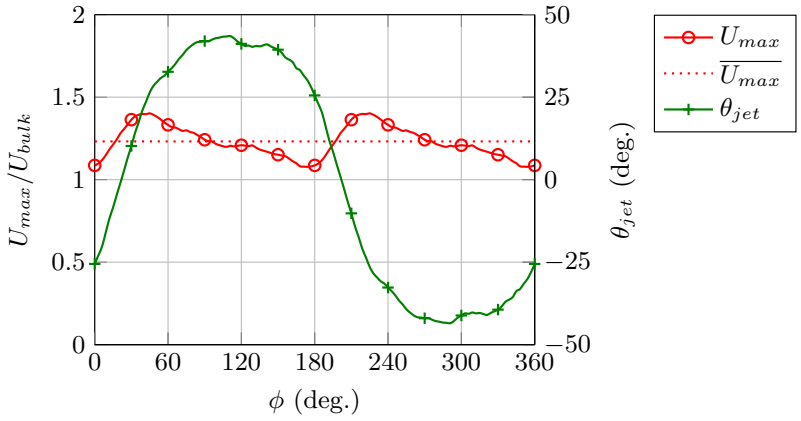

FIGURE 8. The oscillating local maximum velocity U_{max} and deflection angle θ_{jet} at $r/d_h = 2$. Note that only every 10th data point is marked.

being affected by the oscillating jet compared to a steady jet. Note that the maximum deflection angle does not coincide with the opening angle of the affected volume noted in section 4.1. That is because the jet deflection angle is located at the point of maximum velocity and does not take into account the outer shear layer and widening of the jet that yields a further increase in affected volume. The oscillation pattern is mostly sinusoidal with longer dwelling times of the jet at its maximum deflection. Furthermore, figure 8 reveals that the maximum jet velocity varies by approximately $\pm 15\,\%$ of the mean value. The time-resolved maximum jet velocity reaches its largest values shortly before the jet arrives at its maximum deflection. That is also observed in figure 6 (C) where a small portion of fluid is ahead of the neighbouring particles before the jet is fully deflected. The maximum jet velocity reaches its minimum when the jet starts to sweep to the opposite side. Note that the maximum jet velocity is always larger than the reference bulk velocity, which is due to internal boundary layer effects reducing the effective size of the exit area. Woszidlo *et al.* (2015) revealed that the dynamics inside a fluidic oscillator do not only cause the jet to spatially oscillate but also to temporally oscillate due to changes in the effective outlet area for the deflected jet and oscillating pressure losses. The observed oscillation pattern and temporal oscillation of jet properties is characteristic for the employed fluidic oscillator (Ostermann *et al.* 2015*a*). It is noteworthy that the oscillation pattern may affect the presented results. However, the investigation of different oscillation patterns is beyond the scope of this fundamental study. Presumably, the general trends for the jet properties shown in this study are expected to be applicable to other oscillation patterns as well.

Figure 9 shows the jet properties averaged over one oscillation period as a function of the distance to the nozzle. Note that the length of the diverging nozzle l_n is subtracted from r because the jet is only fully exposed to the environment downstream of $r - l_n = 0$. For $r < l_n$ the jet is enclosed which hinders the interaction with the surrounding fluid (figure 1). Thus, the subtraction of l_n allows for an objective comparison to data from the literature. Figure 9 (left) displays the velocity decay. For turbulent axisymmetric steady jets, the velocity decay of the centre line velocity is proportional to $1/r$ (Schlichting & Gersten 2006). Hence, the velocity decay rate may be investigated by evaluating the ratio between global maximum velocity and the local centre line velocity (Quinn & Militzer 1988). However, defining a centre line velocity for a spatially oscillating jet may be misleading because of deflected and time-dependent jet centre lines. Instead, the ratio between the global maximum velocity $U_{max} = \max(\overline{U_{max}}(r))$ and the local maximum

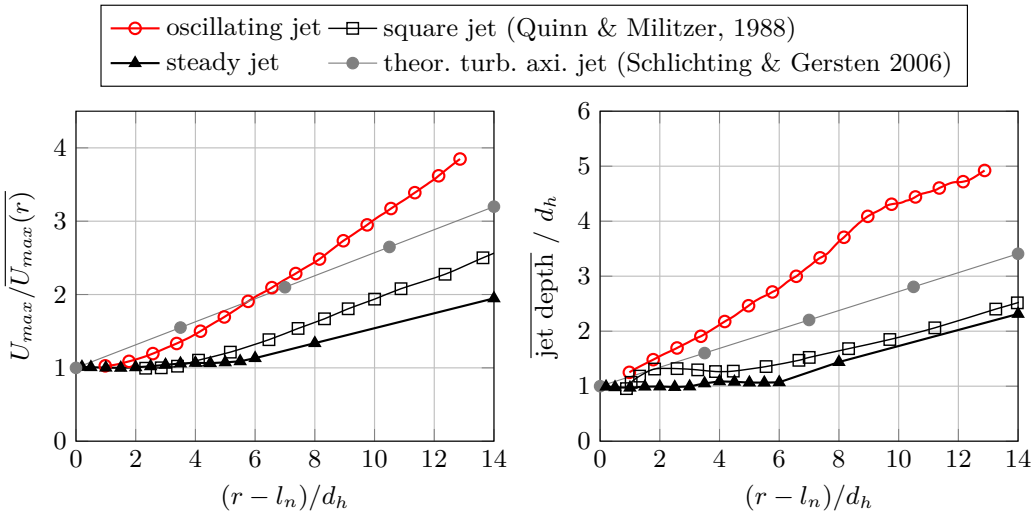

FIGURE 9. Jet properties. Left: the maximum velocity as a function of the distance to the nozzle. Right: the jet depth as a function of r.

velocity $\overline{U_{max}}(r)$ is used. In comparison, this provides an underestimation of the velocity decay rate when the maximum velocity is off-centre, which is the case for square jets in the near field (Quinn 1992). This is likely the reason for the considerable difference between the measured steady jet and the square jet from Quinn & Militzer (1988) who used the conventional definition of the centre line velocity (figure 9, left). Compared to common steady jets, it is evident that the maximum velocity of the oscillating jet decays much faster in the near field without the presence of a sustained potential core. Similar to steady jets, the velocity decay rate of the sweeping jet approaches a constant value downstream of $(r - l_n)/d_h > 6$. Equation 4.2 describes a linear function for the velocity decay similar to Quinn & Militzer (1988) with K being the velocity decay rate and C the virtual origin of the jet. The slope of the linear trend K (i.e., the velocity decay rate) is approximately $K = 0.26$ for the spatially oscillating jet. This is higher than the decay rate of steady jets which is $K = 0.19$ for square jets and $K = 0.17$ for round jets (Quinn & Militzer 1988). The comparably high velocity decay is indicative for a higher momentum transfer to the ambient fluid.

$$\frac{U_{max}}{\overline{U_{max}(r)}} = K\left(\frac{(r - l_n)}{d_h} + C\right) \tag{4.2}$$

The oscillating jet's depth is growing significantly faster in the near field than the depth of common steady jets (figure 9, right). The shallow increase in depth of the measured steady jet close to the nozzle is explained by the unconventional nozzle geometry (i.e., a long divergent outlet) and by the transition from a square to a circular jet (Zaman 1996). However, it compares well to similar data of a square jet that was investigated by Quinn & Militzer (1988). After the transition to an axisymmetric jet (i.e., $(r - l_n)/d_h > 6$), the measured steady jet approaches the theoretical spreading rate for turbulent axisymmetric jets (Schlichting & Gersten 2006). The rates between oscillating and steady jet are particularly different in the near field whereas these differences diminish in the far field. The larger jet depth suggests that the oscillating jet has a high entrainment from the direction normal to the oscillation plane, which is part of the discussion in the subsequent section.

4.3. *Entrainment*

The entrainment of a jet is an indication for its mixing performance. Entrainment is caused by the acceleration of surrounding fluid due to the momentum of the jet. In this study, the entrainment rate is defined from normalized quantities (Eq. 4.3). Note that the denominator defines the distance from the nozzle in unobstructed environment. Therefore, the distance r from the origin at the nozzle throat is corrected by l_n that is the enclosed length of the divergent section of the nozzle. This shift allows for a more objective comparison to traditional steady jets.

$$e = \frac{\partial(\dot{m}/\dot{m}_{supply})}{\partial((r - l_n)/d_h)} \tag{4.3}$$

The determination of the massflow as a function of distance is required for quantifying the entrainment. Equation 4.4 defines the general continuity equation for massflow in a control volume enclosed by the surfaces S.

$$\dot{m}_{total} = \oint_S \rho(\vec{u} \cdot \vec{n})\,\mathrm{d}S \;=\; 0 \tag{4.4}$$

Accordingly, the massflow is determined by integrating the flow through control surfaces. Conventionally, the massflow of a jet is obtained by integrating in Cartesian coordinates over a quasi-infinite cross-section placed normal to the flow direction (Eq. 4.5).

$$\dot{m}_{y,z}(x, \phi) = \rho_0 \int_z \int_y u_x \,\mathrm{d}y\mathrm{d}z \tag{4.5}$$

However, this approach is not suitable for analysing a spatially oscillating jet because it does not account for the changes in the jet's travel length for different jet deflections. Therefore, a cylindrical volume (figure 3, right) enclosed by four surfaces is employed. The massflow through all surfaces is determined individually because it allows distinguishing between the sources of entrainment from different directions (Eqs. 4.6-4.9).

$$\dot{m}_{side}(r, \phi) = \rho_0 \int_{-z_{max}}^{z_{max}} \int_{-\arccos\frac{l_n}{2}}^{\arccos\frac{l_n}{2}} u_r \; r\mathrm{d}\psi\mathrm{d}z \tag{4.6}$$

$$\dot{m}_{base,1,2}(r, \phi) = \pm\rho_0 \int_{l_n}^{r} \int_{-\arccos\frac{l_n}{2}}^{\arccos\frac{l_n}{2}} u_z(z = \pm z_{max}) \; r\mathrm{d}\psi\mathrm{d}r \tag{4.7}$$

$$\dot{m}_{wall}(r, \phi) = -\rho_0 \int_{-z_{max}}^{z_{max}} \int_{-r}^{r} u_x(\psi = \arccos\frac{l_n}{r}) \; \mathrm{d}r\mathrm{d}z \tag{4.8}$$

$$\dot{m}_{total}(r, \phi) = \dot{m}_{side} + \dot{m}_{base,1} + \dot{m}_{base,2} + \dot{m}_{wall} \;=\; 0 \tag{4.9}$$

Note that $\dot{m}_{wall}/\dot{m}_{supply}$ should be one due to the wall preventing any entrainment from upstream of the jet's exit. However, due to measurement constraints, flow field data is only available slightly downstream of the wall. Therefore, the corresponding plane is included in the interrogation (Eq. 4.8). Moreover, the results are not shown for $(r - l_n)/d_h < 2$ because the control volume would be too small to cover the complete jet throughout its oscillation.

It is possible to evaluate in- and outflow through the control surface by integrating positive and negative values of $(\vec{u} \cdot \vec{n})$ in equation 4.4 separately. The in- and outflow are overestimated because vortices such as the circular head vortex (figure 6, C) passing through the surface as well as local turbulence add to the in- and outflow individually but cancel when added together. Despite these limitations, the differentiation between in- and outflow allows to identify flow that would cancel out during the integration. That

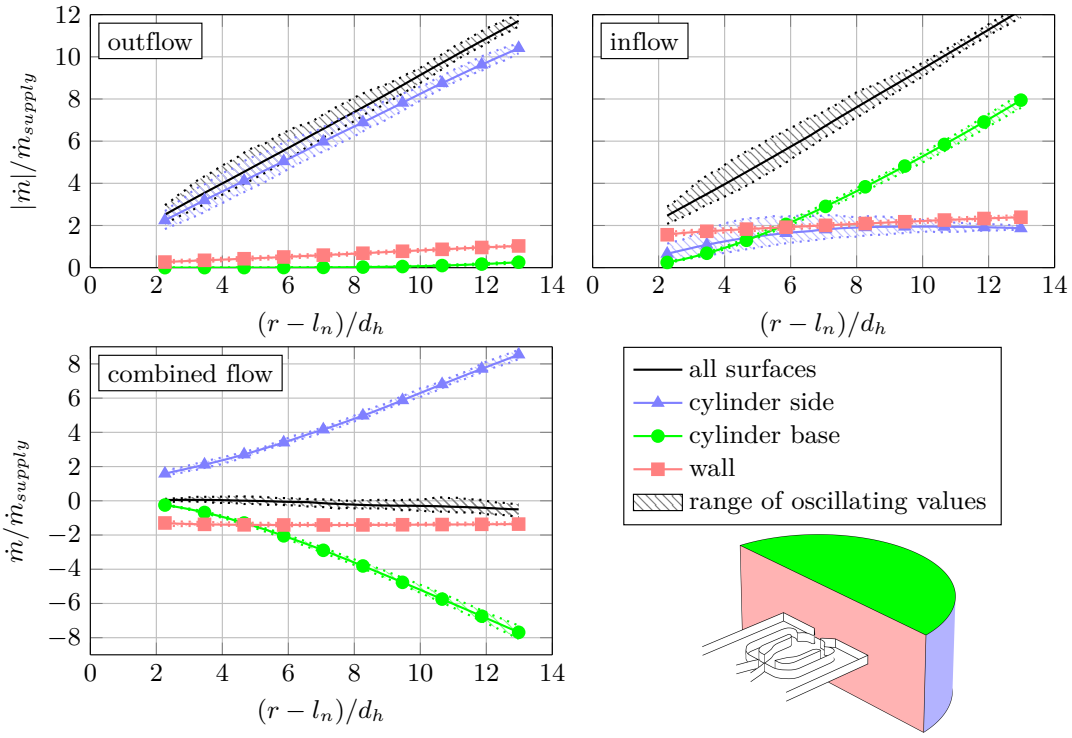

FIGURE 10. Breakdown of the massflow through the individual cylinder surfaces.

is of particular interest because the cylinder side includes the main outflow as well as entrainment manifesting in inflow from the sides.

Figure 10 shows the time-averaged in-, out-, and combined flow for all surfaces enclosing the cylindrical control volume. Almost the complete outflow moves through the cylinder side, which is expected because this is the main flow direction. Some additional outflow through the wall surface is also noticeable. As mentioned, this is likely an overestimation caused by the circular head vortex and turbulence. The same overestimation is evident for the inflow through the wall surface that is expected to be constant at one (i.e., the supply massflow). These effects cancel out for the combined flow that remains constant at slightly larger levels than the supply rate due to the plane's distance from the nozzle. Only little outflow is obtained through the cylinder base, which confirms that the extent of measured velocity planes in z-direction is sufficient to cover the complete flow field. The inflow through the cylinder side is indicative for entrainment from the sides that is expected to originate mostly from the areas of large polar angles $|\psi|$ close to the wall surface. Furthermore, the in- and outflow through the cylinder side is also burdened by recirculation of local vortices and turbulence. Although these effects cancel out in the combined flow, any potential entrainment through this surface is also subtracted from the outflow, which leads to an underestimation of the total entrainment. For $(r - l_n)/d_h > 5$, the inflow through the cylinder bases provide the largest source of inflow. This result infers that the most entrainment for a spatially oscillating jet originates from the direction normal to the oscillation plane, which is consistent with the results for jet depth (figure 9, right). Hence, an increase in the nozzle's aspect ratio to yield a planar, spatially oscillating jet would prevent this source of entrainment. It is suspected that this is one reason for the controversies regarding entrainment of spatially oscillating jets in earlier studies (Platzer *et al.* 1978; Srinivas *et al.* 1988; Raman *et al.* 1993; Mi *et al.* 2001). These studies used planar spatially oscillating jets at high aspect ratios (i.e., aspect ratio > 7). The aspect

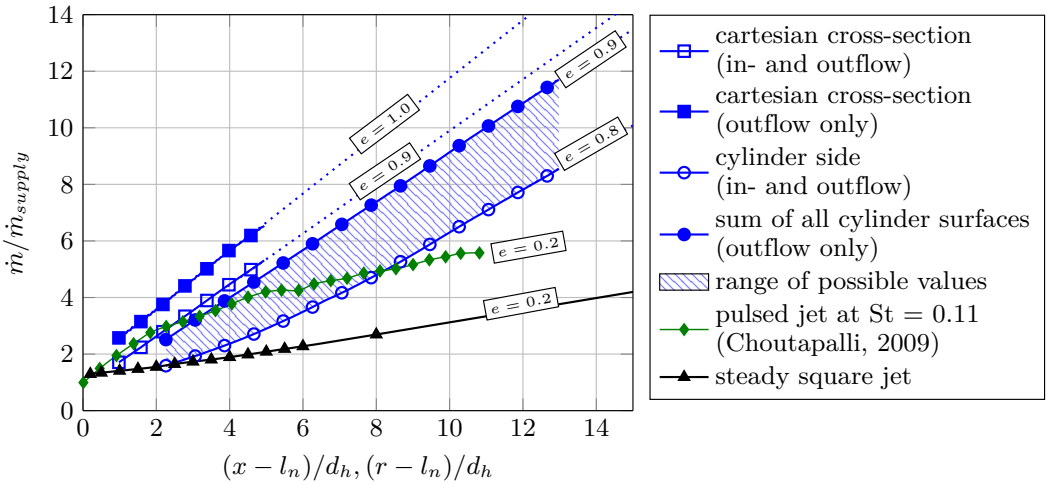

FIGURE 11. Entrainment range for the spatially oscillating jet.

ratio of the jet in this study is one, which renders a direct comparison to the earlier results on spatially oscillating jets meaningless.

It is noteworthy that the sum of the combined in- and outflow through all surfaces is approximately zero over a wide range of distances from the nozzle. Therefore, the flow field fulfils the continuity equation (Eq. 4.4) which provides additional confidence in the data quality. The shaded areas surrounding each line in figure 10 indicate the range of oscillating values throughout one oscillation cycle. This range is comparably large for in- and outflow. The massflow is analysed for each individual snapshot and phase-averaged thereafter (figure 4). These snapshots have a considerable amount of stochastic turbulence that induce such large fluctuation for the in- and outflow. The range of values for the combined flow are more representative because turbulence is cancelled out during the integration. The combined massflow is mostly independent of the phase angle and thus of the instantaneous position of the jet. Therefore, it may be concluded that the significant oscillations in jet velocity throughout one oscillation period (figure 8) are balanced by changes in jet width to yield quasi-steady massflow characteristics.

Figure 10 delineates the massflow through all surfaces individually. It is challenging to extract the correct entrainment of the jet from this data. The sum of outflow through all surfaces certainly overestimates the entrainment because it includes effects such as recirculation from vortices and turbulence that do not contribute to the overall entrainment. In contrast, the combined flow through the cylinder side underestimates the total entrainment because local entrainment from areas close to the wall surface is subtracted throughout the integration (Eq. 4.6). Therefore, the available data and applied methods only allow the conclusion that the actual entrainment is in between these two limits. The resulting range is illustrated in figure 11. The annotated entrainment e is based on the linear trend of the data points furthest away from the nozzle. In order to allow a comparison to other studies, the massflow for Cartesian cross-sections (Eq. 4.5) are added as well. Note that the data of the Cartesian cross-sections is limited to $(x - l_h)/d_h < 5$ because parts of the jet do not go through the domain-limited cross-section farther downstream. As expected, the entrainment obtained by integration over Cartesian cross-sections exceeds the results obtained in cylindrical coordinates due to the jet's underestimated travel distance from the nozzle when the jet is deflected. Although omitted here, it may be possible to correct the data by introducing an effective distance from the nozzle based on an average deflection angle.

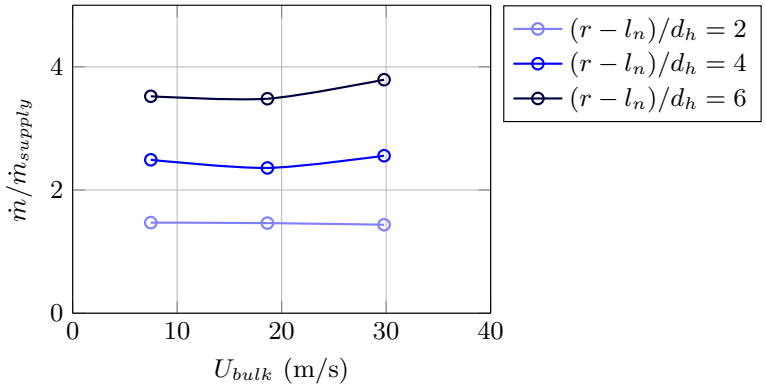

FIGURE 12. The combined massflow through the cylinder side as a function of the supply rate.

The comparison between the entrainment of the spatially oscillating jet and the steady jet in figure 11 reveals that the entrainment rate e of the spatially oscillating jet is increased by at least a factor of four compared to the entrainment rate of a steady jet. This enhancement is expected to be a result of the spatial oscillation that increases the contact area between jet and surrounding fluid in z-direction. It is noteworthy that generally the entrainment rate of square jets is slightly higher (i.e., $e \approx 0.3$) than that measured in this study (Grinstein *et al.* 1995). This discrepancy is a result of the unconventional nozzle geometry (figure 1b). However, the influence of the nozzle geometry and upstream effects are negligible compared to the entrainment enhancement by unsteady jets (Bremhorst 1979). The entrainment rate of the spatially oscillating jet is also higher than that of a pulsed jet at a Strouhal number of 0.11 that was assessed by Choutapalli *et al.* (2009). In the near field of the pulsed jet, the creation of the head vortex is suspected to cause the high initial entrainment rate (Choutapalli *et al.* 2009). This entrainment rate is of the same order as the entrainment rate of the spatially oscillating jet. With increasing distance to the nozzle, the entrainment rate of the pulsed jet decreases to the entrainment rate of a steady jet. This is not observed for the spatially oscillating jet, where the entrainment rate stays constant throughout the range of examined distances. This supports that the high entrainment rate of the spatially oscillating jet is caused by the increased entrainment from the direction normal to the oscillation plane instead of its head vortices.

Figure 12 depicts the entrainment of the spatially oscillating jet at discrete positions for various supply rates. It is evident that the entrainment is not affected by the supply rate. Therefore, the jet Reynolds number has no effect on the entrainment rate. Recalling that the oscillation frequency increases with the supply rate, it is evident that the oscillation frequency does also not change the entrainment rate. This is expected because the Strouhal number does not change with the supply rate. Hence, it supports the statement at the beginning of section 4 that the linear coupling between oscillation frequency and jet velocity does not allow for changing the Strouhal number or the dynamic behaviour of the flow field for the employed fluidic oscillator. Other oscillator designs may therefore experience other results. Note that differing results may also be expected in the sonic regime because the oscillation frequency stagnates once the jet velocity approaches sonic speed (Von Gosen *et al.* 2015).

4.4. *Jet forces*

The oscillating jet acts with a certain force on the surrounding fluid. The magnitude of this jet force acting on the fluid is of interest for several applications such as flow control (i.e., determining the momentum coefficient). It is challenging to measure the jet force due to the spatial motion of the jet. Most studies that are employing the momentum coefficient, use the force F_{bulk} that is based on the assumption of ambient conditions at the jet exit and the jet bulk velocity U_{bulk} in the exit throat A_{outlet} (Eq. 4.10).

$$F_{bulk} = \rho_0 A_{outlet} U_{bulk}^2 \tag{4.10}$$

However, figure 9 (left) shows that the maximum velocity magnitude exceeds the bulk outlet velocity. Therefore, the actual force is likely underestimated. Schmidt *et al.* (2017) measure the thrust of their fluidic oscillators used for flow control by using a one-component balance. Although this provides a measure for the resulting thrust in x-direction, it neglects the lateral component of the jet force that should be included for the correct determination of the total momentum coefficient. Here, the jet force F is determined from the instantaneous velocity fields (section. 3) and phase-averaged thereafter. The infinitesimal force $\mathrm{d}F$ acting on the fluid in normal direction to the control surface is dependent on the local velocity $\vec{u}$ (Eq. 4.11).

$$\mathrm{d}\vec{F} = \rho\vec{u}(\vec{u}\cdot\vec{n})dA \tag{4.11}$$

Spatially integrating the infinitesimal forces cancels out opposing forces. However, they also need to be considered for the jet force magnitude. Therefore, the infinitesimal force magnitude $|\mathrm{d}F|$ is considered, which is a function of the local velocity magnitude acting in surface normal direction (Eq. 4.13).

$$|\mathrm{d}F| = |\rho\vec{u}(\vec{u}\cdot\vec{n})| \tag{4.12}$$

$$= \rho U(\vec{u}\cdot\vec{n}) \tag{4.13}$$

The force magnitudes acting on the fluid are integrated along the cylinder surfaces to yield a total force magnitude F (equation 4.14-4.16).

$$F_{side}(r,\phi) = \rho_0 \int_{-z_{max}}^{z_{max}} \int_{-\arccos\frac{l_n}{2}}^{\arccos\frac{l_n}{2}} U u_r \; r\mathrm{d}\psi\mathrm{d}z \tag{4.14}$$

$$F_{base,1,2}(r,\phi) = \pm\rho_0 \int_{l_n}^{r} \int_{-\arccos\frac{l_n}{2}}^{\arccos\frac{l_n}{2}} U u_z(z=\pm z_{max}) \; r\mathrm{d}\psi\mathrm{d}r \tag{4.15}$$

$$F_{wall}(r,\phi) = -\rho_0 \int_{-z_{max}}^{z_{max}} \int_{-r}^{r} U u_x(\psi = \arccos\frac{l_n}{r}) \; \mathrm{d}r\mathrm{d}z \tag{4.16}$$

Analogous to the massflow determination, it is possible to distinguish between force resulting from in- and outflow by integrating only positive or negative values of $(\vec{u}\cdot\vec{n})$. Note that the forces of in- and outflow are overestimated due to vortices and local turbulence that would cancel out in the combined flow. Figure 13 shows the jet force acting on the fluid along the cylinder surfaces. The forces are normalized by the bulk force (Eq. 4.10). The outflow through the cylinder side results in the dominant force, which supports the selection of a cylindrical control volume. It is constant for all distances to the nozzle. The force resulting from the inflow through the wall surface (i.e., the supply massflow) is the corresponding opposite force. The inflow through the cylinder base (i.e., the entrainment) results in an additional force acting on the fluid. The sum of time-averaged forces from all surfaces is approximately zero, which is consistent with the expected conservation of momentum and adds further confidence in the data quality. The

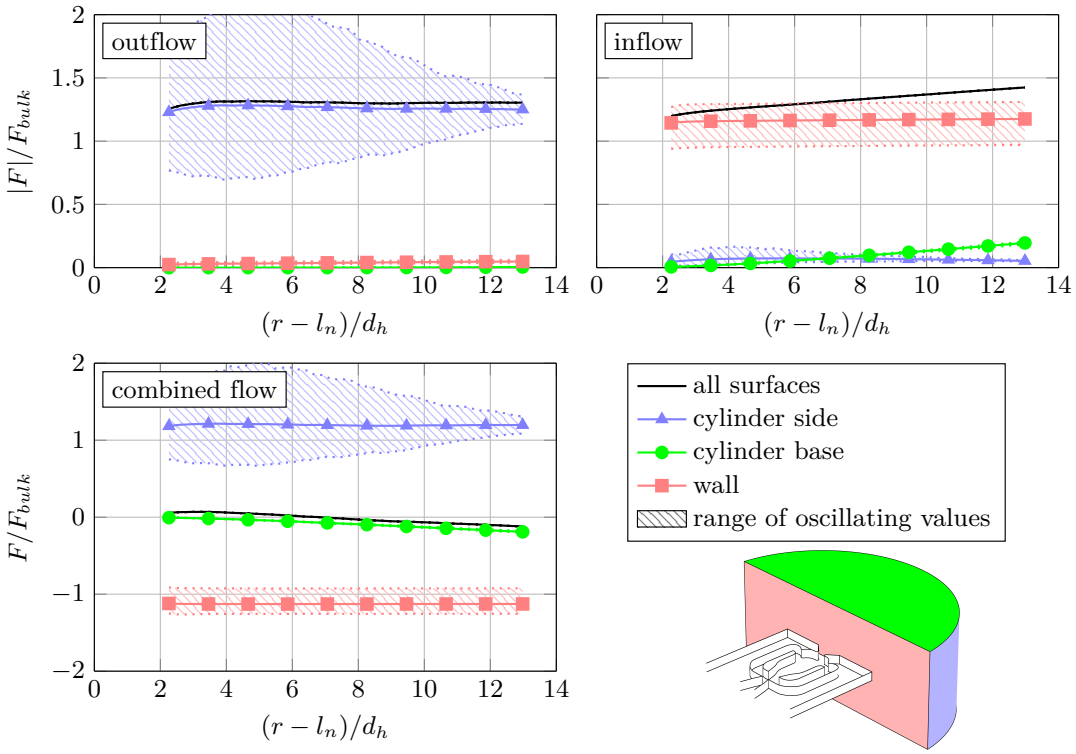

FIGURE 13. Force acting on the fluid integrated along the cylinder surfaces.

slight decrease in total force from all surfaces may be attributed to a streamwise pressure gradient that is not assessed in this study.

Similar to the entrainment, it is not possible to determine the exact force emitted by the spatially oscillating jet. The forces obtained separately by in- and outflow through the cylinder side are overestimated due to turbulence and local vortices. When considering the combined flow, the force created by the inflow due to entrainment from that direction is subtracted from the total force, which yields an underestimated result. Hence, the range of possible values is bound by the force resulting from the total outflow through all surfaces and by the force resulting from the combined flow through the cylinder side. The resulting jet force is between 1.20 and 1.32 times the idealized force F_{bulk}. Thus, a momentum coefficient determined from F_{bulk} for a spatially oscillating jet is underestimated. Similar to the entrainment, the normalized jet force is independent of the supply rate.

The force acting on the fluid over the control surface oscillates throughout one oscillation period. The shaded area in figure 13 illustrates the range of oscillating values. It is evident that at $(r - l_n)/d_h = 5$, the force acting on the cylinder side surface oscillates most. This is caused by changing convection speeds that are a result of the oscillating jet velocity (figure 8). As the jet moves from side to side, its exit velocity decreases and then increases again later within the oscillation period. The flow emitted at the later instance overtakes the previously emitted flow due to the higher jet velocity. This behaviour results in a temporary increase in force over the control surface followed by the opposite effect of a temporary force deficiency.

5. Conclusion

A spatially oscillating jet with an outlet throat aspect ratio of one is emitted by a fluidic oscillator into a quiescent environment. The three-dimensional flow field is measured plane-by-plane employing a stereoscopic PIV system. Simultaneously acquired time-resolved pressure signals from inside the nozzle enable to phase-average velocities and jet properties. The phase-averaged flow field visualizes the jet's spatial oscillation and emphasizes the spread of fluid over a large area. Dominant flow features include alternating circular head vortices that are created repetitively when the jet is fully deflected. The head vortices convect downstream at a constant convection speed. They are similar to the starting vortex known from steady jets. Hence, the jet injects increased vorticity into the surrounding flow field. This may be advantageous for flow control applications that rely on mixing enhancement.

Quantitative jet properties are determined using a cylindrical coordinate system. The cylindrical coordinate system allows for an assessment of jet properties at constant distances from the nozzle throat through one oscillation cycle. The jet's properties are temporally oscillating, which is caused by the internal geometry of the employed fluidic oscillators. Different geometries will yield a different oscillation behaviour. In future studies, it may be of interest to examine the influence of the jet's oscillation pattern and other specific geometric details of the employed fluidic oscillator on the fundamental observations made in this study. For the investigated spatially oscillating jet, the jet's maximum velocity decay rate is considerably higher than that of a comparable steady jet accompanied by a significant increase in jet depth. Both observations are indicative for a higher momentum transfer to the quiescent environment and thus for a higher entrainment. Conceptual constraints only allow providing a range of possible entrainment values for the spatially oscillating jet. Even within this range, the entrainment of the spatially oscillating jet exceeds the entrainment of a steady jet by at least a factor of four. Most of the additional massflow is entrained from the direction normal to the oscillation plane because of the enlarged contact area between accelerated fluid and quiescent environment. The benefit of this three-dimensional effect is expected to be limited to small outlet aspect ratios. For higher outlet aspect ratios, the contribution of entrainment from the normal direction would decrease resulting in a decreased overall entrainment. This effect is one reason for previous controversies regarding the entrainment of spatially oscillating jets. In contrast, the oscillation frequency does not have any obvious effects on the entrainment within the investigated range of supply rates. This result supports the assumption that the Strouhal number accounts for changes in the dynamic behaviour of the flow field. Due to the coupling between oscillation frequency and supply rate for the employed fluidic oscillator, the Strouhal number is constant for all supply rates and oscillation frequencies in this study. It is left for future studies to analyse the effect of the Strouhal number.

The jet force of the spatially oscillating jet is shown to exceed the force of an idealized steady jet with the same massflow by up to 30 %. This result may be of particular interest for the momentum coefficient that is generally used for comparing different flow control actuators. For flow control studies, the momentum coefficient is often based on the idealized steady jet approximation. Measuring the correct jet force is challenging because the lateral component of the instantaneous jet force cancels out during one oscillation period. However, it may be possible to correct for the underestimation by considering the jet deflection angle and oscillation pattern. It should be noted that for many flow control applications, these spatially oscillating jets are commonly operated in the compressible flow regime, which will make the correct assessment of total jet force even more challenging. Here, numerical approaches may provide a useful tool to confirm the presented results and extend the scope of this work.

REFERENCES

Bremhorst, K. 1979 Unsteady subsonic turbulent jets. In *Recent Developments in Theoretical and Experimental Fluid Mechanics*, pp. 480–500. Springer.

Bremhorst, K. & Hollis, P. G. 1990 Velocity field of an axisymmetric pulsed, subsonic air jet. *AIAA Journal* **28** (12), 2043–2049.

Choutapalli, I., Krothapalli, A. & Arakeri, J. H. 2009 An experimental study of an axisymmetric turbulent pulsed air jet. *Journal of Fluid Mechanics* **631**, 23.

Faris, G. N. 1963 Some Entrainment Properties of a Turbulent Axi-Symmetric Jet. *Tech. Rep.*. Mississippi State Univ Mississippi State Dept of Aerophysics.

Garcia, D. 2010 A fast all-in-one method for automated post-processing of PIV data. *Experiments in Fluids* **50** (5), 1247–1259.

Gregory, J. & Tomac, M. N. 2013 A Review of Fluidic Oscillator Development. *43rd AIAA Fluid Dynamics Conference* .

Grinstein, F. F., Gutmark, E. & Parr, T. 1995 Near field dynamics of subsonic free square jets. A computational and experimental study. *Physics of Fluids* **7** (6), 1483.

Haller, G. 2001 Lagrangian structures and the rate of strain in a partition of two-dimensional turbulence. *Physics of Fluids* **13** (11), 3365.

Jeong, J. & Hussain, F. 1995 On the identification of a vortex. *Journal of Fluid Mechanics* **285**, 69.

Krothapalli, A., Baganoff, D. & Karamcheti, K. 1981 On the mixing of a rectangular jet. *Journal of Fluid Mechanics* **107**, 201–220.

Lacarelle, A. & Paschereit, C. O. 2012 Increasing the Passive Scalar Mixing Quality of Jets in Crossflow With Fluidics Actuators. *Journal of Engineering for Gas Turbines and Power* **134** (2), 21503.

Mi, J., Nathan, G. J. & Luxton, R. E. 2001 Mixing Characteristics of a Flapping Jet from a Self-Exciting Nozzle. *Flow, Turbulence and Combustion* **67** (1), 1–23.

Ostermann, F., Woszidlo, R., Nayeri, C. & Paschereit, C. O. 2015*a* Experimental Comparison between the Flow Field of Two Common Fluidic Oscillator Designs. *53rd AIAA Aerospace Sciences Meeting* .

Ostermann, F., Woszidlo, R., Nayeri, C. N. & Paschereit, C. O. 2015*b* Phase-Averaging Methods for the Natural Flowfield of a Fluidic Oscillator. *AIAA Journal* **53** (8), 2359–2368.

Phillips, E. & Wygnanski, I. J. 2013 Use of Sweeping Jets During Transient Deployment of a Control Surface. *AIAA Journal* **51** (4), 819–828.

Platzer, M. F., Simmons, J. M. & Bremhorst, K. 1978 Entrainment characteristics of unsteady subsonic jets. *AIAA Journal* **16** (3), 282–284.

Quinn, W. R. 1992 Streamwise evolution of a square jet cross section. *AIAA Journal* **30** (12), 2852–2857.

Quinn, W. R. & Militzer, J. 1988 Experimental and numerical study of a turbulent free square jet. *Physics of Fluids* **31** (5), 1017.

Raman, G., Hailye, M. & Rice, E. J. 1993 Flip-flop jet nozzle extended to supersonic flows. *AIAA Journal* **31** (6), 1028–1035.

Ricou, F. P. & Spalding, D. B. 1961 Measurements of entrainment by axisymmetrical turbulent jets. *Journal of Fluid Mechanics* **11** (1), 21–32.

Schlichting, H. & Gersten, K. 2006 *Grenzschicht-Theorie (German Edition)*. Springer.

Schmidt, H.-J., Woszidlo, R., Nayeri, C. N. & Paschereit, C. O. 2015 Drag reduction on a rectangular bluff body with base flaps and fluidic oscillators. *Experiments in Fluids* **56** (7).

Schmidt, H. J., Woszidlo, R., Nayeri, C. N. & Paschereit, C. O. 2017 Separation control with fluidic oscillators in water. *Experiments in Fluids* **58** (8), 106.

Seele, R., Tewes, P., Woszidlo, R., McVeigh, M. A., Lucas, N. J. & Wygnanski, I. J. 2009 Discrete Sweeping Jets as Tools for Improving the Performance of the V-22. *AIAA Journal of Aircraft* **46** (6), 2098–2106.

Sforza, P. M., Steiger, M. H. & Trentacoste, N. 1966 Studies on three-dimensional viscous jets. *AIAA Journal* **4** (5), 800–806.

Sieber, M., Ostermann, F., Woszidlo, R., Oberleithner, K. & Paschereit, C. O. 2016

Lagrangian coherent structures in the flow field of a fluidic oscillator. *Physical Review Fluids* **1** (5).

Simmons, J. M., Platzer, M. F. & Smith, T. C. 1978 Velocity measurements in an oscillating plane jet issuing into a moving air stream. *Journal of Fluid Mechanics* **84** (1), 33–53.

Srinivas, T., Vasudevan, B. & Prabhu, A. 1988 Performance of Fluidically Controlled Oscillating Jet. In *Turbulence Management and Relaminarisation* (ed. H. W. Liepmann & R. Narasimha), pp. 485–494. Springer.

Viets, H. 1975 Flip-Flop Jet Nozzle. *AIAA Journal* **13** (10), 1375–1379.

Von Gosen, F., Ostermann, F., Woszidlo, R., Nayeri, C. N. & Paschereit, C. O. 2015 Experimental Investigation of Compressibility Effects in a Fluidic Oscillator. *53rd AIAA Aerospace Sciences Meeting* .

Woszidlo, R., Ostermann, F., Nayeri, C. N. & Paschereit, C. O. 2015 The time-resolved natural flow field of a fluidic oscillator. *Experiments in Fluids* **56** (6).

Wygnanski, I. J. & Fiedler, H. 1969 Some measurements in the self-preserving jet. *Journal of Fluid Mechanics* **38** (3), 577–612.

Zaman, K. B. M. Q. 1996 Axis switching and spreading of an asymmetric jet: the role of coherent structure dynamics. *Journal of Fluid Mechanics* **316**, 1–27.

The interaction between a spatially oscillating jet emitted by a fluidic oscillator and a crossflow

Florian Ostermann[1]†, Rene Woszidlo[1], C. Navid Nayeri[1] and C. Oliver Paschereit[1]

[1]Technische Universität Berlin, Berlin, 10623, Germany

(Received xx; revised xx; accepted xx)

This experimental study investigates the fundamental flow field of a spatially oscillating jet emitted by a fluidic oscillator into an attached crossflow. Dominant flow structures, such as the jet trajectory and dynamics of streamwise vortices are discussed in detail aiming to understand the interaction between the spatially oscillating jet and the crossflow and to identify possible reasons for the high efficacy of spatially oscillating jets in applications. A moveable stereoscopic particle image velocimetry (PIV) system is employed for the plane-by-plane acquisition of the flow field. The three-dimensional, time-resolved flow field is obtained by phase-averaging the PIV results based on a pressure signal from inside the fluidic oscillator. The influence of velocity ratio and Strouhal number is assessed. Compared to a common steady jet, the spatially oscillating jet penetrates to a lesser extent into the crossflow's wall-normal direction in favour of a considerable spanwise penetration. The flow field is dominated by streamwise oriented vortices, which are convected downstream at the speed of the crossflow. The vortex dynamics exhibit a strong dependence on Strouhal number. For small Strouhal numbers, the spatially oscillating jet acts similar to a vortex-generating jet with a time-dependent deflection angle. Accordingly, it forms time-dependent streamwise vortices. For higher Strouhal numbers, the crossflow is not able to follow the motion of the jet, which results in a quasi-steady wake that forms downstream of the jet. The results suggest that the flow field approaches a quasi-steady behaviour when further increasing the Strouhal number.

1. Introduction

Jets in crossflow are a fundamental flow scenario where a jet of one fluid is injected into a crossflow of a second fluid. It is relevant in many technical applications, which include but are not limited to fuel injectors, air conditioning of vehicles, flow actuators, and central venous catheters. The variety and amount of applications have motivated a long history of scientific research on the complex interaction between the injected jet and the crossflow. Fric & Roshko (1994) and Kelso *et al.* (1996) provide an overview of several fundamental flow features that dominate the flow field of a steady jet injected into a crossflow (figure 1). They describe the governing mechanisms, behaviours, and effects of these flow features. One example are shear-layer vortices that are unsteady vortices at the windward side of the jet's shear layer. Other examples are tornado-like wake vortices forming downstream in the wake of the jet or a horseshoe vortex that originates from the roll-up of the oncoming crossflow boundary layer. The most prominent flow feature is the counter-rotating vortex pair because it prevails far downstream thereby dominating the

† Email address for correspondence: florian.ostermann@tu-berlin.de

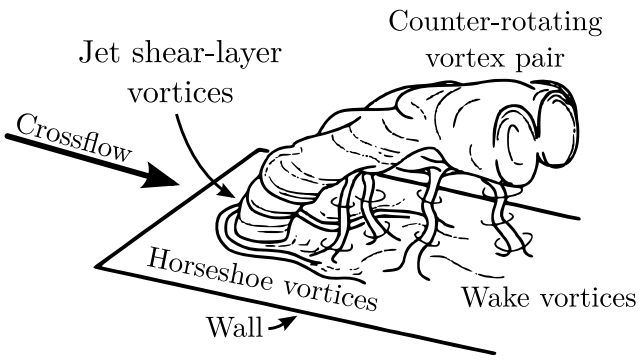

FIGURE 1. Dominant flow structures of a steady jet in crossflow (Fric & Roshko 1994).

flow field (Kamotani & Greber 1972; Fearn & Weston 1974). A comprehensive review of the research and more details on the individual flow features of steady jets interacting with a crossflow are provided by Margason (1993) and Mahesh (2013).

The flow field of a jet in crossflow changes significantly when the injected jet is oscillating spatially or temporally. Eroglu & Breidenthal (2001) investigate the flow field of a pulsed (i.e., temporally oscillating) jet in crossflow. They show that additional vortex rings are created, which dominate the flow field. In comparison to steady jets, they quantify that the penetration depth of pulsed jets at optimized pulsing frequency and jet to crossflow velocity ratio is significantly larger. Furthermore, the pulsing of the jet enhances the mixing performance.

Spatially oscillating jets in crossflow are employed by Lacarelle & Paschereit (2012). They reveal a superior mixing performance of spatially oscillating jets compared to steady jets in crossflow, which is quantified by high-speed laser-induced fluorescence measurements. Other studies demonstrate a high effectiveness of spatially oscillating jets for flow control applications. For example, Seele *et al.* (2009) successfully employ spatially oscillating jets for delaying flow separation on a V-22 aerofoil. Schmidt *et al.* (2015) use spatially oscillating jets for preventing flow separation on base flaps of a bluff body thereby reducing the drag. These studies utilize fluidic oscillators, also known as flip-flop nozzles or sweeping jet actuators, for generating spatially oscillating jets. They are able to generate a spatially oscillating jet without requiring moving parts because the spatial oscillation is solely caused by their internal geometry. The basic principle of one category of fluidic oscillators (i.e., an oscillator with two feedback channels) is illustrated in figure 2. A steady supply of fluid is provided through the inlet nozzle forming a jet inside the mixing chamber. Due to the Coanda effect, the jet will attach to either mixing chamber wall such that the emitted jet is deflected at the outlet as indicated by the dashed grey lines (figure 2). Some fluid is diverted into the feedback channel where it is led back to the inlet interacting with the main jet. This interaction causes the jet to flip to the other side where the process repeats itself. Hence, the fluidic oscillator emits a self-sustained, self-initiated spatially oscillating jet. More details on the working principle of these devices are provided by Woszidlo *et al.* (2015) and Sieber *et al.* (2016). Gregory & Tomac (2013) provide a comprehensive review on fluidic oscillators including other types of oscillators.

Although the effectiveness of spatially oscillating jets for various applications was proved in several studies, the driving mechanisms behind their performance remain unclear. This is mostly contributed to the lack of knowledge on the underlying fundamental flow field because most studies describe the time-averaged effect on global quantities or are limited to qualitative information. This shortcoming is caused by the naturally sustained

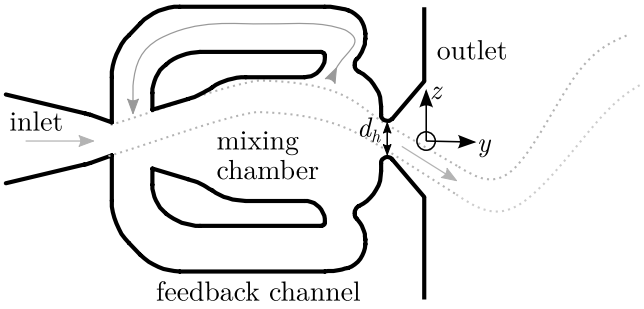

FIGURE 2. Working principle of a fluidic oscillator.

oscillation as well as the three-dimensionality and time-dependence of the flow field, which are challenging to be investigated experimentally. Numerical studies are also rare because of the required temporal and spatial scales, and the lack of sufficient experimental data for validation. Ostermann *et al.* (2017*c*) study the properties of a spatially oscillating jet emitted into a quiescent environment. They identify a dominant head vortex alternately created when the jet is fully deflected. The wider spread of the jet compared to a steady jet in combination with a small nozzle aspect ratio on the order of unity increases the entrainment significantly, which may suggest an enhanced mixing capability. However, the data is limited to a quiescent environment without a crossflow being present. Some qualitative information on the flow field of a spatially oscillating jet in crossflow is provided by Woszidlo & Wygnanski (2011). They use china clay for surface flow visualization on a wall downstream of the oscillator to yield a footprint of flow structures inside the flow field. They identify multiple vortices close to the nozzles and propose that an increase in streamwise vorticity causes the effectiveness for separation control. However, the surface flow visualization only provides an insight into the time-averaged behaviour at the wall and does not yield any information about the flow field dynamics. Additionally, flow structures that are not located at the wall or or only exist temporarily at positions where the jet wipes away the flow visualization paint are not included. Pack Melton & Koklu (2016) employ particle image velocimetry (PIV) for acquiring velocity fields on a semi-span wing model equipped with fluidic oscillators for separation control. The time-averaged cross-sectional velocity fields located downstream of the fluidic oscillators exhibit numerous areas of high vorticity which indicates streamwise vortices. The limitation to time-averaged, two-dimensional data does not provide information about the dynamics or driving mechanism of the streamwise oriented vortices. Recently, Ostermann *et al.* (2017*a*) visualized the three-dimensional, time-resolved flow field of a spatially oscillating jet based on phase-averaged PIV data. They identify a pair of counter-rotating vortices with the sense of rotation opposite to the counter-rotating vortex pair of a steady jet in crossflow. Their dataset is further used for validating numerical studies (Hossain *et al.* 2017; Aram *et al.* 2018) which analyse the influence of parameters such as the velocity ratio and the angle between oscillation plane and crossflow direction. The presented experimental study focuses on the fundamental interaction between a spatially oscillating jet and a crossflow. The objective of this study is the identification of fundamental, dominant flow features and jet properties, which may support the high efficacy of spatially oscillating jets in applications.

2. Setup and Instrumentation

The spatially oscillating jet is emitted by a fluidic oscillator with two feedback channels. The design is illustrated in figure 2. This particular design is chosen because the

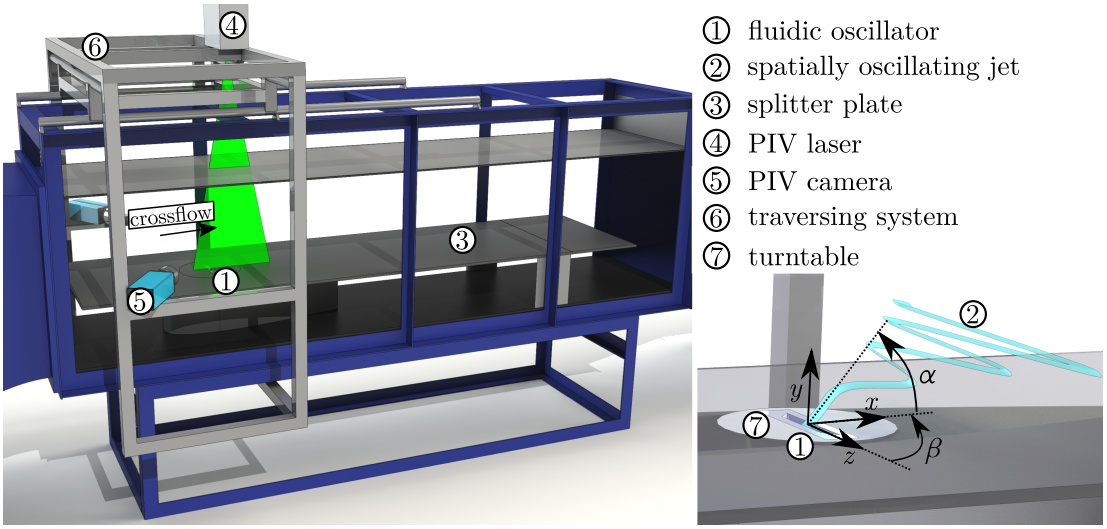

FIGURE 3. The experimental setup.

fundamental properties of its ejected jet were part of experimental and numerical studies (Aram *et al.* 2017; Ostermann *et al.* 2017*c*). Furthermore, this type of fluidic oscillator was employed in various flow control applications (e.g., Raman *et al.* 2005; Phillips & Wygnanski 2013; Koklu & Owens 2017). For this study, the fluidic oscillator is milled from acrylic glass and closed airtight by a cover plate. The outlet throat cross-sectional area is $10 \times 10\,\mathrm{mm}^2$ (i.e., $A_{outlet} = 100\,\mathrm{mm}^2$) yielding a hydraulic diameter d_h of 10 mm. The oscillator is supplied with pressurized air through a massflow controller by Teledyne Hastings. The massflow controller is able to set massflows $\dot{m}_{supply}$ in a range from 0 to 200 kg/h at an accuracy of better than 0.7 % full scale.

The fluidic oscillator is mounted to a turntable inside the wind tunnel (figure 3, right). The divergent part of the nozzle is flush with the flat plate. The setup allows to change the inclination angle α and side angle β. In this study, both angles are set to 90° resulting in the oscillation plane being perpendicular to the direction of the crossflow. The wind tunnel is an open-return, suction wind tunnel that is able to provide crossflow velocities of up to 25 m/s at a turbulence level of less than 0.15 %. The length of the test section is 2 m and the cross-sectional area is approximately $0.5 \times 0.5\,\mathrm{m}^2$. A splitter plate is installed inside the test section guaranteeing a fresh boundary layer development. It reduces the test section height to 37 cm ($37\,d_h$). An adjustable ceiling of the test section allows for controlling the streamwise pressure gradient that is set to zero in this study. The splitter plate is equipped with a trailing edge flap and a elliptical leading edge. The trailing edge flap was adjusted so that no separation occurs at the leading edge. Tripping tape is applied at the leading edge assuring a turbulent boundary layer. At a crossflow velocity of $U_\infty = 15\,\mathrm{m/s}$, the crossflow boundary layer thickness of $U = 0.99U_\infty$ is experimentally determined to be 16 mm ($1.6\,d_h$) at the oscillator outlet. The momentum thickness is 1.6 mm ($0.16\,d_h$) and the shape factor is 1.4. It is noteworthy, that for different crossflow velocities, the boundary layer thickness varies in a limited range between $1.3\,d_h$ and $1.9\,d_h$. The origin of the employed coordinate system is located in the middle of the outlet nozzle (figure 2) with the x-axis being oriented in the direction of the crossflow and the y-axis being oriented in the wall-normal direction (figure 3, right).

The velocity ratio R and the oscillation frequency f_{osc} are parameters of interest in the presented study. The velocity ratio is defined as the ratio between bulk outlet velocity U_{bulk} and crossflow velocity U_∞ (Eq. 2.1). The bulk outlet velocity U_{bulk} is the theoretical

exit velocity assuming a top-hat velocity profile and ambient conditions (i.e., ambient density ρ_0) at the oscillator throat (Eq. 2.2). The jet Reynolds number based on the smallest considered bulk velocity and the hydraulic diameter of the oscillator throat is 9000, which is well within the turbulent regime of a pipe flow.

$$R = \frac{U_{bulk}}{U_\infty} \tag{2.1}$$

$$U_{bulk} = \frac{\dot{m}_{supply}}{\rho_0 A_{outlet}} \tag{2.2}$$

A stereoscopic PIV system measures velocities inside the flow field (figure 3, left). It consists of two pco.2000 cameras by PCO equipped with 100 mm objectives by Canon. The cameras record 6 double-images per second at a resolution of 4 megapixels. The laser light is provided by a Quantel Evergreen 200 mJ laser. The laser light is spanned to a laser sheet by an appropriate system of optical lenses. The laser sheet thickness is approximately 2 mm. The correct timing between the components is assured by a synchronizer manufactured by ILA GmbH. The PIV system is mounted on a two-axis traversing system that is fixed to the wind tunnel. The traversing system enables for movement of the PIV system in streamwise and spanwise direction without requiring a new calibration. Seeding particles (Di-Ethyl-Hexyl-Sebacat) with a particle size of 0.5 µm are added to the oscillator supply and the crossflow. The air that is supplied to the seeding generator providing the seeding for the oscillator is diverted downstream of the massflow controller. Hence, the seeded air does not add to the total supply rate. A bypass equipped with a valve controls the amount of added seeding particles.

The three-dimensional velocity field is acquired plane-by-plane. The planes are oriented in streamwise direction because this allows for taking advantage of the flow field symmetry and for minimizing the most erroneous out-of-plane velocity component. The distance between the individual planes is chosen in accordance to velocity gradients. The smallest distance is 2 mm ($0.2\,d_h$). Each acquired three-dimensional velocity field consists of 22 planes with each containing 8000 PIV snapshots. The domain extends from -15 mm to 160 mm in streamwise direction (i.e., $-1.5\,d_h \leqslant x \leqslant 16\,d_h$), from 0 mm to 140 mm in y-direction (i.e., $0 \leqslant y \leqslant 14\,d_h$), and from -8 mm to 130 mm in spanwise direction (i.e., $-0.8\,d_h \leqslant z \leqslant 13\,d_h$). Some PIV planes are located at negative z for validating the flow field symmetry. The maximum extent of y and z is chosen to be already in the freestream. The PIV snapshots are post-processed with PIVView by PivTech. The final resolution in the x- and y-direction is 1 vector/mm. The acquisition of the three-dimensional flow field is an extensive effort. Therefore, additional measurements of flow field cross-sections are conducted at discrete streamwise positions in order extend the amount of available parameter configurations. In the cross-sections, the final resolution is 1 vector/mm in the y- and z-direction.

The internal fluidic oscillator geometry is equipped with pressure sensors (HDO Series by Sensortechnics) with a response time faster than 10 µs. These pressure sensors are used for measuring the time-resolved pressure inside the oscillator simultaneously to the PIV measurements. The sensors are sampled at 16 kHz. The simultaneous acquisition of pressure and velocities enables a temporal correlation between both. Therefore, the pressure signal provides a reference for the phase-averaging process that is explained in more detail in the subsequent section.

3. Data Analysis

Acquiring the time-resolved flow field is challenging due to the absence of an external trigger and the naturally induced oscillation of the fluidic oscillator, which results in fluctuating oscillation frequencies. Therefore, phase-averaging based on a reference signal is employed. This method is suggested by Ostermann *et al.* (2015) for the flow field of fluidic oscillators. The following steps are executed to acquire the periodic flow field:

(i) The differential pressure between the feedback channel inlets is used as the reference signal. The signal is filtered forward and backward using a Butterworth low pass filter to further increase the signal quality.

(ii) A running auto-correlation with a signal fragment size of approximately half an oscillation period is employed to identify the oscillation periods. Every zero-crossing of the correlation coefficient is defined as the starting point of one half-period. The phase angles in between the starting points are evenly segmented. The definition of $\phi = 0°$ is not unique but depends on the chosen signal fragment. Therefore, all results are phase-aligned by applying a repeatable definition for the period starting point. In this study, the zero-crossing of the differential pressure between the feedback channel inlets (i.e., the reference signal) is chosen as the period starting point. This point coincides with the jet leaving the nozzle without a deflection. Depending on the chosen zero-crossing sign change, the jet moves from negative to positive direction or vice versa. In this study, it moves from negative to positive z.

(iii) A phase angle is assigned to each PIV snapshot. All snapshots within a $\pm 1.5°$ window are averaged. Since 8000 snapshots per measurement are acquired, this leaves on average 66 snapshots per phase angle window.

The described procedure yields a time-resolved representative oscillation period that is referred to as the phase-averaged flow field $\mathbf{u}(\mathbf{x}, \phi)$.

Phase-averaging provides a temporal correlation between the individually measured velocity planes of the three-dimensional flow field. This enables the assembly of the sequentially measured, two-dimensional velocity planes to a three-dimensional flow field. Velocities in between the planes are interpolated using three-dimensional spline interpolation. The spline interpolation may impose local minima and maxima in the velocity field, which results in artefacts of the spatial gradients. In order to reduce this effect, the resulting flow field is smoothed by a self-optimized smoothing algorithm suggested by Garcia (2010). It is based on a discrete cosine transformation of the flow field and a generalized cross validation for adjusting the smoothing parameter. The resulting flow field is mirrored at the x-y planes at $z = 0$ and phase-shifted by 180°, yielding the complete flow field.

The phase-averaged flow field is investigated and visualized using Eulerian and Lagrangian methods. Vortices are identified and localized using the Q-criterion. Hunt *et al.* (1988) define vortices as a positive second invariant Q of $\nabla\mathbf{u}$ (Eq. 3.1) in combination with the local pressure being lower than the ambient pressure. Although the local pressure is not measured, the Q-criterion provides an indication for the location of vortices. For the additionally-acquired velocity cross-sections of the flow field, the gradient in x direction is not available. There, a two-dimensional equivalent is used for identifying vortices (Eq. 3.2). The correct vortex identification is validated by comparing the results qualitatively to the available three-dimensional flow fields.

$$Q = -\frac{1}{2}\left(\left(\frac{\partial u}{\partial x}\right)^2 + \left(\frac{\partial v}{\partial y}\right)^2 + \left(\frac{\partial w}{\partial z}\right)^2\right) - \frac{\partial u}{\partial y}\frac{\partial v}{\partial x} - \frac{\partial u}{\partial z}\frac{\partial w}{\partial x} - \frac{\partial v}{\partial z}\frac{\partial w}{\partial y} \qquad (3.1)$$

$$Q_x = -\frac{1}{2}\left(\left(\frac{\partial v}{\partial y}\right)^2 + \left(\frac{\partial w}{\partial z}\right)^2\right) - \frac{\partial v}{\partial z}\frac{\partial w}{\partial y} \tag{3.2}$$

Lagrangian post-processing methods are enabled by tracing virtual particles through the phase-averaged, three-dimensional flow field using the fourth order Runge-Kutta method. Tracing a high-resolution structured grid of virtual particles backward in time and highlighting all particles originating from the jet yields an instantaneous streak volume. This visualization technique is intuitive due to the similarity to ink visualization. It provides an overview of the qualitative behaviour and structure of the jet. However, it does not contain flow structures inside the crossflow. For visualizing flow structures in jet and crossflow, the finite-time Lyapunov exponent (FTLE) is a suitable tool because it contains flow structures of the jet and the crossflow (Haller 2001). The FTLE quantifies the attraction rate of neighbouring virtual particles thereby highlighting dominant flow structures inside the flow field. Here, the backward FTLE is employed. Neighbouring virtual particles (i.e., $|\Delta\mathbf{x}| = 1\,\mu\text{m}$) are traced through the flow field over two oscillation periods back in time. The flow field boundary condition in negative x- and both z-directions is set to steady crossflow, which prevents particles from leaving the flow field. Note that the described Lagrangian post-processing methods are only applicable to the phase-averaged, three-dimensional flow field.

4. Results

The discussion of the presented results is divided into several parts. First, a qualitative overview of the flow field for three velocity ratios is given. It provides an initial insight into the flow field highlighting the most prominent flow features. Thereafter, the jet trajectory is analysed quantitatively and potential challenges determining the trajectory of spatially oscillating jets are discussed. Last, the effect of the oscillation frequency and its influence on the vortex dynamics is examined.

Two parameters are varied independently in this study: the velocity ratio R and the oscillation frequency f_{osc}. Other parameters such as the inclination angle or the oscillator geometry are left for future parametric studies because it is expected that the general flow features and observed trends are transferable to other spatially oscillating jets as well. The employed fluidic oscillator (figure 2) emits a spatially oscillating jet with specific oscillation characteristics (i.e., the oscillation pattern). The oscillation pattern is characterized by the maximum deflection angle, the temporal variation of the deflection angle and the temporal variation of jet properties (e.g., maximum jet velocity and jet momentum). Figure 4 displays the jet deflection angle and maximum jet velocity over one oscillation period as a characterization of the oscillation pattern. The jet properties are extracted from PIV data with the crossflow being present including potential crossflow-induced effects. Therefore, the oscillation pattern is expected to differ from the results of the similar oscillator in a quiescent environment. Ostermann *et al.* (2017*c*) define the oscillation pattern for the same oscillator geometry in quiescent environment. The deflection angle is the direction of the velocity vector with the maximum velocity magnitude in wall-normal y- and spanwise z-direction. The maximum jet velocity is defined as the magnitude of this vector including the streamwise component. It is evident that the employed fluidic oscillator design causes a predominate sinusoidal oscillation pattern with longer dwelling times of the jet at the maximum deflection angle of $\theta_{max} \approx 50°$. This corresponds to the opening angle of the outlet nozzle. The time it takes for the jet to switch to the other side is comparably short. The maximum jet velocity also oscillates in time. This temporal oscillation is caused by the internal dynamics of the oscillator, which induce an oscillating pressure loss across

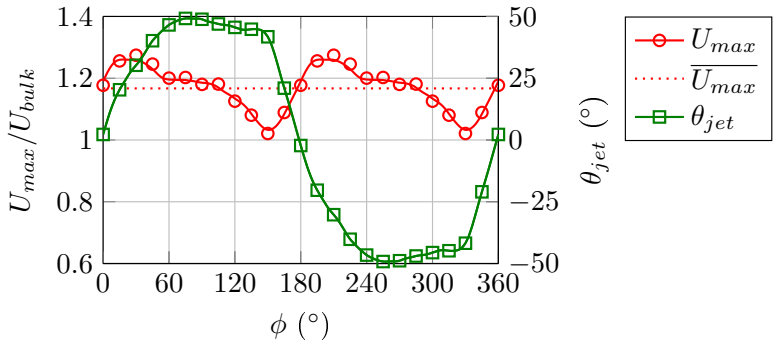

FIGURE 4. Oscillating jet properties with crossflow present in the x-z plane at $y = 0.2\,d_h$. For $U_{bulk} = 50\,\mathrm{m/s}$ and $U_\infty = 10\,\mathrm{m/s}$. Only every 5th data point is marked. The solid lines are spline regression lines.

the device (Woszidlo *et al.* 2015). The jet velocity reaches its maximum before the jet is at its maximum deflection. Afterwards, the maximum velocity decreases until reaching its minimum when the jet starts to sweep to the opposite side. Note that the maximum velocity exceeds the theoretical bulk velocity at all times due to the internal boundary layers that reduce the effective exit area. Therefore, the actual velocity ratio is higher than the calculated velocity ratio based on the bulk velocity (Eq. 2.1). The described oscillation pattern may change with varying supply rates. It is validated that the changes in the oscillation pattern are negligible within the range of supply rates examined in this study. Nevertheless, the supply rate, expressed by U_{bulk}, is kept constant for the majority of velocity ratios. The velocity ratio is set by adjusting the crossflow velocity only. This prevents changing the oscillation pattern by not having to change the supply rate. Furthermore, this assures a constant quality of the phase-averaging process, which may also be linked to the jet supply rate due to the increasing oscillation frequency.

4.1. *Qualitative overview*

The three-dimensional, phase-averaged flow field for three velocity ratios is illustrated for half a period in figure 5. The FTLE is used for visualizing the flow features. A video that shows an animation of figure 5 for a complete period is provided as supplemental material (Movie 1). In the animation and online version of figure 5, the FTLE is coloured according to the origin of the particles forming the flow feature, which allows for distinguishing between flow features in the jet and in the crossflow. A partly transparent, dark, thin surface delineates the interface between jet and crossflow. Accordingly, it represents the envelope of the jet's instantaneous streaklines. The spatial oscillation of the jet is evident in figure 5 for all velocity ratios. At $\phi = 0°$ the jet exits the nozzle without being deflected. At $\phi = 90°$ it is fully deflected for all velocity ratios. Besides these few similarities, it is apparent that the flow fields of the different velocity ratios differ fundamentally. At $R = 1$, the jet remains close to the wall. It does not penetrate deep into the crossflow and its spanwise movement is very limited. This is a result of the small momentum difference between jet and crossflow, which prevents the jet from penetrating deeper into the crossflow. Figure 5 (A) annotates the undisturbed boundary layer of the crossflow, which indicates that the interaction between jet and boundary layer is limited to a small area downstream of the nozzle. No other dominant flow features are apparent, although some are indicated inside the jet (figure 5, B). In fact, a small vortex is occasionally present inside the jet, which is mainly interacting with the crossflow boundary layer (Ostermann *et al.* 2017*b*).

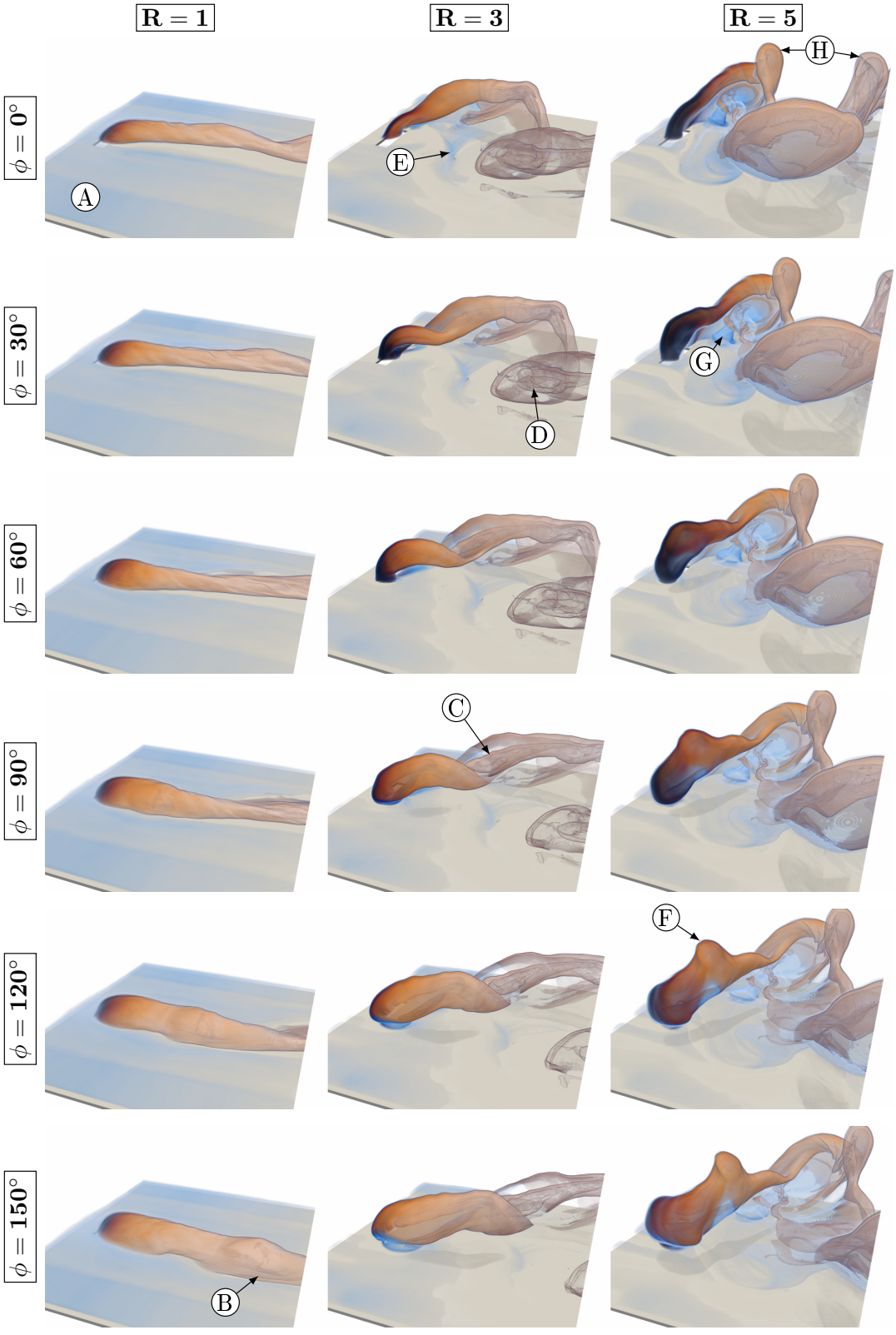

FIGURE 5. Flow field visualization. The shading indicates the FTLE; its colour distinguishes between jet and crossflow (i.e., orange: jet, blue: crossflow). The dark surfaces indicate the interface between jet and crossflow. Annotations are explained in the text.

For a velocity ratio of $R = 3$, the increased jet momentum yields a deeper penetration into the crossflow in the wall-normal as well as in the spanwise direction (figure 5, $R = 3$). This enables the jet to affect a larger area downstream of the nozzle. The jet penetration is quantified in section 4.2. Compared to $R = 1$, the interaction between jet and crossflow appears more complex. Dominant flow structures tear the structure of the jet apart yielding a convoluted interface between jet and crossflow. A dominant streamwise oriented vortex is formed when the jet is fully deflected at both sides (figure 5, C). This streamwise vortex is convected downstream as a vortex package by the crossflow (figure 5, D). The FTLE also exhibits some less dominant flow structures inside the crossflow (figure 5, E). These structures are only indirect results of the spatially oscillating jet, as no jet particles are carried inside. The crossflow boundary layer is significantly affected by the jet as almost no undisturbed boundary layer is apparent.

The complexity in the flow field of $R = 5$ is even further increased compared to the other velocity ratios. As anticipated, the increased momentum allows for an even deeper jet penetration into the crossflow in the wall-normal and in the spanwise direction. A local peak in the penetration is indicated by the FTLE (figure 5, F). A similar peak is observed for the same oscillator design in a quiescent environment by Ostermann *et al.* (2017*c*). This peak is caused by the oscillation pattern which implies that the maximum jet velocity occurs before the jet is fully deflected (i.e., during the movement from one side to the other). This temporal increase in jet velocity is accompanied by an increase in momentum, which causes a deeper penetration into the crossflow. It is suspected that the reason for this effect in the $R = 5$ flow field is the higher velocity ratio. For smaller velocity ratios, it is proposed that the higher crossflow velocity and altered vortex dynamic alleviate this effect.

Another reason for the increased complexity in the flow field for the higher velocity ratios is the smaller distance between the flow features. Figure 5 (H) shows the two local maxima in the jet's crossflow penetration created by the jet half a period apart. For smaller velocity ratios, the 180° symmetric counterparts of the flow features are not apparent because the streamwise extent of the data is limited.

The flow field of $R = 5$ exhibits a different vortex dynamic compared to $R = 3$. The dominant vortices evident for $R = 3$ (figure 5, C) are not as clear anymore, which is most likely a result of other structures interacting with these vortices. A new upright standing wake vortex is apparent for $R = 5$, which consists of particles originating from the crossflow only (figure 5, G). This vortex is formed by the crossflow between the wall and the jet downstream of the nozzle when the jet is fully deflected. It is convected downstream before it dissipates after a short time. Generally, the FTLE shows that only streamwise vortices prevail far downstream beyond the end of the measured region. Spanwise- and wall-normal-oriented vortices are only present in the near field. Therefore, the streamwise vortices are of most interest for applications of spatially oscillating jets in crossflow. A more quantitative investigation of these streamwise vortices is presented in section 4.4.

4.2. *Jet trajectory*

The visual inspection of the time-resolved flow field in section 4.1 reveals that the jet penetration is dependent on the velocity ratio. Generally, the jet penetration is best described by the jet trajectory. However, investigating the jet trajectory of a spatially oscillating jet is challenging because its trajectory is three-dimensional and time-dependent. Mahesh (2013) suggests various definitions for the jet trajectory:

(i) The streamline originating from the centre of the nozzle is frequently defined as the jet trajectory for common steady jets. This definition is not transferable to the

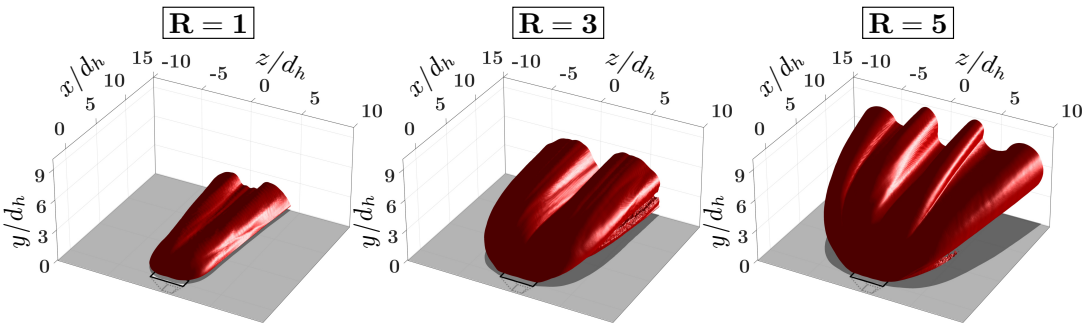

FIGURE 6. Time-averaged envelopes of jet streaklines.

spatially oscillating jet because it yields time-dependent trajectories that may be affected by vortices. Therefore, the trajectory originating from the centre of the nozzle does not necessarily follow the centre line of the jet. That is why it is not suitable for judging the instantaneous jet trajectory or penetration into the crossflow. The same limitation applies to streaklines originating from the centre of the nozzle.

(ii) The position of the local velocity maxima along x is also a definition for the jet trajectory of steady jets. This definition is only suitable for a spatially oscillating jet in the near field. The reason for this limitation is the rapid decay of the maximum velocity, which is shown by Ostermann *et al.* (2017*c*) for spatially oscillating jets in a quiescent environment. This rapid decay hinders the distinction between jet and crossflow in the far field. Furthermore, the oscillating jet exit velocity (figure 4) causes discontinuities in the jet trajectory.

(iii) The maximum scalar concentration along x is often used in investigations on mixing between a jet and a crossflow. Data on the concentration is not available for the current dataset. However, if it were available, it would yield a time-averaged trajectory. It is expected that the concentration is higher at the centre plane of the oscillation due to the jet passing by twice during one oscillation period. Hence, the approach would leave uncertainties regarding the maximum spanwise penetration. Therefore, it is anticipated that the maximum scalar concentration along x is not a suitable tool for capturing the penetration in the spanwise direction.

All suggested definitions for the jet trajectory are not well suited for the investigated spatially oscillating jet. Therefore, a different approach is pursued in this study. The maximum penetration is extracted from the time-averaged envelope covering all instantaneous streaklines originating from the nozzle. Hence, the envelope encloses the volume where at least one particle of the jet is located once in a period. Note that the streaklines are determined from the phase-averaged flow field, which eliminates any turbulent mixing.

Figure 6 displays the envelope of streaklines for three velocity ratios. It is evident that the envelopes differ significantly in form and size. For $R = 1$ and $R = 3$, the maximum penetration is achieved when the jet is fully deflected, which is a result of the jet's long dwelling time at its maximum deflection allowing for a deep penetration into the crossflow. In contrast, $R = 5$ exhibits two local maxima of maximum penetration. The two maxima are caused by the temporal increase in jet penetration due to the change in maximum jet velocity, which is described in section 4.4 (figure 5, F).

Three maximum penetration lengths are considered for a quantitative analysis of the penetration at each position x:

(i) the maximum penetration in the wall-normal direction y_{max}
(ii) the maximum penetration in the spanwise direction z_{max}
(iii) the maximum total penetration of the jet τ_{max}

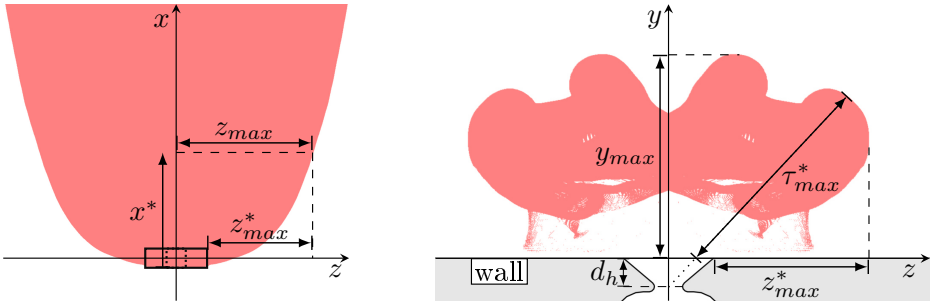

FIGURE 7. The streakline envelope of $R = 5$ with corrected penetration scales. The top view of the envelope (left) and a cross-section through the envelope at $x^*/d_h = 6$ (right).

Additional adjustments are necessary in order to compare the results to steady jet trajectories. This is required because the employed definition considers streaklines originating from the complete nozzle including the divergent part instead of one line originating from the centre of the nozzle. The half width of the nozzle orifice is subtracted in order to compensate for the different lengths of the jet being exposed to the crossflow (figure 7). The nozzle orifice extends $-1.6\,d_h \leqslant z \leqslant 1.6\,d_h$. Hence, the penetration in the spanwise direction is defined by z^*_{max} by subtracting $1.6d_h$ and thus moving the origin of the streakline that causes the deepest penetration in the spanwise direction to $z = 0$ (Eq. 4.2). Accordingly, the streamwise coordinate x is corrected by adding $0.5\,d_h$ because the nozzle extends $-0.5\,d_h \leqslant x \leqslant 0.5\,d_h$ and the streakline yielding the deepest penetration originates from the most upstream edge of the nozzle (Eq. 4.1). The centre of the jet deflection is located upstream the orifice at $y = -1d_h$ (i.e., at the throat). Hence, the total penetration of the jet into the crossflow τ is also corrected, because the potentially angled jet is not fully exposed to the crossflow due to the diverging part of the nozzle (Eq. 4.3). Figure 7 delineates the corrected lengths on a two-dimensional slice through the envelope.

$$x^* = x + 0.5\,d_h \tag{4.1}$$

$$z^*_{max} = z_{max} - 1.6\,d_h \tag{4.2}$$

$$\tau^*_{max} = \max\left[\left(1 - \frac{d_h}{y + d_h}\right)\sqrt{(y + d_h)^2 + z^2}\right] \tag{4.3}$$

Although some corrections are applied, the employed method for extracting the penetration depths is an overprediction for the jet trajectory because it only yields the steepest trajectory. This trajectory is most likely not existent because the penetration depths are extracted from the time-averaged envelope. However, this method is suitable for discussing the maximum penetration of the jet into the crossflow and provides an indication on how the penetration compares to steady jets. Figure 8 shows the maximum penetration depths. Similar to the trajectory of common steady jets, the coordinates are normalized by Rd_h. This normalization was found to be suitable for the far field of steady jets (Mahesh 2013). The penetration in the wall-normal direction y of the spatially oscillating jet coincides well when normalized by Rd_h. The offset that is evident for $R = 1$ is caused by the determination of U_{bulk}. The outlet velocity U_{bulk} is determined assuming a top-hat velocity profile at the outlet throat. For small velocity ratios, it is suspected that the crossflow causes a separation inside the nozzle exit, which increases the actual exit velocity yielding a higher velocity ratio than expected. An envelope of steady jet trajectories from the literature is added to allow for comparing the wall-normal penetration between spatially oscillating jet and steady jet (Mahesh 2013). Note that the

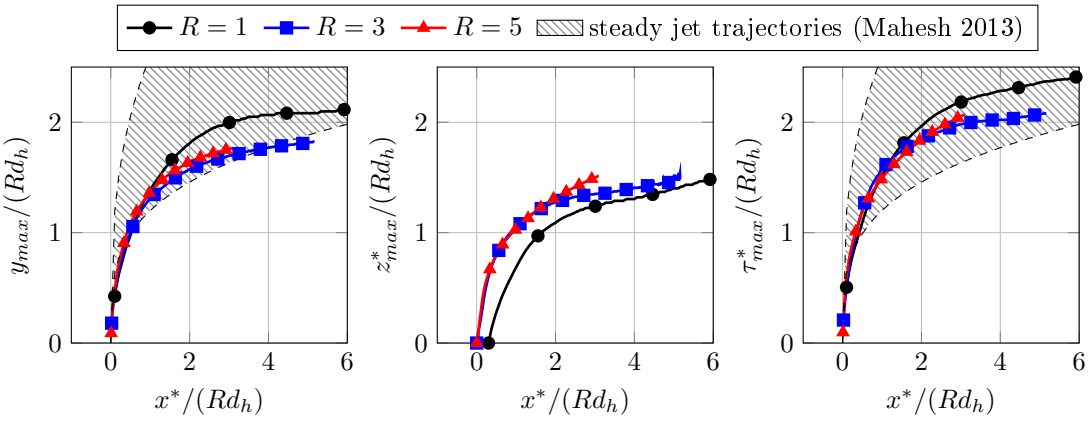

FIGURE 8. Maximum extent of time-averaged streak volume envelope in y-direction (left), in z-direction (centre), and the maximum total penetration (right). Only every 100th data point is marked.

limits for the steady jet trajectories do not represent actual trajectories but rather the limits of possible parameter configurations of equation 4.4. Mahesh (2013) provides the range for the respective parameters to be $1.2 \leqslant A \leqslant 2.6$ and $0.28 \leqslant B \leqslant 0.35$ spanning the envelope of possible trajectories and containing all experimental trajectories collected by Margason (1993).

$$\frac{y}{Rd_h} = A\left(\frac{x}{Rd_h}\right)^B \tag{4.4}$$

Figure 8 (left) reveals that the wall-normal penetration of a spatially oscillating jet is smaller than any common steady jet trajectory. Recalling that the pursued determination of penetration depths results in an overprediction for the trajectory emphasizes the effect because the actual trajectory of the jet is expected to be even closer to the wall. The reason is the spatial unsteadiness of the jet which does not provide enough time for the jet to penetrate deeper into the crossflow, especially when it is in the process of moving from side to side. The penetration in the spanwise direction is even weaker than in the wall-normal direction (figure 8, centre), which is a result of the limited jet deflection. Figure 8 (centre) indicates that the velocity ratio $R = 5$ results in a higher penetration in the spanwise direction than $R = 3$ in the far field, which is probably caused by differing vortex dynamics that are discussed in section 4.4. For $R = 1$, the penetration in the spanwise direction close to the nozzle is smaller than the considered nozzle correction of $1.6d_h$. It is suspected that this is due to the crossflow hindering the jet to attach to the diverging walls of the outlet. The penetration in the wall-normal and the spanwise direction does not represent the maximum penetration into the crossflow because the jet deflection angle is not considered. Taking into account the jet deflection yields the total maximum penetration τ^* shown in figure 8 (right). There, the envelopes lay in between the trajectories of common steady jets in the near field. However, in the far field the gradient declines, yielding trajectories closer to the wall than steady jets. This decrease in gradient is caused by the fast decay in maximum velocity of the spatially oscillating jet as observed in a quiescent environment (Ostermann *et al.* 2017*c*).

It may be suspected that the changes in the jet trajectory are not only attributed to the velocity ratio but also to the jet velocity accompanied by varying oscillation patterns or different boundary layers due to varying crossflow velocities. Figure 9 shows the time-resolved deflection angle as close to the nozzle as possible for four scenarios. Note that the deflection angle is extracted from the mirrored, three-dimensional flow field,

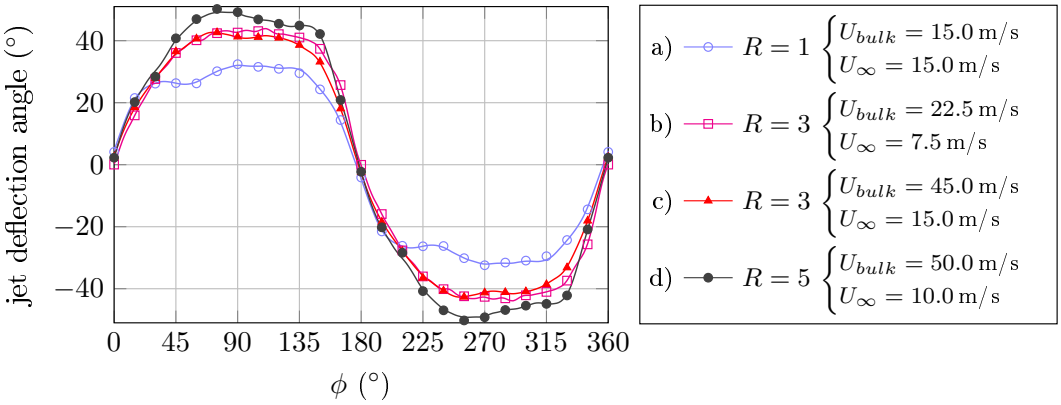

FIGURE 9. The local jet deflection angle at $y = 0.2\,d_h$ for four scenarios. Only every 5th data point is marked. The solid lines are spline regression lines.

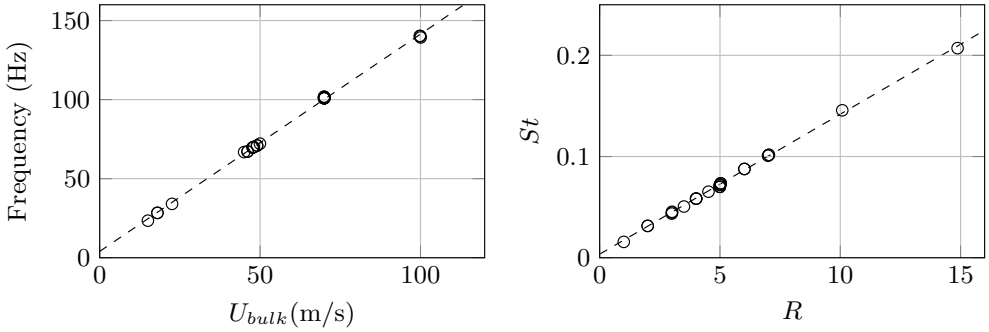

FIGURE 10. Left: The oscillation frequency over the supply rate. Right: The Strouhal number as a function of the velocity ratio.

which explains the symmetric values. It is evident that the crossflow velocity U_∞ does not have a significant influence because scenario (b) and (c) have a different crossflow velocity but a similar deflection angle. This indicates that the influence of the boundary layer on the jet for the selected velocities is negligible. The same applies for the jet velocity U_{bulk} that is also different between scenario (b) and (c). This shows that the oscillation pattern does not change with U_∞ or U_{bulk}. Furthermore, it reveals that the oscillation frequency, which is proportional to the jet velocity, does also not influence the deflection angle. Hence, it is expected that in this study the velocity ratio is the only parameter affecting the jet trajectory. The reason for the independence of the flow field and the oscillation frequency is discussed in the following section 4.3.

4.3. *Relationship between velocity ratio and Strouhal number*

The oscillation frequency is proportional to the supply rate for most common fluidic oscillators when operated well within the subsonic regime (Schmidt *et al.* 2017). Figure 10 (left) displays the oscillation frequency as a function of the jet exit velocity U_{bulk} for the employed fluidic oscillator. A linear regression line emphasizes the linear dependency between the oscillation frequency and the jet velocity. This linear dependency is a consequence of the oscillator's internal flow dynamics, which is discussed in detail by Woszidlo *et al.* (2015). The linear relationship is limited to the subsonic flow regime as it is present for all supply rates in this study.

Commonly, the effects of unsteady flow phenomena are compared by using the Strouhal number. The corresponding equation 4.5 relates the oscillation period time to the time a

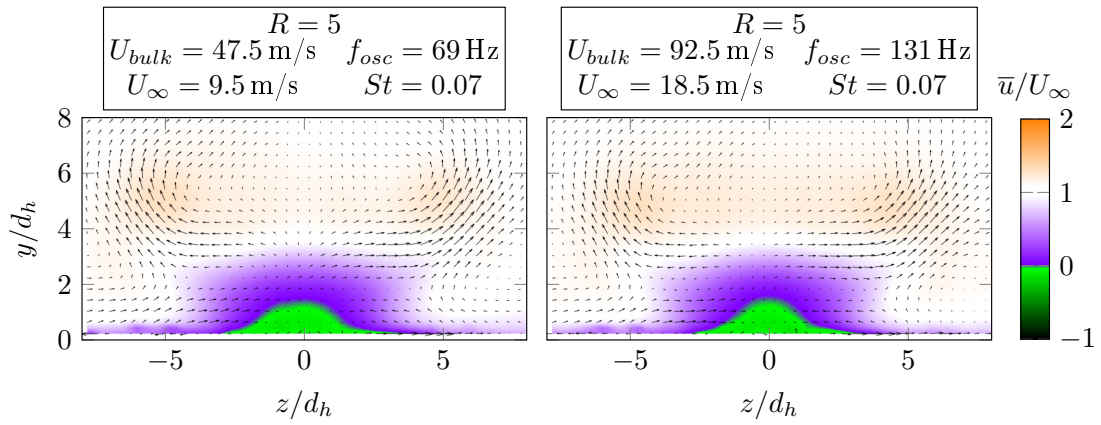

FIGURE 11. A cross-section through the time-averaged velocity field at $x/d_h = 5.5$ for two oscillation frequencies at the same velocity ratio.

particle travels a distance d_h at crossflow velocity U_∞.

$$St = \frac{f_{osc} \cdot d_h}{U_\infty} \tag{4.5}$$

Schmidt *et al.* (2017) show that the product of oscillation frequency and a characteristic length scale of the oscillator (e.g., d_h) is a linear function of U_{bulk} (Eq. 4.6), which is independent of the oscillator scale and supply fluid (i.e., fluids density).

$$f_{osc} \cdot d_h = C \cdot U_{bulk} + D \tag{4.6}$$

The slope C depends on the design of the oscillator. The offset D is negligibly small for the employed oscillator as evident in the linear regression in figure 10 (left) . When equation 4.6 with $D = 0$ is substituted into equation 4.5, the Strouhal number becomes a function of the velocity ratio R (Eq. 4.7).

$$St = \frac{C \cdot U_{bulk}}{U_\infty} \;=\; C \cdot R \tag{4.7}$$

Equation 4.7 illustrates that the Strouhal number is linearly coupled with the velocity ratio, which is validated in figure 10 (right) for the investigated parameter combinations. Therefore, it is not possible in this study to change the Strouhal number and velocity ratio independently with the one employed oscillator design. In fact, if the oscillation frequency is varied by changing the jet velocity while maintaining the same velocity ratio (and therefore Strouhal number) the normalized flow field quantities do not change. This is confirmed in figure 11 by a cross-section through the time-averaged flow field of two parameter combinations that yield the same velocity ratio and Strouhal number. It is evident that the normalized velocities agree very well.

Since the Strouhal number is linearly dependent on the velocity ratio, the amount of parameters reduces to one. This prevents from distinguishing between the driving parameters behind effects described in this study. However, based on the general observations from steady and pulsed jets in crossflow, and based on the character of the discussed effects, it can be assessed which parameter may be of more importance. For example, it is determined that the penetration depth is rather dependent on the velocity ratio than on the Strouhal number. In contrast, effects changing the dynamics of the flow field as discussed in the subsequent section, are expected to be dominated by the Strouhal number. A complete confirmation of the provided discussions requires

additional experiments or numerical studies with different velocity ratio to Strouhal number dependencies, which are beyond the scope of this work and left for future studies.

The coupling between Strouhal number and velocity ratio allows for transferring results from this study to different setups employing the same oscillator design because the Strouhal number is independent of the oscillator scale and working fluid density according to equation 4.7 and Schmidt *et al.* (2017). Hence, the results may be relevant to applications that generally use smaller oscillators at higher oscillation frequencies. However, this is limited by compressibility effects, which are not captured in the current study. Furthermore, the transferability is limited to the particular design because even small adjustments in the design (e.g., longer feedback channels) would result in a different constant C.

4.4. *Vortex dynamics*

In section 4.1, the FTLE enables the identification of dominant flow structures (figure 5). In this section, Eulerian analysis methods are employed to capture and explain the dynamics of the most dominant flow structures (i.e., the wake and the streamwise oriented vortices) in more detail. First, the time-averaged flow field is assessed for various velocity ratios (i.e., Strouhal numbers), hence providing an overview of the flow features and the dependence on the velocity ratio. Then, the vortex dynamics are described using the time-resolved flow field for two velocity ratios accompanied by a discussion of mechanisms that govern these dynamics.

Figure 12 depicts the time-averaged flow field in a cross-section located at $x = 11\,d_h$ for various velocity ratios. The vectors and streamlines visualize the direction and magnitude of the in-plane velocity vectors (i.e., v and w). Note that the shown field of view cover only half of the symmetric flow field. The streamlines indicate deviations from the symmetry that are small. Figure 12 omits small velocity ratios $R < 3$ because of the practical relevance. However, the identified trends are transferable to smaller velocity ratios greater than one (Ostermann *et al.* 2017*b*). The quantities are normalized to enable a comparison between the velocity ratios. The vorticity is normalized by $St \cdot U_\infty$. Since the Strouhal number is linearly dependent on the velocity ratio (Eq. 4.7), the normalization by $St \cdot U_\infty$ is proportional to the jet velocity U_{bulk}. Analogously, the two-dimensional Q-criterion Q_x is normalized by $St \cdot U_\infty^2$ that is proportional to the product of U_{jet} and U_∞.

Figure 12 (left) illustrates the time-averaged, streamwise velocity component $\overline{u}$. It is apparent that with increasing velocity ratio a wake region forms indicated by a significant streamwise velocity deficit. For $R = 15$ even local regions with reverse flow are evident, which implies a considerable recirculation bubble downstream of the jet extending more than 10 nozzle diameters. Figure 12 (centre and right) depicts the time-averaged, streamwise vorticity $\overline{\omega_x}$ and two-dimensional Q-criterion $\overline{Q_x}$ respectively. It allows to identify streamwise oriented vortices in the cross-section. For small velocity ratios $R \leqslant 4$, one vortex is indicated by the streamlines and Q-criterion on either side of the line of symmetry. These symmetric vortices are previously discussed in figure 5. With increasing velocity ratio, the vortices move away from the wall and from the line of symmetry. For $R \geqslant 5$, a second vortex evolves on either side of the line of symmetry. The resulting vortex pair is equal in strength and opposite in their sense of rotation. It is expected that increasing the velocity ratio beyond $R = 15$ will not change the number of vortices.

The existence of streamwise vortices in the time-averaged flow field emphasizes their dominance in the flow field. However, it is anticipated that their strength and location vary throughout the complete oscillation period. A cross-section through the phase-averaged flow field is displayed in figure 13 to assess the dynamic behaviour. The cross-section is placed at $x = 5.5\,d_h$. This location is preferred to the previous location (i.e., $x = 11\,d_h$)

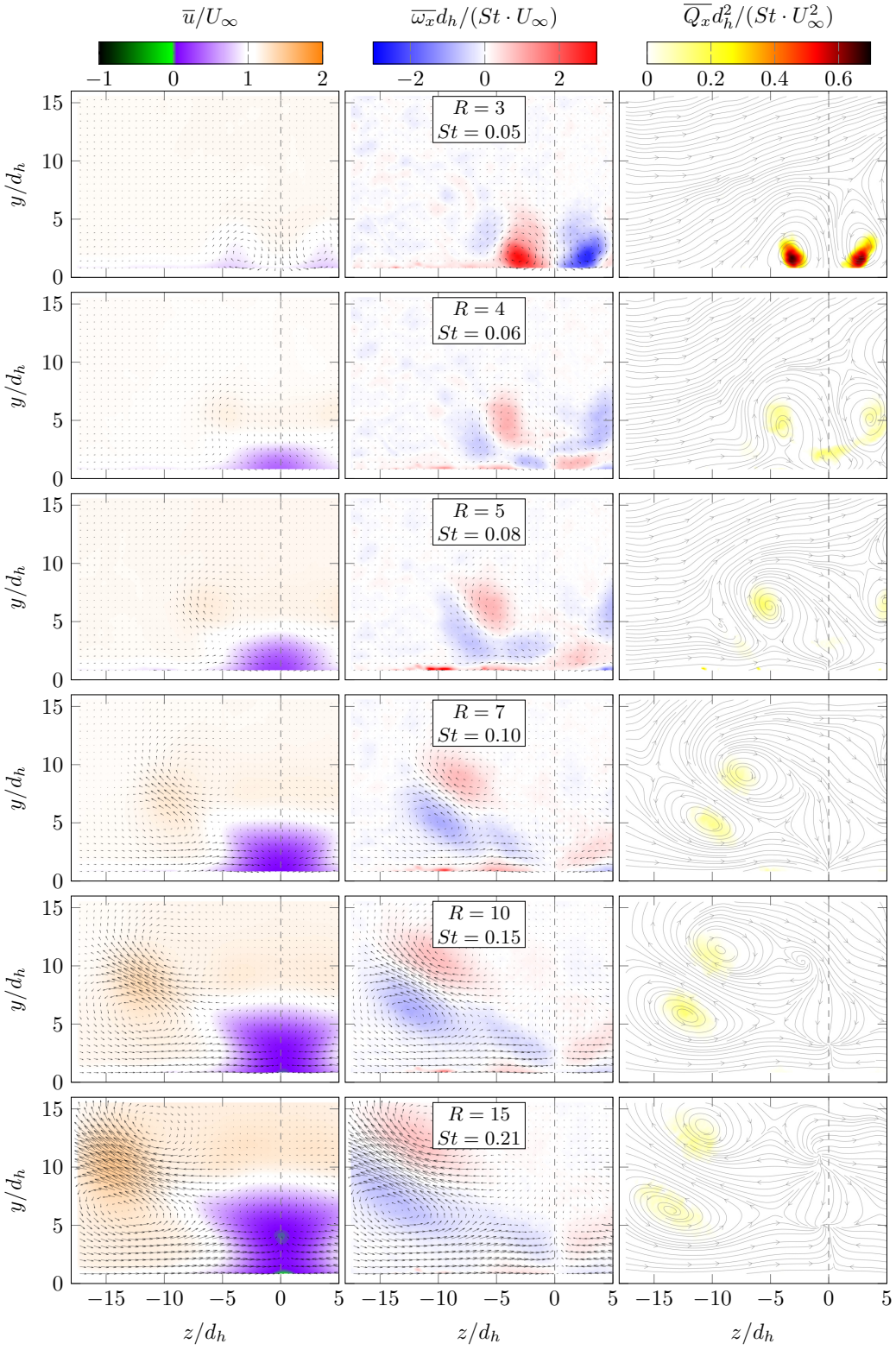

FIGURE 12. Cross-sections through the time-averaged flow field at $x/d_h = 11$. The streamwise velocity component u (left), the streamwise vorticity (centre), and the Q-criterion (right). Note that only half of the flow field is shown (i.e., $z < 0$).

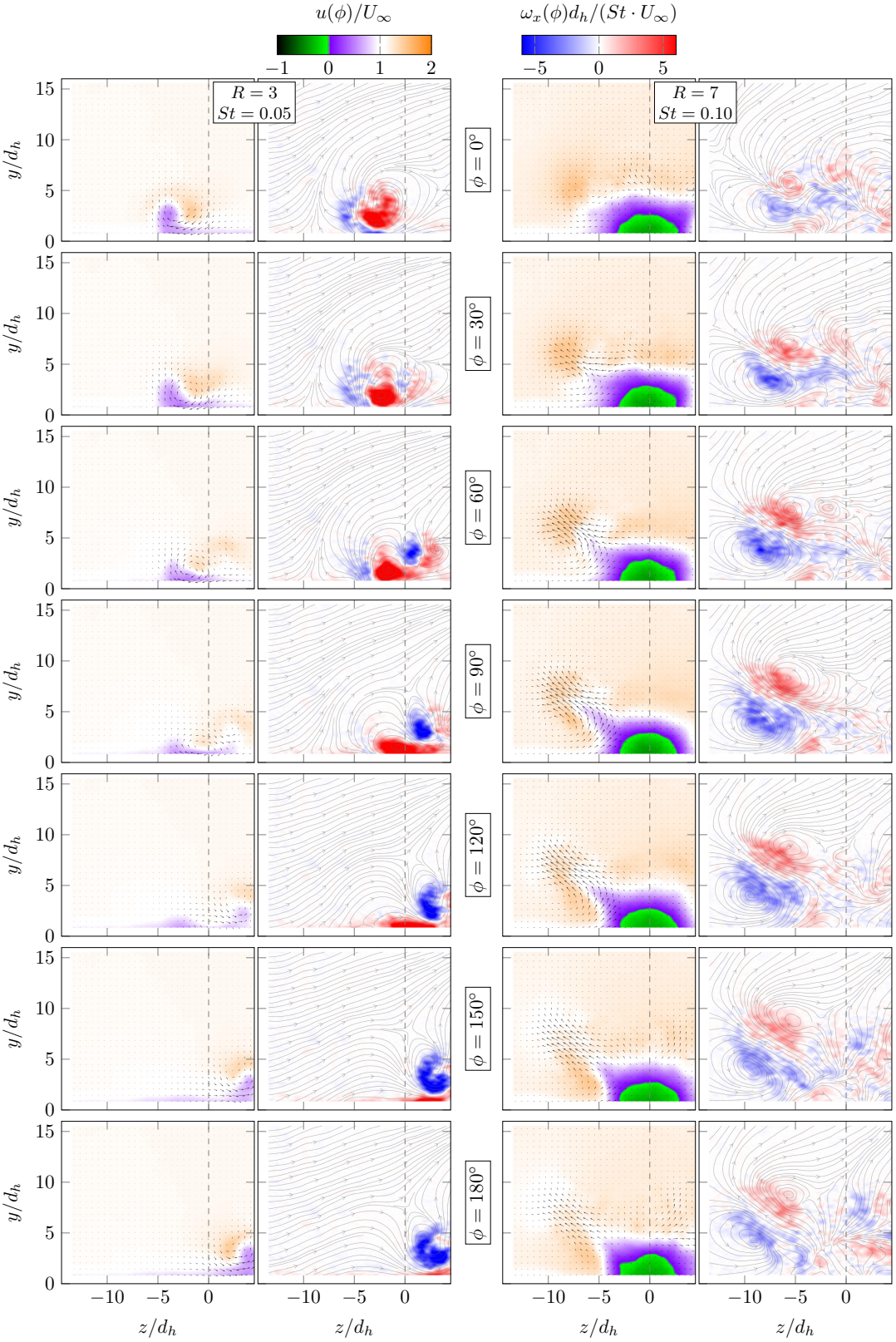

FIGURE 13. Cross-sections through the phase-averaged flow field at $x/d_h = 5.5$ for two velocity ratios each with the streamwise velocity component u left and the streamwise vorticity ω_x right. Note that only half of the flow field is shown (i.e., $z < 0$).

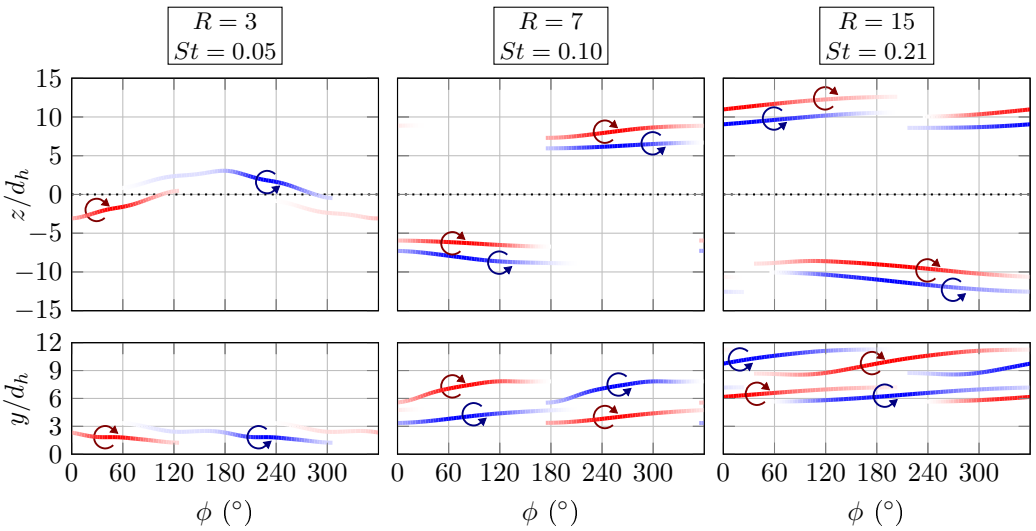

FIGURE 14. Traced vortex cores at $x/d_h = 5.5$. The arrows denote the sense of rotation. The shading indicates the magnitude of Q_x.

because it is located closer to the nozzle, which emphasizes the differences between the velocity ratios. The convection velocity of the flow features changes with the velocity ratio resulting in a phase-lag between the shown velocity ratios at one specific downstream location x. A large distance to the nozzle would amplify this effect. However, it is noteworthy that the qualitative behaviour and findings made for this cross-section apply for the downstream positions as well. An animation of figure 13 over a complete period is available as supplemental material (Movie 2).

Figure 13 exhibits that the most dominant difference between the low and high velocity ratio is the wake downstream of the oscillating jet. For $R = 3$, only a small velocity deficit is evident, which forms downstream of the instantaneous jet position, following the jet motion. In contrast, $R = 7$ exhibits an almost steady recirculation bubble downstream of the oscillating jet. The recirculation bubble does not follow the movement of the jet.

Figure 13 reveals that the vortex dynamics differ significantly between the velocity ratios. For additional quantitative information on the position of the vortices, figure 14 delineates the y- and z-position of the most dominant vortices as a function of the phase angle. The position of the vortices is identified using the two-dimensional Q-criterion in combination with the vorticity. The shading of the lines indicates the normalized quantity of Q. For $R = 3$, the streamwise oriented vortices are alternating in strength. They move from side to side following the movement of the jet. Only one vortex is dominant on either side of the line of symmetry. For $z < 0$ this vortex is rotating in positive direction. It is accompanied by a region of negative streamwise vorticity not forming an individual vortex as visible in figure 13 ($R = 3$, $\phi = 0°$). When the jet moves to the opposite side, three vortices are existent simultaneously at one instance of time (figure 13, $R = 3$, $\phi = 60°$). One of these vortices represent the remnants of the former dominant vortex for $\phi = 0°$ that diffuses at the wall while the two new vortices form and follow the movement of the jet. Note that these new vortices are not captured in figure 14 because only the positions of the dominant vortices are shown. One of the two new vortices evident in figure 13 ($R = 3$, $\phi = 60°$) becomes the dominant vortex at $z > 0$ rotating in negative direction (figure 14, $R = 3$). The other one disappears resulting in the aforementioned region of streamwise vorticity accompanying the dominant vortex (analogue to figure 13, $R = 3$, $\phi = 0°$).

The flow field for $R = 7$ contains two dominant vortices with opposite sense of rotation on either side of the line of symmetry. These vortices are coexistent and equal in strength and size. In comparison to $R = 3$, the vortices are weaker but larger (figure 13). They remain almost fixed at one position without following the movement of the jet. When the jet moves to the opposite side, the vortex pair disappears and its 180°-counterpart is created at the symmetric position (figure 14, $R = 7$). In comparison to $R = 3$, the flow field of $R = 7$ exhibits an almost bi-stable behaviour with fixed vortices that exist through half of the period. Figure 14 also contains the position of the dominant vortices in the flow field of $R = 15$. It is evident that the qualitative vortex dynamics is similar between $R = 15$ and $R = 7$ although the position of the vortices changes due to the increased penetration depth. However, it is apparent that with increasing velocity ratio, the relative duration of the vortices during one oscillation period increases.

The observed differences in the vortex dynamics between the velocity ratios indicate a change in the interaction between jet and crossflow. This is best described by using the Strouhal number because it is a characteristic metric for the dynamic behaviour of the flow field (Eq. 4.5). Substituting the oscillation period time $f_{osc} = 1/T_{osc}$ (i.e., the oscillator timescale) and a representative convective timescale of the crossflow $T_\infty = d_h/U_\infty$ in equation 4.5 yields the ratio between the timescales (Eq. 4.8).

$$St = \frac{T_\infty}{T_{jet}} \tag{4.8}$$

With increasing Strouhal number, the ratio of timescales becomes larger inferring that the difference in timescales between jet and crossflow grows. Recalling that the Strouhal number is the ratio between local and global inertia, the time T_{adapt} required by the crossflow to adapt to a new flow situation due to its inertia is proportional to the convective timescale T_∞. Hence, the ratio between T_{adapt} and T_{jet} also increases with Strouhal number (Eq. 4.9). This relationship supports the previous argument for the relative duration of the vortices increasing with Strouhal number between $R = 7$ and $R = 15$ in figure 14.

$$\frac{T_{adapt}}{T_{jet}} \propto \frac{T_\infty}{T_{jet}} = St \tag{4.9}$$

The Strouhal number also points to the reasons for the apparent change in vortex dynamics between $R = 3$ and $R = 7$ (figure 13). For small Strouhal numbers (i.e., $T_{adapt} << T_{Jet}$), the crossflow is able to fully adapt to all instantaneous deflection angles of the jet. Therefore, the crossflow experiences a quasi-steady jet with a changing deflection angle. This instantaneous jet behaves similar to a vortex generating jet (VGJ) known from the literature (e.g., Johnston & Nishi 1990; Rixon & Johari 2003). This is supported by the instantaneous flow field being qualitatively similar to the flow field of a VGJ. Vortex generating jets create a pair of counter-rotating vortices with one dominant vortex. The other one, that is located between the angled jet and the wall, is much weaker (Rixon & Johari 2003). The instantaneous spatially oscillating jet exhibits the same vortex structure: one vortex is dominant and prevails downstream; the other vortex is weaker or only indicated by vorticity (figure 13, $R = 3$). The oscillating deflection angle of the jet causes the changing position of the vortices. It is also the reason for the observed, simultaneous existence of three vortices in figure 13 ($R = 3$, $\phi = 60°$). When the jet exits the nozzle without a deflection, it acts similar to a conventional steady jet in crossflow forming a counter-rotating vortex pair. These vortices are convected downstream passing by the previous dominant vortex that is located inside the boundary layer and therefore experiences a smaller convection velocity.

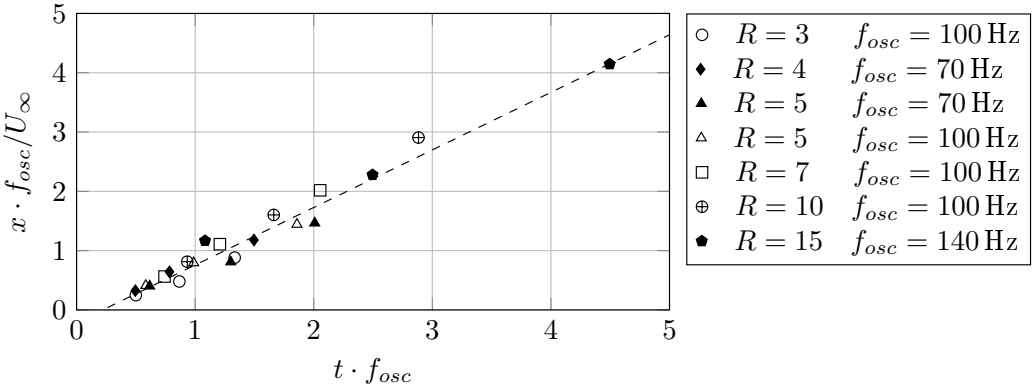

FIGURE 15. Normalized x-location of the vortex with negative sense of rotation (i.e., $\omega_x < 0$) at $z > 0$ as a function of time for various velocity ratios and oscillation frequencies. The dashed line represents a linear regression line.

For high Strouhal numbers (i.e., $T_{adapt} \rightarrow T_{jet}$), the crossflow is not able to fully adapt to the motion of the jet due to its inertia. Instead, the crossflow experiences a quasi-steady delta-shaped jet and forms a corresponding quasi-steady wake including the recirculation bubble. This is evident for $R = 7$ in figure 13 ($R = 7$) where the wake is fixed at one position and its shape does not change throughout the period. The jet's oscillation pattern, that is characterized by long dwelling times at the maximum deflection, enables the jet to penetrate beyond the wake region when it is fully deflected. Therefore, the crossflow experiences the jet at its maximum deflection as a periodically existent, angled, quasi-steady jet (i.e., similar to a pulsed VGJ) with a constant deflection angle of approximately $\theta_{max} = 50°$ at either side of the line of symmetry. This quasi-steady VGJ forms corresponding vortices that are evident in figure 14 ($R \geqslant 7$). An increase in Strouhal number is accompanied by higher velocity ratios which increase the penetration depth of the jet (section. 4.2). This larger penetration increases the distance between the angled jet and the wall, which enables the jet to create two vortices that are equal in strength and size instead of one dominant vortex (figure 13, $R = 7$). Therefore, it may be expected that the number of dominant vortices is not solely dependent on the Strouhal number. Presumably, an oscillating jet that achieves higher velocity ratio at smaller Strouhal numbers would exhibit two dominant vortices on either side although the crossflow is able to fully adapt to the instantaneous deflection of the jet.

Figure 5 (F) suggests that the streamwise distance between the vortices decreases with velocity ratio and therefore Strouhal number. The streamwise distance Δx is dependent on the convection velocity (Eq. 4.10). The convection velocity may be determined by tracing the downstream position of the vortices.

$$\Delta x = \frac{\text{convection velocity}}{f_{osc}} \tag{4.10}$$

Figure 15 shows the non-dimensional, streamwise position of one vortex extracted from three cross-sections located 5.5, 10, and 20 nozzle diameters downstream of the nozzle for various scenarios. The horizontal axis designates the oscillation periods and the vertical axis stands for the normalized convection velocity. The points mark the timestamps of the vortex being present in one specific cross-section. This timestamp is defined as the centre between appearance and disappearance of the vortex inside the cross-section. It is evident that the streamwise vortex positions collapse onto a single straight line independent of the velocity ratio or oscillation frequency. The slope of this line

is one. Therefore, the convection velocity of the vortices is equal to U_∞ for all scenarios and downstream locations. No Reynolds number effects are evident within the limits investigated in this study. Thus, the convection velocity U_∞ governs the distance between the vortices (Eq. 4.11). Replacing $f_{osc} = 1/T_{osc}$ and $U_\infty = d_h/T_\infty$ in equation 4.11 yields the distance between the vortices as a function of the Strouhal number (Eq. 4.13). Accordingly, the distance decreases with increasing Strouhal number. For $St \rightarrow \infty$, the distance approaches zero yielding a quasi-steady flow field. It is anticipated that a quasi-steady flow field is experienced long before Δx approaches zero because of two reasons. First, the crossflow inertia causes the vortices to be sustained although the jet is not located at this position anymore. Second, possible upstream and downstream effects cause the vortices to interact with their predecessors from the previous period supporting a quasi-steady behaviour. First indications for a quasi-steady flow field are evident for $R = 15$ in figure 14 where the vortices last longer than the jet is located at its maximum deflection angle. Similar observations are made for vortex generating jets by Hansen & Bons (2006), who state that the effect of the pulsed jet does not immediately end when the pulse is turned off.

$$\Delta x = \frac{U_\infty}{f_{osc}} \tag{4.11}$$

$$\Delta x = d_h \frac{T_{osc}}{T_\infty} \tag{4.12}$$

$$\frac{\Delta x}{d_h} = St^{-1} \tag{4.13}$$

5. Conclusion

The presented study investigates the fundamental interaction between a spatially oscillating jet and a crossflow. The oscillation plane is oriented perpendicular to the crossflow to provide a fundamental scenario for comparison with a common steady jet in crossflow. The velocity ratio and oscillation frequency are the considered parameters to understand the basic interaction between the jet and the crossflow. Although the results of this study also suggest the importance of other parameters for applications, a detailed parametric assessment is beyond the scope of this work and left for future experimental or numerical studies.

It is demonstrated that varying the oscillation frequency without changing the velocity ratio does not alter the normalized flow field. This is caused by the employed fluidic oscillator design that exhibits a linear dependency between supply rate and oscillation frequency. As a result, the Strouhal number is linearly coupled to the velocity ratio in this study, which prevents changing velocity ratio and Strouhal number individually. However, this also implies that the properties derived in this study are transferable to the same oscillator design with different scales or working fluids as long as no compressibility effects are present.

The crossflow penetration of the spatially oscillating jet in the wall-normal direction is weaker than that of a comparable common steady jet in favour of a larger spanwise extent. This enables the jet to affect a considerably larger downstream region than a steady jet. It is suspected that the penetration depth in wall-normal and spanwise direction depends mainly on the oscillation pattern and the velocity ratio. Presumably, the Strouhal number also has an effect due to the changing vortex dynamics that may alter the jet trajectory.

The flow field is dominated by streamwise vortices. These vortices may be one reason for the high efficacy of spatially oscillating jets for separation control or mixing enhancement

because it induces a considerable amount of wall-normal and lateral velocities. The driving mechanism behind the vortices is similar to a vortex generating jet with changing deflection angle. The number of the vortices (i.e., two or four) is proposed to depend on the velocity ratio that influences the jet's penetration depth. The dynamic of the vortices is linked to the Strouhal number and velocity ratio. The Strouhal number determines whether the crossflow is able to adapt to new flow field situations such as the jet's changing deflection angle. With increasing Strouhal number, the crossflow is not able to fully adapt to the changing jet deflection angle and forms a quasi-steady wake. The velocity ratio influences the size of this wake. The relative duration of the vortices at one streamwise position during one oscillation period is increasing with Strouhal number. They are convected downstream at the speed of the crossflow. Therefore, the distance between the same vortices of two periods is inversely proportional to the Strouhal number. Hence, it is expected that increasing the Strouhal number beyond the investigated range in this study eventually yields a quasi-steady flow field.

It is noteworthy that the influence of Strouhal number and velocity ratio on the vortex dynamics is expected to be transferable to other types of spatially oscillating jets generated by means other than the employed fluidic oscillator. However, the linear relationship between velocity ratio and Strouhal number may differ for other fluidic oscillator designs. For future studies it is recommended to disconnect the two parameters and validate the arguments made in the current work. Furthermore, the influence of the jet's oscillation pattern remains unknown and may also be subject of future numerical or experimental investigations.

Acknowledgements

The authors gratefully acknowledge the funding from the Deutsche Forschungsgemeinschaft (DFG Project PA 920/34-1).

REFERENCES

Aram, S., Lee, Y., Shan, H. & Vargas, A. 2017 Computational fluid dynamic analysis of fluidic actuator for active flow control applications. *AIAA Journal* pp. 1–10.

Aram, S., Shan, H., Ostermann, F. & Woszidlo, R. 2018 Computational validation and analysis of interaction of a sweeping jet and an attached turbulent flow. In *2018 AIAA Aerospace Sciences Meeting*. American Institute of Aeronautics and Astronautics.

Eroglu, A. & Breidenthal, R. E. 2001 Structure, penetration, and mixing of pulsed jets in crossflow. *AIAA Journal* **39** (3), 417–423.

Fearn, R. & Weston, R. P. 1974 Vorticity Associated with a Jet in a Cross Flow. *AIAA Journal* **12** (12), 1666–1671.

Fric, T. F. & Roshko, A. 1994 Vortical structure in the wake of a transverse jet. *Journal of Fluid Mechanics* **279**, 1.

Garcia, D. 2010 A fast all-in-one method for automated post-processing of PIV data. *Experiments in Fluids* **50** (5), 1247–1259.

Gregory, J. & Tomac, M. N. 2013 A Review of Fluidic Oscillator Development. *43rd AIAA Fluid Dynamics Conference* .

Haller, G. 2001 Lagrangian structures and the rate of strain in a partition of two-dimensional turbulence. *Physics of Fluids* **13** (11), 3365.

Hansen, L. & Bons, J. 2006 Flow measurements of vortex generator jets in separating boundary layer. *Journal of Propulsion and Power* **22** (3), 558–566.

Hossain, M. A., Prenter, R., Lundgreen, R. K., Agricola, L., Ameri, A., Gregory, J. W. & Bons, J. P. 2017 Investigation of crossflow interaction of an oscillating jet. In *55th AIAA Aerospace Sciences Meeting*. American Institute of Aeronautics and Astronautics.

Hunt, J.C.R., Wray, A.A. & Moin, P. 1988 Eddies, streams, and convergence zones in turbulent flows. *Center of Turbulence Research Report CTR-S88* p. 193.

Johnston, J. P. & Nishi, M. 1990 Vortex generator jets - means for flow separation control. *AIAA Journal* **28** (6), 989–994.

Kamotani, Y. & Greber, I. 1972 Experiments on a Turbulent Jet in a Cross Flow. *AIAA Journal* **10** (11), 1425–1429.

Kelso, R. M., Lim, T. T. & Perry, A. E. 1996 An experimental study of round jets in cross-flow. *Journal of Fluid Mechanics* **306**, 111.

Koklu, M. & Owens, L. R. 2017 Comparison of sweeping jet actuators with different flow-control techniques for flow-separation control. *AIAA Journal* **55** (3), 848–860.

Lacarelle, A. & Paschereit, C. O. 2012 Increasing the Passive Scalar Mixing Quality of Jets in Crossflow With Fluidics Actuators. *Journal of Engineering for Gas Turbines and Power* **134** (2), 21503.

Mahesh, K. 2013 The interaction of jets with crossflow. *Annual Review of Fluid Mechanics* **45** (1), 379–407.

Margason, R. J. 1993 Fifty Years of Jet in Cross Flow Research. *AGARD conference proceedings* **538**.

Ostermann, F., Godbersen, P., Woszidlo, R., Nayeri, C. N. & Paschereit, C. O. 2017*a* Sweeping jet from a fluidic oscillator in crossflow. *Physical Review Fluids* **2** (9).

Ostermann, F., Woszidlo, R., Nayeri, C. N. & Paschereit, C. O. 2015 Phase-Averaging Methods for the Natural Flowfield of a Fluidic Oscillator. *AIAA Journal* **53** (8), 2359–2368.

Ostermann, F., Woszidlo, R., Nayeri, C. N. & Paschereit, C. O. 2017*b* Effect of velocity ratio on the flow field of a spatially oscillating jet in crossflow. In *55th AIAA Aerospace Sciences Meeting*. American Institute of Aeronautics and Astronautics.

Ostermann, F., Woszidlo, R., Nayeri, C. N. & Paschereit, C. O. 2017*c* Properties of a spatially oscillating jet emitted by a fluidic oscillator. *Journal of Fluid Mechanics (submitted)* .

Pack Melton, L. G. & Koklu, M. 2016 Active flow control using sweeping jet actuators on a semi-span wing model. *54th AIAA Aerospace Sciences Meeting* .

Phillips, E. & Wygnanski, I. J. 2013 Use of Sweeping Jets During Transient Deployment of a Control Surface. *AIAA Journal* **51** (4), 819–828.

Raman, G., Packiarajan, S., Papadopoulos, G., Weissman, C. & Raghu, S. 2005 Jet thrust vectoring using a miniature fluidic oscillator. *Aeronautical Journal* **109** (1093), 129–138.

Rixon, G. S. & Johari, H. 2003 Development of a steady vortex generator jet in a turbulent boundary layer. *Journal of Fluids Engineering* **125** (6), 1006.

Schmidt, H.-J., Woszidlo, R., Nayeri, C. N. & Paschereit, C. O. 2015 Drag reduction on a rectangular bluff body with base flaps and fluidic oscillators. *Experiments in Fluids* **56** (7).

Schmidt, H. J., Woszidlo, R., Nayeri, C. N. & Paschereit, C. O. 2017 Separation control with fluidic oscillators in water. *Experiments in Fluids* **58** (8), 106.

Seele, R., Tewes, P., Woszidlo, R., McVeigh, M. A., Lucas, N. J. & Wygnanski, I. J. 2009 Discrete Sweeping Jets as Tools for Improving the Performance of the V-22. *AIAA Journal of Aircraft* **46** (6), 2098–2106.

Sieber, M., Ostermann, F., Woszidlo, R., Oberleithner, K. & Paschereit, C. O. 2016 Lagrangian coherent structures in the flow field of a fluidic oscillator. *Physical Review Fluids* **1** (5).

Woszidlo, R., Ostermann, F., Nayeri, C. N. & Paschereit, C. O. 2015 The time-resolved natural flow field of a fluidic oscillator. *Experiments in Fluids* **56** (6).

Woszidlo, R. & Wygnanski, I. J. 2011 Parameters governing separation control with sweeping jet actuators. *29th AIAA Applied Aerodynamics Conference* .

Chapter 5 | Discussion

The publications contain the results of the present work. In the following, the main results are reviewed and their scope of transferability as well as limitations and shortcomings are discussed, which extends the information of the respective publication. Furthermore, it is emphasized how each publication contributes to the present work and affects the subsequent studies. Future work extending each individual publication as well as this dissertation is suggested, and possible challenges of the suggested work are discussed.

5.1 Phase-Averaging Methods

The primary objective of publication **I** with regards to the present work is to identify a suitable and reliable phase-averaging method for the flow field of a spatially, naturally oscillating jet. Therefore, the phase-averaging method should meet specific requirements:

1. Measurement equipment involved in the phase-averaging method should not impose an additional disturbance to the flow field.

2. The phase-averaging method should be applicable for a plane-by-plane acquisition of a time-resolved, three-dimensional flow field. Hence, it needs to provide a temporal correlation between the individually acquired PIV planes.

3. The phase-averaging method should be transferable to other setups and reproduce a similar, reliable result without extensive validation being required.

4. The method should be applicable to high oscillation frequencies compensating the small sampling rates of low-speed PIV systems. Although modern high-speed PIV systems are able to achieve sampling rates of several kilo Hertz, they are expensive and the employed CMOS chips record images with a smaller resolution and a higher noise level compared to the CCD chips usually used in low-speed PIV cameras. Hence, the image quality is expected to be worse than that of a low-speed PIV system. Therefore, a phase-averaging method not based on time-resolved PIV measurements is preferred.

Various phase-averaging methods based on mathematical and physical approaches are assessed and compared regarding their performance on a flow field of a spatially oscillating jet emitted into a quiescent environment (publication **I**).

One noteworthy phase-averaging technique is the proper orthogonal decomposition (POD) because it is frequently used for phase-averaging (e.g., Bobusch et al., 2013a; Perrin et al., 2007; van Oudheusden et al., 2005). Phase-averaging based on the POD has the advantage that samples from low-speed PIV alone are sufficient for phase-averaging. The results are independent of the sampling rate. However, publication **I** reveals some critical limitations of the POD which need to be considered when employing POD for phase-averaging. First, the available

data needs to contain information uniquely assignable to every phase-angle. For a spatially oscillating jet, this implies that the jet needs to be visible within the acquired data through the complete period. Second, the oscillation should be captured within one dominant pair of modes. Preferably, the time-resolved mode coefficients of the two modes have a half-period phase-lag and exhibit sinusoidal temporal behavior. If these limitations are not obeyed by capturing only a part of the oscillating flow field or the primary modes contain more than one dominant frequency, the phase-angles extracted from the mode coefficients may tend to specific phase-angles, which yields an incorrect assignment of snapshots to phase-angles. The correct phase-angle allocation can be validated by inspecting the distribution of the allocated phase-angles. If no phase-locking occurs while measuring, the number of snapshots per phase-angle window should be approximately constant for a naturally oscillating flow field. Based on this limitation, an improved POD phase-averaging method is suggested in publication **I**. This improved method eliminates the limitation by enforcing an even distribution of snapshots over all phase-angles. Although this prevents the phase-angle bias, it does not fix the reasons and leaves uncertainties regarding the correct snapshot to phase-angle allocation. The reason for the discussed limitation is successfully eliminated by Sieber et al. (2016b). They introduce the spectral proper orthogonal decomposition (SPOD) that closes the gap between POD and Fourier decomposition. This combination accomplishes that each POD mode contains only one specific frequency. They use the flow field of publication **I** as a benchmark case revealing that the results improve significantly when using the SPOD. However, the SPOD requires time-resolved data. This requirement opposes the requirements for the searched phase-averaging method because it is based on high-speed PIV data. Furthermore, it does not provide a temporal correlation between individually acquired PIV planes in its pure form. However, the correlation between the planes may be achieved by an additional, simultaneously acquired PIV plane serving as a reference (Morton and Yarusevych, 2016). Due to the requirement on time-resolved PIV data and the additional effort required for the temporal correlation between the individual PIV planes, the SPOD is not further considered for phase-averaging.

Publication **I** identifies phase-averaging based on a reference signal as suitable for phase-averaging the flow field of a spatially oscillating jet. Indeed, it fulfills all requirements requested in the beginning of this section. However, it exhibits some limitations and drawbacks:

1. The success of the phase-averaging depends on the quality of the reference signal. A poorly conditioned signal may yield wrong phase-angle allocations that result in blurring of flow structures. The running autocorrelation used for identifying the period starting points alleviates this problem because it is less susceptible to noise due to its statistical approach. Nonetheless, the choice of a signal fragment for the autocorrelation introduces a certain degree of subjectivity. An inappropriate fragment may impose a frequency, which degrades the quality of the results. A fragment of approximately one half to one oscillation periods is used in publications **I**-**IV**. The fragment starts at the first zero crossing of the reference signal, which does not necessarily provide a unique period starting point, but it ensures a constant, reproducible quality.

2. A phase-lag between the position where the reference signal is acquired and the flow field that is phase-averaged is present in most cases. As long as the phase-lag is smaller than one period, the effect of the phase-lag is negligible. However, the phase-lag is of particular importance, when more than one period is captured inside a naturally oscillating flow field.

The proposed method is not able to capture previous periods inside the flow field because the duration of these periods may differ from that of the current period. Therefore, the structures from the previous periods are rather time-averaged instead of phase-averaged. With increasing temporal distance between the individual flow structure and the reference signal, this effect is intensified. This challenge is present in publications **I**-**III** because more than one oscillation period are captured inside the flow field. However, the constant jet force over the streamwise direction that is determined in publication **III** suggests that the effect of phase-lag on global quantities is not noticeable. In most scenarios investigated in publication **IV**, the flow field contains only flow structures of one oscillation period. Structures from the previous periods leave the measured volume within one oscillation period due to the convection by the crossflow.

3. The phase-averaging method is unable to capture corrupt oscillation periods such as the jet leaving one side and attaching to the same side again. This would disturb the phase-averaging process because the phase-angle allocation of the corresponding snapshots is wrong. An examination of the individual oscillation period lengths identified by the phase-averaging method allows to localize these oscillation periods and to omit the corresponding snapshots during phase-averaging. However, this potential issue was not observed in the present work, which indicates that the fluidic oscillator provides a continuous jet oscillation.

4. The employed phase-averaging technique is able to phase-average based on one dominant frequency. All flow structures not correlated to this dominant frequency are time-averaged and thus not identifiable. This disadvantage is of particular importance when the flow field exhibits two dominant frequencies. One example is the resonance frequency inside the angled oscillator (publication **I**). For small supply rates, the amplitude of the pressure oscillations inside the feedback channel is not high enough to affect the jet and the phase-averaging method works as expected. However, when further increasing the supply rate, the amplitude of the resonance frequency increases. It is suspected that at some point the resonance begins to influence the oscillation of the jet. For high supply rates, one publication associated to the present work proposes that the resonance phenomenon inside the angled oscillator causes the jet to jitter around its spatial oscillation (von Gosen et al., 2015). The phase-averaging method in its current form is not able to capture this effect. With small modifications, it may be possible to phase-average based on two frequencies. However, this squares the number of phase-averaging windows and, thus, the number of required snapshots for sufficient quality of the phase-averaged results. This immense number of required snapshots is not feasible for PIV measurements.

The quality of the phase-averaging technique may be improved by pursuing iterative approaches. For example, the phase-angle allocation may be improved by correlating the snapshots within one phase-angle window to the corresponding phase-averaged flow field. Then, the snapshots are weighted according to their degree of similarity and averaged within a phase-angle window again. This was also tried in the present work. However, no additional gain in quality was achieved. Instead, this iterative approach reduced the effective number of considered snapshots, which retained noise. However, it may be a suitable approach for other flow fields.

5.2 Internal Flow Field of a Fluidic Oscillator

The internal flow field of a fluidic oscillator is investigated in publication **II**. Publication **II** aims to identify the driving mechanisms for the spatial oscillation of the jet. It concludes that the volume flow through the feedback channels feeds into a recirculation bubble that pushes the jet to the other side. However, the limitation to one specific oscillator makes it challenging to distinguish between effect and cause of the oscillating jet. Therefore, it is left for future studies that include different oscillator geometries to validate this suggestion. Nevertheless, it is reasonable that the oscillation frequency is dependent on the volume flow through the feedback channel. Hence, the internal velocities dictated by the supply rate and the internal length scales govern the oscillation frequency, which was validated in later studies. Schmidt et al. (2017) reveal that the ratio between the oscillation frequency multiplied with a characteristic length (e.g., d_h) and the bulk outlet velocity is constant independent of the working fluid and oscillator scale. Therefore, the jet Strouhal number based on this particular design is constant as shown in publication **III**. This suggests that the results on the internal and external flow field of a fluidic oscillator are transferable to other studies investigating similar oscillators with different scales or working fluids. However, this is limited by compressibility effects. Von Gosen et al. (2015) reveal that the internal velocities inside the oscillator converge when the jet exit velocity approaches $\mathrm{Ma}_{jet} = 1$. Correspondingly, the oscillation frequency also converges, which causes the jet Strouhal number to change.

Publication **II** reveals that the jet properties of the spatially oscillating jet also oscillate temporally. The reasons are suggested to be a varying counter-pressure and changes in the effective outlet area. Although it is not differentiated between the reasons in publication **II**, it is plausible that the oscillating massflow is solely caused by the changing counter-pressure. It is anticipated that the massflow controller does not counteract the oscillation of the counter-pressure due to the system's inertia. This implies that the supply rate provided throughout the publications is the time-averaged supply rate. Instead of the oscillator being fed by steady supply rate, the oscillator is supplied by a steady pressure. The error made by the false assumption of a steady supply rate is small because the massflow oscillates only by approximately 5%. However, the steady pressure supply may have consequences for the comparison to other studies. For example, numerical studies often set a constant velocity as the inlet condition for achieving a certain massflow (e.g., Aram et al., 2017). These studies will most likely not capture the oscillating properties caused by the varying counter-pressure. However, the oscillation caused by changes in the effective outlet area are captured. Since in applications and experiments, it is not practicable to provide a constant supply of massflow, it is suggested to introduce a constant inlet pressure in numerical studies. The constant inlet pressure represents a more realistic boundary condition because it captures the complete temporal oscillation of the jet properties.

The oscillation of the jet properties as well as the variation in time of the deflection angle are characteristic for the investigated oscillator design. In publications **III** and **IV**, it is referred to as oscillation pattern that describes the oscillation of the jet. Publication **II** provides such an oscillation pattern for the angled oscillator including the maximum deflection angle and the temporal variation of the jet properties at the outlet. A similar characterization is provided by an associated publication (Ostermann et al., 2015) for the curved oscillator. These described oscillation patterns are used in publications **III** and **IV** for providing a characterization of the spatial oscillation. In both studies, the patterns are validated in the external flow field with and without a crossflow being present.

Publications **I** and **II** reveal that the angled oscillator exhibits some unexpected behavior of the oscillation pattern: with increasing supply rate, the maximum jet deflection angle decreases. Furthermore, a resonance phenomenon inside the feedback channels may affect the oscillation of the jet. Therefore, the oscillation pattern is dependent on the supply rate. This dependency is troublesome for the pursued research on the fundamental flow fields of spatially oscillating jets because the changing oscillation pattern would need to be considered for every supply rate individually, which increases the complexity of these studies. Therefore, the measurements are repeated for the curved oscillator that exhibits the same working principle (figure 2.1). The results are presented in an associated publication: Ostermann et al. (2015) reveal that the curved oscillator exhibits a larger deflection angle due to the diverging part of the nozzle acting as a Coanda surface. The streamlined geometry improves the performance of the oscillator in terms of pressure requirements. The oscillation pattern is not affected by the supply rate for the range of investigated supply rates (i.e., incompressible flow). Therefore, the curved oscillator was used in the subsequent research on the fundamental flow fields (i.e., publications **III** and **IV**).

The transferability of the findings regarding the internal flow field in publication **II** is controversial because the results are limited to one particular oscillator design and determined from two-dimensional measurements. Especially the two-dimensionality leaves uncertainties regarding the influence of the aspect ratio and boundary layer effects at the top and the bottom of the oscillator. Bobusch (2015) states that for an aspect ratio of one or higher, the internal dynamics do not change because boundary layer effects at the top and the bottom of the oscillator are negligible. Therefore, the results in publication **II** are not limited to one particular aspect ratio and may be transferred to higher aspect ratios (i.e., deeper cavities). The scale of the oscillator is also not a limitation because Schmidt et al. (2017) show that the oscillation frequency over the supply rate behavior is independent of the scale of the oscillator. This information was derived by comparing measurements on fluidic oscillators with different scales. In this comparison, the results from publication **II** are included. This supports that the finding of publication **II** are transferable to other studies employing the same oscillator design. However, this is limited by compressibility effects that are not captured in publication **II**.

5.3 Properties of a Spatially Oscillating Jet in a Quiescent Environment

Publication **II** visualizes the flow field of a spatially oscillating jet emitted into a quiescent environment. In corresponding associated publications, some jet properties are extracted from this flow field, which indicate that the jet properties differ significantly compared to a steady jet (Gaertlein et al., 2014; Ostermann et al., 2015). However, the limitation to two-dimensional data leaves uncertainties regarding the third dimension. Furthermore, it does not account for meandering of the jet, which may affect the jet properties. Motivated by these shortcomings, publication **III** investigates the three-dimensional flow field of the spatially oscillating jet. A moveable stereo PIV system provides three-dimensional data. It aims to quantify jet properties of a spatially oscillating jet emitted into a quiescent environment. The focus of publication **III** is the entrainment of a spatially oscillating jet because this provides an indication for the mixing performance. In order to make the results more transferable to applications, a wall encloses the oscillator outlet to block additional entrainment from upstream of the oscillator. The oscillator

outlet is installed flush with the wall. It is noteworthy that the divergent outlet of the nozzle is kept, although previous studies reveal that it is not necessary for generating a spatially oscillation jet (Bobusch et al., 2013b). However, the divergent outlet of the nozzle is added to the geometry in most studies because it extends the outlet, which is required when the oscillator is being installed at an inclination angle. Since the diverging outlet is suspected to affect the oscillation pattern of the jet, it is added to enable a better transferability of the results.

The jet properties of the spatially oscillating jet in publication **III** are compared to other jets. In order to make this comparison meaningful, the jet properties are determined using a cylindrical coordinate system with the origin coinciding with the point of rotation of the jet (i.e., the center of the nozzle throat). This approach allows for a better comparison to other jets because it considers the varying travel distance of the jet depending on its instantaneous deflection angle. This approach requires highly resolved three-dimensional flow field data whose acquisition requires considerable effort. Therefore, the data in publication **III** is limited to three supply rates only. However, the general trends identified for these supply rates may allow future studies to better judge the jet properties by using a Cartesian coordinate system. This may simplify the acquisition of the velocity data in the future. It may also be possible to correct the properties from Cartesian coordinates by considering the instantaneous deflection angle based on a pressure signal from inside the oscillator in addition to the flow field information provided in publications **II** and **III**.

The entrainment of the spatially oscillating jet is found to be significantly enhanced compared to a conventional steady jet (publication **III**). This is contrary to earlier studies that quantify the entrainment to be smaller than that of a steady jet (Mi et al., 2001; Raman et al., 1993; Srinivas et al., 1988). Publication **III** identifies the reason for this difference: the previous studies measured the entrainment of a planar spatially oscillating jet. In this work, a three-dimensional jet is investigated with an outlet aspect ratio of one. In this scenario, most entrainment comes from the direction normal to the oscillation plane. With increasing aspect ratio, the ratio between the entrainment from the normal direction and the total entrainment decreases and so does the benefit over steady jets. For planar jets, the entrainment from the normal direction is negligible compared to the total entrainment, which reduces the beneficial effect of spatial oscillations on the entrainment. One may suspect that one reason for the comparably high entrainment are the head vortices that are present in the flow field because similar vortices are identified to be the reason for the high entrainment of pulsed jets. However, the vortices would entrain fluid from all directions equally not only from the direction normal to the oscillation plane. Therefore, it is suggested that the spatial oscillation of the jet increases the entrainment because the contact area between accelerated fluid and the quiescent environment in the direction normal to the oscillation plane is increased. In contrast, the entrainment from the lateral direction is suspected to be smaller than that of a steady jet because the jet partially entrains its own residuals. This argument is supported by the earlier studies on the planar jet that quantify the entrainment to be less than that of a steady jet. The enhanced entrainment for the normal direction implies that a smaller aspect ratio may be beneficial to enhance the entrainment further. However, when reducing the aspect ratio below one, the boundary layer at the top and the bottom of the oscillator may have an effect that is not captured in the present study. Therefore, it is left for future parametric studies to optimize the aspect ratio for a maximum of entrainment. Furthermore, the oscillation pattern of the oscillator is expected to have a significant impact on the entrainment, which needs also to be quantified in future studies.

Beside the entrainment, the jet force is of interest in various applications. For example, flow control applications usually compare flow control concepts by considering the momentum coefficient C_μ that involves the jet force. The momentum coefficient is the ratio between momentum of the jet and momentum of a crossflow. In most studies, the momentum coefficient is estimated from the theoretical bulk velocity. Alternatively, it is measured using a balance. In both cases, the actual jet momentum is underestimated. This is due to the fact that the momentum coefficient is based on the jet bulk velocity, which does not consider local peaks in jet velocity that are evident in the spatially oscillating jet. In contrast, the momentum coefficient based on measurements of the force does not take into account the lateral force of the jet because the lateral force averages to zero over one oscillation period. Therefore, the correct estimation of the jet force magnitude is challenging. Publication **III** addresses this challenge by determining the jet force magnitude from the velocity field. In an incompressible flow field, the jet force magnitude should stay constant. However, a small decrease in magnitude with distance to the nozzle is expected because of turbulent dissipation, a streamwise pressure gradient, and small velocities not being captured by the PIV system. In publication **III**, the determined jet force stays constant over the streamwise coordinate, which provides additional support for the quality of the data. It also validates the correct determination of the entrainment. The actual jet force magnitude exceeds the jet force based on the theoretical bulk velocity by up to 30%. Therefore, future studies considering the momentum coefficient of a spatially oscillating jet should take into account that the actual momentum coefficient exceeds the theoretical coefficient. For other oscillation patterns and thus oscillator designs, it is expected that the offset differs from the 30%. Furthermore, compressibility effects need to be considered. However, it is reasonable that for all spatially oscillating jets, the actual jet force always exceeds the theoretical one.

Throughout publication **III**, it is questioned how much the oscillation pattern influences the individual findings. Due to the limitation to one specific design, it is challenging to distinguish between the effects caused by the temporal oscillation and the effects caused by the spatial oscillation. One example for this dilemma are the head vortices that are alternately created at either side when the jet is fully deflected (publication **III**). On the one hand, these vortices may be caused by the spatial oscillation. On the other hand, it may be an effect of a sudden increase in jet momentum similar to pulsed jets. The results indicate that the spatial oscillation causes the vortices because both spatially oscillating jets created by the angled and the curved oscillator create these vortices although the oscillation patterns differ (publications **II** and **III**). From an Eulerian perspective at one fixed position in the external flow field, the velocity amplitude caused by the temporal oscillation (i.e., $\pm 15\%$) is considerably smaller than the velocity amplitude caused by the spatial oscillation (i.e., $\pm 100\%$). Hence, it is anticipated that the temporal oscillation does not significantly affect the flow field. However, it requires future studies to validate this. An example would be to use a rotating Pitot tube that emits the spatially oscillating jet. This academic scenario would not involve a temporal oscillation of jet properties. Therefore, it would certainly extend the understanding of the mechanisms.

5.4 The Spatially Oscillating Jet Interacting with a Crossflow

In publications **I** to **III**, the spatially oscillating jet is emitted into a quiescent environment. This scenario was chosen because its resulting symmetry simplifies the investigation. It is a suitable scenario to explain the basic mechanism inside the fluidic oscillator as well as comparing the jet properties of a spatially oscillating jet to that of a steady jet. However, it leaves the open question how the jet interacts with a crossflow as it does in most applications. For that reason, publication **IV** investigates the interaction between the spatially oscillating jet and a crossflow building on the findings from the previous publications.

Publication **IV** examines the effect of the velocity ratio and the oscillation frequency on the flow field. It is shown that changing the oscillation frequency without changing the velocity ratio does not influence the normalized flow field. Therefore, the dynamics are not affected by the oscillation frequency. This implies that the flow field dynamic is not affected by the oscillation frequency when the velocity ratio is kept constant. The flow field dynamic is usually characterized by the Strouhal number. The linear dependency between supply rate and oscillation frequency of the employed fluidic oscillator causes this Strouhal number to be solely dependent on the velocity ratio. This limits the parameters that affect the flow field to one in this study: the Strouhal number coupled with the velocity ratio. On the one hand, this coupling is beneficial because it enhances the transferability to other studies using the same oscillator design. For the same oscillator design, these studies experience the same Strouhal number to velocity ratio coupling independently of the oscillator size or working fluid. This is because the product of a characteristic length scale and oscillation frequency is solely dependent on the supply rate in the incompressible flow regime as suggested by Schmidt et al. (2017). On the other hand, the coupling between Strouhal number and velocity ratio is disadvantageous because it is not possible to distinguish between effects caused by the Strouhal number and effects caused by the velocity ratio. However, some unproven suggestions are made in publication **IV** based on experience with similar flow features in other flow fields. These assumptions remain to be validated. This may be done experimentally with a different oscillator concept that allows to change supply rate and oscillation frequency independently. One example for achieving this decoupling is a two-stage fluidic oscillator as suggested by Bauer et al. (2014). Another possibility is replacing the feedback channels with a pressure supply controlled by switching valves that force a defined frequency of the jet's spatial oscillation.

The three-dimensional, phase-averaged flow field of a spatially oscillating jet in a crossflow consists of various flow features that are suspected to have a significant impact on the performance of spatially oscillating jets in applications. For example, the jet trajectory provides information about the regions that are affected by the jet. In publication **IV**, the jet trajectory is extracted from the envelope of streakvolumes because this approach is found to be the only approach yielding reasonable results despite the spatial oscillation. The investigated oscillating jet does not penetrate into the crossflow in the wall-normal direction as much as a conventional steady jet. Due to this shallow trajectory, the jet stays close to the wall. If this is advantageous or disadvantageous depends on the application. The weak penetration into the wall-normal direction is in favor of a considerable penetration into the spanwise direction. This is beneficial in most applications because the jet is able to affect a larger area downstream of the jet orifice. Therefore, one spatially oscillating jet may replace several steady jets, which may reduce the amount of

the required supply rate. The penetration into the crossflow is dependent on the velocity ratio. Similar to steady jets, a higher velocity ratio yields a deeper penetration into the crossflow. The penetration is also expected to be linked to the oscillation pattern. The long dwelling times of the jet at its maximum deflection is suspected to allow the jet to penetrate deeper into the spanwise direction. In contrast, the short switching times prevent the jet from penetrating deeper into the wall-normal direction. Hence, a more sinusoidal movement of the jet is presumed to achieve a deeper penetration into the wall-normal direction in favor of a smaller penetration into the spanwise direction. This hypothesis may be validated by investigating different types of fluidic oscillators or imposing specific oscillation patterns using switching valves instead of the feedback channels.

Several vortices are identified inside the flow field of a spatially oscillating jet that interacts with a crossflow. Their behavior and existence are dependent on the Strouhal number and velocity ratio. For small Strouhal numbers, two streamwise oriented vortices that are similar to the counter-rotating vortex pair of steady jets are created at either side of the jet. When the jet is deflected, the vortices differ in strength whereas the vortex between jet and wall is weaker. When the jet is fully deflected and the penetration into the crossflow is insufficient, the distance between the wall and the jet may be too small for the second vortex to form. The described behavior compares well to a vortex-generating jet with a changing deflection angle. These vortices are considered to be one of the driving mechanism behind the effectivity of fluidic oscillators in flow control applications. The vortices induce a significant amount of lateral and normal velocity inside the flow field, which increases the mixing performance. For separation control, this is also beneficial because the vortices transport energetic fluid from the crossflow towards the wall.

With increasing Strouhal number, the crossflow is not able to adapt to the changing deflection angle of the jet. Publication **IV** shows for this case, that the vortices are created when the jet is fully deflected. The distance between the same vortices created in two periods decreases because the convection of the vortices during one period declines with the Strouhal number. Eventually, the phase-averaged flow field is supposed to approach the time-averaged flow field. From an application perspective, this effect is most likely beneficial because it produces a quasi-steady system of streamwise oriented vortices. Therefore, one spatially oscillating jet can replace two vortex generating jets that would be required for achieving a similar system of vortices. However, for high Strouhal numbers, a quasi-steady wake forms downstream of the jet. This wake is probably disadvantageous because it causes drag. The drag is expected to exceed the drag of vortex generating jets or passive vortex generators that cause a smaller wake. Presumably, this disadvantage is alleviated by decreasing the inclination angle between jet and crossflow. This would reduce the size of the wake while keeping the quasi-stationary behavior of the vortices. It is left for future studies to validate this suggestion.

The data in publication **IV** is limited to the phase-averaged flow field because phase-averaging is necessary to compose the three-dimensional flow field from the individually measured planes. In section 5.1, it is discussed that phase-averaging eliminates all flow features not correlated to the dominant frequency. Hence, unsteady flow features known from steady jets in crossflow may also be present in the flow field of the spatially oscillating jet although they are not captured in the results due to the phase-averaging (e.g., shear layer vortices, wake vortices, and the horseshoe vortex). In fact, the numerical study of Hossain et al. (2017) identifies some

unsteady vortex structures inside the three-dimensional, time-resolved flow field, which are not captured in publication **IV** because their behavior does not correlate to the oscillation frequency. It is unknown whether these flow features have a dominant effect on the flow field and the effectiveness of spatially oscillating jets. Based on the Strouhal number, it may be argued that for high Strouhal numbers, the influence of the stochastic flow features vanishes in comparison to the dominant streamwise oriented vortices because the crossflow is not able to adapt to these stochastic structures. However, numerical studies are required to validate this assumption and to provide a more detailed description of flow features that are not identified in publication **IV**.

Overall, the results of publication **IV** provide an overview of the flow structures inside the fundamental flow field of a spatially oscillating jet in interaction with a crossflow. The results are suitable to be used for validation of numerical studies, which was already done by Hossain et al. (2017) and Aram et al. (2018). Furthermore, the results provide a foundation for future parametric studies. The experimental effort involved in publication **IV** suggests that numerical studies are more appropriate for a parametric study. Focus of future studies should be the oscillation pattern, the decoupling of velocity ratio and Strouhal number, and different installation angles.

5.5 Concluding Remarks & Future Work

The present work analyzes the fundamental flow field properties of spatially oscillating jets. The included publications build on each other with increasing flow field complexity. Eventually, the publications pave the way to investigate the three-dimensional flow field of spatially oscillating jets emitted into a quiescent environment and into a crossflow. The results reveal the basic mechanisms and flow field properties of spatially oscillating jets, which enables constructive parametric studies and optimization of specific flow field properties. Characteristic properties of the flow field that are relevant for applications are compared to other jets (i.e., steady and pulsed jets). This allows identifying flow field properties that may contribute to the high effectiveness of fluidic oscillators in specific applications. These are the increased spanwise effect of the oscillating jet, the comparably high entrainment, and the streamwise oriented vortices formed inside a crossflow.

Although the work is only limited to few parameters, the potential influence of other parameters is discussed. Throughout the publications and especially in chapter 5 of the present work, suggestions are made how to optimize the properties according to the needs of specific applications. Furthermore, the previous sections discuss the transferability of the individual findings. However, these suggestions require validation. Numerical studies are especially suitable for validating the suggestions of this work because they are able to capture a much larger space of parameters than experimentally feasible. Furthermore, numerical studies are capable of acquiring the three-dimensional, time-resolved flow field, which enables to identify flow features that are not captured in the present work due to the necessity of phase-averaging. The presented data allows validating these numerical studies thereby approving the numerical approach. Possibly, the data set also allows the confirmation of simplified scenarios to reduce computational costs.

The previous sections of this chapter address several questions, which are left open by the publications and suggest specific future work. Besides these publication-specific questions many other, more general questions regarding the implementation of fluidic oscillators in applications

remain:

1. The present work investigates the fundamental flow field and extracts flow features that may be beneficial for examples for mixing enhancement or separation control. However, the fundamental flow field is not able to resolve the actual effect in these applications. It is proposed for future studies to quantify the mixing performance of a spatially oscillating jet. For example, simultaneous PIV and planar laser induced fluorescence measurements in a water tunnel allow for quantifying the mixing performance and validating the reasons for this. For quantifying the effect in separation control, the fundamental flow field may be extended by a crossflow separation to identify how the flow features actually aid in avoiding this separation.

2. The investigation on the fundamental flow field identifies some flow field properties that are suspected to be beneficial in various applications. However, these beneficial properties are not free of cost. It is required to assess the efficiency of fluidic oscillators and spatially oscillating jets in terms of energy requirements.

3. The influence of compressibility effects is omitted in the present work. However, in most applications of fluidic oscillators that involve gas as a working fluid compressibility effects are to be expected. Therefore, it needs to be investigated how compressibility effects alter the fundamental flow field. Some first experimental studies are already conducted on this topic. One example is the associated publication by von Gosen et al. (2015) that is not included in the present work because it would go beyond the scope. Von Gosen et al. (2015) confirm that the working principle of a fluidic oscillator is not affected by compressibility effects. In fact, fluidic oscillators are even able to emit a supersonic, oscillating jet. The properties of this jet are expected to significantly differ from that of the incompressible jet.

4. Most applications use an array of fluidic oscillators for generating several spatially oscillating jets instead of one isolated one. So far, it is unknown how the flow field is affected by neighboring spatially oscillating jets. It is anticipated that the interaction depends on the distance between the oscillators and whether the oscillation is synchronized or random. So far, most studies use randomly oscillating jets, which suggests that the interaction between neighboring jets does not hinder the effectivity of spatially oscillating jets. However, the knowledge on the fundamental interaction between neighboring, spatially oscillating jets is required to allow further optimization. Investigating the flow field of multiple oscillators involves several new challenges. Especially multiple oscillators at random phase impose the challenge of phase-averaging. Although phase-averaging based on several conditions (i.e., the individual oscillation periods for each oscillator) is generally possible, it is not feasible because it requires an unrealistic amount of data for achieving a sufficient number of samples per phase-angle window. Hence, an investigation of multiple oscillating jets is limited to time-averaged flow fields. The present work helps with interpreting these time-averaged flow fields and discussing the interaction between neighboring spatially oscillating jets.

The suggested future studies significantly increase the flow field complexity and introduce several new parameters, which prevents measurements that are as extensive as those performed in the present work. However, the fundamental results of the present work enable to understand

and discuss the increased complexity while the amount of available data is reduced. Therefore, the information on the fundamental flow fields of the present work provides a foundation for a more detailed analysis and optimization of spatially oscillating jets for specific applications.

Bibliography

(excluding bibliography of publications I-IV)

Angrist, S. W. Fluid control devices. *Scientific American*, 211(6):80–89, 1964. ISSN 00368733.

Aram, S., Lee, Y., Shan, H., & Vargas, A. Computational fluid dynamic analysis of fluidic actuator for active flow control applications. *AIAA Journal*, pages 1–10, 2017. doi:10.2514/1.j056255.

Aram, S., Shan, H., Ostermann, F., & Woszidlo, R. Computational validation and analysis of interaction of a sweeping jet and an attached turbulent flow. In *56th AIAA Aerospace Sciences Meeting*. American Institute of Aeronautics and Astronautics, 2018. doi:10.2514/6.2018-1798.

Arwatz, G., Fono, I., & Seifert, A. Suction and oscillatory blowing actuator modeling and validation. *AIAA Journal*, 46(5):1107–1117, 2008. doi:10.2514/1.30468.

Bauer, M., Lohse, J., Haucke, F., & Nitsche, W. High-lift performance investigation of a two-element configuration with a two-stage actuator system. *AIAA Journal*, 52(6):1307–1313, 2014. doi:10.2514/1.j052639.

Becker, H. A. & Massaro, T. A. Vortex evolution in a round jet. *Journal of Fluid Mechanics*, 31 (03):435–448, 1968. doi:10.1017/s0022112068000248.

Bergh, H. & Tijdeman, H. Theoretical and experimental results for the dynamic response of pressure measuring systems. *Nationaal lucht-en ruimtevaartlaboratorium*, 1965. doi:10.13140/2.1.4790.1123.

Bobusch, B. C., Woszidlo, R., Bergada, J. M., Nayeri, C. N. N., & Paschereit, C. O. Experimental study of the internal flow structures inside a fluidic oscillator. *Experiments in Fluids*, 54(6), 2013a. doi:10.1007/s00348-013-1559-6.

Bobusch, B. C., Woszidlo, R., Krüger, O., & Paschereit, C. O. Numerical investigations on geometric parameters affecting the oscillation properties of a fluidic oscillator. In *21st AIAA Computational Fluid Dynamics Conference*. American Institute of Aeronautics and Astronautics, 2013b. doi:10.2514/6.2013-2709.

Bobusch, B. C. *Fluidic devices for realizing the shockless explosion combustion process*. Doctoral thesis, Technische Universität Berlin, 2015. doi:10.14279/depositonce-4351.

Boillot, A. & Prasad, A. K. Optimization procedure for pulse separation in cross-correlation PIV. *Experiments in Fluids*, 21(2):87–93, 1996. doi:10.1007/bf00193911.

Bremhorst, K. Unsteady subsonic turbulent jets. In *Recent Developments in Theoretical and Experimental Fluid Mechanics*, pages 480–500. Springer Berlin Heidelberg, 1979. doi:10.1007/978-3-642-67220-0_49.

Bremhorst, K. & Hollis, P. G. Velocity field of an axisymmetric pulsed, subsonic air jet. *AIAA Journal*, 28(12):2043–2049, 1990. doi:10.2514/3.10520.

Brindise, M. C. & Vlachos, P. P. Proper orthogonal decomposition truncation method for data denoising and order reduction. *Experiments in Fluids*, 58(4), 2017. doi:10.1007/s00348-017-2320-3.

Campagnuolo, C. J. & Lee, H. C. Review of some fluidic oscillators. Technical Report HDL-TR-1438, Harry Diamond Laboratories, Washington, D.C., 1969.

Cerretelli, C. & Kirtley, K. Boundary layer separation control with fluidic oscillators. *Journal of Turbomachinery*, 131(4), 2009. ISSN 0889504X. doi:10.1115/1.3066242.

Craven, P. & Wahba, G. Smoothing noisy data with spline functions. *Numerische Mathematik*, 31:377–403, 1978. ISSN 0029-599X. doi:10.1007/bf01404567.

Crittenden, T. M. & Raghu, S. Combustion powered actuator with integrated high frequency oscillator. *International Journal of Flow Control*, 1(1):87–97, 2009. ISSN 1756-8250. doi:10.1260/1756-8250.1.1.87.

Crow, S. C. & Champagne, F. H. Orderly structure in jet turbulence. *Journal of Fluid Mechanics*, 48(03):547, 1971. doi:10.1017/s0022112071001745.

de Baar, J. H. S., Percin, M., Dwight, R. P., van Oudheusden, B. W., & Bijl, H. Kriging regression of PIV data using a local error estimate. *Experiments in Fluids*, 55(1), 2014. doi:10.1007/s00348-013-1650-z.

Eroglu, A. & Breidenthal, R. E. Structure, penetration, and mixing of pulsed jets in crossflow. *AIAA Journal*, 39(3):417–423, 2001. ISSN 0001-1452. doi:10.2514/2.1351.

Fearn, R. & Weston, R. P. Vorticity Associated with a Jet in a Cross Flow. *AIAA Journal*, 12 (12):1666–1671, 1974. ISSN 0001-1452. doi:10.2514/3.49576.

Feldwisch, J. M. Experimental study of a fluidic oscillator's time-resolved flow field. Bachelor's thesis, Hermann-Föttinger-Institut, Technische Universität Berlin, 2015.

Fric, T. F. & Roshko, A. Views of the transverse jet near field. *Physics of Fluids*, 31(9): 2390–2390, 1988. doi:10.1063/1.4738825.

Fric, T. F. & Roshko, A. Vortical structure in the wake of a transverse jet. *Journal of Fluid Mechanics*, 279:1, 1994. ISSN 0022-1120. doi:10.1017/S0022112094003800.

Gaertlein, S., Woszidlo, R., Ostermann, F., Nayeri, C., & Paschereit, C. O. The time-resolved internal and external flow field properties of a fluidic oscillator. *52nd AIAA Aerospace Sciences Meeting*, 2014. doi:10.2514/6.2014-1143.

Garcia, D. A fast all-in-one method for automated post-processing of PIV data. *Experiments in Fluids*, 50(5):1247–1259, 2010. ISSN 1432-1114. doi:10.1007/s00348-010-0985-y.

Godbersen, P. Experimental investigation of lagrangian structures in the time-resolved, three-dimensional flow field of a spatially oscillating jet in crossflow. Master's thesis, Hermann-Föttinger-Institut, Technische Universität Berlin, 2017.

Gregory, J. & Tomac, M. N. A Review of Fluidic Oscillator Development. *43rd AIAA Fluid Dynamics Conference*, 2013. doi:10.2514/6.2013-2474.

Gregory, J. W., Sullivan, J. P., & Raghu, S. Visualization of jet mixing in a fluidic oscillator. *Journal of Visualization*, 8(2):169–176, 2005. doi:10.1007/bf03181660.

Gregory, J. W., Sullivan, J. P., Raman, G., & Raghu, S. Characterization of the microfluidic oscillator. *AIAA Journal*, 45(3):568–576, 2007. doi:10.2514/1.26127.

Gregory, J. W., Gnanamanickam, E. P., Sullivan, J. P., & Raghu, S. Variable-frequency fluidic oscillator driven by a piezoelectric bender. *AIAA Journal*, 47(11):2717–2725, 2009. doi:10.2514/1.44078.

Gärtlein, S. The time-resolved internal flow field of a fluidic oscillator. Master's thesis, Hermann-Föttinger-Institut, Technische Universität Berlin, 2014.

Gruber, M. R., Nejadt, A. S., Chen, T. H., & Dutton, J. C. Mixing and penetration studies of sonic jets in a mach 2 freestream. *Journal of Propulsion and Power*, 11(2):315–323, 1995. doi:10.2514/3.51427.

Guyot, D., Paschereit, C. O., & Raghu, S. Active combustion control using a fluidic oscillator for asymmetric fuel flow modulation. *International Journal of Flow Control*, 1(2):155–166, 2009. ISSN 1756-8250. doi:10.1260/175682509788913335.

Haller, G. & Yuan, G. Lagrangian coherent structures and mixing in two-dimensional turbulence. *Physica D: Nonlinear Phenomena*, 147(3-4):352–370, 2000. doi:10.1016/s0167-2789(00)00142-1.

Hossain, M. A., Prenter, R., Lundgreen, R. K., Agricola, L., Ameri, A., Gregory, J. W., & Bons, J. P. Investigation of crossflow interaction of an oscillating jet. In *55th AIAA Aerospace Sciences Meeting*. American Institute of Aeronautics and Astronautics, 2017. doi:10.2514/6.2017-1690.

Jentzsch, M. P., Taubert, L., & Wygnanski, I. J. On the use of sweeping jets to trim and control a tailless aircraft model. In *35th AIAA Applied Aerodynamics Conference*. American Institute of Aeronautics and Astronautics, 2017. doi:10.2514/6.2017-3042.

Jeong, J. & Hussain, F. On the identification of a vortex. *Journal of Fluid Mechanics*, 285:69, 1995. doi:10.1017/s0022112095000462.

Johari, H., Pacheco-Tougas, M., & Hermanson, J. Penetration and mixing of fully modulated turbulent jets in crossflow. *AIAA Journal*, 37(7):842–850, 1999. doi:10.2514/2.7532.

Keane, R. D. & Adrian, R. J. Optimization of particle image velocimeters. I. double pulsed systems. *Measurement Science and Technology*, 1(11):1202–1215, 1990. doi:10.1088/0957-0233/1/11/013.

Kelso, R. M. & Smits, A. J. Horseshoe vortex systems resulting from the interaction between a laminar boundary layer and a transverse jet. *Physics of Fluids*, 7(1):153, 1995. ISSN 10706631. doi:10.1063/1.868736.

Kelso, R. M., Lim, T. T., & Perry, A. E. An experimental study of round jets in cross-flow. *Journal of Fluid Mechanics*, 306:111, 1996. ISSN 0022-1120. doi:10.1017/S0022112096001255.

Kirshner, J. M. & Katz, S. *Design Theory of Fluidic Components*. Academic Press Inc, 1975. ISBN 978-0-12-410250-7.

Koklu, M. & Owens, L. R. Comparison of sweeping jet actuators with different flow-control techniques for flow-separation control. *AIAA Journal*, 55(3):848–860, 2017. doi:10.2514/1.j055286.

Lacarelle, A. & Paschereit, C. O. Increasing the Passive Scalar Mixing Quality of Jets in Crossflow With Fluidics Actuators. *Journal of Engineering for Gas Turbines and Power*, 134 (2):21503, 2012. ISSN 07424795. doi:10.1115/1.4004373.

Mahesh, K. The interaction of jets with crossflow. *Annual Review of Fluid Mechanics*, 45(1): 379–407, 2013. ISSN 0066-4189. doi:10.1146/annurev-fluid-120710-101115.

Margason, R. J. Fifty Years of Jet in Cross Flow Research. *AGARD conference proceedings*, 538, 1993.

Martinke, S. Experimentelle Erfassung eines periodischen, dreidmensionalen Strömungsfeldes mittels Stereo-PIV. Bachelor's thesis, Hermann-Föttinger-Institut, Technische Universität Berlin, 2016.

Mi, J., Nathan, G. J., & Luxton, R. E. Mixing Characteristics of a Flapping Jet from a Self-Exciting Nozzle. *Flow, Turbulence and Combustion*, 67(1):1–23, 2001. ISSN 13866184. doi:10.1023/A:1013544019463.

Morton, C. & Yarusevych, S. Reconstructing three-dimensional wake topology based on planar PIV measurements and pattern recognition analysis. *Experiments in Fluids*, 57(10), 2016. doi:10.1007/s00348-016-2240-7.

Muppidi, S. & Mahesh, K. Study of trajectories of jets in crossflow using direct numerical simulations. *Journal of Fluid Mechanics*, 530:81–100, 2005. ISSN 0022-1120. doi:10.1017/S0022112005003514.

Muppidi, S. & Mahesh, K. Two-dimensional model problem to explain counter-rotating vortex pair formation in a transverse jet. *Physics of Fluids*, 18(8):085103, 2006. doi:10.1063/1.2236304.

Ostermann, F., Woszidlo, R., Nayeri, C., & Paschereit, C. O. Experimental Comparison between the Flow Field of Two Common Fluidic Oscillator Designs. *53rd AIAA Aerospace Sciences Meeting*, 2015. doi:10.2514/6.2015-0781.

Ostermann, F., Godbersen, P., Woszidlo, R., Nayeri, C. N., & Paschereit, C. O. Sweeping jet from a fluidic oscillator in crossflow. *Physical Review Fluids*, 2(9), 2017. doi:10.1103/physrevfluids.2.090512.

Papamoschou, D. & Hubbard, D. G. Visual observations of supersonic transverse jets. *Experiments in Fluids*, 14(6):468–476, 1993. doi:10.1007/bf00190201.

Perrin, R., Braza, M., Cid, E., Cazin, S., Barthet, A., Sevrain, A., Mockett, C., & Thiele, F. Obtaining phase averaged turbulence properties in the near wake of a circular cylinder at high reynolds number using POD. *Experiments in Fluids*, 43(2-3):341–355, 2007. doi:10.1007/s00348-007-0347-6.

Platzer, M. F., Simmons, J. M., & Bremhorst, K. Entrainment characteristics of unsteady subsonic jets. *AIAA Journal*, 16(3):282–284, 1978. ISSN 0001-1452. doi:10.2514/3.7523.

Raghu, S. Feedback-free fluidic oscillator and method. US Patent 6,253,782, 2001.

Raman, G., Hailye, M., & Rice, E. J. Flip-flop jet nozzle extended to supersonic flows. *AIAA Journal*, 31(6):1028–1035, 1993.

Raman, G. & Cornelius, D. Jet mixing control using excitation from miniature oscillating jets. *AIAA Journal*, 33(2):365–368, 1995. ISSN 0001-1452. doi:10.2514/3.12444.

Raman, G. & Raghu, S. Miniature fluidic oscillators for flow and noise control - transitioning from macro to micro fluidics. *AIAA Fluids 2000 Conference and Exhibit*, 2000. doi:10.2514/6.2000-2554.

Raman, G. & Raghu, S. Cavity Resonance Suppression Using Miniature Fluidic Oscillators. *AIAA Journal*, 42(12):2608–2612, 2004. doi:10.2514/1.521.

Scarano, F. & Riethmuller, M. L. Advances in iterative multigrid PIV image processing. *Experiments in Fluids*, 29(7):S051–S060, 2000. doi:10.1007/s003480070007.

Schlichting, H. & Gersten, K. *Grenzschicht-Theorie (German Edition)*. Springer, 2006. ISBN 3540230041.

Schmidt, H.-J., Woszidlo, R., Nayeri, C. N., & Paschereit, C. O. Drag reduction on a rectangular bluff body with base flaps and fluidic oscillators. *Experiments in Fluids*, 56(7), 2015. ISSN 1432-1114. doi:10.1007/s00348-015-2018-3.

Schmidt, H. J., Woszidlo, R., Nayeri, C. N., & Paschereit, C. O. Separation control with fluidic oscillators in water. *Experiments in Fluids*, 58(8):106, 2017. ISSN 1432-1114. doi:10.1007/s00348-017-2392-0.

Seele, R., Tewes, P., Woszidlo, R., McVeigh, M. A., Lucas, N. J., & Wygnanski, I. J. Discrete Sweeping Jets as Tools for Improving the Performance of the V-22. *AIAA Journal of Aircraft*, 46(6):2098–2106, 2009. doi:10.2514/1.43663.

Sforza, P. M., Steiger, M. H., & Trentacoste, N. Studies on three-dimensional viscous jets. *AIAA Journal*, 4(5):800–806, 1966. ISSN 1533-385X. doi:10.2514/3.3549.

Sieber, M., Ostermann, F., Woszidlo, R., Oberleithner, K., & Paschereit, C. O. Lagrangian coherent structures in the flow field of a fluidic oscillator. *Physical Review Fluids*, 1(5), 2016a. ISSN 2469-990X. doi:10.1103/PhysRevFluids.1.050509.

Sieber, M., Paschereit, C. O., & Oberleithner, K. Spectral proper orthogonal decomposition. *Journal of Fluid Mechanics*, 792:798–828, 2016b. doi:10.1017/jfm.2016.103.

Sonnenberger, R., Graichen, K., & Erk, P. Fourier averaging: a phase-averaging method for periodic flow. *Experiments in Fluids*, 28(3):217–224, 2000. ISSN 1432-1114. doi:10.1007/s003480050381.

Spyropoulos, C. E. A sonic oscillator. In *Proceedings of the Fluid Amplification Symposium*, volume 3, pages 27–52, 1964.

Srinivas, T., Vasudevan, B., & Prabhu, A. Performance of Fluidically Controlled Oscillating Jet. In Liepmann, H. W. & Narasimha, R., editors, *Turbulence Management and Relaminarisation*, pages 485–494. Springer, 1988. ISBN 978-3-642-83283-3. doi:10.1007/978-3-642-83281-9_33.

Stouffer, R. D. & Bower, R. Fluidic flow meter with fiber optic sensor. US Patent 5,827,976, 1998.

Tomac, M. N. & Gregory, J. W. Internal jet interactions in a fluidic oscillator at low flow rate. *Experiments in Fluids*, 55(5), 2014. doi:10.1007/s00348-014-1730-8.

v. Krzywoblocki, M. Z. Jets - review of literature. *Jet propulsion*, 26(9):760–779, 1956. ISSN 0095-8751.

van Oudheusden, B. W., Scarano, F., van Hinsberg, N. P., & Watt, D. W. Phase-resolved characterization of vortex shedding in the near wake of a square-section cylinder at incidence. *Experiments in Fluids*, 39(1):86–98, 2005. doi:10.1007/s00348-005-0985-5.

Viets, H. Flip-Flop Jet Nozzle. *AIAA Journal*, 13(10):1375–1379, 1975. doi:10.2514/3.60550.

von Gosen, F., Ostermann, F., Woszidlo, R., Nayeri, C., & Paschereit, C. O. Experimental investigation of compressibility effects in a fluidic oscillator. *53rd AIAA Aerospace Sciences Meeting*, 2015. doi:10.2514/6.2015-0782.

Wang, C., Gao, Q., Wang, H., Wei, R., Li, T., & Wang, J. Divergence-free smoothing for volumetric PIV data. *Experiments in Fluids*, 57(1), 2016. doi:10.1007/s00348-015-2097-1.

Wang, C., Gao, Q., Wei, R., Li, T., & Wang, J. Weighted divergence correction scheme and its fast implementation. *Experiments in Fluids*, 58(5), 2017. doi:10.1007/s00348-017-2307-0.

Wassermann, F., Hecker, D., Jung, B., Markl, M., Seifert, A., & Grundmann, S. Phase-locked 3D3C-MRV measurements in a bi-stable fluidic oscillator. *Experiments in Fluids*, 54(3), 2013. doi:10.1007/s00348-013-1487-5.

Winter, M. Rekonstruktion und Optimierung eines Windkanals. Bachelor's thesis, Hermann-Föttinger-Institut, Technische Universität Berlin, 2015.

Wong, C. Y., Nathan, G. J., & Kelso, R. M. The naturally oscillating flow emerging from a fluidic precessing jet nozzle. *Journal of Fluid Mechanics*, 606, 2008. doi:10.1017/s0022112008001699.

Wygnanski, I. J. & Fiedler, H. Some measurements in the self-preserving jet. *Journal of Fluid Mechanics*, 38(3):577–612, 1969.

Xue, D., Zhang, C., & Crawfis, R. Rendering implicit flow volumes. In *IEEE Visualization 2004*. IEEE Computer Society, 2004. doi:10.1109/visual.2004.90.

Zaman, K. B. M. Q. Spreading characteristics and thrust of jets from asymmetric nozzles. In *34th AIAA Aerospace Sciences Meeting and Exhibit*, 1996. doi:10.2514/6.1996-200.

Associated Publications

Ostermann, F., Woszidlo, R., Gaertlein, S., Nayeri, C., & Paschereit, C. O. Phase-averaging methods for a naturally oscillating flow field. In *52nd Aerospace Sciences Meeting*. American Institute of Aeronautics and Astronautics, jan 2014. doi: 10.2514/6.2014-1142.

Gaertlein, S., Woszidlo, R., **Ostermann, F.**, Nayeri, C., & Paschereit, C. O. The time-resolved internal and external flow field properties of a fluidic oscillator. *52nd AIAA Aerospace Sciences Meeting*, jan 2014. doi: 10.2514/6.2014-1143.

Ostermann, F., Woszidlo, R., Nayeri, C., & Paschereit, C. O. Experimental Comparison between the Flow Field of Two Common Fluidic Oscillator Designs. *53rd AIAA Aerospace Sciences Meeting*, jan 2015. doi: 10.2514/6.2015-0781.

Von Gosen, F., **Ostermann, F.**, Woszidlo, R., Nayeri, C. N., & Paschereit, C. O. Experimental Investigation of Compressibility Effects in a Fluidic Oscillator. *53rd AIAA Aerospace Sciences Meeting*, jan 2015. doi: 10.2514/6.2015-0782.

Ostermann, F., Woszidlo, R., Nayeri, C. N., & Paschereit, C. O. The time-resolved flow field of a jet emitted by a fluidic oscillator into a crossflow. *54th AIAA Aerospace Sciences Meeting*, jan 2016. doi: 10.2514/6.2016-0345.

Sieber, M., **Ostermann, F.**, Woszidlo, R., Oberleithner, K., & Paschereit, C. O. Lagrangian coherent structures in the flow field of a fluidic oscillator. *Physical Review Fluids*, 1(5), 2016. ISSN 2469-990X. doi: 10.1103/PhysRevFluids.1.050509.

Ostermann, F., Woszidlo, R., Nayeri, C. N., & Paschereit, C. O. Effect of velocity ratio on the flow field of a spatially oscillating jet in crossflow. In *55th AIAA Aerospace Sciences Meeting*. American Institute of Aeronautics and Astronautics, jan 2017. doi: 10.2514/6.2017-0769.

Ostermann, F., Godbersen, P., Woszidlo, R., Nayeri, C. N., & Paschereit, C. O. Sweeping jet from a fluidic oscillator in crossflow. *Physical Review Fluids*, 2(9), 2017. ISSN 2469-990X. doi: 10.1103/physrevfluids.2.090512.

Aram, S., Shan, H., **Ostermann, F.**, & Woszidlo, R. Computational Validation and Analysis of Interaction of a Sweeping Jet and an Attached Turbulent Flow. In *56th AIAA Aerospace Sciences Meeting*. American Institute of Aeronautics and Astronautics, jan 2018. doi: 10.2514/6.2018-1798.

Woszidlo, R., **Ostermann, F.**, & Schmidt, H.-J. Fundamental Properties of Fluidic Oscillators for Flow Control Applications. *AIAA special issue (submitted)*. 2018.